Universidade do Porto
Faculdade de Engenharia
FEUP

MSc Thesis

Technology development and structural mechanics of composites built of spread tow thin-ply technology

Albertino José Castanho Arteiro

Porto, 2012

Universidade do Porto
Faculdade de Engenharia
FEUP

MSc Thesis

Technology development and structural mechanics of composites built of spread tow thin-ply technology

Albertino José Castanho Arteiro

Advisor
Prof. Dr. Pedro P. Camanho

Department of Mechanical Engineering (DEMec)
Faculty of Engineering (FEUP)
University of Porto (UP)

A Thesis submitted for the degree of
Master of Science in Mechanical Engineering
to the Faculty of Engineering, University of Porto

Porto, 2012

> *"We come to love not by finding a perfect person,*
> *but by learning to see an imperfect person perfectly"*
>
> Sam Keen

À Carina
e aos meus pais

Acknowledgements

First of all, I would like to express my gratitude to Prof. Dr. Pedro P. Camanho, my advisor, for the opportunity in collaborate in this work, for all the knowledge imparted during this thesis and the MSc course, and for all the ideas, advices, contributions, support, and availability during the development of this thesis.

I would like to thank all the support provided by Dr. Giuseppe Catalanotti during the development and execution of the experimental test program, and the indefatigable work done with the parametric model for the finite element analysis, the run of the simulations, and their postprocessing, without whom such work would not be possible.

I also would like to thank the help and valuable advising provided by Hilal Ercin, PhD candidate, during the development and execution of the experimental test program, particularly during organization, setup and specimens preparation.

I also express my gratitude to Dr. José Xavier, from the Center of Research and Technology of Agro-Environmental and Biological Sciences of the University of Trás-os-Montes e Alto Douro, for making possible the use of digital image correlation during the experimental program, for his availability to move to the Faculty of Engineering of the University of Porto bringing with him all the equipment, for his expertise, and for his patience during data processing.

I acknowledge all the help provided by Ing. Miguel Figueiredo, and all those who collaborated during the experimental program, for making possible the fulfillment of such experimental tests.

I also acknowledge Chomarat, Aldila, VX Aerospace, and Prof. S. W. Tsai, for providing the material used in the experimental program carried out on this thesis.

And because this thesis marks the end of a five years path at the Faculty of Engineering, I would like to express my heartfelt gratitude to my Professors and colleagues, and all those that, somehow, contributed for my professional and personal growth. Particularly I would like to thank Prof. Dr. António Torres Marques for the opportunity in collaborate in a grant for research initiation and for the fantastic advices, Prof. Dr. Paulo Tavares de Castro for all the encouraging, Prof. Dr. Marc Zupan for the ideas, advices, support, and encouraging provided since the day we met, Prof. Dr. António Ferreira for giving me the chance to participate in the course held by Prof. J. N. Reddy during the ICCS16, Prof. Dr. Francisco Pires, for the opportunity to participate in the study for the Colep CCL company, and Prof. Dr. Renato Natal Jorge and Dr. Marco Parente for the opportunity in collaborate in a grant for research initiation at such an early stage of my academic path.

Finally, I am totally grateful to my girlfriend, Carina, my parents, José Alberto and Maria Virgília, and all my family, for their patience, for wishing the best for me, and for expecting the best of me.

Abstract

When developing new manufacturing technologies and new composite materials, understanding their potential benefits and drawbacks with respect to manufacturing, processing, material properties, design, and cost-effectiveness is extremely important, in order to guarantee their successful introduction on the market. Due to the increasing use of carbon fiber reinforced polymers in the airframe, when promising new technologies appear, aircraft manufacturers try to follow up their development, aiming to improve the performance of the aircraft structures based on these materials.

One new technology of interest is the spread tow thin-ply technology, in which the produced laminates consist of particularly flat plies, with thicknesses as low as 0.02 mm. The potential benefits of such low grade plies are several. However, in spite of the several studies in the literature reporting the advantages of using thin plies (sublaminate scaling), this was not studied in detail in an industrial context.

In this thesis, the technology development of the spread tow thin-ply technology is assisted, in terms of planning and authoring an experimental program focused on the structural integrity of the thin-ply laminates, with particular emphasis in size effects, notched strength, bearing strength, and fracture toughness of such materials. In addition, analytical and numerical analyses were conducted in order to improve understanding and predict the mechanical behavior of thin-ply laminates.

The experimental results show that unrecoverable severe damage, such as extensive transverse cracking and delamination, are virtually absent in thin-ply laminates. However, this ability of thin-ply laminates to suppress damage development before failure may ultimately result in a material slightly more sensitive to notches and hole size effects. Still, no substantial differences were found either in the effects of hole size or in the notch sensitivity of the thin-ply laminates when compared with other carbon/epoxy systems designed for aircraft structural applications. Regarding the translaminar fracture toughness, taken in the literature as the main potential problem of these composite materials, in spite of the slightly lower laminate fracture toughness, the fracture toughness of the 0° ply was predicted as very similar to that of other carbon/epoxy systems used in the aircraft industry. In addition, a severe notch sensitivity was not observed in these materials. The bolt-bearing strength of the thin-ply laminates was also studied, and very interesting results were obtained, since the thin-ply laminates exhibited a superior performance over a carbon/epoxy system typically used in aircraft structural construction. This superior performance was attributed to the ability of thin-ply laminates to block onset and propagation of damage mechanisms such as delamination, fiber kinking, matrix cracking, and through-the-thickness shear cracking.

Due to the importance of accurate, physically-based and fast strength prediction methods for composite laminates with stress concentrations, particularly for preliminary sizing and for optimization of aircraft composite structures, fast design tools based on closed-form solutions were used in the prediction of size effects and notch sensitivity of thin-ply laminates. In addition to the ease of use, the closed-form models used in this thesis were able to reasonably predict both tensile and compressive notched responses of the thin-ply laminates. However, because it does not require any inverse identification from a notched experimental test, and due to its promising generality and versatility, the finite fracture mechanics model was considered to be the best suited one to predict the macroscopic size effects on carbon/epoxy composite laminates, as well as the notch sensitivity, by means of design charts and a recently introduced dimensionless parameter, designated *notch sensitivity factor*. Based on these predictions, despite some concerns regarding this issue, these closed-form models showed that the thin-ply materials do not exhibit a severe notch sensitivity, since their notched responses were not so different from those exhibited by the alternative carbon/epoxy systems, which is in agreement with the experimental results obtained.

To assess the effect of ply thickness and the effect of stitching in non-crimp fabrics on the interlaminar mechanical response of thin-ply laminates, a numerical study based on the finite element method was also carried out in this thesis. Zero-thickness decohesion elements were used to simulate delamination in finite element models of unnotched and open-hole laminates, aiming to assess the effect of ply thickness and the effect of stitching on the resistance to free-edge delamination onset. These numerical predictions showed that the introduction of an open-hole results in a substantial decrease of the resistance to delamination onset. Regarding the effect of ply thickness, the numerical predictions also showed that decreasing the ply thickness, the resistance to delamination onset increases, even when non-crimp fabric bi-layers are used and the number of interfaces for delamination is kept constant. On the other hand, regarding the effect of the number of interfaces for delamination (or effect of stitching), no conclusive results were obtained, since they were difficult to understand, and no physical explanation was found.

Resumo

Aquando do desenvolvimento de novas tecnologias de fabrico e de novos materiais compósitos, é extremamente importante perceber as suas potenciais vantagens e desvantagens no que diz respeito ao fabrico, ao processamento, às propriedades do novo material, ao projeto de componentes e à relação custo-benefício, de modo a garantir o seu sucesso aquando da sua introdução no mercado. Dado o crescente uso de materiais compósitos reforçados com fibra de carbono na fuselagem e outras estruturas da aviação, quando novas tecnologias promissoras surgem, os fabricantes de aeronaves procuram seguir o seu desenvolvimento, com o objetivo de melhorar a performance das estruturas fabricadas com estes materiais.

Uma tecnologia de elevado interesse é a tecnologia de fabrico de laminados ultrafinos conhecida por *tow spreading*, capaz de fabricar laminados constituídos por camadas ultrafinas, com espessuras que podem ser de 0.02 mm. As potenciais vantagens da utilização de laminados com camadas tão finas são diversas. Contudo, apesar dos vários estudos existentes na literatura reportando as vantagens da utilização de laminados com camadas ultrafinas, a sua aplicação não foi ainda estudada em detalhe num contexto industrial.

Com o trabalho desenvolvido nesta tese, pretende-se contribuir para o desenvolvimento tecnológico do *tow spreading*, em termos de planeamento e execução de um extenso programa experimental focado na integridade estrutural dos laminados ultrafinos, com particular ênfase na resistência ao entalhe, nos efeitos das dimensões do furo central na resistência mecânica destes laminados, na resistência ao esmagamento e na tenacidade à fratura destes materiais. Para além disso, foram conduzidas análises analíticas e numéricas com o objetivo de prever e, assim, melhor compreender o comportamento mecânico dos laminados ultrafinos.

Os resultados experimentais demostram que dano severo permanente, como fissuração transversal e delaminagem, são praticamente inexistentes nos laminados ultrafinos. Contudo, a capacidade destes laminados para suprimir o desenvolvimentos de dano antes da rotura pode, em última instância, conduzir a um material mais sensível ao entalhe e às dimensões do furo central. No entanto, não se verificaram diferenças substanciais relativamente a outros sistemas compósitos de carbono/epóxi tipicamente utilizados na indústria aeronáutica. Quanto à tenacidade à fratura translaminar, tida na literatura como sendo o maior potencial problema dos laminados ultrafinos, apesar da tenacidade à fratura do laminado ser ligeiramente inferior, as previsões para a tenacidade à fratura da camada a 0° dão valores muito próximos dos obtidos para laminados de carbono/epóxi usados na indústria aeronáutica. Para além disso, não se verificou qualquer tipo de comportamento frágil da parte dos laminados ultrafinos estudados. Foi ainda conduzido um estudo sobre a resistência dos laminados ultrafinos ao esmagamento em ligações aparafusadas, tendo-se obtido resultados muito interessantes, uma vez que a performance dos laminados ultrafinos foi superior à demonstrada pelos laminados de carbono/epóxi usados na construção de estruturas na indústria aeronáutica. A elevada resistência dos laminados ultrafinos ao esmagamento em ligações aparafusadas é atribuída à capacidade destes laminados para dificultar a iniciação e propagação de mecanismos de dano tais como a delaminagem, a microencurvadura das fibras, a microfissuração da matriz e as fissuras de corte através da espessura.

Dada a importância de dispôr de métodos cada vez mais precisos e eficientes para a previsão da resistência de laminados com concentrações de tensões, em particular para cálculo preliminar e otimização de estruturas aeronáuticas em materiais compósitos, são aqui utilizadas ferramentas de cálculo rápido baseadas em soluções simples para previsão dos efeitos das dimensões do furo central e previsão da sensibilidade dos laminados ultrafinos ao entalhe. Para além da facilidade de aplicação destes modelos, eles demonstraram-se capazes de prever razoavelmente o comportamento dos laminados ultrafinos com entalhes, quer em tração, quer em compressão. No entanto, entre os vários modelos utilizados, dado que não necessita de qualquer tipo de identificação inversa, e dada a sua promissora generalidade e versatilidade, o modelo da mecânica da fratura finita demonstrou ser o mais adequado para a previsão dos efeitos macroscópicos das dimensões dos entalhes nos laminados ultrafinos estudados, assim como da sua sensibilidade ao entalhe, através de cartas paramétricas e de um parâmetro adimensional denominado *fator de sensibilidade ao entalhe*. Baseando-se nestas previsões, e apesar das preocupações demonstradas relativamente ao comportamento à fratura destes materiais, os modelos utilizados demonstram que os laminados ultrafinos não apresentam um comportamento frágil, uma vez que a resposta na presença de um entalhe não demonstrou ser muito diferente da exibida por outros laminados de carbono/epóxi, confirmando os resultados experimentais obtidos.

De modo a estudar o efeito da espessura da camada e o efeito das “pregas” (“*stitching*”) em tecidos ortogonais denominados *non-crimp fabric* na resistência interlaminar de laminados ultrafinos, foi conduzido um estudo numérico em elementos finitos. Para simular delaminagem foram utilizados elementos coesivos, com o objetivo de estudar o efeito da espessura da camada e o efeito das “pregas” na resistência à iniciação de delaminagem nos bordos livres. As previsões obtidas com estes modelos mostraram que a introdução de um furo central conduz a uma diminuição substancial da resistência à iniciação de delaminagem. Relativamente ao efeito da espessura da camada, os resultados da análise numérica demostraram que diminuindo a espessura da camada, a resistência à iniciação de delaminagem aumenta, mesmo quando são utilizados *non-crimp fabrics* e quando o número de interfaces para delaminagem é mantido constante. Por outro lado, relativamente ao efeito do número de interfaces para delaminagem (ou efeito das “pregas”), não foram obtidos resultados conclusivos, uma vez que estes foram difíceis de interpretar, não tendo sido encontrada qualquer justificação física para os mesmos.

Contents

List of Figures

List of Tables

Chapter 1

Introduction

When developing new manufacturing technologies and new composite materials, understanding their potential benefits and drawbacks with respect to manufacturing, processing, material properties, design, and cost-effectiveness is extremely important to guarantee their successful introduction on the market. Due to the increasing use of carbon fiber reinforced polymers in the airframe, when promising new technologies appear, aircraft manufacturers try to follow up their development, aiming to improve the performance of the aircraft structures based on these materials. Herein, a new technology of interest, the spread tow thin-ply technology, is presented and its technology development assisted. In this chapter, a brief introduction to the increasing importance of composite materials in the design and development of new structures, particularly for the aircraft industry, is given. Then, the motivation and the objectives of this thesis are exposed. Finally, its organization, is presented.

1.1. Background

As the term indicates, a ***composite material*** arises from the macroscopic combination of two or more different materials, resulting in a third useful material with superior properties than those of the individual constituent materials acting independently [1–3]. Typically, composite materials refers to materials having strong fibers — continuous or non-continuous — or particles acting as the reinforcement, surrounded by a weaker matrix material, which distributes the reinforcements, protect them against all environmental influences, and also transfer the loads over them. Particularly, a composite may consist of polymers that have endless fibers imbedded in them, the so-called *fiber reinforced plastics* (FRP). Advanced FRP are often fabricated in the form of laminates, consisting of one or more thin layers, called *laminae* or *ply*, stacked together, each one oriented in a given direction.

However, man-made composites have existed for thousands of years [4, 5]. In fact, this concept of a *macroscopic combination of two or more different materials resulting in a third useful material* is common in nature. There are several examples of such materials in nature, such as the muscular systems in animals and wood, which comprise a combination of fibrous systems surrounded by a matrix material. The first evidences of man-made composite materials appeared in the Egyptian era, where straw and mud where burnt together by the Israelites to form tougher bricks for construction, and where strips of stems of the papyrus plant were laid up side by side and put on top of each other in perpendicular directions by the Egyptians to manufacture papyrus paper. Later, the Mongols invented the first composite bow using a combination of wood, bone and animal tissues, bonded with animal glue, pressed and wrapped with birch bark, providing the Mongols with smaller, incredibly manageable, and extremely powerful and accurate bows. Not too far, the Japanese samurai manufactured their swords combining a softer steel in the inner core of the blade with a hard steel, forged with a U shape, in the outer region of the blade, providing it with high toughness and high superficial hardness. In the 19th century, steel reinforced concrete appeared, revolutionizing architecture and civil engineering. But the advanced composite materials as they are known today gained shape in the 20th century, with the advent of the glass fibers in the 1930's, their application in the quickly growing aeronautic industry and in the naval industry, mainly during the world war II, the beginning of the space age in the 1950's, the first patent for production of carbon fibers in the 1960's, and the introduction of boron and aramid fibers in the late 1960's and early 1970's, respectively.

Even so, the high technology of composites has evolved in the aerospace industry only in the last thirty years, whose rapidly expanding applications in the recent past have provided much optimism for the future of this technologically advanced materials. Filament-wound pressure vessels using glass fibers were the first strength critical application of modern composites. After these, many US Air Force programs promoted the introduction of aircraft structures made of composites. The F-111 horizontal stabilizer was the first flight-worthy composite component. Then, that was followed by the production of composite parts such as stabilizers and rudders for military aircrafts such as the F-14, F-15 and F-16, and in the early 1980's composite materials start to be part of commercial aircrafts too, namely in the Boeing 767, the Antonov 124 and the Airbus A310-300. Nowadays, nearly all aircrafts use composites extensively [4].

Besides aircraft industry, application of advanced FRP is gradually increasing in a wide spectrum of industrial components and customers, gradually evolving from secondary non-load bearing applications to primary load bearing structural applications. One reason is because components made of composite materials can be engineered to offer outstanding mechanical (stiffness and strength), fatigue, ballistic, thermal, corrosion, and electromagnetic properties, always with reduced weight. Such characteristics promote/improve use of renewable energy and generally result in far more sustainable lifestyle. This is becoming even more apparent as the significance of life cycle assessment is being recognized. Another reason is due to all existing processing techniques. Composites give designers and engineers tremendous freedom in terms of both form and function. Compound curves and complex geometries can be readily incorporated, maximizing structural integrity and performance. Furthermore, composites also favor the development of integrated design when a part or component is suitable be manufactured in "*one shot*", avoiding laborious joining and fitting operations.

1.2. Thesis motivation

Knowledge of constituent material properties is important when defining a composite structure for a given application and in understanding how that structure will respond to the various stimuli likely to be imposed on it [6]. When new composites arise, resulting from the development of new manufacturing technologies, understanding their potential benefits and drawbacks with respect to manufacturing, processing, material properties, design, and cost-effectiveness is extremely important, in order to guarantee their successful introduction on the market.

Due to the increasing use of carbon fiber reinforced polymers (CFRP) in the airframe, when promising new technologies appear, aircraft manufacturers try to follow up their development, aiming to improve the performance of CFRP-based aircraft structures. One new technology of interest is the **spread tow technology**, in which the produced laminates consist of particularly flat plies, with thicknesses as low as 0.02 mm.

The potential benefits of such low grade plies are several. Per given laminate thickness, more plies can be accommodated, leading to a possibility of using smaller relative fiber angles in adjacent plies, which is considered beneficial when it comes to delamination between plies. In addition, there exists an in-situ effect characterized by a small strength increase of the thin plies contained within a given laminate thickness, and it is considered that the spread tow plies exhibit improved fiber orientation and distribution, potentially leading to fewer weak zones. However, in spite of the several studies in the literature reporting the advantages with respect to delamination of using thin plies (sublaminate scaling), this was not studied in detail in an industrial context. Furthermore, the in-situ effect and respective consequences needs to be further understood, and the improvements on fiber orientation and distribution exhibited by the spread tow plies are not quantified well yet.

1.3. Thesis objectives

This thesis aims to assist in the technology development of the spread tow thin-ply technology, in terms of planning and executing an experimental program. Hereby focus is placed on attempts to identify and explore potential benefits of such technology in a systematic manner. In addition, analytical and numerical analyses are conducted to improve the understanding and the prediction of the mechanical behavior of thin-ply laminates.

In addition to an accurate description of the current state-of-the-art, available test data, and literature review concerning the potential benefits of using laminates with thin plies, this thesis includes the realization of an experimental test program where some issues addressed by the literature, and other issues yet unexploited regarding the mechanical behavior of carbon fiber thin-ply laminates are investigated and discussed. This program includes investigations on the size effects, notched strength, bearing strength, and fracture toughness. Particular emphasis is given to the damage mechanisms and failure modes of such material, assessed by means of advanced techniques such as digital image correlation. A comparison with typical aerospace grade CFRP will define the performance of the tested thin-ply laminates.

In order to assess the validity of the available analytical tools in predicting the notched behavior of the thin-ply laminates, the results obtained in the experimental test program are compared with the predictions of methods such as the inherent flaw method, the point stress method, and the average stress method. The predictions of the finite fracture mechanics, recently proposed for the prediction of the size effects in aerospace grade CFRP, are also assessed.

Finally, because nowadays the use of reliable computational tools is essential for the design and development of new composite structures for the aeronautic industry, a set of numerical analyses are carried out using the finite element method to assess the advantages of thin-ply laminates with respect to delamination resistance. Such analyses may improve understanding on the mechanical behavior of thin-ply laminates and assess the validity of such computational methods in predicting the onset and growth of damage in these materials.

1.4. Thesis layout

This thesis has been structured according to the objectives described previously, so that each chapter approaches one different topic.

In chapter 2 a detailed review of the state-of-the-art regarding the recent developments of the spread tow thin-ply technology, the available test data, including processing and characterization of the thin-ply laminates, and the potential benefits of using laminates with thin plies (sublaminate scaling) is given. Because this is a multinational project, the description of the recent developments of the spread tow thin-ply technology and the review of the available test data are mainly based on the work performed by the worldwide partners assisting in the development of this technology. On the other hand, the potential benefits of using laminates with sublaminate scaling is based on a review of the studies available in the literature regarding the effect of ply thickness on the performance of composite laminates. Finally, this review also includes a brief description of a recent case study elaborated by one of the partners of this project concerning innovative design using these materials.

In chapter 3 the experimental test program that will support the technology development of the spread tow thin-ply technology, carried out during this thesis, is described. Some of the most relevant mechanical properties of the thin-ply laminates are studied. Particular emphasis is given to the size effects, notched strength, bearing strength, and fracture toughness of such materials. Therefore, plain strength tension and compression, open-hole tension and compression, notched tension and compression, bolt bearing, and over-height compact tension tests are part of the experimental program described in chapter 3.

In chapter 4 the results of the experimental program carried out during this thesis are shown and discussed in detail. In addition, the results obtained for the thin-ply laminates are compared with other carbon/epoxy systems typical of aeronautical applications, namely the T800/M21 and the IM7-8552 carbon/epoxy systems. Such comparison is important in defining the performance of the thin-ply laminates studied in this thesis.

In chapter 5 fast design tools based on closed form solutions, derived from models such as the inherent flaw model, the point stress and average stress models, and the recently proposed finite fracture mechanics model, are presented. Then, these models are used in the analysis of the thin-ply laminates studied in this work and a comparison with other material systems is presented. Finally, the accuracy and reliability of the analyses based on the presented models are discussed.

In chapter 6 an overview of the most common numerical modeling techniques employed in the prediction of damage onset and evolution in composite materials is presented. It includes a description of the composite damage mechanisms, the importance of damage scale when representing/simulating damage in composite materials, and the basic theories behind crack initiation and propagation in composite materials. Then, an overview of the different approaches used when modeling damage in composite materials, namely the micromechanics approach, the continuous damage mechanics approach, and the discrete damage mechanics approach (the last two on the basis of mesomechanics), and their application to composite materials is given.

In chapter 7 the advantages of having laminates with thin plies in the onset of delamination is further investigated. A decohesion element implemented as an ABAQUS® user subroutine (UEL) for implicit analysis is used to simulate free-edge delamination in unnotched and open-hole specimens. The decohesion elements are placed between the plies of the laminate, simulating their interface. A comparative study is performed with laminates having alternative stacking sequences.

Finally, in chapter 8, the main conclusions regarding the work carried out during this thesis are presented. The main aspects to retain from the state-of-the-art of the spread tow thin-ply technology, the experimental test program and respective results, the analysis methods, and the numerical analysis performed during the development of this thesis are presented. Then, because this thesis is just a first step on the understanding of the behavior of thin-ply laminates with notches, future work that needs to be carried out in order to fully characterize the structural integrity of these promising materials is proposed.

Chapter 2

State-of-the-art and literature review

In the domain of commercial aircraft, advanced laminated composites, namely carbon fiber reinforced polymers, have seen an increasing use in structural applications in the airframe and other aeronautical structures. In order to satisfy the increasing demands required to carbon laminates, and fiber reinforced polymers in general, new technologies are being developed. One of this technologies — the spread tow thin-ply technology — is able to produce composites in which the laminate consists of particularly flat plies, which enables dry ply thicknesses as low as 0.02 mm. The laminates made of such thin plies, hereafter referred to as *thin-ply laminates*, comprise several potential advantages. This chapter aims to describe the recent developments regarding this brand new technology, the work already done in the processing and characterization of such new materials, the potential benefits of using such thin-ply laminates, and, finally, a brief description of a recent case study concerning innovative design using these materials. Because this is a multinational project, the description of the recent developments of the spread tow thin-ply technology, the review of the available test data, and the case study presented are mainly based on the work performed by the worldwide partners assisting in the development of this technology. On the other hand, the potential benefits of using laminates with thin plies (sublaminate scaling) is based on a review of the studies available in the literature regarding the effect of ply thickness on the performance of composite laminates.

2.1. Introduction

The use of composite materials in structural applications has significantly increased during the last years. This trend is mainly because composite materials have properties which are very different from conventional isotropic engineering materials. Particularly, composite materials exhibit superior specific properties (strength-to-weight and stiffness-to-weight ratios), fatigue resistance, corrosion resistance, and thermal stability, making them well suited for structures in which the weight is a fundamental variable in the design process [7]. In addition, composite materials are also well suited for damage tolerant design by the proper selection of fiber reinforcement patterns at damage critical regions, achieving better stress redistribution and load paths redirection [8]. Structural components requiring high stiffness and strength, impact resistance, complex shape and high volume production are suitable candidates to be manufactured using composite materials [7].

In the domain of commercial aircraft, advanced laminated composites, namely carbon fiber reinforced polymers (CFRP), have seen an increasing use in structural applications in the airframe and other aeronautical structures, mainly because composite components, when compared with other materials, are characterized by (i) weight saving, which leads to fuel saving, increase in payload, and/or increase in range, improving performance, (ii) good fatigue resistance, which leads to enhanced life and savings in the long-term cost of the component, and (iii) good corrosion resistance, which means fewer requirements for inspection, resulting in savings on maintenance cost [3, 9]. However, damage behavior of laminated composites is quite different from that of commonly used materials (metals, for instance), usually more complicated, and dependent on the properties of the constituent materials, fiber orientation, stacking sequence, nature of loading, etc. [10].

The typical damage behavior of laminated composites include transverse microcracking, fiber-breakage and delamination. Usually, transverse microcracking through the thickness of the ply occurs as the first-ply failure mode, followed by delamination damage. Fiber-breakage usually happens at the last stage of the failure. However, a catastrophic failure can occur only with microcracking and delamination damage, without fiber breakage [10].

In order to satisfy the increasing demands required to carbon composites, and fiber reinforced polymers in general, new technologies are being developed. One of this technologies — the **spread tow thin-ply technology** — is able to produce composites in which the laminate consists of particularly flat plies, which enables dry ply weights of less than 100 gsm[1]. The flat tapes are achieved by mechanically spreading large tows down to the flat tape-shape. These flat tapes can be woven to an orthogonal fabric with minimal crimp — the so-called **non-crimp fabric** (NCF) — as shown in figure 2.1.

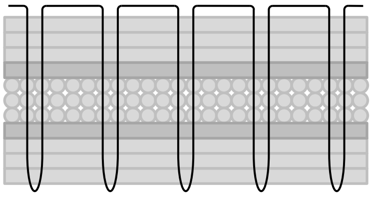

Fig. 2.1. Stitched non-crimp fabric (after Rolfes et al. [11]).

This thin-ply NCF is seen as an innovative building-block layer that can potentially lead to major changes in how composite laminates will be designed and made in the future. There are several potential advantages regarding the use of these thin plies:

- Per given laminate thickness, more plies can be accommodated. This may lead to a possibility of using smaller relative fiber angles in adjacent plies, which is considered beneficial when it comes to delamination between plies.
- There exists an "in-situ" effect, related with the presence of thin plies within a given laminate thickness, that may conduct to an increase of the laminate strength and

---

[1] Unofficial unit symbol for *grams per square meter* (g/m^2).

damage tolerance. In fact, thin-ply laminates are intrinsically stronger than thick-ply laminates.

- It is considered that the spread tow plies display improved fiber orientation and distribution, potentially leading to fewer weak zones.

Furthermore, according to Tsai [12], mentor of this multinational project regarding **bi-angle thin-ply NCF laminates**, a brand new approach is possible with this recently developed technology:

1. Anisotropy of unbalanced laminates is recommended to take advantage of bend-twist coupling, not available when balanced laminates are used.
2. Homogenization of a laminate is made possible by use of highly repeated sublaminates. This process is further enhanced because thin plies (75 gsm) are now available for use.
3. Designing and testing of anisotropic plates are different from orthotropic (balanced) plates. It is important to know their transformation relations, i.e., how stiffness and strength change as the reference angles change. Therefore, new testing procedures may be necessary, e.g. off-axis testing instead of the traditional on-axis testing.
4. Conventional 4-angle laminates are more prone to have early microcracking than 2-angle laminates, where plies are made more compatible, leading to higher strength. Two-angle laminates are also easier to homogenize than laminates with 3- or 4-angle sublaminates. It has been demonstrated that laminates with as few as 16 bi-angle layers or a total of 32 plies would be sufficiently homogenized so asymmetric lay-up would not warp.
5. Two-ply layers, like [0/25], are difficult to make with conventional lay-up from prepreg because (i) shallow angles, like 25°, lead to large scrap and need larger working tables, and (ii) with thin plies, the cost and time of lamination will be higher. The unique thin-ply NCF by Chomarat not only overcomes these two challenges but also compete with laminated composites made from uni-tape in both performance and cost.
6. With bi-angle layers, 1-axis lay-up of laminates is possible. This can be 7 times faster than the traditional 4-axis lay-up.
7. Homogenized anisotropic plates can be analysed and optimized in a fraction of time, say, 1/32 or 3% of conventional ply-by-ply models.

However, further studies should be conducted in order to better quantify the main advantages of the spread tow thin-ply technology, namely:

- The benefits of using smaller relative fiber angles in adjacent plies, namely when it comes to delamination between plies, were not studied in detail in an industrial context.
- The in-situ effect still is not well understood.
- The improved fiber orientation and distribution displayed by the spread tow plies, which potentially leads to fewer weak zones, is not well quantified yet.

- Finally, potential benefits should be identified in a systematic manner using experimental programs; furthermore, finite element (FE) based analysis should be carried out to improve understanding and prediction of the mechanical behavior of the thin-ply laminates.

2.2. Spread tow thin-ply technology

2.2.1. Recent technology development

Although multiaxial technology exists since the 1980s, multiaxial carbon reinforcements produced since then are mainly based in the 0, 90 and ±45° directions, with areal weights equal to or higher than 200 gsm per carbon ply. With the acquisition of skills in **fiber spreading**, in the early 2000s, that technological hurdle was cleared and new reinforcements with low areal weights were developed [13].

Among the first manufacturers to adopt the **spread tow thin-ply technology**, Chomarat, committing themselves to Tsai's project (see, for example, [14]), converted a mass-production tool into a unique manufacturing process able to produce its own range of multiaxial carbon reinforcements — C-PLY™ — with low areal weights and low angles (below 30°) [13]. With this new manufacturing process, Chomarat is able to produce high quality thin-ply NCF with a tow spreading process, resulting in areal densities as low as 75 gsm per ply (or 150 gsm per bi-angle layer) [14].

The thin-ply NCF manufacturing process of Chomarat includes three steps [13]:

Spreading Achieving a ply weight of 75 gsm requires skills in a specific spreading process which consists of laying the yarns flat and straight at uniform tension before spreading them to form a ply that is uniform in weight, width and thickness.

Ply forming Done on a multiaxial machine, but instead of laying down the yarns as in the standard technique, unidirectional (UD) plies are placed on top of one another in the desired directions. Obtaining reduced angles (20°–30°) required the design of new machine kinematics.

Combining This last step of the process serves to tie the plies together and consolidate the laminate. It is based on a very fine stitch to reduce the impact of foreign materials and the creation of voids as much as possible.

Although Chomarat is now able to produce thin-ply multiaxial carbon reinforcements (C-PLY™), spread tow thin-ply technology can also be used with other types of fibers, including E-glass, S2-glass and aramid.

Oxeon AB (Bôras, Sweden) also produces its own unbalanced spread tow carbon fabrics and spread tow carbon tapes, the trademarked TeXtreme®. Oxeon manufactures TeXtreme® carbon tapes with areal weights from 21 gsm, and ply thicknesses as low as 0.02 mm, resulting in improved fiber alignment in and out of plane. Regarding the TeXtreme® carbon fabrics, Oxeon states that they perform similarly to cross-ply constructions of UD tape, and that they are considerably more drapable and less susceptible to delamination. The TeXtreme® carbon fabrics have higher fiber volume fraction and fewer interlacing points than a traditional woven fabric, and therefore correspondingly lower crimp frequency and crimp angle. Its construction is based in longer fiber floats (20 to 50 mm), minimizing fiber waviness and allowing the filaments to immediately carry tensile or compressive load without first having to straighten. Furthermore, it uses tapes from the spread process instead of yarns in the weaving process (that can be incorporated in individually adjustable angular orientations $+\alpha/-\beta$), resulting in a flatter fabric, with a better surface finish than conventional ones (see High-Performance Composites magazine and Oxeon websites, `http://www.compositesworld.com/articles/spread-tow-fabrics-reduce-waveboard-weight` and `http://www.oxeon.se/index.php?page=textreme`, respectively).

Another group producing thin-ply laminates is the North Thin Ply Technology, LLC (Penthalaz, Switzerland), a joint venture of the US company North Technology Group and the Swiss company Createx. According to North Thin Ply Technology, LLC, they are able to produce thin-ply structures with a ply weight of 30 gsm, but they can go as low as 18 gsm. At the moment they manufacture dry or pre-impregnated thin-ply spread filament UD tapes, or use automated tape laying to make customized pre-assembled stacks of plies off-the-mold for easy and fast handling. In addition, North Thin Ply Technology, LLC has available a software package to deal with thin-plies and optimize design simulations. Examples of applications using the thin-ply laminates of North Thin Ply Technology, LLC include Formula 1 body panels, primary structures in light aircrafts, helicopter tails, and masts, booms and spreaders for sailing boats [15].

2.2.2. Tow spreading

According to Sihn et al. [10], there have been a few efforts to reduce the ply thickness below that of the conventional ply of 0.125 mm thickness. However, it required costly and slow processes, likely to damage the fibers in the ply during processing. For these reasons, the recently introduced **tow spreading technology**, developed by the Industrial Technology Center in Fukui Prefecture, Fukui-city, Japan, marks a new trend in the development of new processing techniques for laminated composites manufacturing.

This new process to continuously open fiber tows was firstly proposed by Kawabe et al. [16] and consists of a roll part for its preliminary opening and a pneumatic part for its main opening — see figure 2.2. According to Kawabe et al. [16], this process was successfully applied to carbon and glass fiber tows and a much more widely opened tow can be obtained by this combined method, as compared with any of the singular processes.

In a more recent work, Sihn et al. [10] used this tow spreading method for spreading conventional thick fiber tows, such as 12 K filament tows, to make particularly flat plies (spread width of 16–32 mm), which were used in the production of thin-ply laminates. Thick tows were efficiently spread without damaging any fibers by means of a constant airflow through sagged fiber filaments. The tow passes through a spreading machine that is equipped with an air duct and a vacuum that sucks the air downward through the air duct, which is located between the guide rolls — see figure 2.3. As the air flows through the air duct with the help of the vacuum, the tow sags downward towards the air flow direction so that it loses tension and results in a tension-free state momentarily. With the uniform airflow continuously operating on the tow, it could be spread continuously and stably [10].

Figure 2.4, adapted from Sihn et al. [10], shows how the present tow spreading method works with the help of airflow. When air flows around both sides of the tow, the difference in the velocity of the airflow, near and away from the tow, results in a pressure difference

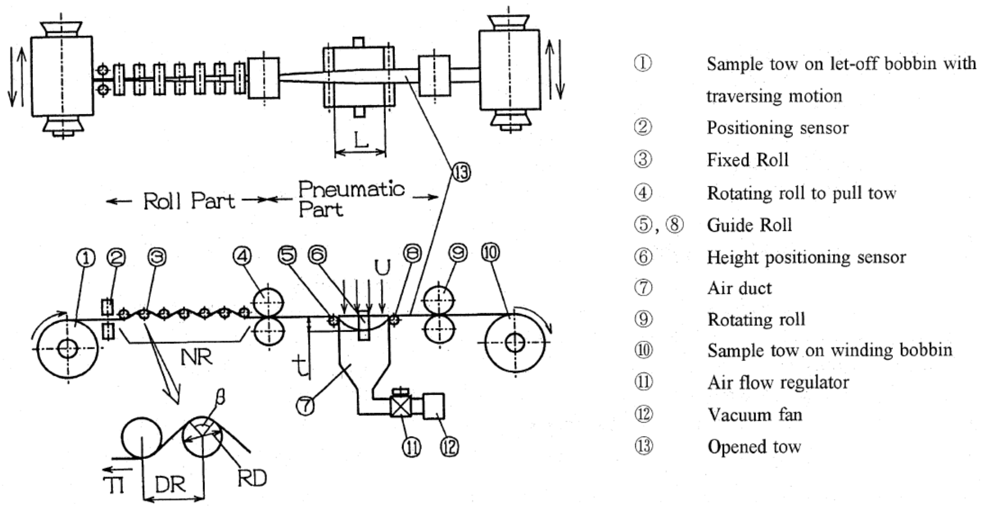

Fig. 2.2. Tow spreading process developed at the Industrial Technology Center of Fukui Prefecture, Fukui-city, Japan: overall figure of the opening system consisting of a combination of roll and pneumatic methods [16].

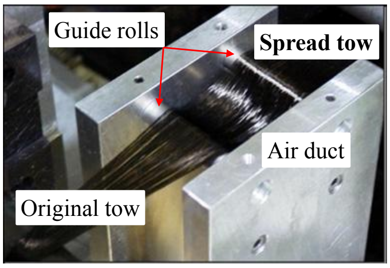

Fig. 2.3. Spreading machine air duct [10].

at these locations. This pressure difference creates an aerodynamic force that helps the filament fibers to lose the tension momentarily (leftmost schematic). As the tow spreading
begins, air flows bet e and faster (middle
and rightmost sche er the tow thickness
becomes. This met icient, being able to
produce thin-plies o al plies thickness of
0.125 mm [10].

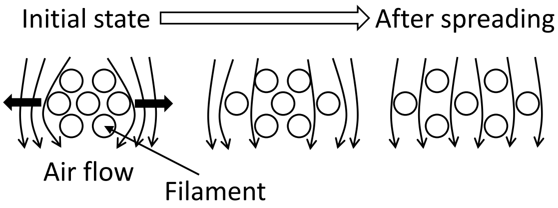

Fig. 2.4. Schematic front view of the tow spreading process with the help of airflow (adapted from reference [10]).

In July 2002, Harmoni Industry Co., Ltd., from Fukui-city, obtained a patent for manufacturing the tow spreading machines based on the previously described pneumatic, airflow process (see Harmoni Industry Co., Ltd. website: `http://www.harmoni.co.jp/02/company/index.html`). But, more recently, a Japanese company named Technomax Corp. has developed a method for spreading fibers with ultrasonic energy (see High-Performance Composites magazine website: `http://www.compositesworld.com/columns/a-technological-brake-for-the-carbon-supply-roller-coaster`). Ultrasonic tow spreading technology development started around 1995, and around 2005 a fiber-spreading machine was completed and was presented by Technomax Corp. (see figure 2.5), together with various data and states of spread fiber and products using spread fibers (see JEC Composites website: `http://www.jeccomposites.com/news/composites-news/innovative-technology-carbon-and-aramid`).

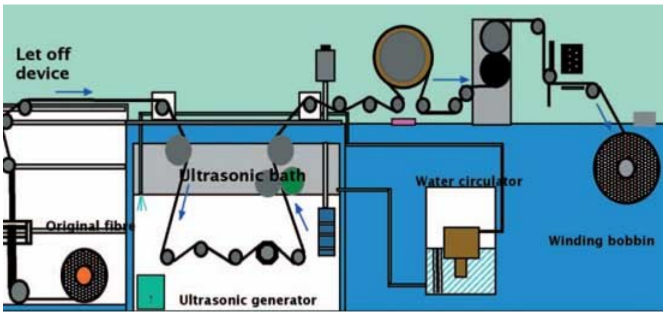

Fig. 2.5. Schematic of the ultrasonic fiber-spreading machine developed by Technomax Corp. (see JEC Composites website above).

2.2.3. Thin-ply NCF production

Fabric reinforcements show great potential for application in primary structures for the aerospace and aeronautic industries. Indeed, to meet the growing demand of enhanced out-of-plane properties, higher impact resistance, low manufacturing costs and easily handling and storage, crimp configurations of fiber yarns have been introduced as a first attempt to develop appropriate substitutes of traditional UD laminates. In the last two decades, NCF systems have been developed and proposed as reliable textile reinforcements able to provide enhancements in the out-of-plane and impact performance, preserving, at the same time, low manufacturing costs. NCF are generally thicker but more flexible than UD fiber tapes, and the storage, lay-up and draping costs with respect to the manufacturing of final parts can be reasonably reduced [17]. Although the yarns can cause a reduction of the in-plane tension and compression performance when compared with traditional UD laminates, generating dangerous failure mechanisms such as kink band, matrix cracks and delamination initiation points, the reinforcements in the through-the-thickness direction, provided by the stitching, can significantly improve the resistance to delamination, the damage (impact) resistance and the through-the-thickness strength [17, 18].

The unique NCF machine at Chomarat is currently able to mass produce [0/45] thin-ply NCF and, in the near future, will mass produce [0/25] thin-ply NCF. Figure 2.6, presented by Tsai [12], shows the machine setup of Chomarat. Off-axis plies are laid down in the flat conveyor belt and a 0° ply is placed over it. Then both plies are stitched together to form the NCF. Figure 2.7 shows a 1.27 m wide T700 NCF produced by Chomarat.

One unique feature not shown in figure 2.6 is the off-line spreading process of the starting tows, shown in figure 2.8, which converts the conventional tows into a finely aligned unidirectional thin sheet with a mass areal density of 75 gsm, by means of a pneumatic device, as described in section 2.2.2. According to Tsai [12], when the thin plies are stitched together to form a NCF, fiber dispersion in each ply is as uniform as a conventional prepreg.

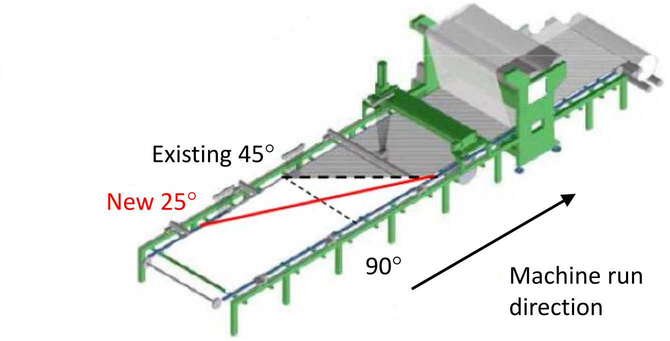

Fig. 2.6. Uniqu ed by Tsai [12].

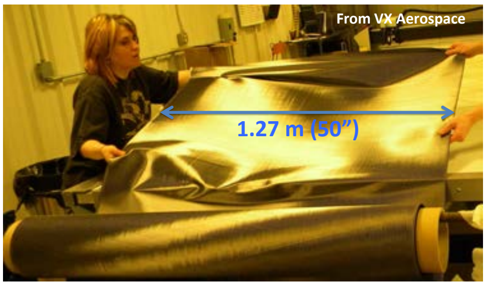

Fig. 2.7. Bi-angle NCF, with 150 gsm (or 0.125 mm thick). Picture from VX Aerospace [12].

The superior strength property of this thin-ply NCF is comparable to multi-directional laminates made from unidirectional prepregs. This is particularly true when combined bending and twisting loads and deformations are present.

Fig. 2.8. Thin plies obtained with the tow spreading technology at Chomarat.

2.3. Processing thin-ply NCF

Traditional aerospace and aeronautic high-performance composite laminates based on UD reinforcements generally provide unsurpassed in-plane specific properties, but the manufacturing costs are typically very high, since these laminates are generally based on UD prepreg tapes. In addition, the use of liquid modeling techniques in the manufacturing of laminates based on UD reinforcements generally conduct to imperfections unacceptable for the aerospace and aeronautic industries, due to the lack of rigidity of the UD bundles when dry and during injection of the resin. On the other hand, textile composites, and in particular laminated composites based on NCF reinforcements, offer economically attractive alternatives to the traditional prepreg composites used in the aerospace and aeronautic industries. Indeed, NCF composites not only are suitable for prepreg production, but also guarantee the highest quality standards when manufactured using liquid modeling techniques, mainly because the stitches provide the necessary rigidity to the fiber bundles, avoiding their displacement during handling of the dry reinforcement and during resin injection.

The tow spread thin-ply reinforcements are suitable for all lamination techniques, including hand lay-up (HLU), prepreg, liquid resin infusion (LRI), resin transfer molding (RTM), vacuum assisted resin transfer molding (VARTM), pultrusion, and resin film infusion (RFI). In the next sections, the experimental work regarding the application of some of these processing techniques to thin-ply NCF will be reviewed.

2.3.1. Prepregs of thin-ply NCF

Among the possible applications of thin-ply NCF reinforcements, its application in **prepregs** (*pre-impregnates*) production is of great interest, namely for high-end structural applications, where outstanding strength combined with easy handling and lay-up are required.

The first prepreg of biaxial thin-ply NCF was produced by Aldila [19], using their AR-2527 epoxy resin system and the C-PLY™ biaxial [0/77.5], C-PLY™ biaxial [0/45], and C-PLY™ biaxial [0/−45] fabrics of Chomarat. The prepregs were successfully produced with 150 gsm fiber areal weight and 35% (nominal) resin content, exhibiting quite manageability and excellent quality, with consistent resin content across the web and no warpage or distortion during the manufacturing process. The AR-2527 epoxy resin is a toughened epoxy with a 120°C curing temperature (curing can be done inside or outside autoclave), with 0.76% moisture absorption at saturation and with excellent outgassing properties.

Aldila [19] also determined the mechanical properties of laminates produced with C-PLY™ biaxial [0/77.5] AR-2527 epoxy prepregs and compared to a laminate made with a standard-modulus carbon 34-700 (24 K) uni-tape AR-2527 epoxy prepreg. Some outstanding properties were found, namely lower fibre and panel areal weight, lower thickness per ply, and higher open-hole tension and compression ultimate strengths.

2.3.2. Infusion of thin-ply NCF

Three different configurations of bi-angle NCF test panels from Chomarat (which comprise the new spread tow thin-ply technology) were manufactured via **infusion** by VX Aerospace and Advaero Technologies [20], namely [±77.5], [0/45] and [0/−45]. Furthermore, VX Aerospace also processed bi-angle NCF for a representative aircraft part with compound curvature, in order to evaluate the ability of the material to drape and form compound curves.

A Gerber CNC cutting table was used to nest and cut the bi-angle NCF. According to Skillen and Kelkar [20], the material was sufficiently tight so that there were any problem with vacuum hold-on[2]. A wheel knife was selected instead of a drag knife, and the cutting pressure was increased (from a 103 kPa setting, typical for 3K prepregs, to 138 kPa). Although cutting the dry bi-angle NCF in general was similar to other dry carbon fabrics, Skillen and Kelkar [20] pointed some issues when cutting this material:

---

[2] Sometimes dry wovens require a cover sheet of non-porous (typically plastic) sacrificial material for processing on a cutting table

- As is typical of dry material, the individual pieces are less stable once cut and subject to shape change, so they must be handled carefully. The bi-angle NCF performs better in this regard than most woven fabrics.
- The stitching is lightweight, but it is also closely spaced.
- Cut pieces remain stable, although when the part shape requires cuts parallel to the fiber direction, loose carbon slivers are problematic. Removing these slivers from the table before lifting the part greatly reduces the risks of contaminating the laminate.
- When cutting parallel to the fiber direction, it is not always possible to cut all of the stitching material. Operators must finish the cut by hand before lifting the part. This helps to minimize loose sliver problems as well.

Some panel kits, for test specimen production, were infused with **HVARTM**[3], a proprietary infusion process of Advaero. They had fiber volume fractions of 66%. An aircraft representative part was also infused with HVARTM, in order to explore the ability of the material to drape and form compound curves. Before infusing, bi-angle NCF were placed dry and made conform before bagging. Some spray adhesive was used. Some interesting observations were highlighted by Skillen and Kelkar [20], concerning the infusion procedures of bi-angle NCF, as compared to traditional woven fabrics, and the ability of bi-angle NCF to drape and form compound curves:

- Although bi-angle NCF handle differently, it still is quite manageable.
- This material allowed seamless transitions on curved shapes.
- Flow control is more critical with bi-angle NCF. When infusing a traditional woven, flowing too fast is generally not a problem. However, it was noticed that rapid infusion could displace the fibers of bi-angle NCF, something which was most notable when the flow direction was more normal to the fiber orientation. Reducing and modulating the leading edge eliminated this tendency.
- The HVARTM process is more suitable for this type of modulation than traditional VARTM, especially when dealing with toughened epoxies.
- Because kitting and lay-up time can be reduced in volume production due to the single-axis asymmetric lay-up and infusion via HVARTM process was not difficult, bi-angle NCF processing costs will be lower.

2.3.3. Pultrusion of thin-ply NCF

In the **pultrusion** process, griping plates or tractor-puller systems are used to alternatively grab and pull the pultruded material/profile at a constant speed, making possible the production of structural composite profiles on a continuous basis. Reinforcing materials are pulled from spools through a heated die which compacts the material into the final geometry and cures the resin. Resin is applied to the preform through a wet-bath or an injection station, and the wet fibre/resin assembly, along with inserts or cores (where applicable), moves through the heated portion of the die. Under the appropriate temperature and pressure conditions, the resin cures before the material exits the downstream end of the die [21].

---

[3] HVARTM – Heat vacuum assisted resin transfer molding.

The continuous basis composite production made possible with pultrusion technology makes this the most cost-effective technique for fabricating high-performance structural composite parts. According to KaZaK Composites [21], pultruded products can be produced at a cost that approaches raw material cost (≈20% higher) in large-scale production, once labor and other overhead costs fall into the noise level of calculations on a per-kilogramme basis. Since this is essentially a single step process from material forming to finished cure, pultrusion can produce composite parts far more rapidly than any other technology.

KaZaK Composites [21] already successfully pultruded a high-quality 305 mm wide and 2.3 mm thick panel, with a fiber volume fraction of 61%, made of $[0/45/0/-45]_{8T}$ thin-ply NCF and Epon 862 / Lindau LS-81K epoxy (with no fillers), which expectedly created some challenges related to reinforcement handling and processing. A two-zone heated die was used, with an entry temperature of 177°C and an exit temperature of 166°C. The pultrusion speed was 15 cm/min.

In a first challenge, KaZaK Composites' equipment for slitting regular fabric rolls proved to be inadequate for the rather delicate thin-ply NCF, whose individual angle plies tend to unstitch and fray under the action of the cutting disk. So, gentle care and the use of a different type of rotary cutter addressed this hurdle, which is unlikely to occur in large-scale production of larger structures, assuming fiber rolls may become manufactured in the exact widths needed and more specialized cutting equipment may become available.

A second expected challenge was based on previous experience with biaxial fibers ([±45°]), which tend to shift due to the pull loads. This concern did not materialize, as the 0° plies had sufficient load carrying capability, without inducing any changes of the 45° plies.

According to KaZaK Composites [21], the quality of the thin-ply NCF pultruded panel was excellent, exhibiting an expected twist angle for this asymmetric lay-up (1.5%). This feature combined with the low cost, high throughput and large-scale manufacturability typical of pultrusion makes this technique highly suitable for composite structures made of thin-ply NCF.

2.3.4. Resin film infusion of thin-ply NCF

KaZaK Composites [21] also already studied the application of **RFI** in the manufacturing of bi-angle thin-ply NCF panels. Firstly, a panel was manufactured via RFI-vacuum. The lay-up of bi-angle carbon fiber plies $[60°/85°]_{16T}$ and Gurit SA80 epoxy film layers[4] (×22) was bagged and subjected to vacuum, first at 80°C for increased resin flow and tow impregnation and then at 120°C for full cure. Vacuum level was of 686 mmHg. Due to the very low transverse permeability of the fibers and possibly due to the presence of glass veils supporting the resin film layers, excess resin could not be transferred from the lay-up out into the breather layer, resulting in a thicker than expected cured panel, with a non-uniform ply-to-ply resin distribution. This panel had 89 mm × 89 mm × 3 mm and a fibre volume fraction of 47%.

In order improve the quality of RFI based panels, KaZaK Composites [21] also manufactured a panel via RFI-hot press. Based on the prior finding that transverse resin outflow is

---

[4] Gurit SA80 film 250 g/m^2 epoxy + 25 g/m^2 glass veil support, 127 µm.

minimal, the lay-up for the pressed panel was allowed to include only as much resin as theoretically predicted, as in a prepreg calculation. A lay-up of carbon fiber plies $[60°/85°]_{16T}$ and Hexcel 8552 thin film epoxy layers[5] (×10) was pressed (10 atm) and maintained at two temperature stages (wet-out at 110°C, and cure at 180°C), resulting in a good quality panel, of as-predicted thickness 2.3 mm (a 610 mm × 610 mm panel was hot-pressed), with consistent ply-to-ply resin distribution and only 1.5% twist angle/warping, and with high fiber volume fraction, 61%.

2.4. Available test data

2.4.1. Equivalent elementary UD properties

Chomarat [22], in order to characterize its **biaxial thin-ply NCF material**, a new bi-angle building block with a patent pending by Stanford University and Chomarat, tested special samples to obtain the **equivalent elementary UD properties**. Longitudinal and transverse properties were measured in coupons of 15 mm width taken from plates in the 0° and 90° directions, made with UD plies using the base ply manufactured on the NCF machine by spreading the tow (T700-12K) and tape laying it in parallel directions. These UD plates were made of 32 plies impregnated with RTM6 resin in a flat sheet mould by RTM, resulting in a final ply thickness of 2 mm and a volume fraction of 71%. Shear properties are measured in [±45] coupons (also of 15 mm width) taken from plates manufactured using the same process used to manufacture the UD plates, resulting in a volume fraction of approximately 67%.

The material data for the *thin-ply NCF T700/RTM6* from Chomarat is given in table 2.1, where E_1 and E_2 are the longitudinal and transversal Young moduli, respectively, G_{12} is the shear modulus, ν_{12} is the major Poisson ratio, X_T and Y_T are the longitudinal and transversal tensile strengths, respectively, S is the shear strength, and V_f is the fiber volume fraction. All data were normalized for a fiber volume fraction of 57% using the MICMAC software (see, for instance, reference [23]), and can be used in classical laminate theory analysis of the NCF material. However, strength data for longitudinal and transverse compression, X_C and Y_C, respectively, are not yet determined [22].

Tab. 2.1. Material data for the thin-ply UD T700/RTM6 from Chomarat for a volume fraction (V_f) of 57% [22].

$E_1 = 123$ GPa	$E_2 = 7.7$ GPa	$G_{12} = 4.1$ GPa	$\nu_{12} = 0.28$
$X_T = 2582$ MPa	$Y_T = 57$ MPa	$S = 105$ MPa	$V_f = 57\%$

In order to characterize the **stitching effect**, Chomarat [22] also measured the tensile properties of [0/90] coupons, obtained by cutting samples at 45° of the [±45] plates, and compared to the [0/90] properties of stitched materials from [0/90] plates with conventional NCF stitching and a volume fraction of 57%. According to Chomarat [22], and as observed in table 2.2, the main difference between the two material is due to the volume fraction, whereby it can be concluded that stitching does not degrade the tensile properties of the NCF material.

---

[5] Hexcel 8552 thin film 160 g/m^2 epoxy, no veil, 127 μm.

Tab. 2.2. Stitching effect on [0/90] thin-ply NCF plates from Chomarat [22].

Plate	V_f	Orientations	E_l [GPa]	σ_l^{max} [MPa]
[±45]	65–69	[0/90]	71	1335
[0/90]	56–57		66.6	1292

2.4.2. Bi-angle thin-ply NCF properties

Bi-angle thin-ply NCF, comprising lay-ups such as [0/25] and [0/45], are particularly suitable for application to many components subjected to combined bending and twisting loads and deformations, such as wings, stabilizers, turbine fan blades, wind turbine blades, rotor blades for helicopters, propellers, shafts, torsional rods, and many sporting goods, like tennis rackets, golf shafts, pole vault poles, masts for yachts, and racing cars [12, 24, 25]. Unbalanced laminates, with anisotropic layers, have shear coupling, i.e., its stretching and distortion are coupled. This means that, unlike quasi-isotropic laminates, anisotropic lay-ups under bending or twisting loading result in both types of deformation simultaneously. It is an opportunity to select the material and ply orientations so the resulting stretching and distortion can work against or for each other for the benefit of laminate performance, something not available when traditional balanced building blocks are used [25, 26]. This feature has been long recognized for its potential for controlling or designing the deformation counter-effects on each of the loading types, usually referred to as *passive aeroelastic tailoring* [25]. So, instead of avoiding such coupling, it is possible to reduce weight simply by using anisotropy, that is unique in composite materials [26]. For instance, a simple laminate, such as $[0/\phi]_{8S}$, can be designed for suppressing one of the deformation modes (zero tip deflection or zero tip rotation) despite combined loading [25].

When shear or twisting moment are fully reversible, orthotropic lay-ups, such as [0/±25/0] and [0/±45/0] will be needed. These configurations can easily be made by stacking or folding [0/25] and/or [0/−25], and [0/45] and/or [0/−45], respectively. For fuselage and other components where both normal stresses are in the same order of magnitude, quasi-isotropic configurations such as [0/±45/90], formed using 2-axis lay-up of [0/45] and/or [0/−45], would be recommended when using bi-angle NCF [12, 24].

In the following sections, some issues regarding testing of anisotropic materials, namely bi-angle laminates, the effects of bi-angle lay-ups in the NCF properties, and the available test data and numerical studies concerning bi-angle NCF properties will be described.

2.4.2.1. Testing anisotropic materials

Testing anisotropic materials, such as bi-angle [0/25] and [0/45] lay-ups, is not so obvious as testing orthotropic or isotropic materials, since it has to rely on knowing the transformation relations. Tsai [12] adresses this issue using the graph presented in figure 2.9. It shows the normalized stiffness components of the [0/25] T700 NCF/RTM6 bi-angle thin ply laminate. Only 3 components, A^*_{11} in yellow, A^*_{66} in pink and A^*_{61} in blue, need to be showed due to symmetry. If this anisotropic laminate, [0/25], is rotated −12.5°, it is possible to define symmetry axis of [±12.5] and [±77.5], as shown in figure 2.9. At these laminate orientations, the shear coupling component A^*_{61} will be zero. A^*_{11} is symmetric with respect to this −12.5° axis, and its value repeats every 180°. Shear component A^*_{66}

is also symmetric with respect to this axis, except it repeats itself every 90°. Shear coupling component A^*_{61} is anti-symmetric with respect to this axis and repeats itself every 180°.

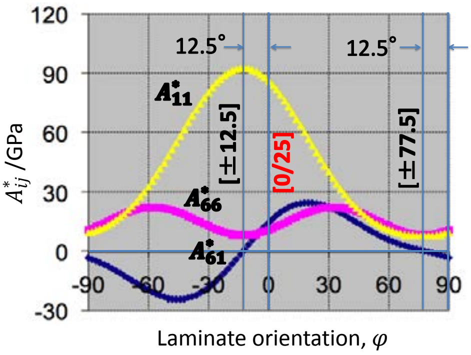

Fig. 2.9. Normalized stiffness components of the [0/25] T700 NCF/RTM6 bi-angle thin ply laminate, presented by Tsai [12].

This exact transformation relation is very important in understanding an anisotropic material like [0/25]. It is not possible to simply test a coupon with this unbalanced material because a combined stress condition (axial load and nonzero shear, from the shear coupling) will appear at the grips of the test coupon. This can be overcome by using a long specimen or, much more convenient, by knowing the transformation relations, i.e., how the rotation of reference coordinate axes change. Following this approach, it is not necessary to test this material along the 0° axis. Therefore, testing of [0/25] and [0/45] lay-ups (as well as other unbalanced, anisotropic materials) is more accurately accomplished when testing coupons cut along the bisector [±12.5] and [±22.5], respectively, which are orthotropic and do not exhibit shear coupling.

Alternatively, anisotropic specimens can be tested using oblique end-tabs, schematically shown in figure 2.10, as proposed by Sun and co-authors [27–29]. An explicit expression of the oblique angle can be obtained as a function of the off-axis angle and composite properties. According to Sun and Chung [29], the oblique angle ϕ can be determined from the relation,

$$\cot\phi = -\frac{\overline{S}_{16}}{\overline{S}_{11}} \tag{2.1}$$

where $\overline{S}_{11}$ and $\overline{S}_{16}$ are components of the compliance matrix in the loading coordinate system xy, defined in terms of the in-plane elastic material constants E_1, E_2, G_{12} and ν_{12} and the off-axis angle θ as [30],

$$\overline{S}_{11} = \frac{\cos^4\theta}{E_1} + \frac{\sin^4\theta}{E_2} + \frac{1}{4}\left(\frac{1}{G_{12}} - 2\frac{\nu_{12}}{E_1}\right)\sin^2 2\theta \tag{2.2a}$$

$$\overline{S}_{16} = -\left(\frac{2}{E_2} + 2\frac{\nu_{12}}{E_1} - \frac{1}{G_{12}}\right)\sin^3\theta\cos^3\theta + \left(\frac{2}{E_1} + 2\frac{\nu_{12}}{E_1} - \frac{1}{G_{12}}\right)\cos^3\theta\sin\theta \tag{2.2b}$$

According to Sun and Chung [29], an oblique-shaped end-tab is able to ensure the axial displacement that is necessary in off-axis specimens under uniaxial loading. Finite element analysis and experiments indicated that the oblique tab is more suitable than the conventional rectangular tab for uniaxial off-axis testing. Furthermore, according to Kawai et al.

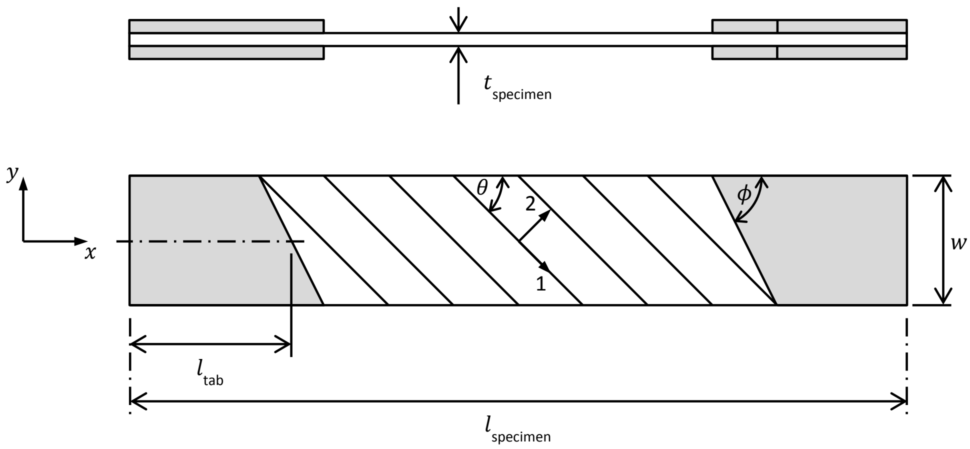

Fig. 2.10. Off-axis tensile specimen with oblique end-tabs [30].

[31], the oblique end-tabs effectively relax the end-constraint effect and almost remove the inhomogeneous state of deformation in the initial linear elastic range, avoiding failure near the loading tabs.

2.4.2.2. The effect of bi-angle lay-ups in NCF properties

To understand the effect of using bi-angle lay-ups with shallow off-axis angles, figure 2.11 shows the increasing first-ply-failure (FPF) strength of various [0/ϕ] bi-angle laminates in combined bending and twisting stress ratios (σ_6/σ_1) as the off-axis angle ϕ decreases, as presented by Tsai [12]. Going from right to left, one can see that FPF strength increases when the failure of two plies are getting closer. This increase in FPF is attributed to an increasing compatibility between both plies as the off-axis angle decreases. In laminates with higher off-axis angles, like [0/90] or [0/±45/90], compatibility between plies is more difficult. In these cases, one or more plies often fail prematurely creating microcracking. In this combined state of stresses, the FPF increase means that micro cracks are suppressed. So, a higher working stress is possible. In the case of [0/90] on the extreme right, there is a huge gap between both plies. Under uniaxial tensile or with small shear stress (10% or less), the [90] fails at 500 MPa while potentially the strength can reach over twice that much, or 1150 MPa shown by a blue line of $X/2$ (assuming a longitudinal tensile strength X of 2300 MPa). Note that, for an off-axis angle of 25° or less, the FPF strength can exceed the rule-of-mixtures predicted value of $X/2$, due to the presence of combined stresses, for example, when σ_6/σ_1 is 0.2.

Observing figure 2.11, one can expect that the gap between the FPF and the LPF (last-ply-failure) will be the smallest for shallow angle lay-ups, such as [0/20] and [0/25]. When the off-axis ply angle increase, it is clear that the gaps between FPF and LPF are much higher; so, as one can see from this analysis presented by Tsai [12], it becomes a challenge whether a laminate can be used beyond FPF, i.e., whether or not microcracking can be tolerated. Using bi-angle NCF, the strength at FPF is sufficiently high and microcracking can be avoided altogether. Furthermore, the prediction of FPF is more accurate than the often empirically based LPF.

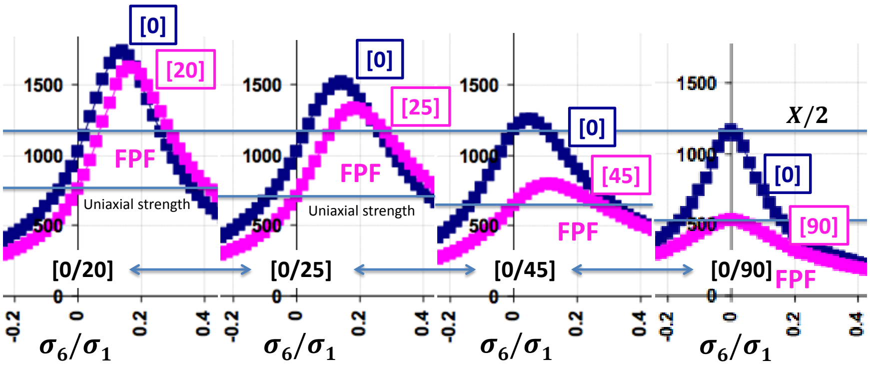

Fig. 2.11. First-ply-failure of [0/ϕ] bi-angle laminates, where ϕ = 20, 25, 45, 90 and assuming $X = 2300$ MPa: maximum laminate stress σ_1 (MPa) that causes failure in [0] and [ϕ] plies (lower stressed ply controls FPF). Viewgraph presented by Tsai [12].

2.4.2.3. Uniaxial stiffness and strength of bi-angle laminates

According to Tsai [12], the **uniaxial stiffness** and **strength** (always **FPF**) of [±ϕ] and [0/±ϕ/0] lay-ups can be addressed taking figure 2.12.

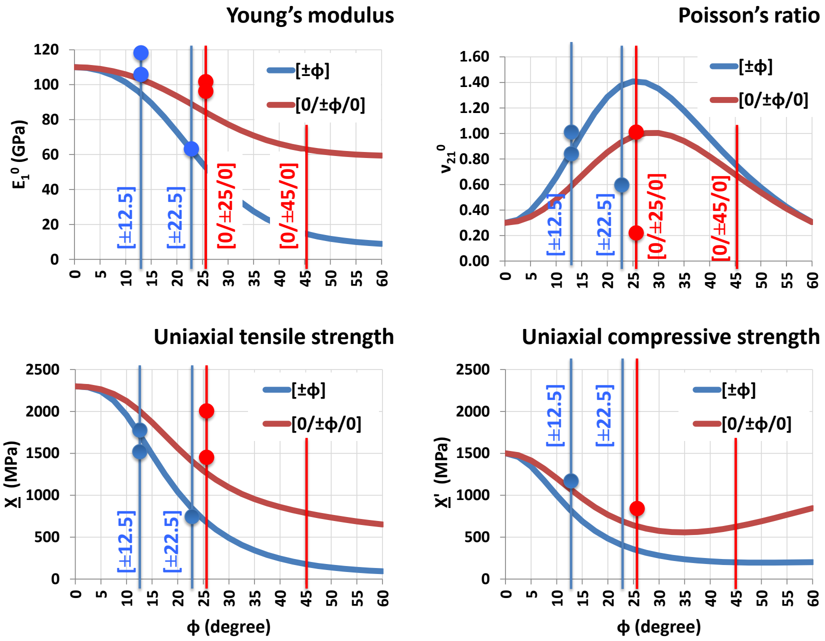

Fig. 2.12. Uniaxial stiffness and strength of bi-angle NCF, presented by Tsai [12]. Charts show the theoretical curves and corresponding data (represented dots) for longitudinal Young modulus, Poisson ratio, uniaxial tensile strength and uniaxial compressive strength.

As one can see in figure 2.12, longitudinal Young modulus (E_1^0) and uniaxial tensile strength (X) achieve the highest values within shallow angles, namely [±12.5] or [±22.5] for [±ϕ] lay-ups, and [0/±25/0] or [0/±45/0] for [0/±ϕ/0] lay-ups. Furthermore, test data (blue and red dots for [±ϕ] and [0/±ϕ/0] lay-ups, respectively) presented in figure 2.12 shows satisfactory agreement with those theoretical results (blue and red curves) presented by Tsai [12].

Regarding uniaxial compressive strength (X'), observing figure 2.12, it is also possible to conclude that, generally, within shallow angles, higher strength may be achieved. Figure 2.12 also shows that test data is reasonable agrees with the theoretical results. However, it is interesting to note that uniaxial compressive strength of [0/±25/0] lay-up is only slightly higher than [0/±45/0] lay-up. So, because [0/±45/0] lay-up has lower costs, if everything else is equal, this lay-up should be chosen. Because many structures either carry compressive loads or are subjected to bending, often controlled by compressive strength, which usually is lower than uniaxial tensile strength and difficult to measure due, in part, to many different test methods, uniaxial compressive strength is, many times, the driving property in composites design, together with damage tolerance [12, 32].

2.4.2.4. Tensile strength test data and numerical studies

A set of experimental tests were performed at the NASA Marshall Space Flight Center using anisotropic [±12.5] and [±22.5] and orthotropic [0/±25/0] and [0/±45/0] configurations. According to Tsai and Nettles [24], high strength was observed for both smooth and open-hole tensile specimens. Low stress concentration factors (SCF) for open-hole specimens of 1.8 for [±12.5], 1.0 for [±22.5] and 1.7 for [0/±25/0] (nowhere 3.0) were also observed. Furthermore, no delamination was observed among [±12.5] and [0/±25/0] broken specimens (see figure 2.13), which might be attributed to the toughness of the material afforded by the thin plies used in the NCF.

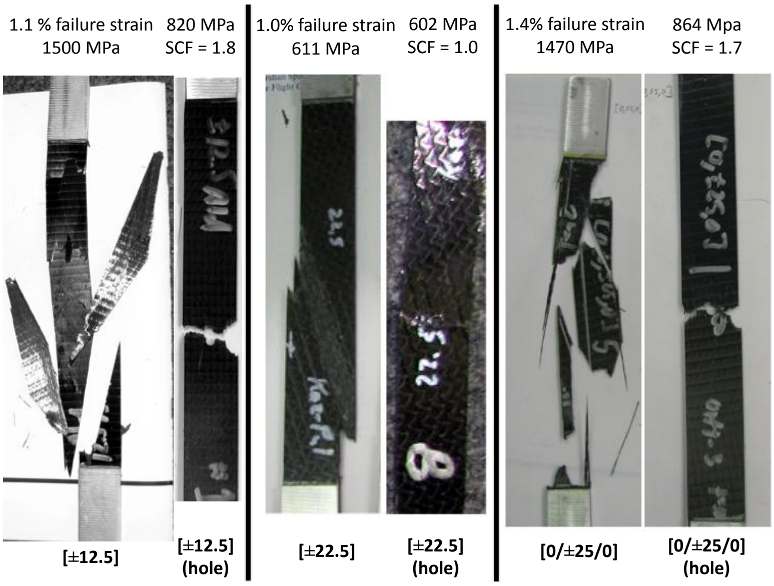

Fig. 2.13. Smooth and open-hole tensile coupons (photos presented by Tsai [12]).

In addition, fatigue tensile tests were also carried out, in order to evaluate the stitching effect in bi-angle NCF. According to Tsai and Nettles, thus far, the effect of stitching was not noticeable, as it was found when characterizing the equivalent elementary UD properties (section 2.4.1). Tsai and Nettles [24] justify this behavior, in part, with the high quality of the NCF produced by tow spreading.

In a numerical study, Ridha and Tay [33] compared the structural performance of bi-angle $[\pm 12.5]_S$ and quasi-isotropic $[0/\pm 45/90]_S$ laminates using the software Abaqus® with an additional user-defined material property (stiffness) degradation method (MPDM) code.

Simple tensile and open-hole tension (OHT) tests were simulated for this purpose. Ridha and Tay [33] report that the stress-strain curves from the simulations show a significant superiority of the bi-angle $[\pm 12.5]_S$ laminate over the quasi-isotropic $[0/\pm 45/90]_S$ laminate:

- The FPF stress of the bi-angle laminate is almost 4 times that of the quasi-isotropic laminate.
- The maximum strength of the bi-angle laminate is more than twice that of the quasi-isotropic laminate.

According to Ridha and Tay [33], these results show that the bi-angle ply is suitable for structures that have highly directional loading directions (wings, wind turbine blades, beams, etc.), while the quasi-isotropic laminate, on the other hand, is too conservative and not optimized for such structures.

Ridha and Tay [33] also studied NCF laminates with the $[0/\pm 25/0]_S$ arrangement. According to the authors, simulations show that this arrangement gives a slightly lower OHT strength in the 0° direction as compared to the $[\pm 12.5]_S$ arrangement. However, its transverse OHT strength is more than 5 times the transverse OHT strength of the $[\pm 12.5]_S$ and more than half the OHT strength of the quasi-isotropic laminates. Furthermore, the transverse OHT FPF stress of the $[0/\pm 25/0]_S$ is slightly higher than the quasi-isotropic one, and the OHT strength of the $[0/\pm 25/0]_S$ is superior than the $[0/\pm 45/0]_S$ laminate, while its transverse OHT strength is not far below the $[0/\pm 45/0]_S$. So, according to Ridha and Tay [33], the $[0/\pm 25/0]_S$ arrangement is a better choice than the $[\pm 12.5]_S$ when a significant OHT strength improvement is needed from the typical quasi-isotropic $[0/\pm 45/90]_S$ or $[0/\pm 45/0]_S$ laminates without compromising too much on transverse OHT strength.

Besides the stress-strain curves, Ridha and Tay [33] also evaluated the progressive damage during their analysis, which can also help to identify the onset of FPF, the failure mechanism and the failure locations. According to this study, the OHT simulation on the quasi-isotropic laminate shows early matrix failure in the 90° plies, which are very weak and compliant in the loading direction. For this particular case, for example, 90° plies should not be used in order to achieve higher performance in terms of strength and stiffness.

In a more recent study [34], Ridha and Tay were able to design both notched and unnotched failure envelopes of $[0/\pm 45/0]_S$ and quasi-isotropic $[0/\pm 45/90]_S$ thin-ply NCF. The used model was a 25.4 mm × 25.4 mm plate with a 4.24 mm diameter hole, made of T700 NCF/RTM6 with a fiber volume fraction of 64% (material properties can be seen in table 2.3). Again, a MPDM code with energy based damage evolution was used. Selected failure criteria were maximum stress for fiber and Tsai-Wu for matrix. The obtained failure envelopes for open-hole and unnotched $[0/\pm 45/0]_S$ and quasi-isotropic $[0/\pm 45/90]_S$ thin-ply T700 NCF/RTM6 plates are shown in figure 2.14. This figure also shows the 60% and 70% unnotched failure envelopes for $[0/\pm 45/0]_S$ and quasi-isotropic $[0/\pm 45/90]_S$ thin-ply plates, respectively.

2.4.2.5. Compressive strength and damage tolerance test data

As mentioned in section 2.4.2.3, compressive strength and damage tolerance are, many times, the driving properties in composites design. Particularly, open-hole compression

Tab. 2.3. Material properties of T700 NCF/RTM6, with a fiber volume fraction of 64%, used by Ridha and Tay [34].

E_1	140.8	GPa	ν_{12}	0.3		X_T	2944	MPa
E_2	9.3	GPa	$\nu_{23}{}^a$	0.5		X_C	1983	MPa
E_3	9.3	GPa	ν_{13}	0.3		Y_T	66	MPa
G_{12}	5.8	GPa	$G_{Ic}{}^b$	60.0	N/mm	Y_C	220	MPa
$G_{23}{}^a$	3.0	GPa	$G_{nc}{}^c$	0.2	N/mm	S	93	MPa
G_{13}	5.8	GPa	$G_{sc}{}^c$	1.0	N/mm	V_f	64	%

a. Assumption based on Daniel and Ishai — reference [2].
b. Assumption based on Laffan et al. — reference [35].
G_{Ic} – fiber direction critical strain energy release rate.
c. Assumption based on Hallett et al. — reference [36].
G_{nc} – transverse direction mode I critical strain energy release rate.
G_{sc} – transverse direction mode II critical strain energy release rate.

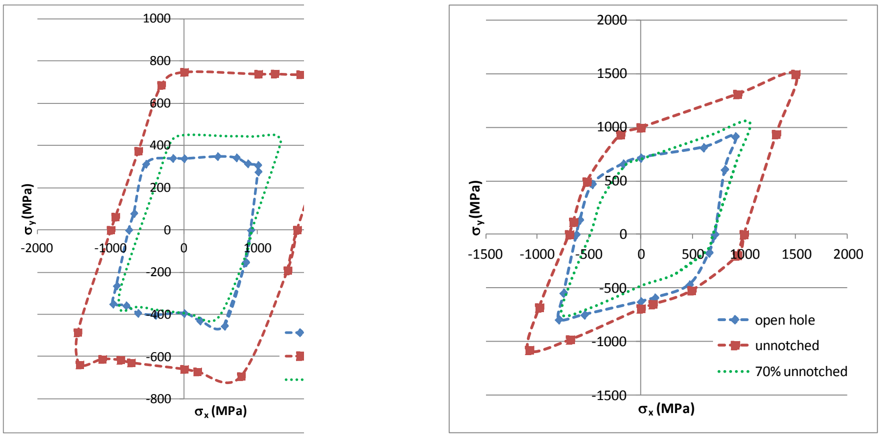

Fig. 2.14. Failure envelopes for open-hole and unnotched $[0/\pm45/0]_S$ (left) and quasi-isotropic $[0/\pm45/90]_S$ (right) thin-ply T700 NCF/RTM6 plates, obtained by Ridha and Tay [34].

(OHC) and compression after impact (CAI) strengths commonly prescribe the design limit of the composite structures for many applications [32].

Tsai and Nettles [24] reported some OHC and CAI tests carried out in $[\pm12.5]_{16T}$ specimens from RTM (KaZaK), HVARTM (Advaero) and prepreg (Aldila) thin-ply NCF panels and in $[\pm22.5]_{16T}$ specimens from pultruded (KaZaK) thin-ply NCF panels. However, according to Tsai and Nettles, it was difficult to make definitive conclusions, namely due to the limited number of tests and lack of laminates made from uni-tapes for direct comparison. Even so, according to the authors, there seems to be some consistencies in the ranking of CAI and OHC tests; furthermore, the absolute values of CAI tests showed that bi-angle thin-ply NCF appears to be competitive.

More recently, Tsai's group [37] carried out some additional preliminary OHC tests using quasi-isotropic $[0/45/90/-45]_{6T}$ laminates made of thin-ply NCF and "equivalent aerospace grade" prepregs. NCF specimens were taken from a $[0/45/90/-45]_{6T}$ 1.78 mm thick panel made by VX Aerospace. In turn, "aerospace grade" specimens were taken from a 1.57 mm thick panel manufactured with a 145 gsm IM7/MTM-45 prepreg, and layed-up as $[0/45/90/-45]_{3T}$. The NCF laminate is slightly thicker than its "equivalent aerospace grade" prepreg laminate due to more resin richness between plies; additionally, some voids are present in the NCF specimens towards the 0° side. Specimens were 38.1 mm wide and contained a 6.35 mm hole. Testing was performed according to ASTM D-3410 with a 25.4 mm gage length. All failures were compressive in nature, emanating from the hole, and there was essentially no difference in the OHC strength of the two laminates tested thus far.

2.4.3. Homogenized thin-ply NCF laminates

It is part of the current practice restrict composite laminates construction to four ply angles (0°, 90° and ±45°), balanced plies (with matching +/– off-axis plies), mid-plane symmetry, uniaxial non-interactive properties (like *fixed strain allowable*), and discrete (integer) ply combinations, conducting to heterogeneous laminates [12, 26, 38, 39]. In turn, using fewer ply angles (namely only 2 angles), and using them as continuous variables, makes homogenization much easier and leads to many benefits for laminate design, such as reduced ply failure modes and simpler laminate optimization, not possible when using the traditional heterogeneous approach [4, 12, 26, 39]. In fact, it becomes easy to realize enormous weight and cost savings when using homogenized, asymmetric laminates, since continuous stacking becomes possible, i.e, one do not have to be concerned where the mid-plane is and flip the stack sequence for the upper part of the laminate to make it symmetric, making continuous stacking not only easier when laying-up but also less prone to error. However, many current practice by industry does not take advantage of this [12].

For this reason, Tsai and Papila [39] recommend using $[0/25]_{16T}$ or $[0/45]_{16T}$, instead
of the $[0_p/\pm$. In fact, ac-
cording to T asymmetric
laminates di he resulting
laminate car genized stiff-
ness and str l strains), as
one can see,

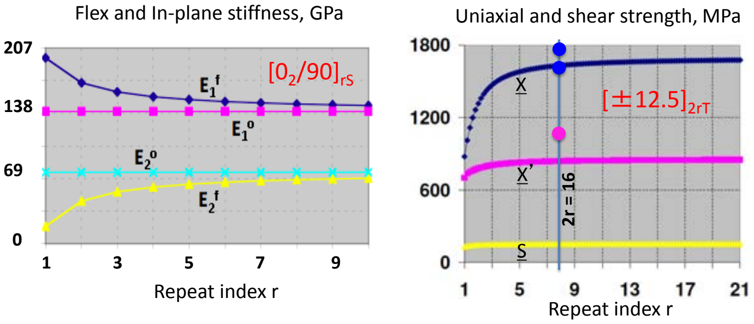

Fig. 2.15. Homogenization of stiffness and strength, presented by Tsai [12]. *Repeating index* (r) is the easiest parameter for homogenization of laminates. It is made simpler if the sublaminate have only two angles and if it is made with thin plies.

Figure 2.16 shows, in the top row, the warpage strain components of freshly cured laminates (before any moisture is absorbed). In the bottom row, figure 2.16 shows the same laminates after moisture is absorbed in long term. Note that warpage strain components are reduced as moisture is absorbed. In the two charts on the right, one can see that, at a repeated index (r) equal to 8, one can have 16 layers of [0/25]. The total number of plies will be 32 and this laminate will be only 2 mm thick. According to Tsai [12], and as one can

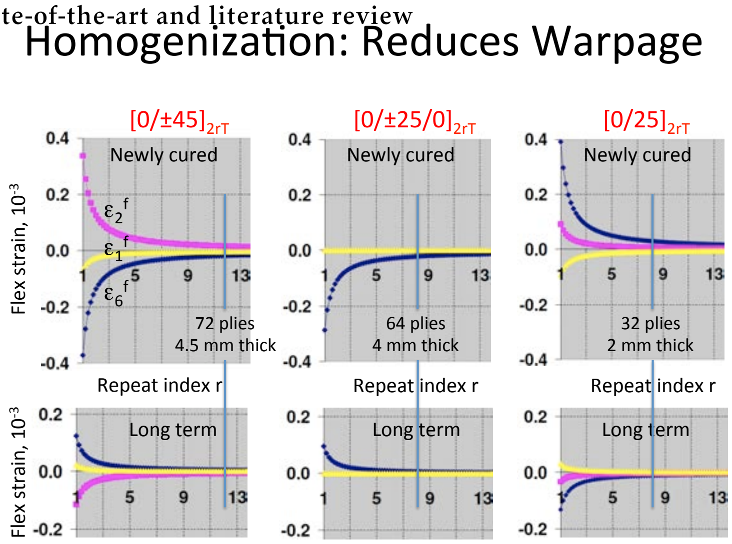

Fig. 2.16. Residual flexural strains of newly cured and long term $[0/\pm45]_{2rT}$, $[0/\pm25/0]_{2rT}$ and $[0/25]_{2rT}$ thin-ply NCF, according to Tsai's group (r is the *repeat index*).

easily conclude, this laminate is homogenized, since all the warpage strain components are vanishingly small. However, it is also clear that the higher the number of plies, the more homogenization is achieved. Thus 16 [0/25] repeated layers is the minimum value. As the number of ply angles increase from two to three, in the laminates on the left and the middle charts, the same degree of homogenization as the bi-angle case of [0/25] will require higher number of repeated layers and thicker laminates. In the middle case, [0/±25/0] layers, one would need a 64-ply laminate with thickness of 4 mm, and in the left case, [0/±45] layers, one would need 72 plies and a 4.5 mm thick laminate.

According to Tsai and Papila [39], asymmetric stacking is made more effective using bi-angle NCF, because the desired off-axis ply is pre-plied with the 0° ply. Thus, 1-axis lay-up can be many times faster than 4-axis lay-up (typically 7× faster). For fuselage applications, 2-axis lay-up is recommended (as mentioned in section 2.4.2), which is still more efficient than 4-axis lay-up. Several sources [4, 12, 26, 39–41] report that:

- Improved quality, lay-up accuracy, higher speed, greater productivity and reduced scrap can all be derived from thin-ply NCF. Ply drop by sublaminate instead of individual ply would be possible.
- Homogenized laminates can be tapered using a much simpler ply drop strategy than heterogeneous laminates (as simple as that for metals). However, the minimum number of repeats may have to be increased, so that the minimum thickness of a tapered laminate is of, at least, 16 bi-angle layers, for a bi-angle laminate (or 32 or higher for three or four angle laminates).
- Tapering can be guided by shape optimization tools not available to heterogeneous laminates (namely those often used in metals).
- Laminate sizing is made simpler as the off-axis ply angle is a much better and continuous variable than the discrete ply change of p, q and/or r in $[0_p/\pm45_q/90_r]_S$.
- Greater laminate strength and toughness are achieved using bi-angle thin-ply NCF because its ply strength can be more easily matched than when using four ply angles.
  - The FPF envelope is larger and can be used for design with a much higher level

  of confidence than last ply failure LPF, which requires empirical constants to represent matrix degradation (see section 2.4.2.3).

  - Micro-cracking is avoided in FPF design (see section 2.4.2.3).

- Homogenization can make design faster and simpler. It would be like designing with aluminum, which is homogenous; the only difference is that bi-angle material is anisotropic, while aluminum is isotropic. Furthermore, instead of using the traditional ply-by-ply method to determine ply failures, the lowest of which is FPF, the equivalent stiffness and strength of a laminate can be calculated directly, using, for instance, the anisotropic Tsai-Wu quadratic failure criterion[6], as soon as homogenization is ensured. The same procedure can be followed also for the homogenized LPF predictions as the laminate parameters are updated for LPF (the LPF parameters are obtained by repeating the strength predictions, but with the degraded ply material properties[7] — see table 2.4).
  - Failure criterion of anisotropic bi-angle lay-ups (such as [0/25]) can be derived from equivalent orthotropic lay-ups (such as [±12.5], in this case) through transformation (when using a quadratic failure criterion like Tsai-Wu).
  - Anisotropy level does not put adverse effects on the accuracy of the equivalent FPF envelopes, since the homogenized laminate failure envelopes for FPF are all in very good agreement with the ply-by-ply analysis.
  - The ply-by-ply LPF envelopes with discontinuities may be hard to implement in automated design cycles, whereas equivalent LPF envelopes are also ellipsoids similar to the FPF envelopes and well behaved functions, which can easily be incorporated parametrically in the design tools.
  - The homogenized laminate failure envelopes for LPF are also all in good agreement with the ply-by-ply analysis.
  - Bi-angle thin-ply NCF homogenized laminates with shallow off-axis plies do not have a significant FPF and LPF distinction, whereby FPF predominantly derives the design.
  - The use of equivalent properties rather than the ply-by-ply approach in numerical design analysis (such as the finite element method) can significantly shorten the overall CPU time and memory needed for simulations, especially when the number of layers in the laminate is large. This is particularly interesting when composites design procedures involve optimization.
  - However, the use of equivalent properties is limited to linear analysis, which means that nonlinear effects such as progressive damage or delamination are not considered.

---

[6] When failure theory is not a single-valued, differentiable (because of discontinuous first derivatives), transformable, and linear scaling function (like maximum strain or Hashin criteria), there is no unique transformation relation, making failure prediction for anisotropic plates extremely complicated. However, a failure theory based on a quadratic function, like Tsai-Wu criterion, can offer not only mathematical integrity but also linearly scalable strength ratios.

[7] The degradation scheme traditionally impose a degradation factor, d, in the range of 0.1–0.2, on the matrix material properties and reflected onto the matrix dominating ply properties using micromechanics relations (see, for instance, reference [4, 42]), whereas the longitudinal ply modulus is kept at its intact value.

Tab. 2.4. Ply and laminate parameters for FPF and LPF analyses. Example provided for bi-angle thin-ply NCF [0/25] building block [40].

FPF stiffness and strength parameters*			LPF stiffness and strength parameters**		
Ply Stiffness	Laminate Stiffness	Laminate Strength	Degraded Ply Stiffness	Degraded Lam. Stiffness	Laminate Strength
$E_{11} = 110$	$E^0_{11} = 70.3$	$X = 718$	$E_{11} = 110$	$E^0_{11\_LPF} = 63.5$	$X_{LPF} = 862$
$E_{22} = 7.4$	$E^0_{22} = 8$	$X' = 666$	$E_{22} = 1.87$	$E^0_{22\_LPF} = 5.0$	$X'_{LPF} = 745$
$\nu_{12} = 0.3$	$\nu^0_{12} = 0.5$	$Y = 71$	$\nu_{12} = 0.06$	$\nu^0_{12\_LPF} = 0.6$	$Y_{LPF} = 71$
$G_{12} = 4.2$	$G^0_{12} = 8$	$Y' = 221$	$G_{12} = 1.0$	$G^0_{12\_LPF} = 6.6$	$Y'_{LPF} = 221$
		$S = 209$			$S_{LPF} = 209$
		$S' = 101$			$S'_{LPF} = 112$

*Stiffness and strength data are in GPa and MPa, respectively.

**The laminate LPF strength parameters (X_{LPF}, X'_{LPF}, Y_{LPF}, Y'_{LPF}, S_{LPF}, and S'_{LPF}) are the strength predictions computed by ply-by-ply analysis under basic loading scenarios.

So, according to Tsai and Papila [39], homogenization will not only reduce cost through simpler asymmetric 1-axis lay-up, and create stronger and tougher laminates through suppression of micro-cracking (FPF design) and edge delamination (thin plies), but also allow huge cost savings and good accuracy in design optimization (instead of ply-by-ply analysis).

2.5. Thin-ply laminates — potential benefits

2.5.1. Summary

According to several sources [10, 13, 14, 20, 43], thin-ply laminates offer a broad range of new advantages. These include:

- Using plies with an areal density of 75 gsm (or 150 gsm per bi-angle layer), a 2 mm thick laminate will have 32 plies (16 bi-angle layers), which ensures laminate homogenization, making irrelevant the location and reversing the stacking order at the mid-plane and resulting in no thermal warpage. This enables a simpler lay-up process, reducing component production, processing time, cost, waste and stacking errors.
- Closed-form and rapid solutions for stress and strength analysis are made possible, and better optimized laminates will lead to further weight and/or cost reduction.
- Because the layers are more finely dispersed, thin plies form stronger and tougher laminates. With bi-angle thin-ply NCF, the strength properties of the composite are optimized, matrix cracking is limited (bringing first ply failure closer to total failure of the material) and stiffness is also increased, by coupling the bending and torsional stresses of the structure; superior strength and consistency in defining safety factors may be achieved, making this material much more competitive.
- Higher fiber dispersion and uniformity of plies, conducting to less resin rich areas. When used in woven fabrics, thin plies improve mechanical properties by diminishing tow flexure (smaller crimp angle).
- Potential to use heavy tow yarns, such as 100 K and 200 K, to cost-effectively obtain wider tows (which may help to reduce costs in laminated composites production), or smaller tows such as 12 K.

- Improved surface appearance. Thin-ply NCF show unique uniformity of the tow spreading.

In addition to these general advantages, potential benefits with respect to structural integrity of thin-ply laminates also must be accounted for. In fact, the fracture process of high performance composite laminates is quite complex, involving both intralaminar (e.g. matrix cracking, fiber fracture) and interlaminar (delamination) damage mechanisms. The basic failure mechanisms, namely matrix cracking, fiber-matrix shearing, fiber tensile failure, fiber kinking (microbuckling), and delamination, must be understood. However, only a few studies in the literature regard exhaustively the effect of ply thickness (and potential advantages of using thin-ply laminates) in these failure modes. A review concerning the effect of ply thickness in the structural integrity of composite laminates, including in-situ effects, delamination resistance, impact resistance/damage tolerance, and translaminar fracture toughness, is presented in the next sections.

2.5.2. In-situ effects

The effect of ply thickness on the onset of ply damage (matrix cracking and delamination), usually predicted using ply criteria, is extremely important [44, 45]. The *transverse tensile strength* and *shear strength* of a ply are function of ply thickness, ply position in the laminate, and fiber orientation of the adjacent plies, whereby they cannot be treated as material properties; in fact, the actual strengths of a ply when it is embedded in a multidirectional laminate are typically higher than those measured in unidirectional coupons, due to the constraints imposed by the neighboring plies [44–53], conducting to a delay of transverse cracking/fiber kinking. This is a deterministic size effect that occurs at the meso-mechanical level, known as the **in-situ effect**, which can be taken into account by using *fracture mechanics models* that predict the relation between the ply thickness, its fracture toughness and the in-situ strengths, whose accurate determination is necessary for implementation of any physical based failure criteria for matrix cracking in constrained plies (see, for instance, references [47–52]).

Parvizi et al. [54], in the late 1970s, performed tensile tests in E-glass/epoxy cross-ply laminates with constant fiber volume fraction, constant longitudinal-ply (0°) thickness and different transverse-ply (90°) thicknesses. All specimens have been loaded up to 1.4% strain. It was observed that, as the thickness of the 90° plies is reduced, transverse cracking changes from multiple occurrences to slow crack growth, small edge cracks and, finally, complete crack suppression, evidencing cracking constraint in the 90° plies, later called as the in-situ effect.

Camanho et al. [45] discusses the effect of ply thickness on the *in-situ strengths* using the fracture mechanics based models proposed by Camanho et al. [49], whose results are illustrated in figure 2.17. As one can see, transverse tensile and compressive strengths (Y_T and Y_C, respectively), and in-plane and out-of-plane shear strengths (S_l and S_t, respectively) increase when the thickness of the ply decreases, which as a beneficial effect on the delay of matrix-dominated failure mechanisms such as transverse cracking and fiber kinking.

2.5.3. Delamination

Structural collapse in a composite structure is caused by the evolution of different types of damage mechanisms, such as matrix transverse cracking, fiber fracture and delami-

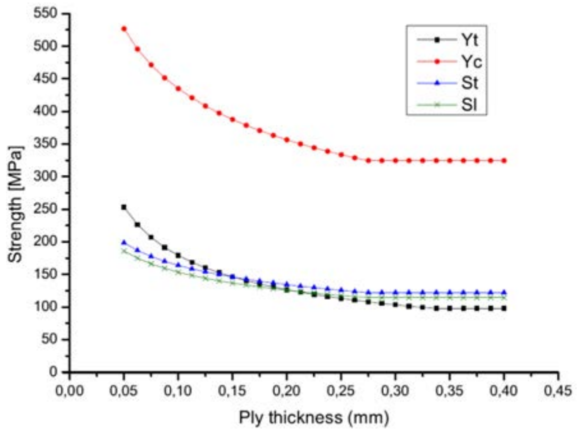

Fig. 2.17. Results for the effect of ply thickness on its in-situ strengths, by Camanho et al. [45].

nation, which strongly depend upon geometry, fiber orientation and stacking sequence [55–59]. **Delamination** (interlaminar damage or interfacial cracking between composite layers) is the result of the failure of the thin resin layer existing between two different oriented plies and is one of the most common types of damage in laminated fiber-reinforced composites due to their relatively weak interlaminar strengths, especially when there is no reinforcement in the thickness direction [50, 55–57, 60–69].

Delamination damage is known to happen because of excessive interlaminar normal and shear stresses at the ply boundaries, and may develop during manufacture (due to incomplete curing or introduction of foreign particles), from impact damage, or from the interlaminar stresses that develop at geometric discontinuities, such as free edges, curved sections, sudden changes of cross sections, ply drop-offs, stiffener terminations and flanges, bonded and bolted joints, and access holes [45, 50, 62–65, 70]; furthermore, delaminations may grow under both static and cyclic loading, affected by a number of other factors such as inhomogeneities, residual thermal strains, matrix curing shrinkage and manufacturing defects [10, 57, 60, 62–65, 67–73]. Delamination growth redistributes the stresses in the plies of a laminate and may influence residual stiffness, residual strength and fatigue life, generally conducting to a significant loss of structural integrity, including reduction of bending stiffness and reduction of the compressive load-carrying capacity due to local buckling [50, 56, 57, 60–65, 70, 72–74].

Delamination is particularly important for the structural integrity of composite structures because, typically, no visual defect is visible on the surface or free edges, making it difficult to detect during inspection [48, 56, 57, 67, 68]. Therefore, the study of the effect of ply thickness in delamination initiation and growth cannot be neglected.

The most common source of delamination appears in the laminate edge — *free-edge delamination* — where high interlaminar stresses are developed due to the mismatch in Poisson contraction of the individual plies with different orientations [71, 75] and due to the fact that fibers are broken at the surface when the specimen is cut (this may happen even for a unidirectional composite) [75]. These edge delaminations typically occur between 90° plies and adjacent angle plies, with delaminations forming initially in a thumbnail shape and rapidly becoming a delaminated strip that grows across the specimen width [71]. Although edge delamination is considered to be a stable fracture process, that may reduce laminate modulus and hence influence tensile strength without causing premature laminate failure (at least under tensile loading) [71], in fact, in some laminates, it leads to premature ply failure initiating at the free edge, with the failure stress depending on the ply thickness [75].

Delamination is also one of the most important fatigue damage mechanisms. This is particularly important, because *mechanical fatigue*, especially *high-cycle fatigue*, is a common cause of failure of structures, such as those used in aircraft and aerospace applications, and it involves several damage mechanisms that result in the degradation of the structure [76–78]. Although polymer matrix composite materials with continuous fibers, in particular carbon fibers, are very effective under high cycle fatigue loading due to the ability of fibers to transmit and disperse the high-frequency vibration loads, these materials, when subjected to high cycle fatigue, usually experience damage initiation by transverse tensile failures in the matrix, resulting in extensive microcracking that, while not affecting the structural response properties and resistance to damage propagation, conducts to local delaminations. Consequently, these local delaminations indicate the onset of damage propagation and failure stages of composites under fatigue loading [8].

Another important precursor of delamination in composite materials is *low velocity impact*. In this type of events, local delaminations arise below and around the impact location, creating local strain concentrations that may lead to nominal laminate failure strains below the in-situ failure strain of the primary load bearing plies [71]. This type of damage is particularly critical for the compressive strength of the impacted composite laminate (as it will be discussed in section 2.5.4).

Based on works carried out by O'Brien [60, 71, 79], one can say that the *strain energy release rate*, G, associated with delamination onset and growth, is a reasonable generic parameter for characterizing the interlaminar fracture behavior of composites, since it accounts for the observed thickness dependence for both edge and local delamination onset, allowing correlation between these two types of delamination. So, the characterization of resistance to delamination in terms of a *critical strain energy release rate*, G_c, is common and widely accepted. However, measurement of resistance to delamination (or *interlaminar fracture toughness*) involves complex data reduction because G_c is a energy-based parameter that is influenced not only by the accuracy of the measured load and displacement, but also by the accuracy of the measured crack length and the change in compliance with crack length [79].

Sihn et al. [10] performed uniaxial tensile static tests on both unnotched and open-hole specimens, and recorded stress-strain curves and took X-ray photos to observe damage modes of failed specimens. In order to study the effect of ply thickness on delamination strength, tow-spread T800C-24K carbon/BT250E epoxy quasi-isotropic specimens, with two different lay-ups, both made from thin plies of 0.04 mm thickness, were used; thick plies were made from stacking 5 thin plies. The results obtained indicate suppression and/or delay of microcracking, delamination and splitting damage with the thin-ply laminated composites, with and without the hole. While thin-ply specimens retain linearity nearly up to the ultimate failure stress, thick-ply specimens show unrecoverable severe damage due to microcracks and delamination. The ultimate strength of thin-ply laminates was approximately 10% higher than that of the thick ones. With the open-hole defect, it was observed a larger increase of the strain and delamination extent near the hole edge of the thick-ply specimens when compared with thin-ply ones; thus, the ultimate strength and strain-to-failure of thin-ply specimens were lower than that of thick-ply specimens, whose damage onset and growth before failure led to lower stress concentrations near the hole.

Wisnom et al. [80] studied the size effects on tensile unnotched specimens. A carbon/epoxy prepreg system (IM7/8552) was used in the manufacture of quasi-isotropic laminates. Stacking sequences were based either in a sublaminate-level scaling, $[45/90/{-45}/0]_{nS}$ (thin-ply laminates), or in a ply-level scaling, $[45_n/90_n/{-45}_n/0_n]_S$ (thick-ply laminates). For the same laminate thickness, thin-ply specimens always showed higher failure stress than thick-ply specimens. Furthermore, while changing the thickness of the laminate by changing the ply block thickness (increase ply thickness) conducted to a decrease in strength, changing the thickness of the laminate by repeating the sublaminate stacking sequence (constant ply thickness in thin-ply laminates) conducted to an increase in strength. All thin-ply specimens behaved similarly, with no load drops or visual indications of damage prior to ultimate failure, characterized by a fairly clean break across the width in the gauge section; so, no delamination occurred before failure. In thick-ply specimens, it was visually observed matrix cracks on the surface and delamination, which propagated at increasing load until catastrophic fiber failure of the unidirectional plies.

O'Higgins et al. [81] carried out an experimental study to determine the OHT characteristics of carbon fiber-reinforced (6376C-HTA(12K)-5.5–29.5%) and S2-glass fiber-reinforced (FM94-27%-S2-187-460) polymer laminates. Particularly, blocked (thick)-ply and dispersed (thin)-ply stacking sequences were analysed, both in the form of cross-ply laminates (respectively $[90_2/0_2]_S$ and $[90/0]_{2S}$). Although the unidirectional strength of blocked-ply and dispersed-ply specimens were not significantly different, results showed that blocked-ply specimens were found to give higher damage levels and OHT strength than dispersed-ply specimens, for both carbon and S2-glass reinforced laminates. In both stacking sequences, damage was characterized by axial splits in the 0° plies accompanied by matrix cracks in the 90° plies; in addition, areas of triangular delamination were evident along the length of the axial splits in both stacking sequences. However, the damage zone in the blocked-ply OHT specimens were much more extensive than those in the dispersed-ply specimens, facilitating the growth of this form of damage and greatly increasing energy absorption.

Green et al. [82] performed an extensive experimental program to study the effect of scaling on the tensile strength of notched composite laminates. In a similar, but more detailed, work Hallett et al. [36] experimentally and numerically evaluated the damage growth in notched composite laminates under tensile loading, through interrupted testing. Particularly, the effect of ply thickness was investigated by testing IM7/8552 carbon/epoxy quasi-isotropic laminates with stacking sequences based either in a sublaminate-level scaling (thin-ply laminates) or in a ply-level scaling (thick-ply laminates). Both works [36, 82] showed that an increase in ply thickness led to a decrease in failure stress, due to the extra energy available for delamination to propagate. For thin-ply laminates, damage was constrained to the outermost sublaminate, inhibiting its propagation through the thickness of the laminate, thus leading to a fiber failure, with either pull-out or brittle appearance. For thick-ply laminates, when the 45/90 interface delamination at the hole propagates across the width and reaches the specimen edge, the delamination propagates along the 45/90 and 90/−45 interfaces, via 90° and −45° matrix cracks, to the −45/0 interface, isolating the 0° plies and conducting to complete gauge section delamination of the −45/0 interface and resulting in an earlier delamination failure. In another work, Pierron et al. [83, 84], besides delamination, investigated the effect of ply thickness in the initial damage process of glass/epoxy quasi-isotropic laminated open-hole tensile test specimens. Two lay-ups with the same thickness were compared, namely $[-45_4/90_4/45_4/0_4]_S$ and $[-45/90/45/0]_{4S}$. Full-field optical measurements based in the grid method were used to conduct such investigation. The authors report that thick-ply laminates sustained much lower loads to first surface cracking, and both specimens showed significant subsurface cracking at the hole (and away from the hole in thin-ply laminates, due to the higher loads sustained) in the 90° plies before the onset of surface cracking.

Similarly, Wisnom and Hallett [69] also performed open-hole tension tests on $[45_m/90_m/-45_m/0_m]_{nS}$ quasi-isotropic IM7/8552 carbon/epoxy laminates with the same stacking sequence and laminate thickness but different ply block thicknesses and numbers of sublaminates, in order to extend the range of data available and clearly demonstrate the effect of ply block thickness on delamination onset and propagation. Results showed that specimens with single 0.125 mm thick plies ($m = 1$, $n = 4$) failed by fiber fracture before reaching the stress necessary to delaminate across the width, with the strength decreasing with increasing hole size. Specimens with 0.5 mm thick blocks of plies ($m = 4$, $n = 1$) all delaminated, with the failure stress increasing with increasing hole diameter (this opposite hole size effect was also observed by Green et al. [82] and Hallett et al. [36]). Finally, specimens with intermediate ply block thicknesses, 0.25 mm ($m = 2$, $n = 2$), showed intermediate response, with small ones failing by delamination and large ones by fiber failure, and constant strength over a range of hole sizes from 1.6 to 12.7 mm diameter. Accordingly, it was notorious that delamination had a crucial role in the in-plane strength, failure mechanism and hole size effect in open-hole tension of quasi-isotropic laminates, leading to premature failure, especially for narrow specimens, small holes and thick ply blocks, due to delamination from the intersection of transverse cracks and from the free edge effect.

Kawabe measured the acoustic response (in terms of number of events, energy and amplitude) of quasi-isotropic $[\pm45/0/90]_S$ coupons under tensile loading. His results were presented by Tsai [12], and are shown in figure 2.18. This figure compares the $[\pm45/0/90]_S$ laminates with normal plies, of 0.12 mm thickness, on the left, with those manufactured using thin plies, of 0.04 mm, on the right. The total thicknesses of both laminates are the same. Thus there will be 3-times the number of plies for the thin-ply laminate than the normal-ply laminate. On the left, the FPF signal started at 250 units and continued until the ultimate failure. In this case, the FPF started at 45% of the LPF for the normal-ply laminate. On the right, the FPF for thin-ply laminates started at 480 units (almost twice), and the signals are very limited between that FPF and LPF at 550 units; in fact, for the thin-ply laminate, FPF started at 87% of the LPF.

At the bottom of figure 2.18, it is shown the top and side views of the broken specimens. As one can see, while the normal-ply laminate (on the left) failed with jagged failure surface and extensive delamination, the thin-ply laminate (on the right) failed with a clean and highly localized surface and showed no delamination. Such dramatic difference between the failure modes is consistent with the extensive acoustic signals of the normal-ply laminate on the left as compared with limited acoustic signals of thin-ply laminate on the right. It is reasonable to assume that thin-ply laminates would be tougher (resistant to

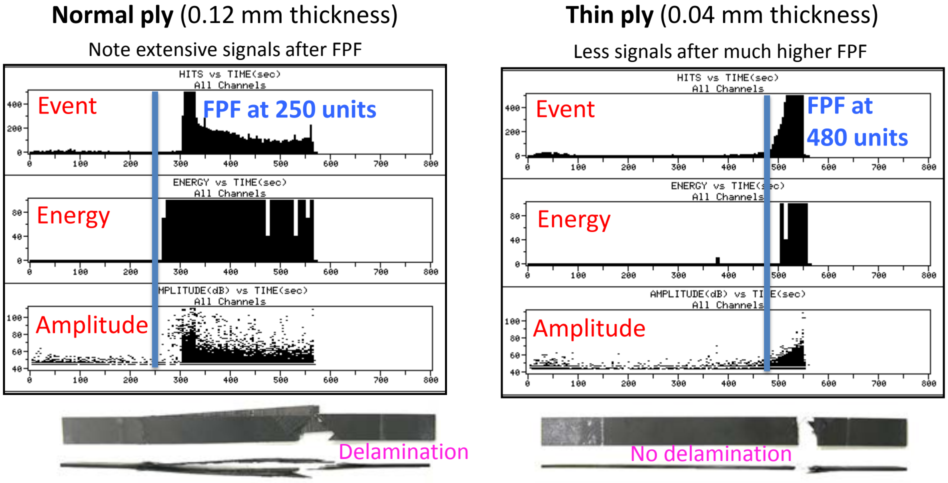

Fig. 2.18. Acoustic response of quasi-isotropic $[\pm45/0/90]_S$ coupons and top and side views of failed coupons. Work performed by Dr. K. Kawabe of Fukui Prefecture Technology Laboratories in Fukui, Japan, presented by Tsai [12].

delamination) than normal-ply laminates, as well as less susceptible to matrix cracking. Similar conclusions regarding tensile static testing and acoustic emission analysis were reported by Yokozeki et al. [32] in a previous study in carbon/toughened epoxy thin-ply laminates.

Moon et al. [85] studied some solutions to improve the resistance against low earth orbit (LEO) environment and the mechanical properties of carbon/epoxy composite laminates for aerospace applications, including the use of thin plies. Quasi-isotropic specimens were used to investigate the effect of thin plies, with two different stacking sequences, namely a $[0/\pm45/90]_S$ lay-up with standard 0.125 mm thick plies and a $[0/\pm45/90]_{2S}$ lay-up with 0.060 mm thick plies. Both lay-ups had the same thickness. Results showed that, by making prepregs with thin plies, the tensile strength was slightly increased, with (12.11%) or without (8.91%) LEO environment exposure. Standard-ply laminates showed sudden large increase in strain and drops of load induced by progressive failures of the specimen, namely cracks, delaminations and fiber breakage (these phenomena were especially evident for the LEO exposed case). In constrast, thin-ply laminates showed stable stress/strain curves (even for the LEO exposed case), meaning that there were less progressive failures before fiber failure due to the high constraint effect between each thin ply.

Recently, Nettles [86] performed some tensile tests in both notched (open-hole) and unnotched specimens excised at orientations parallel to the 0° direction and the 22.5° direction from a 0.91 mm thick $[0/-45/90/45]_{3T}$ (asymmetric) panel made with C-Ply™ bi-angle NCF (T700 fiber) and Aldila's AR-2527 resin (nominal ply thickness of 0.076 mm), which were compared to a typical "aerospace grade" 1.02 mm thick $[45/0/-45/90]_S$ laminate, made with T800/5320 carbon/epoxy laminate (nominal ply thickness of 0.127 mm). The C-Ply™ panel was cured at 135°C with only vacuum pressure (out-of-autoclave). It had a fiber volume of about 55%. The T800/5320 panel was cured at 176°C with 6.8 atmospheres. The fiber volume fraction of this panel was about 63–65%. Cross-sectional views of each of these panels (figure 2.19) showed that both laminates were well consolidated with few voids. As expected, the C-Ply™ laminate demonstrated more resin rich areas (see figure 2.19a) between plies than the T800/5320 laminate since the C-Ply™ laminate was cured with 1 atmosphere of pressure while the T800 panel was cured with a pressure of 6.8 atmospheres. As expected, the T800/5320 laminate had a 38% higher longitudinal tensile modulus than the C-Ply™ laminate since the fibers which constitute the T800/5320 laminate have a 28% higher modulus than the fibers that make up the C-Ply™ laminate[8]. In addition, the T800/5320 laminate had a slightly higher volume fraction of fibers than the C-Ply™ laminate, also leading to a higher modulus being measured for the T800/5320 laminate. Possibly due to the higher strength of the T800 fibers and also to the higher fiber volume fraction of the T800/5320 laminate, generally, the tensile strength of the T800/5320 laminate was higher than the C-Ply™ laminate, except for the unnotched specimens at 22.5°. Photographs of typical failed OHT and unnotched specimens are presented in figures 2.20 and 2.21, respectively. As one can see, no delamination occured in the C-Ply™, contrary to the extensive delaminations observed in the T800/5320 specimens, in both open-hole and unnotched specimens, in both orientations.

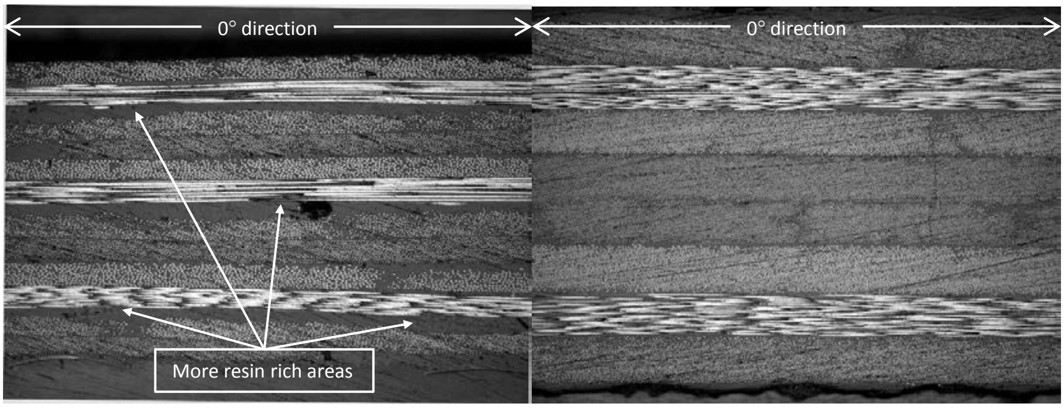

(**a**) C-Ply™ bi-angle NCF laminate. (**b**) T800/5320 laminate.

Fig. 2.19. Cross-sectional photomicrographs of the two panels tested by Nettles [86].

Herakovich, in a historical review regarding the mechanics of composites [59], showed the significant effects of stacking sequence for tensile tests on angle-ply laminates with different stacking sequences. When the $+\theta$ and $-\theta$ layers are stacked in an alternating fashion ($[\pm\theta]_{nS}$), the mode of failure is primarily due to fiber breakage. In contrast, when the $+\theta$ and $-\theta$ layers are grouped together ($[\theta_n/-\theta_n]_S$), edge effects and interlaminar shear stresses dominate; the specimen fails due to delamination at a much lower axial stress. For example, according to Herakovich [59], alternating the layers of a $[\pm 30]_S$ specimen resulted in a 48% increase in strength.

Lee and Soutis [87] investigated the effect of laminate thickness on the compressive behavior of T800/924C carbon/epoxy prepreg composite laminates, by means of static compressive testing in unnotched and open-hole specimens (for open-hole specimens, the diameter to width ratio was 0.1 and the hole diameter was 3 mm). Particularly, they studied the stacking sequence effects on failure strength of quasi-isotropic lay-ups. Stacking sequences were based either in a sublaminate-level scaling, where the basic sublaminate is repeated as often as it is required, $[45/0/-45/90]_{nS}$ (corresponding to the thin-ply lam-

---

[8] According to Toray data sheet, the T800 fiber has a fiber modulus of 294 GPa and a fiber strength of 5880 MPa, while the T700 fiber has a fiber modulus of 230 GPa and a fiber strength of 4900 MPa.

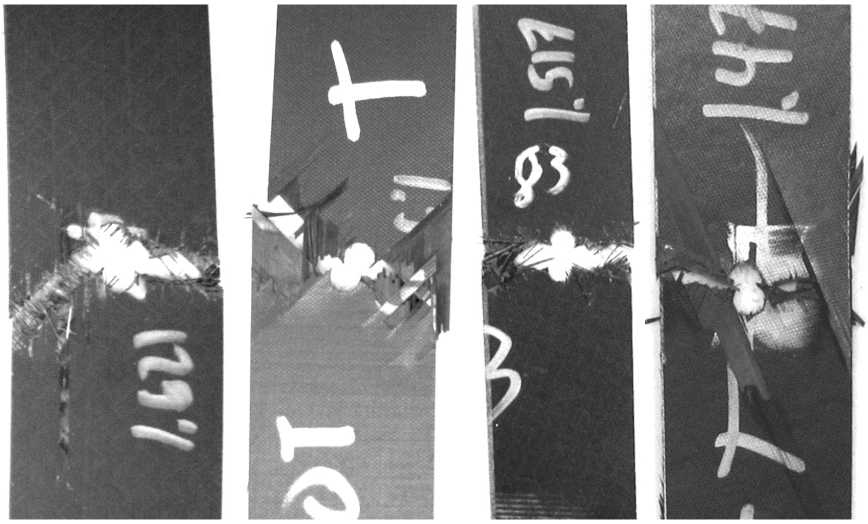

(**a**) C-Ply™ at 0°. (**b**) T800 at 0°. (**c**) C-Ply™ at 22.5°. (**d**) T800 at 22.5°.

Fig. 2.20. Post mortem photographs of the OHT specimens tested by Nettles [86].

(**a**) C-Ply™ at 0°. (**b**) T800 at 0°. (**c**) C-Ply™ at 22.5°. (**d**) T800 at 22.5°.

Fig. 2.21. Post mortem photographs of the unnotched specimens tested by Nettles [86].

inates), or in a ply-level scaling, where plies of the same orientation are stacked together, increasing the effective ply thickness, $[45_n/0_n/{-45}_n/90_n]_S$ (corresponding to the thick-ply laminates). Plies were 0.125 mm thick. Additionally, parameters such as fiber volume fraction, void content, fiber waviness and interlaminar stresses, influencing compressive strength with increasing laminate thickness, were also studied. It was found that the strength values obtained from the sublaminate-level scaled specimens were slightly higher than those obtained from the ply-level scaled specimens, in both unnotched and open-hole specimens. The reason for this effect was explained by the fiber waviness, void content, free edge effect and stress distribution in blocked and unblocked 0° plies. The unnotched sublaminate-level scaled specimens did not show any thickness effects, since their compressive strength was constant regardless of the specimen thickness. The failure, which occurred suddenly in a crushing failure mode, involved a combination of fiber microbuckling in the 0° plies, delamination between 0° and ±45° plies, splitting parallel to the fibers at 0° and ±45° plies, and matrix cracking and crushing in the 90° plies, without a global buckling influence. For the unnotched ply-level scaled specimens, which showed the above failure characteristics but in a more pronounced way, a strength reduction with increasing thickness was observed. Fiber waviness and void content were found to be the main parameters contributing to the thickness effect on the compressive failure strength of the ply-level scaled specimens. The compressive strength of the open-hole specimens, for both studied stacking sequences, increased with increasing thickness, something explained by the introduction of out-of-plane bending in the window area of the anti-buckling device (10 mm wide by 16 mm long), magnifying the stress field near the hole and causing damage initiation and final failure at a lower applied load in the thinner specimens.

Lee and Soutis [88] also examined the effect of specimen size on the axial compressive strength of IM7/8552 carbon/epoxy quasi-isotropic laminates, with blocked plies, $[45_n/90_n/-45_n/0_n]_S$, and distributed plies, $[45/90/-45/0]_{nS}$, of 0.125 mm thickness. Results showed that compressive strengths were similar for both lay-ups, with no evidence of a size effect. All specimens failed within the gauge section suggesting that the test fixture and specimen design used in this work were very much appropriate.

In other studies, Lee and Soutis [89, 90] were focused in the scaling effects on the strength of composites with open holes, including, once again, ply thickness effect. Specimens were fabricated from 0.125 mm thick IM7/8552 carbon/epoxy prepreg tapes. To study ply thickness effect, two quasi-isotropic lay-ups, one with blocked plies, $[45_n/90_n/-45_n/0_n]_S$, and the other with distributed layers, $[45/90/-45/0]_{nS}$, were fabricated. Unnotched and notched (0.2 diameter to width ratio) compressive tests were performed. Unlike the previous results (reference [88]), the unnotched compressive strength of the ply-level scaled specimens was reduced with increasing specimen dimensions, an effect attributed to the blocked 0° ply thickness (increase of fiber waviness and void content), free edge effect and residual thermal stresses. The compressive strength of the sublaminate-level scaled specimens was unaffected regardless of the specimen dimensions. However, unlike a previous work (reference [87]), open-hole compressive strength values obtained from the ply-level scaled specimens were higher than those obtained for the sublaminate-level scaled specimens. This result could be attributed to stress redistribution that occurs due to local damage around the hole. The ply-level scaled specimens developed local damage around the hole, in the form of fiber/matrix splitting, at a lower applied compressive load than the sublaminate-level scaled specimens. This local damage delays the final failure to a higher applied load since the stress concentration factor at the edge of hole is reduced and stress is redistributed in the specimen. If the local damage does not occur, or occurs just prior to the catastrophic failure (which is the case of sublaminate-level scaled specimens), the composite laminate behavior is closer to brittle behavior, resulting in a lower failure load; furthermore, according to this study, the local damage enhances the fracture toughness of the laminate, resulting in a higher notched compressive strength in the ply-level scaled specimens.

Yokozeki et al. [32] focused their study in the experimental characterization of the damage tolerance of thin-ply carbon/toughened epoxy prepreg laminates, by means of OHC testing. A comparative study on MR50K intermediate modulus carbon fiber/#1063EX toughened epoxy laminates with the same in-plane stiffness, total thickness and lay-up ratios using conventional (145 gsm) and thin-ply (75 gsm) prepregs was performed in order to clarify the effectiveness of the compressive and damage tolerance characteristics of spread tow thin-ply laminates. Conventional $[45/0/-45/90]_{2S}$ laminates and thin-ply $[45/0/-45/90]_{4S}$ laminates were used in OHC tests. Plain strength compression results demonstrated an increase in compressive strength (16%) of the thin-ply laminate, though the compressive behaviors of the conventional and thin-ply laminates were almost identical. The OHC strength of thin-ply laminates were also slightly higher (9%) than that of conventional laminates. These results contradict those obtained by Lee and Soutis [89, 90] (described before), where lower stress concentration was found in the thick-ply specimens due to stress redistribution caused by local damage; further studies are necessary in order to clarify the effect of ply thickness in open-hole specimens.

In addition, fatigue tests were also carried out in thin-ply laminates. Nishikawa et al. [43] studied the fatigue behavior of thin and thick-ply carbon/epoxy laminated composites. In this work, plain-woven carbon fiber/epoxy using very thin and wide spread tows were tested under tension-tension fatigue load. The spread tows were obtained using the pneumatic method described in section 2.2.2 and in reference [16]. The experimental results showed that the fatigue lives of spread tow based plain-woven laminates were longer than those of conventional types. It was also observed that fatigue crack formation and propagation were constrained by using thin plies. Similar conclusions regarding tension-tension fatigue testing were reported by Yokozeki et al. [32] when studying carbon/toughened epoxy thin-ply laminates.

In a work conducted by Sihn (see, for instance, reference [10]) and presented by Tsai [12], tensile fatigue tests were also performed in thin and thick-ply carbon/epoxy laminates. Thick plies were made from stacking 5 thin plies, each of these with 0.04 mm thickness. The total thickness of both laminates was 3.2 mm. Figure 2.22 shows the X-ray pictures of these laminates after 73000 cycles of tensile fatigue. Note, on the left, only slight splitting around the open hole on the thin-ply laminate, no delamination along the specimen outer edges, and no microcracking. For the thick-ply laminate, on the right, there are massive delamination around the open hole and outer edges, plus microcracking along all ply angles. So, although considered a preliminary work, these results show that laminates made with thin plies show higher resistance to both microcracking and delamination under fatigue load.

Based on a free-edge stress analysis, Tsai [4] demonstrated that a drastic decrease in the delamination stress is observed as a function of the increasing repeating index of a sublaminate within a laminate structure. His analysis is reprinted in figure 2.23. This increase in strength can also be rationalized by a damage distribution argument; i.e., when the plies in a laminate are dispersed, each ply group represents a smaller percentage of the total laminate.

In turn, Camanho et al. [45] performed a FE analysis to evaluate the influence of ply thickness on the free-edge delamination onset strain and growth using generalized plain strain elements, as shown in figure 2.24, and user defined cohesive elements, previously developed by Turon et al. [56]. Different T700/M21 $[45_n/-45_n/0_n/90_n]_{rS/T}$, $[90_n/45_n/-45_n/90_n]_{rS/T}$ and $[0_n/45_n/-45_n/0_n]_{rS/T}$ symmetric (S) or asymmetric (T) laminates, with 0.04 mm ply thickness, where $n = 1$ and $r > 1$ for thin-ply laminates, and $n > 1$

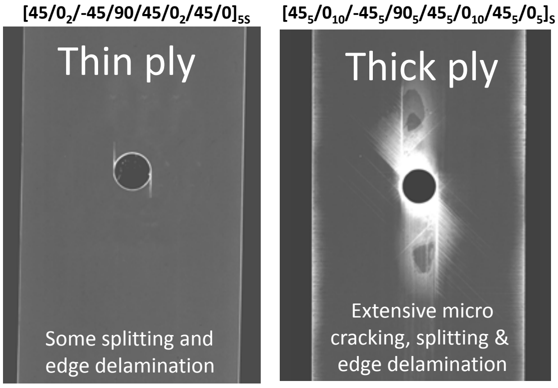

Fig. 2.22. X-ray pictures of specimens subjected to tensile fatigue ($\sigma_{max} = 0.7X_T^L = 70$ ksi, $R = 0.1$, $f = 5$ Hz) at room temperature, after 73000 cycles (ply thickness of 0.04 mm and total laminate thickness of 3.2 mm.). Work performed by Dr. Sangwook Sihn of the University of Dayton Research Institute and presented by Tsai [12].

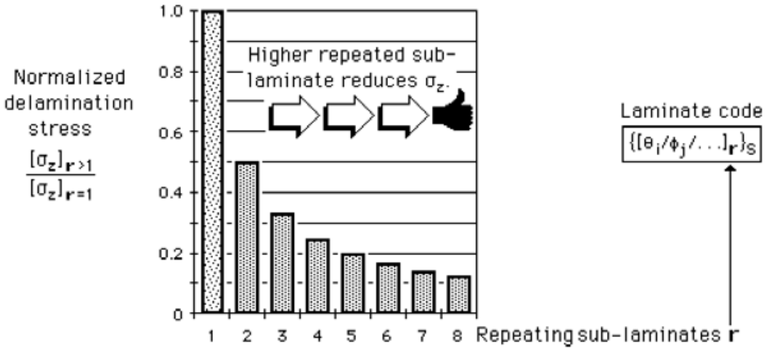

Fig. 2.23. Reduction in interlaminar normal stress as the number of repeated sublaminates increase. Reprinted from Tsai [4].

and r = 1 for the thick-ply (clustered) laminates, were simulated using the FE package Abaqus®. The elastic material properties for material definition were defined through the elastic stiffness parameters of the stress-strain relation, D_{ijkl}.

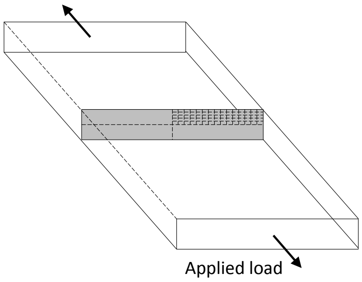

Fig. 2.24. Region of the specimen simulated by Camanho et al. [45].

Figures 2.25, 2.26 and 2.27 show the predictions obtained by Camanho et al. [45] for the opening stresses σ_{22} of the deformed shapes at the free-edges of different laminates using different ply thicknesses. Figure 2.28 shows the predicted strain values corresponding to free-edge delamination for the T700/M21 $[45_n/-45_n/0_n/90_n]_{rS}$ laminates with different ply thicknesses, also obtained by the numerical model of Camanho et al. [45]. As one can easily see, delamination onset strain increases considerably when ply thickness is reduced. These numerical results are a good initial step towards the understanding of the effect of thin plies in delamination resistance.

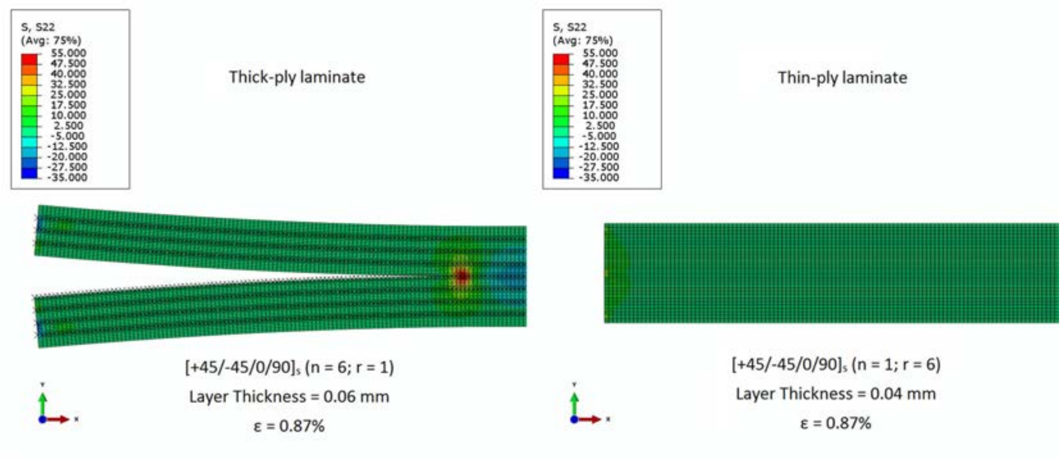

Fig. 2.25. Opening stresses σ_{22} of the deformed thick-ply $[45_6/-45_6/0_6/90_6]_S$ (left) and thin-ply $[45/-45/0/90]_{6S}$ (right) laminates above the critical strain of the thick-ply laminate, simulated by Camanho et al. [45] using the FE package Abaqus®.

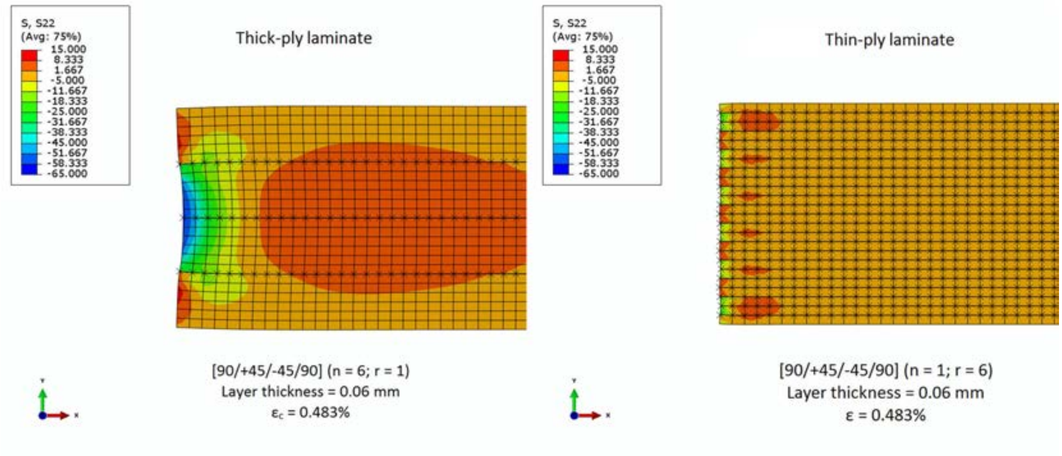

Fig. 2.26. Opening stresses σ_{22} of the deformed thick-ply $[90_6/45_6/-45_6/90_6]_T$ (left) and thin-ply $[90/45/-45/90]_{6T}$ (right) laminates at the critical strain of the thick-ply laminate, simulated by Camanho et al. [45] using the FE package Abaqus®.

Camanho et al. [45] also performed a numerical analysis on the delamination resistance of ply-drops (skin-stiffener) based on thick-ply[9] (clustered) and thin-ply[10] laminates. The skin-stiffener model is shown in figure 2.29. Ply thickness was 0.04 mm, the laminate thickness of the skin was 1.44 mm, and the laminate thickness of the flange was 1.92 mm. Figure 2.30 shows the predictions of the opening stresses σ_{22} of the deformed skin-stiffener

---

[9] A $[45_3/-45_3/0_3/-45_3/45_3/90_3/90_3/-45_3/45_3/0_3/45_3/-45_3]_T$ laminate configuration was used in the skin and a $[45_4/-45_4/0_4/90_4]_{3T}$ laminate configuration was used in the flange to study the delamination resistance of ply-drops consisting of thick-ply laminates.

[10] A $[45/-45/0/-45/45/90/90/-45/45/0/45/-45]_{3T}$ laminate configuration was used in the skin and a $[45/-45/0/90]_{12T}$ laminate configuration was used in the flange to study the delamination resistance of ply-drops consisting of thin-ply laminates.

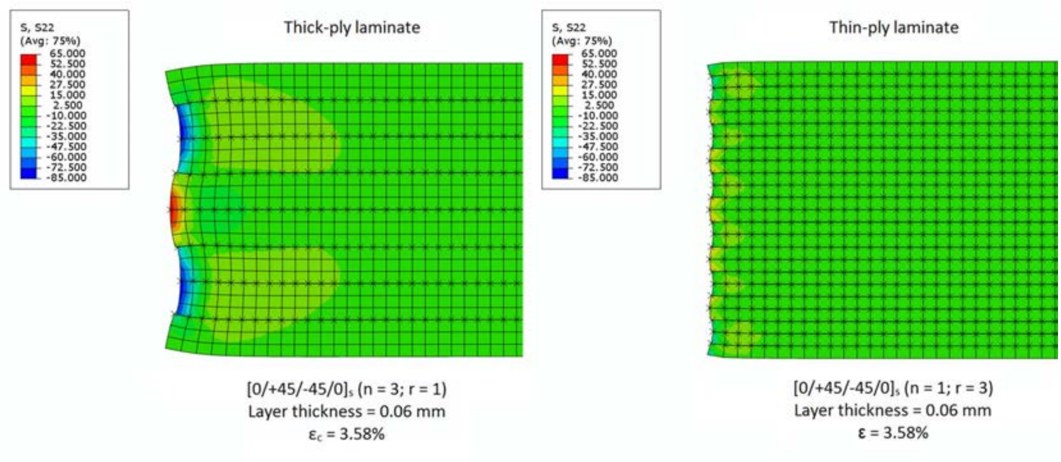

Fig. 2.27. Opening stresses σ_{22} of the deformed thick-ply $[0_3/45_3/-45_3/0_3]_S$ (left) and thin-ply $[0/45/-45/0]_{3S}$ (right) laminates at the critical strain of the thick-ply laminate, simulated by Camanho et al. [45] using the FE package Abaqus®.

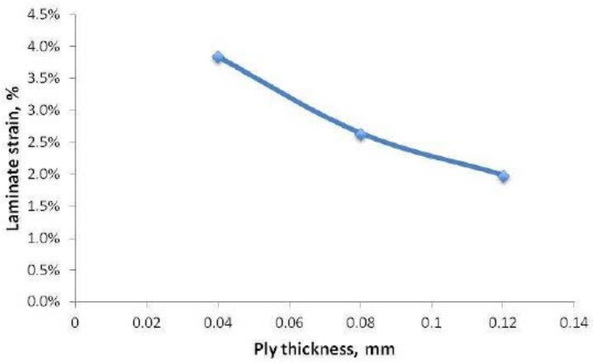

Fig. 2.28. Numerical results for the failure strain of the T700/M21 $[45_n/-45_n/0_n/90_n]_{rS}$ laminates as a function of the ply thickness, obtained by Camanho et al. [45].

models. As one can see, for the same strain, the ply-drop with thick-ply laminates exhibit much higher interlaminar stresses, inducing delaminations much before the ply-drop with thin-ply laminates; i.e., the critical strain for thick-ply laminates was much lower than that for thin-ply laminates (higher delamination resistance).

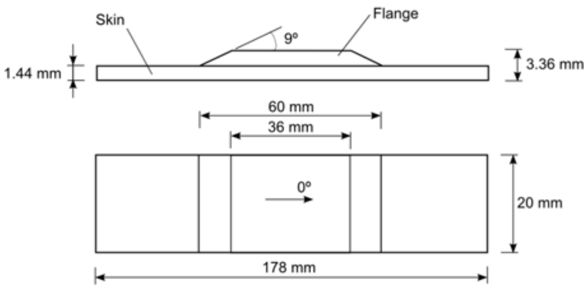

Fig. 2.29. Skin-stiffener model used by Camanho et al. [45] to evaluate delamination resistance of thick-ply (clustered) and thin-ply laminates.

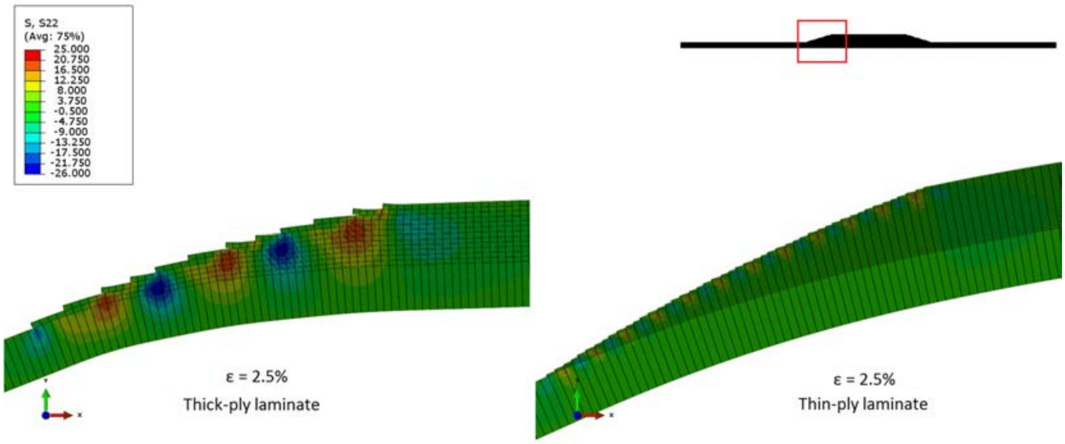

Fig. 2.30. Opening stresses σ_{22} of the deformed thick-ply (left) and thin-ply (right) skin-stiffener models obtained by Camanho et al. [45].

2.5.4. Impact resistance and damage tolerance

In general, load bearing structures made of composite laminates, particularly those used in aircraft and aerospace structures, must have their design driven by damage tolerance considerations (i.e., some level of damage must be assumed to exist in the composite structure), since compression and shear failures become critical when associated with pre-existing matrix cracking and local delamination. In addition, the most common composite laminates used in such applications are considered to be very brittle and very susceptible to impact damage [91]. In composite materials, impact damage is often characterized by the introduction of defects such as matrix cracking and local delamination, considerably reducing residual compressive and shear strengths. So, the effect of ply thickness on **impact resistance** (or **damage resistance**) and **damage tolerance**, which may be assessed by means of **low-velocity impact** (**LVI**) and **compression after impact** (**CAI**) testing, respectively, is also an important feature when analysing the structural integrity of thin-ply laminates. Impact damage occurs due to both global deflections and localized contact forces [92] during an impact event, and may result from the interaction between different failure mechanisms, such as indentation, matrix cracking, fiber-matrix interface debonding, fiber breakage, delamination and, eventually, penetration. Typically termed **barely visible impact damage** (**BVID**), this localized subsurface damage is often left undetected and, therefore, it is considered to be potentially dangerous with respect to the structural integrity of composite structures [74, 93–97].

If thin-ply laminates are able to suppress the onset of the microcracking and delamination damage (as discussed previously), one can expect that the similar superiority can be observed under impact loading [10, 98]. However, according to several authors [95–97, 99], the effect of ply thickness on the damage tolerance, assessed by means of the residual compressive strength, where the greatest reduction in loading is observed due to laminae buckling in the delaminated areas, is not fully clear. In fact, the compressive strength of laminated composites decreases if the size of delaminations created by impact is large, which is expected to occur in thick-ply laminates, but also if the number of delamination planes increases, which happens when the number of plies in a laminate increases [97], as in the case of thin-ply laminates. This observation highlights how important is the evaluation, under both experimental and numerical analysis, of the effect of ply thickness on damage resistance and damage tolerance of laminated composites.

Hitchen and Kemp [93] investigated the effect of the stacking sequence on the impact resistance and damage tolerance of a carbon/toughened epoxy composite laminate, performing LVI and CAI tests. 16-ply T800H/924C composite plates were tested with different stacking sequences, namely, $[\pm45/0_2]_{2S}$, $[(\pm45)_2/0_4]_S$, $[+45/0/-45/0]_{2S}$, $[(0_2/\pm45)_2]_S$, $[0_4/(\pm45)_2]_S$, and $[0/+45/0/-45]_{2S}$. After LVI testing, the lay-ups with higher number of interfaces (thinner plies) showed the smaller total delamination areas, attributed to a higher energy absorption for delamination initiation. The CAI strength, however, showed no trend with the number of interfaces, i.e., ply thickness did not show any effect in the residual strength of the tested plates.

Fuoss et al. [99] experimentally and numerically examined the effect of grouping plies together in the impact resistance of carbon/epoxy composite laminates with 24 plies, by means of LVI testing and quasi-static simulations. Stacking sequences with no ply grouping, groupings of two plies and groupings of three plies were investigated, namely $[-45/0/45/90]_{3S}$, $[-45_2/0_2/45_2/90_2/-45/0/45/90]_S$, $[-45/0/45/90/-45_2/0_2/45_2/90_2]_S$, $[-45_2/0/45/90_2/-45/0_2/45_2/90]_S$ and $[-45_3/0_3/45_3/90_3]_S$. Ply grouping was found to reduce the damage resistance in a laminate; the first lay-up, with no ply grouping, contained the smallest damage area, while the last presented lay-up, with groupings of three plies, had the double of the damage area of the latter. Furthermore, the location of the ply grouping also had an effect on the damage resistance; a larger damage area was observed when the ply grouping occurred near the impact and back faces of the laminate, whereas a better configuration was achieved by uniformly distributing the ply grouping through the laminate (lay-up $[-45_2/0/45/90_2/-45/0_2/45_2/90]_S$). According to the authors, stacking plies with the same fiber orientation together increase the stress concentration at the adjacent interfaces, due to the increased bending stiffness within that ply group, creating larger delaminations. Ply grouping also reduce the number of interfaces available for delamination, since delaminations can occur only at interfaces that contain different fiber orientations between the adjacent plies; since delamination acts as an energy absorbing mechanism, reducing the number of locations available for delamination increases delamination size at the remaining interfaces.

In a study carried out by de Freitas and Reis [96], impact resistance and damage tolerance of two different carbon/epoxy composite systems were assessed by means of LVI and CAI, respectively. Four stacking sequences with 24 plies were used for both composite materials, namely $[-45_3/0_3/45_3/90_3]_S$, $[-45/0/45/90/-45_2/0_2/45_2/90_2]_S$, $[-45_4/45_4/0_3/90]_S$ and $[-45_3/45_3/0_5/90]_S$. Results show that the delaminated area after impact is highly dependent on the number of interfaces between plies, which increases with decreasing ply thickness. Higher delaminated areas were observed in laminates with fewer interfaces, i.e., in laminates with thick plies. However, the compressive residual strength was scarcely affected by stacking sequence.

Sihn et al. [10] conducted LVI testing on thin and thick-ply specimens and compared C-scan images showing the size and depth of the delamination damage due to impact loading. CAI tests were also performed to study damage tolerance of thin and thick-ply laminates. Specimens were made with tow-spread T800C-24K carbon/BT250E epoxy quasi-isotropic laminates, with two different laminations, both made from thin plies of 0.04 mm thickness;

however, thick plies are made from stacking five thin plies. The in-depth C-scan images after the impact loading indicated that the overall sizes of the delamination damage are similar for thin-ply and thick-ply specimens. However, the stress-strain behavior after the CAI tests indicated less severe delamination damage in the thin-ply laminates than in the thick ones. These results contradict those obtained in references [93, 96, 99], previously described.

Yokozeki et al. [32] also experimentally characterized the damage tolerance of thin-ply carbon/toughened epoxy prepreg laminates by means of CAI testing. A comparative study on MR50K intermediate modulus carbon fiber/#1063EX toughened epoxy laminates with the same in-plane stiffness, total thickness and lay-up ratios using conventional (145 gsm) and thin-ply (75 gsm) prepregs was performed in order to clarify the effectiveness of the compressive and damage tolerance characteristics of spread tow thin-ply laminates. Conventional $[45/0/-45/90]_{4S}$ laminates and thin-ply $[45/0/-45/90]_{8S}$ laminates were used in CAI tests. The LVI and CAI test results show that the projected post-impact delamination areas were almost identical between conventional and thin-ply laminates; however, the CAI strength of thin-ply laminates were slightly higher (8%) than that of conventional laminates, which may result from the narrow delamination widths and superior resistance against delamination growth observed in thin-ply laminates. These results agree with those obtained by Sihn et al. [10], while contradicting those obtained in references [93, 96, 99] previously described.

In another study, Yokozeki et al. [98] assessed the damage resistance of spread tow thin-ply laminates by means of out-of-plane transverse loading, i.e., quasi-static indentation, claiming that the tested carbon/toughened epoxy laminates exhibit similar damage process under transverse dynamic and static loading, citing a study of Aoki et al [100]. The same quasi-isotropic MR50K/#1063EX conventional $[45/0/-45/90]_{2S}$ and thin-ply $[45/0/-45/90]_{4S}$ laminates, used in the work previously described, were tested. Results showed that matrix cracking was firstly observed in the back surface ply, and delaminations were induced inside in both conventional and thin-ply laminates. However, in conventional laminates, accumulation and growth of delaminations and matrix cracks were observed, while in thin-ply laminates sudden fiber fractures occurred. Accordingly, it was considered that thin-ply laminates have higher damage resistance against matrix cracking and delaminations under out-of-plane transverse loading than conventional ones, contrary to the conclusions made previously by Yokozeki et al. [32] regarding LVI testing of these laminates.

González et al. [97] studied the effect of ply thickness on rectangular, flat and monolithic laminated composite plates subjected to a drop-weight, LVI loading, according to the ASTM test method (ASTM D7136/D7138M-05), whose results are discussed by Camanho et al. [45]. The stacking sequences used to study ply thickness effect were $[45/0/-45/90]_{4S}$, $[45_2/0_2/-45_2/90_2]_{2S}$ and $[45_4/0_4/-45_4/90_4]_S$, taking the 0° fiber orientation aligned with the longer in-plane dimension of the plate. All laminates have the same thickness, 5.8 mm, since an equal number of plies is used, 32 plies; however, ply thicknesses are different, as well as the number of interfaces for delamination (30, 14 and 6, respectively). These laminates were manufactured using Hexply AS4/8552 carbon-epoxy unidirectional prepreg. For the low-velocity impact testing, three different impact energies are considered, namely 19.3, 28.6 and 38.6 J, and a impactor with a constant mass of 5 kg is used. Despite the fact that all the laminates had the same stiffness, the resulting responses were quite different. Indeed, according to this study, ply thickness reduces the damage resistance of the structure, since the following was observed:

- Increasing ply thickness, both the delamination threshold load (F_d) and the peak force (F_{max}) are reduced under equal impact conditions.
- Increasing ply thickness, the response is elongated in time, and larger delaminations are created due to the reduced number of available interfaces.

In the same study, González et al. [97] also evaluated the effect of ply thickness on damage tolerance, assessed by CAI tests. Unlike impact resistance, the damage tolerance did not seem to be reduced by increasing the ply thickness, because all laminate types showed similar values of the residual compressive load at each impact energy (confirming the results obtained in references [93, 96, 99], previously described).

A more recent experimental study [101], carried out by Tsai's group, analysed the damage tolerance of thin-ply NCF and "equivalent" aerospace grade laminates. Different types of laminates were studied, namely:

- **"Thin" NCF laminates**

  6QT – $[0/45/90/-45]_{6T}$, 1.78 mm thick panel, made by VX Aerospace

- **"Thicker" NCF laminates**

  888 – $[0/45/-45/0]_{8T}$ 2.54 mm thick panel, made by Aldila (non-quasi-isotropic)[11]

  887 – $[0/45/90/-45]_{8T}$ 2.41 mm thick panel, made by Aldila

  Bob – $[0/45/90/-45]_{8T}$ 2.41 mm thick panel, made by VX Aerospace

- **"Aerospace grade" laminates**

  3QT – $[0/45/90/-45]_{3T}$, 1.57 mm thick panel, layed-up with 145 gsm IM7/MTM-45 prepregs (for comparison with NCF *6QT*)

  4QT – $[0/45/90/-45]_{4T}$, 2.29 mm thick panel, layed-up with 145 gsm IM7/MTM-45 prepregs (for comparison with NCF *888* and *Bob*)

Each type of laminate comprised the facesheets of a 98 kg/m^3 aluminum honeycomb core (see the sketch of figure 2.31). Each specimen was 152.4 mm long and 101.6 mm wide. Each sandwich specimen was supported over a steel block and impacted with a 12.7 mm impactor at approximately 6.672 J per mm of facesheet thickness. After impact testing, CAI tests were performed in the impacted specimens. According to Tsai's group [101], the results for ultimate compressive load and ultimate strength (load to failure per cross-sectional area of laminate being tested) provides the following conclusions:

- Although "thin" specimens (*6QT* and *3QT*) have shown little difference in damage resistance, the aerospace grade specimens (*3QT*) exhibited a higher (19%) CAI load carrying capability, i.e., higher damage tolerance.
- Dent depth showed more variation than any other parameter for the "thicker" specimens; the aerospace grade "thick" specimens (*4QT*) did show approximately twice the dent depth of quasi-isotropic "thicker" NCF specimens (*887* and *Bob*). However,

---

[11] No "equivalent" aerospace grade laminate was made for the 888 lay-up, and thus any "apples to apples" comparison is available.

damage diameters were comparable for the quasi-isotropic lay-ups (both NCF and aerospace grade types).

- CAI strength of the *Bob* specimens were considerably lower than comparable laminates.
- "Thicker" aerospace grade laminates (*4QT*) demonstrated a slightly higher (≈5%) CAI strength than the comparable NCF *887* laminates, although the difference is within scatter.

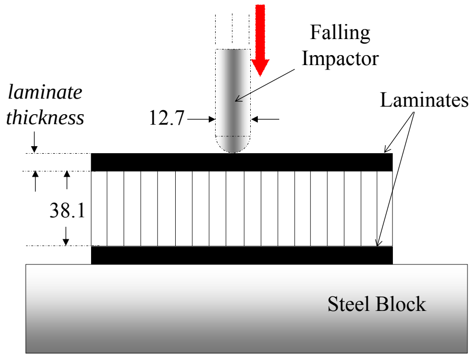

Fig. 2.31. Sketch of the low-velocity impact test performed by Tsai's group [101].

According to the studies presented before, one can easily conclude that the effect of ply thickness on damage resistance and damage tolerance of composite laminates is not yet fully understood. Besides, according to Lopes et al. [38], it is important to ensure that both the in-plane and the bending stiffness of the lay-ups under study are kept constant, to avoid misinterpretations of the results[12], something not regarded in most of the previous studies. Therefore, further studies, including experimental testing together with reliable analytical [97] and numerical (finite element) [102] analysis, would be useful in order to understand the effect of ply thickness on damage resistance and tolerance of composite laminates, particularly using tow-spread thin-ply and thick-ply laminates, designed with the same in-plane and bending stiffness [38].

2.5.5. Translaminar fracture toughness

Characterization and prediction of the **fracture toughness** associated with **translaminar failure modes** (fiber breaking) is also an important issue regarding the effect of ply thickness on damage onset and subsequent propagation [103]. In fact, fracture toughness plays an important role in determining the damage tolerance of composite structures and their behavior during damage propagation [91, 103].

Fiber breaking can take place during both longitudinal tensile or compressive loading and, particularly for carbon/epoxy systems, the energy consumed by these failure processes is much larger than for those involving matrix or matrix-fiber bond failures [104]. When subjected to a direct in-plane loading, laminates may fail under *translaminar fiber tensile failure*, characterized by fiber-matrix debonding and subsequent pull-out, under *translaminar fiber compressive failure*, whose failure can initiate as either shear driven

---

[12] In fact, low-velocity impact events can often be approximated to quasi-static loads, meaning that bending stiffness plays an important role on the way damage develops on an impacted laminate, since, in such situations, the delaminated area is highly dependent on the out-of-plane displacement of the laminate during impact [38].

fiber failure or fiber kinking, and under *intralaminar matrix failure*, characterized by matrix cracking either longitudinally or transversely with respect to the fibers [105]. Because they are intrinsic properties to the material system and, for a given loading condition, formation and propagation of damage within a laminate (its fracture toughness) will be lay-up dependent, these failure modes need to be measured for complete characterization of the damage tolerance of the material, using test configurations such as *compact tension* (*CT*), *center-notched tension* (*NT*) and others [105]. Note also that the experimental determination of the fracture toughness is important not only for material characterization but also for numerical modeling [104].

According to a review article by Laffan et al. [105], although translaminar fracture toughness has received relatively little attention from the scientific community in the past, partially due to (i) a lack of confidence in composite materials, resulting in them not being used in primary structures where this type of characterization is more useful, and (ii) a lack of modeling capabilities which can use the parameters effectively, nowadays, this type of characterization plays an increasingly important role, mainly due to the application of large composite primary structures, namely on the most recent long range aircrafts, where most major structure components, not only of the wings but also of the fuselage, now consist of composites [106]. The collection of work relating to tensile failure reveals a varied approach in terms of specimen configuration, size and data reduction, despite the existence of an ASTM standard (namely ASTM E1922 - 04). However, still according to Laffan et al. [105], works on compressive failure are found to be even less comprehensive.

Although fracture toughness can be characterized by parameters such as the *critical stress intensity factor* (K_{Ic}) or the *critical energy release rate* (G_{Ic}), it may be presented more accurately in the form of a *resistance curve* (*R-curve*), plotting the change in the critical energy release rate with crack growth. From this statement, it becomes clear that crack growth stability is necessary for good data acquisition. However, R-curves are not currently addressed by the ASTM E1922 - 04 standard [105].

2.5.5.1. Compact tension (CT)

According to Laffan et al. [105], the **compact tension** (**CT**) configuration is perhaps the most widely used specimen configuration for translaminar fracture toughness measurement of composites. The most widely used data reduction method has been through the determination of K_{Ic}, as recommended by ASTM E399 for metals, or, less prone to error, through the determination of G_{Ic}. However, *R-curves* can also be experimentally obtained, representing more accurately the translaminar fracture behavior of the tested composite system.

The CT configuration has been also used for characterization of the compressive fracture toughness of composite laminates, by reversal of the loading configuration — **compact compression** (**CC**) [105]. Furthermore, in order to resolve some problems with undesirable failure modes, such as damage beneath the central loading point in three point bending and crack growth perpendicular to the desired growth direction in compact tension (particularly in highly orthotropic laminates), an **over-height compact tension** (**OCT**) configuration, developed at the University of British Columbia (see, for instance, references [107, 108]), is being used in translaminar fracture toughness testing of composite laminates. The OCT configuration is particularly suitable for testing the translaminar fracture toughness of tougher material systems, where the previously mentioned undesirable failure modes tend to appear.

Compact tension type tests are usually devised such that extraneous damage modes are minimized and that brittle type crack progresses from the pre-machined notch in order that a laminate or fiber direction fracture toughness can be measured [108]. However, Li et al. [108] experimentally investigated the interaction between subcritical damage in the form of splitting and delamination, promoted by proper laminate design, with progressive fiber failure. Particularly, they investigated the effect of having dispersed and blocked plies in the thickness direction, by means of interrupted testing, to capture the damage process as it occurred before the onset of fiber failure (ultrasonic C-scanning and X-ray was used to determine the extent of delamination). The material used was the IM7/8552 carbon/epoxy prepreg system with a nominal ply thickness of 0.125 mm. There were altogether eight different lay-ups, namely dispersed cross-ply $[0/90]_{4S}$ and $[0/90]_{8S}$ and quasi-isotropic $[45/90/-45/0]_{2S}$ and $[45/90/-45/0]_{4S}$ lay-ups, and blocked cross-ply $[0_2/90_2]_{2S}$ and $[0_4/90_4]_{2S}$ and quasi-isotropic $[45_2/90_2/-45_2/0_2]_S$ and $[45_4/90_4/-45_4/0_4]_S$ lay-ups. OCT tests were used together with an anti-buckling support attached to the back face of the specimen to evaluate stable crack growth so that the composite damage zone could be investigated. Results showed that in dispersed-ply laminates, damage growth was restricted, promoting fiber failure and crack growth through the whole thickness since the local stress at the notch tip is higher due to the reduced notch "blunting" by the damage. Load curves of dispersed ply specimens were approximately linear before the first load drop and the through-thickness crack progresses across the width of the specimen in a series of small "jumps" which result in further load drops. For these laminates, the overall trend is for the crack growth to progress at approximately constant load, with much smaller load jumps in the quasi-isotropic laminates than in cross-ply laminates, which might suggest that 45° and −45° plies could help reduce the stress accumulation in 0° plies and foster smoother or more stable fiber breakage progressing. In contrast, blocked-ply laminates promoted a larger amount of splitting and delamination and cause a larger process zone; due to this splitting and delamination, the load curves showed a larger degree of nonlinearity. These laminates generally failed suddenly due to blocked plies pulling out via delamination. It was also observed that damage initiation (FPF) of blocked-ply laminates occurred earlier than in dispersed-ply laminates with the same thickness. However, this results in a significant reduction of the stress concentration at the notch tip that ultimately results in a tougher laminate. Finally, it was noticed that in the case of blocked-ply laminates the process zone has become so large that the specimen size was no longer sufficient; if the delamination were to be allowed to continue to grow in a large specimen, eventually the fiber failure stress at the notch would be exceeded and a through-thickness crack would start to propagate.

Laffan et al. [103] investigated the usage of different data reduction methods for calculation of the translaminar fracture toughness of carbon/epoxy laminates using the CT specimen configuration, namely the area method, the ASTM E399 testing standard method (established for isotropic materials, particularly metals), the J-integral/VCCT[13] method (based on FE analysis), the compliance calibration method (CC) and the modified compliance calibration method (MCC), using optically measured crack length and effective crack length. According to the authors, the area method is simpler, but must use optically measured crack growth (Δa), becoming more sensitive to errors for low Δa and insensitive

---

[13] Virtual Crack Closure Technique

to R-curve effects for large Δa, and, for stick-slip crack growth, it requires interpolating the load vs. displacement curve between critical loads. The ASTM E399 testing standard method allows to choose the initial a/w ratio which gives accurate initiation values, but relies on optically measured crack length, and the use of a function $f(a/w)$ for isotropic materials renders it inappropriate. The J-integral/VCCT method eliminates any error from differentiating a fitted curve such as that in CC and MCC methods, but relies on optically measured crack length and the use of FE analysis adds complexity. The CC method works well if the compliance vs. crack length curve can be sufficiently populated, but, once again, relies on optically measured crack length and points for compliance calibration curve are dictated by specimen crack jumps, which may result in areas not being populated. Finally, the MCC method does not require optical crack length measurement (when using effective crack length), but requires additional experimental work or adds the complexity of using FE analysis to obtain the compliance vs. crack length curve.

Following the previously mentioned work, Laffan et al. [35] also studied the size and lay-up effects in the *in-situ ply fracture toughness* associated with mode I fiber tensile failure (G^0_{Ic})[14] in carbon/epoxy laminates. According to the authors, there is not any significant effect of scaling the specimen in-plane size; however, specimens significantly smaller than the lower proposed in-plane size can result in undesirable failure modes, such as shear out of the loading holes, and specimens significantly larger than the upper proposed in-plane size has negligible effect on results and would seem impractical in terms of material usage. On the other hand, the thickness of the specimen demonstrated a significant effect in the fracture toughness of the tested carbon/epoxy laminates. In fact, the thicker specimen showed lower fracture toughness (28% for initiation and 14% for propagation), though not being visible any significant difference between the lengths of pulled-out fibers and between fracture surfaces of thinner and thicker specimens. Furthermore, the thick specimen showed an increasing R-curve trend, contrary to what happened with the thin specimen. Unfortunately, according to Laffan et al., there is not sufficient available testing to make any solid conclusion about this issue, and therefore further studies are required.

Regarding lay-up effects, Laffan et al. [35] measured the R-curves of $[(90/0)_8/90]_S$, $[(90_2/0)_8/90]_S$ and $[(90/0_2)_8/90]_S$ carbon/epoxy laminates. According to Laffan et al., the apparent toughness of the fiber tensile failure mode (G^0_{Ic}) was found to increase (almost twice) when the thickness of the 0° layer was increased, attributed to an increase in fiber pull-out in the thicker 0° layers.

However, the experimental work carried out by Laffan et al. [35] does not provide sufficient data to conclude about the effect of ply thickness in the translaminar fracture toughness of composite laminates. Therefore, further studies are required; particularly, a comparison between thin-ply (obtained by tow spreading, for instance) and thick-ply laminates is recommended. Furthermore, use of an alternative method to measure the R-curves, based on the Digital Image Correlation (DIC) technique [109], is also recommended. This method involves an automated algorithm that post-processes the full-field data provided by the DIC system during the CT test (and, eventually, the CC test) and it

---

[14] According to Laffan et al. [105], because the toughnesses of the epoxy matrix failure modes are much lower than that of the carbon fibers, the critical energy release rate for the fiber tensile failure for carbon/epoxy systems mode is thus expressed as,

$$G^0_{Ic} \approx \frac{t_{lam}}{t_0} G^{lam}_{Ic}$$

where t_{lam} and t_0 are, respectively, the laminate and total 0° thicknesses.

is used to automatically detect the crack tip location, quantifying the crack length without any visual inspection. Based on the surface displacement and strain fields obtained from the DIC technique, the J-integral can be calculated and the crack R-curve computationally generated, obviating the need of any complex pre- and post-processing of the test data [109].

2.5.5.2. Center Notched Tension (NT)

The **center-notched tension** (**NT**) configuration has also been used for the testing of the composite fracture toughness of composite laminates (see, for instance, reference [110]). In addition, this configuration has also been used for characterization of the compressive fracture toughness of composite laminates, namely carbon/epoxy laminates, by reversal of the loading configuration used in tensile fracture toughness testing — **center-notched compression** (**NC**) [105, 110]. However, the NT configuration does not exhibit stable crack growth, and therefore is not suitable for the R-curve characterization.

2.5.5.3. Other testing configurations

Other testing configurations have been used for translaminar fracture toughness characterization of composite laminates. Also derived from an existing ASTM standardized configuration for metals, such as the CT configuration, **three point bending** (**3PB**) configuration has been used for translaminar fracture toughness characterization of composite laminates [105]. Other configurations are the **single/double edge notched tension** (**SENT/DENT**) configurations. According to Laffan et al. [105], these configurations have been used for translaminar fracture toughness characterization of carbon, E-glass, Kevlar and boron/epoxy systems.

2.6. Case study: wind turbine blades

Ha presented some numerical studies (see, for instance, references [111] and [112]) concerning innovative design of wind turbine blades comprising bi-angle thin-ply NCF. In this studies, Ha uses a multi-scale approach based on micromechanics of failure (MMF) and a fully-coupled aerodynamic-structural iterative analysis for adaptive wind blade designs.

Ha's studies [111, 112] try to take advantage of the particular properties of bi-angle thin-ply NCF building block, namely the great reduction of out-of-plane stresses due to uniform homogenization of folded layers, which increases delamination resistance, and the expected higher fatigue life (compared to conventional NCF).

Furthermore, according to Ha [111, 112], the twist/bend coupling of bi-angle NCF laminates can be effective and economical among several passive and active control methods. In his aerodynamic-structural iterative analysis, where several iterations of the aerodynamic analysis (aerodynamic efficiency through lift and drag forces) followed by structural analysis (prediction of deflection, ultimate strength, buckling load and fatigue life) are performed, Ha includes the bend-twist and/or sweep-twisting coupling behavior in order to alleviate passively the aerodynamic loads and to obtain the proper blade design.

Chapter 3

Experimental test program

In spite of the more recent advances in computational methods, numerical analysis techniques are still not sophisticated enough to adequately predict results under every set of conditions, and consequently all numerical methods still need to be validated through experimental testing. Therefore, execution of experimental test programs, in particular with respect to the mechanical characterization, is essential in the development of any composite material and in the design of any composite component, particularly for the commercial aircraft industry, whose structural certification is always supported by experimental testing. In this chapter, the experimental test program carried out during this thesis, aiming to assist in the technology development of the spread tow thin-ply technology, is described.

3.1. Introduction

Knowledge of constituent material properties is important when defining a composite structure for a given application and in understanding how that structure will respond to the various stimuli likely to be imposed on it [6]. With the introduction of new composite materials, resulting from the development of new manufacturing technologies, understanding their potential benefits and drawbacks is extremely important. Particularly, the mechanical characterization of such materials is unavoidable. A reliable assessment of the mechanical properties of such materials is primordial in order to accurately relate those properties with the real needs and alternative solutions.

In spite of the more recent advances in computational methods, numerical analysis techniques are still not sophisticated enough to adequately predict results under every set of conditions [113]. Because of this lack of generality, all numerical methods still need to be validated through experimental testing. Therefore, execution of experimental programs, in particular with respect to the mechanical characterization, is essential in the development of any composite material and in the design of any composite component. Indeed, commercial aircraft structures are generally certified by analysis always supported by experimental tests [113].

Because the spread tow thin-ply technology is a technology of interest, particularly for the aircraft industry, this thesis includes the realization of an experimental test program that will support the technology development of this technology by studying some of the most relevant mechanical properties of the thin-ply laminates. Particular emphasis is given to the size effects, notched strength, bearing strength, and fracture toughness of such materials. Therefore, plain strength tension and compression, open-hole tension and compression, notched tension and compression, bolt bearing, and over-height compact tension tests on two different thin-ply laminates are part of this experimental program. Later, within this thesis, the experimental results will be used to validate closed-form design tools proposed herein for the understanding and prediction of the mechanical behavior of the thin-ply composite laminates.

3.2. Material selection and characterization

The material used within this experimental program is the carbon non-crimp fabric (NCF) C-Ply™ T700/AR-2527 epoxy system prepreg material from Aldila Golf Corp (P/N C-PLY BXO/+45 150 T3,4 12K HS-AR2527). This prepreg material is made with the tow-spread C-Ply™ T700 [0/−45] NCF bi-angle layers from Chomarat. The T700 carbon fiber, from Toray, is a high performance carbon fiber produced by the treatment of an acrylic fiber precursor, with pyrolysis, surface treatment, and sizing processes. Table 3.1 shows the ply elastic and strength properties of the tow-spread thin-ply C-Ply™ T700 NCF from Chomarat. E_1 and E_2 are the longitudinal and transversal Young modulus, respectively, G_{12} is the shear modulus, ν_{12} is the major Poisson ratio, X_T and X_C are the longitudinal tensile and compressive strengths, respectively, Y_T^{ud} and Y_C are the transverse tensile and compressive strengths, respectively, S_L^{ud} is the in-plane shear strength, V_f is the fiber volume fraction, and E_f and X_f are, respectively, the T700 carbon fiber's Young modulus and tensile strength.

Tab. 3.1. Ply properties of thin-ply (75 gsm) C-Ply™ T700 NCF from Chomarat.

E_1	110.0	GPa	X_T	2300	MPa	S_L^{ud}	93	MPa
E_2	7.4	GPa	X_C	1500	MPa	V_f	50+	%
G_{12}	4.2	GPa	Y_T^{ud}	66	MPa	E_f	210	GPa
ν_{12}	0.3		Y_C	220	MPa	X_f	4900	MPa

Two different thin-ply laminates are investigated. The first thin-ply laminate, hereafter referred to as *lay-up 1*, is a $[(0/-45)/(90/45)]_{6\mathrm{T}}$ 24-ply thick asymmetric laminate (about 2.0 mm thick), made with 15.24 cm (6") wide C-Ply™ [0/−45] NCF bi-angle strips and 1.27 cm (1/2") stagger, with seams (thus, for each C-Ply™ NCF bi-angle layer, every 15.24 cm the −45° plies have seams). The second thin-ply laminate investigated during this thesis, hereafter referred to as *lay-up 2*, is a $[(0/-45)/(45/0)/(90/45)/(-45/90)]_{\mathrm{S}}$ 16-ply thick laminate (about 1.3 mm thick), without seams. The 0° fiber orientation is coincident with the loading direction. Note that lay-up 2 is symmetric by C-Ply™ [0/−45] NCF bi-angle layer, but not-symmetric by ply. Ply thickness is around 0.08 mm for both laminates.

These laminates were manufactured at VX Aerospace, USA. The cure cycle had an high temperature of 143°C (290°F) and was conducted according to the following steps: (i) ramp up to 107°C (225°F) for 1 hour, (ii) hold at 93°C (200°F) for 40 minutes, (iii) ramp up to 143°C (290°F) for 20 minutes, (iv) hold at 135°C (275°F) for 2 hours, and (v) lower temperature to 60°C (140°F) for 45 minutes. Lay-up 1 was delivered as a 0.465 m^2 (5 sq ft) plaque and lay-up 2 was delivered as a 0.557 m^2 (6 sq ft) plaque. Each plaque was cut to the specimens nominal dimensions using a diamond-coated disk.

3.3. Strain gaging

3.3.1. Selection of strain gages

In this experimental program, MICRO-MEASUREMENTS & SR-4® general purpose strain gages are used. Grid resistance is 350.0 Ω ± 0.6%, which, associated with a high voltage supply, promotes a better hysteresis effect and the zero load stability. Gage factor is 2.125 ± 0.5% (@ 24°C). The strain gages already incorporate electrical wiring, making installation easier, without the danger of damaging the composite material. The grid size is several times bigger than the fiber diameter, allowing the characterization of the composite. Although this strain gages are compensated for steel, because tests will be conducted at room temperature, which is considered to be constant, any effect of small temperature variation is neglected.

The strain gages are connected to the data acquisition system in quarter-bridge using the three wires technique. This technique allows the system to be calibrated so that temperature variations do not affect the measured data.

3.3.2. Surface preparation

Surface preparation is of crucial importance in strain gaging, because it influences the quality of the adhesion between the test specimen and the strain gage. If this quality is not sufficiently good, results will not be valid. Surface preparation starts with careful manual abrasion of the specimen surface using fine-grain sandpaper (herein, INDASA RHYNOWET PLUS P 320 sandpaper is used). After obtaining a smooth surface (without hurting the specimen surface), it is cleaned with acetone to remove all the possible dust generated during the manual abrasion process. Careful must be taken in order to do not dirty the cleaned surface, for instance protecting it with adhesive tape.

3.3.3. Strain gage bond

After surface preparation, orientation guidelines are drawn upon the specimen surface to aid the correct alignment of the strain gage. Finally, the strain gage is glued using the M-BOND 200 ADHESIVE KIT, a two-components cyanoacrylate adhesive certified for strain gage use. After applying the adhesive, a one-minute thumb pressure must be applied, and a minimum two-minute delay before tape removal.

3.4. Digital image correlation

In the field of experimental mechanics, many optical methods provide full-field images, requiring a large amount of data to be analysed. The computer-aided processing of these images is one of the primary applications of digital image processing. All the techniques based on digital image processing, together with appropriate post-processing algorithms, allow a high degree of automation. Particularly interesting is the ability of some of these techniques to retrieve displacement and strain fields by computations of the camera images only. In these techniques, an important issue is speckle pattern recognition [114]. Most of these techniques record pattern images before and after deformation at different load steps, retrieving the displacement fields by remapping the images after deformation to the reference image in the undeformed state [114–116]. Today's image processing software allows the measurement of stress, strain, deformation, shape and fringe pattern analyses.

The experimental monitoring of damage and fracture phenomena in composite materials is an innovative research area, which attracts more and more attention through an increasing interest in the failure behavior of these materials [114]. In this experimental program, the **digital image correlation** (DIC) technique is used to determine the surface in-plane displacement and strain fields and observe damage initiation and propagation.

DIC is an optical-numerical full-field displacement measuring technique increasingly used in experimental mechanics. This technique allows the qualitative and quantitative study of the mechanical behavior of materials determining the in-plane displacement and strain fields at the surface of objects with painted speckle patterns under any kind of loading conditions [115]. In this work, an automatic algorithm, based on the work of Grégoire [116] and used by Catalanotti et al. [109], that post-processes the full-field data provided by the DIC system during tests is used to recognize discontinuous displacement fields and detect microcrack initiation and growth.

Before testing, the test specimens are sprayed with white and black ink to generate a speckle pattern, i.e., a random and contrasted distribution of granular spots, as required by the DIC system. A single-camera ARAMIS DIC software developed by GOM [117] is used. This measurement system is equipped with an 8-bit Baumer Optronic FWX20 camera (resolution of 1624×1236 pixels, pixel size of 4.4 μm, and sensor format of 1/1.8") coupled with a 200 mm Nikkon lens. The depth of the optical field can the extended using one or two extension tubes of 20 mm, placed between the lens and the camera. The lens is adjusted in order to be in focus with regard to the surface of interest, and the lens aperture is then closed to $f/11$ to improve the depth of field during testing. For the over-height compact tension tests, an Opto Engineering® TC 23 36 bi-telecentric lens is used.

For mobility and adaptability, the camera was mounted on a tripod, which was positioned facing the testing machine (see figure 3.1). During set up, the optical system was positioned perpendicular to the surface of the specimen mounted into the testing machine. A laser pointer together with a mirror were used to facilitate a correct alignment. The light source is finally adjusted in order to guarantee an even illumination of the specimen's surface and to avoid over-exposition (i.e., the saturation of pixels over the field of view).

Fig. 3.1. DIC measurement system used during the experimental program.

In the DIC technique, the displacement field is measured by analyzing the geometrical deformation of the images of the surface of interest, recorded before and after loading. For this purpose, the initial (undeformed) image was mapped by square facets (subsets), within which an independent measurement of the displacement is calculated. Therefore, the facet size, on the plane of the object, will characterize the displacement spatial resolution. The facet step (i.e., the distance between adjacent facets) can also be set either for controlling the total number of measuring points over the region of interest, or for enhancing the spatial resolution by slightly overlapping adjacent facets. Typically, a larger facet size will improve the precision of the measurements but also will degrade the spatial resolution. Thus, a compromise must be found according to the application to be handled, particularly attending to the size of the region of interest, the optical system (magnification), and the quality of the average speckle size obtained by the spray paint [109]. In this experimental program, a facet size of 15×15 pixels was chosen. The facet step was also set to 15×15 pixels to avoid statistically correlated measurements.

Since both thin-ply laminates are asymmetric, the displacement fields are measured in surfaces with different fiber orientations. So, for the lay-up 1 laminate the displacement field is measured in a surface with the fibers oriented at 45°, whereas for the lay-up 2 laminate the displacement field is measured in a surface with the fibers oriented at 0°. With such analysis, it is possible to assess which differences may occur in the surfaces with different fiber orientations of asymmetric laminates under the different types of loading conditions tested in this thesis, in particular the differences in the stress concentrations and transverse cracking onset and propagation.

3.5. Plain strength tests

The knowledge of the laminate elastic properties and unnotched strengths is essential in the mechanical characterization of a composite material, and is a required parameter for failure criteria, as well as for analytical and numerical models. In fact, the analytical determination of the laminate strength is clearly a complicated task, particularly due to the well-known in-situ effect and due to the fact that after the first matrix crack the laminate can still support increasing loads until fiber fracture, that usually corresponds to final failure in laminates without stress concentrations [118].

3.5.1. Tensile plain strength

The purpose of the unnotched tension test is to evaluate the elastic properties of the laminate and its mechanical behavior when subjected to tensile efforts. Table 3.2 shows the unnotched tensile test matrix, where w is the specimens nominal width and L is the specimens nominal length. All tests were performed under displacement control in a servo-hydraulic MTS 810 testing machine (*Load Unit* 318.25, *Service Manifold* 298.12 C), using a force transducer (661.20 F-03) of 100 kN.

Tab. 3.2. Tensile plain strength test matrix.

Laminate	# specimens	w [mm]	L [mm]	Speed [mm/min]	Acquisition [Hz]
Lay-up 1	3	25	250	2.0	5
Lay-up 2	3	25	250	2.0	5

One specimen per laminate was instrumented with two strain gages placed in the longitudinal and transversal directions, as shown in figure 3.2. A Spider data acquisition system was used, with a sample frequency set to 50 Hz. Figure 3.2a also shows the in-plane nominal dimensions of the specimens.

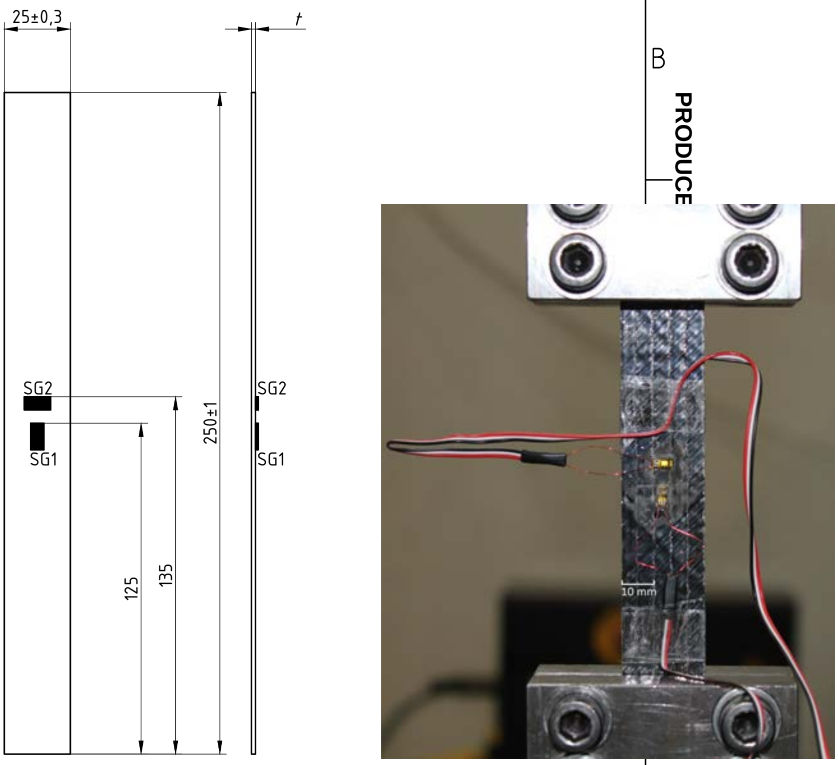

(**a**) Schematic drawing (*t* is the laminate thickness). Dimensions in mm.

(**b**) Gripped specimen before testing.

Fig. 3.2. Tensile plain strength test specimen.

The DIC technique was used to assess transverse cracking formation in one specimen per laminate, using a 200 mm Nikkon lens together with one extension tube of 20 mm. The working distance (defined between the specimen's surface and the support of the camera) was set to 1371 mm (1346 mm from the specimen to the front of the lens and 25 mm from the front of the lens to the camera). The lens was adjusted to be in focus with regard to the surface of interest. The shutter time was set to 10 ms. The captured region was of approximately 33×43 mm^2, which defines a conversion factor of about 0.0265 mm/pixel.

During the experimental procedure, the dimensions of each specimen were recorded to determine the applied stress. Coarse-grain sandpaper strips (IMPERIAL CRD 40) were inserted between each specimen and the grips to avoid sliding, taking particular care in the alignment of the longitudinal axis of the gripped specimen with the test direction. The grips were clamped with a bolt torque of 55–60 Nm; however, it was reduced to 45 Nm in two specimens of the thinner lay-up 2 (specimens AAT22 and AAT23) to avoid failure within the grips. It was observed that, for these specimens, a bolt torque of 45 Nm was adequate to avoid both failure and sliding within the grips. Each specimen was tested until failure occurs, recording afterwards the maximum load and laminate's failure mode and location.

The laminate modulus of elasticity, E^L, is obtained from the unnotched tensile test as,

$$E^L = \frac{\Delta\sigma}{\Delta\varepsilon} \tag{3.1}$$

where $\Delta\sigma$ is the tension difference applied between the 1000 and 3000 $\mu\varepsilon$ points on the stress-strain diagram, and $\Delta\varepsilon$ is the strain difference between the same points (whose nominal value is 2000 $\mu\varepsilon$). The laminate major Poisson ratio, ν_{12}^L, is obtained as,

$$\nu_{12}^L = -\frac{\Delta\varepsilon_T}{\Delta\varepsilon_L} \tag{3.2}$$

where $\Delta\varepsilon_T$ and $\Delta\varepsilon_L$ are, respectively, the strain changes in the transverse and longitudinal directions. Finally, the laminate tensile strength, X_T^L, which is obtained from the plain strength tensile test, is determined as,

$$X_T^L = \frac{P_{max}}{A} \tag{3.3}$$

where P_{max} is the maximum load before rupture occurs and A is the mean cross-sectional area of the specimen.

3.5.2. Compressive plain strength

The purpose of the unnotched compression test is to evaluate the mechanical behavior of the laminate when subjected to compressive efforts. However, the assessment of the compressive mechanical behavior of a laminate is more complex than when dealing with tensile conditions. Therefore, a special test rig developed to minimize out-of-plane bending (buckling) is used in this experimental program. Table 3.3 shows the unnotched compression test matrix, where w is the specimens nominal width and L is the specimens nominal length. All tests were performed under displacement control in a servo-hydraulic MTS 810 testing machine (*Load Unit* 318.25, *Service Manifold* 298.12 C), using a force transducer (661.20 F-03) of 100 kN.

Tab. 3.3. Compressive plain strength test matrix.

Laminate	# specimens	w [mm]	L [mm]	Speed [mm/min]	Acquisition [Hz]
Lay-up 1	3	25	305	2.0	5
Lay-up 2	3	25	305	2.0	5

One specimen per laminate was instrumented with two strain gages placed in the longitudinal direction, but in opposite faces of the specimen, as shown in figure 3.3. With this configuration, one is able to assess if non-negligible out-of-plane bending occurs. A Spider data acquisition system was used, with a sample frequency set to 50 Hz. Figure 3.3a also shows the in-plane nominal dimensions of the specimens.

During the experimental procedure, the dimensions of each specimen were recorded to determine the applied stress. The alignment of the longitudinal axis of the gripped specimen with the test direction is made using two guiding pins with a diameter of 6 mm in the ends of the specimen (see figure 3.3). The compression rig was clamped with a bolt torque of 8 Nm. Each specimen was tested until failure occurs, recording afterwards the maximum load and laminate's failure mode and location.

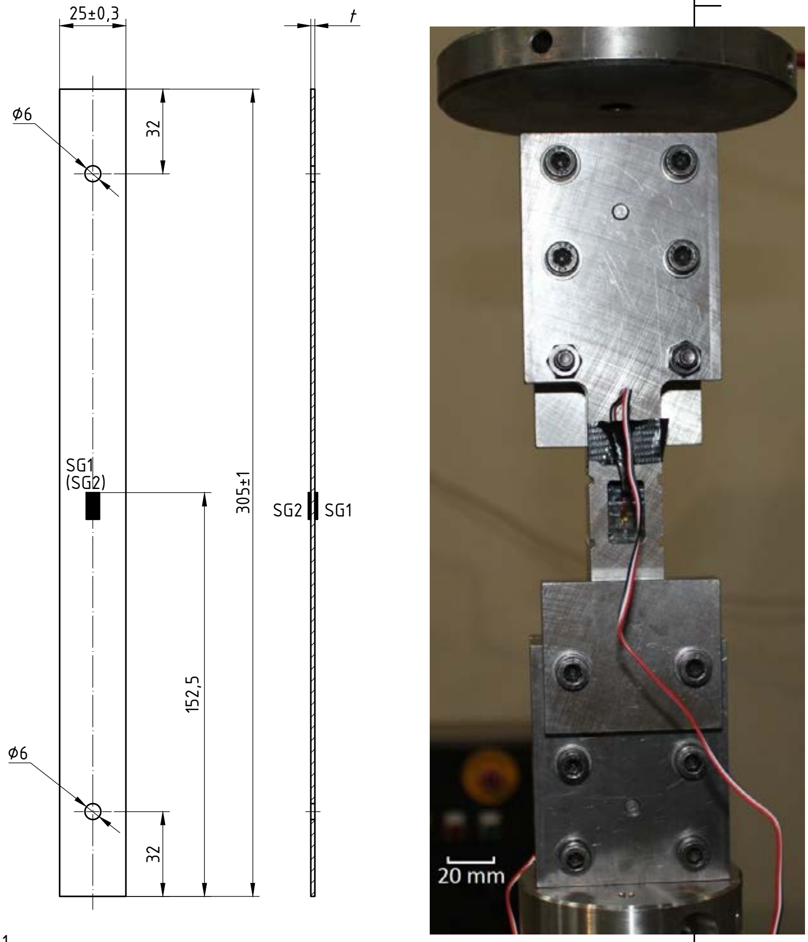

(**a**) Schematic drawing (*t* is the laminate thickness). Dimensions in mm.

(**b**) Test assembly before testing.

Fig. 3.3. Compressive plain strength test specimen.

The laminate compressive strength, X_C^L, which is obtained from the plain compressive tensile test, is determined as,

$$X_C^L = \frac{P_{max}}{A} \tag{3.4}$$

where P_{max} is the maximum load before rupture occurs and A is the mean cross-sectional area of the specimen.

3.6. Center-notched tests

Center-notched tests are typically used to measure the laminate fracture toughness. This property is required to assess the brittleness of the laminate and, for instance, for the prediction of size effects, i.e., for the strength prediction of open-hole laminates loaded in both tension and compression [110].

3.6.1. Notched tension

The purpose of the notched tension (NT) test is to measure the laminate tensile fracture toughness, an essential material property in composites design with respect to the resistance to crack propagation and stress concentrations. Later in this thesis, based in a work of Camanho et al. [119], this property is used in a closed-form design tool to predict size effects on thin-ply laminates (see chapter 5).

Table 3.4 shows the NT test matrix, where w is the specimens nominal width, $2a$ is the nominal length of the notch, and L is the specimens nominal length. The width to notch length ratio used in this experimental program is $w/(2a) = 7.5$[1]. The central notch was obtained using a milling machine, ensuring a distance of 1 mm between the notch faces. The notch tip was not sharpened; indeed, based on the work of Camanho and Catalanotti [110], no relevant difference between the fracture toughness of specimens with and without sharpened notch tips is expected. It is expected that the damage zone at the peak load is significantly longer than the separation of the crack faces. However, in future works, the relevance of sharpening the notch tips can be assessed testing thin-ply NT specimens with and without sharpened notch tips.

Tab. 3.4. Notched tension test matrix.

Laminate	# specimens	w [mm]	$2a$ [mm]	L [mm]	Speed [mm/min]	Acquisition [Hz]
Lay-up 1	3	30	4	250	2.0	5
Lay-up 2	3	30	4	250	2.0	5

All tests were performed under displacement control in a servo-hydraulic MTS 810 testing machine (*Load Unit* 318.25, *Service Manifold* 298.12 C), using a force transducer (661.20 F-03) of 100 kN. One specimen per laminate was instrumented with one strain gage placed in the longitudinal direction, as shown in figure 3.4. A Spider data acquisition system was used, with a sample frequency set to 50 Hz. Figure 3.4a also shows the in-plane nominal dimensions of the specimens.

The DIC technique was used to assess transverse cracking formation in one specimen per laminate, using a 200 mm Nikkon lens together with one extension tube of 20 mm. The working distance (defined between the specimen's surface and the support of the camera) was set to 1371 mm (1346 mm from the specimen to the front of the lens and 25 mm from the front of the lens to the camera). The lens was adjusted to be in focus with regard to the surface of interest. The shutter time was set to 10 ms. The captured region was of approximately 33×43 mm^2, which defines a conversion factor of about 0.0265 mm/pixel.

During the experimental procedure, the dimensions of each specimen were recorded to determine the applied stress. Coarse-grain sandpaper strips (IMPERIAL CRD 40) were inserted between each specimen and the grips to avoid sliding. The alignment of the longitudinal axis of the gripped specimen with the test direction is made using two guiding pins with a diameter of 4 mm in the ends of the specimen (see figure 3.4). The grips were clamped with a bolt torque of 55–60 Nm; however, it was reduced to 45 Nm in one specimen of the thinner lay-up 2 (specimen AANT23) to avoid failure within the grips. It was observed that, for this specimen, a bolt torque of 45 Nm was adequate to avoid both failure and sliding within the grips. Each specimen was tested until failure occurs, recording

---

[1] Initially, a notch length of 5 mm was foreseen (width to notch length ratio of $w/(2a) = 6$); however, due to an error during the milling process, it was changed to 4 mm, resulting in a width to notch length ratio of $w/(2a) = 7.5$. Note that this is not a problem, since linear elastic fracture mechanics assumptions require a width to notch length ratio as higher as possible, and the ratio between the notch length (4 mm) and the notch height (1 mm) is still adequate.

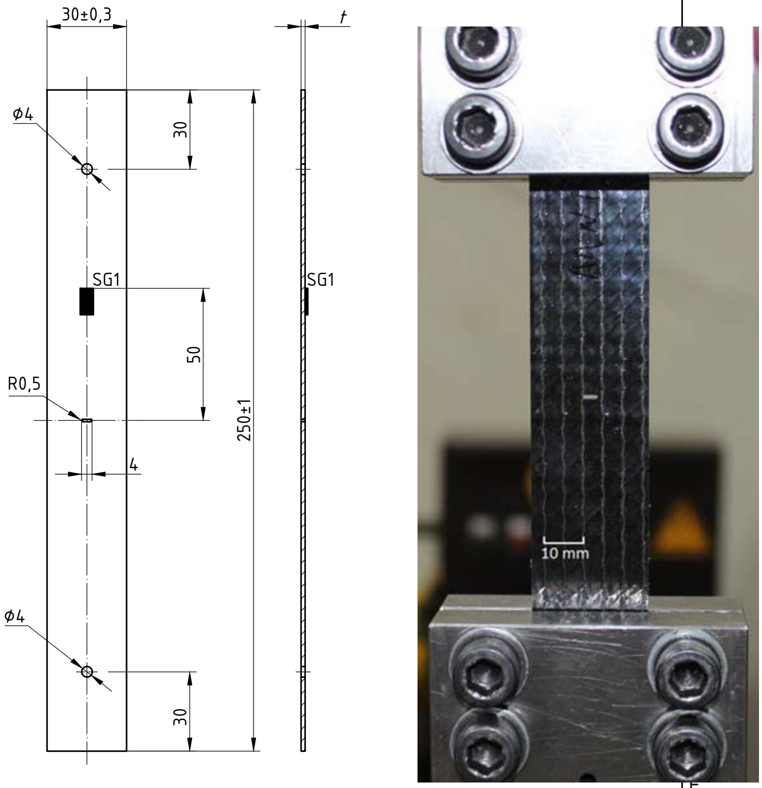

(**a**) Schematic drawing (*t* is the laminate thickness). Dimensions in mm.

(**b**) Gripped specimen before testing.

Fig. 3.4. Notched tension test specimen.

afterwards the maximum load and laminate's failure mode and location.

The laminate remote tensile stress at failure, $\bar{\sigma}_T^\infty$, is determined as,

$$\bar{\sigma}_T^\infty = \frac{P_{max}}{A} \tag{3.5}$$

where P_{max} is the maximum load before rupture occurs and A is the mean cross-sectional area of the specimen.

Neglecting the three-dimensional stress field that occurs at the vicinity of a notch in a composite laminate, the laminate tensile fracture toughness, K_T^L, is obtained using the laminate remote tensile stress at failure, $\bar{\sigma}_T^\infty$, according to the following equation [110],

$$K_T^L = \chi Y \bar{\sigma}_T^\infty \sqrt{\pi a} \tag{3.6}$$

where Y is the geometric factor that accounts for the finite width of the specimen, obtained as,

$$Y = \frac{1 - 0.5\dfrac{a}{w} + 0.37\left(\dfrac{a}{w}\right)^2 - 0.044\left(\dfrac{a}{w}\right)^3}{\sqrt{1 - \dfrac{a}{w}}} \tag{3.7}$$

and the parameter χ accounts for the orthotropy of the composite laminate, given as,

$$\chi = 1 + 0.1(\rho - 1) - 0.016(\rho - 1)^2 + 0.002(\rho - 1)^3 \tag{3.8}$$

with,

$$\rho = \frac{\sqrt{E_x E_y}}{2G_{xy}} - \sqrt{\nu_{xy}\nu_{yx}} \tag{3.9}$$

where E_x and E_y are the laminate Young modulus in the orthotropy axes, G_{xy} is the laminate shear modulus in the orthotropy axes, and ν_{xy} and ν_{yx} are the corresponding Poisson ratios. For the thin-ply laminates studied in this experimental program, though asymmetric, $\rho = 1$, and consequently $\chi = 1$. It should be noted, however, that equations (3.8) and (3.9) were derived for unidirectional test specimens and are used here in the analysis of multidirectional composite laminates.

From the laminate tensile fracture toughness, K_T^L, it is possible to estimate the tensile fracture toughness of the 0° plies, K_T^0, using a methodology proposed by Camanho and Catalanotti [110]. This methodology is an analytical closed-form solution based on fracture mechanics and lamination theory, and was originally developed for symmetric, balanced laminates, though applied to asymmetric laminates here. The three-dimensional nature of the stress field in the vicinity of the notch is neglected, which means that all possible damage mechanisms that result from the three-dimensional stress field, such as delamination, are lumped into a through-the-thickness macrocrack. So, considering a notched laminate, take $\Omega_0^{(i)}$ as the ratio between the mean remote failure stress of a group of plies that represent the balanced sublaminate (i) and the remote failure stress of the 0° sublaminate (i.e. a sublaminate with all plies with the fibers aligned with the loading direction), given as,

$$\Omega_0^{(i)} = \frac{\bar{\sigma}^{(i)}}{\bar{\sigma}^0} \tag{3.10}$$

which is easily calculated from lamination theory [120], since it only depends on the elastic properties of the plies and on the lay-up of the laminate. The mean remote failure stress of the balanced sublaminate (i), $\bar{\sigma}^{(i)}$, and that of the 0° plies, $\bar{\sigma}^0$, can also be calculated from linear elastic fracture mechanics as,

$$\bar{\sigma}^{(i)} = \frac{K_T^{(i)}}{\chi^{(i)} Y \sqrt{\pi a}} \tag{3.11}$$

$$\bar{\sigma}^0 = \frac{K_T^0}{\chi^0 Y \sqrt{\pi a}} \tag{3.12}$$

where $K_T^{(i)}$ and K_T^0 are the fracture toughness of sublaminate (i) and of the 0° plies, respectively. Note that, assuming self-similar crack propagation along all the sublaminates considered, the laminate tensile fracture toughness is,

$$K_T^L = \frac{\sum_{(i)}^{N} K_T^{(i)} t^{(i)}}{t^L}, \quad (i) \neq 90\ ° \tag{3.13}$$

where $t^{(i)}$ is the thickness of the sublaminate (i), N is the number of sublaminates considered, and t^L is the total thickness of the laminate. Note that, in equation (3.13), the tensile fracture toughness of the 90° plies can be neglected, since fiber fracture do not occur in these plies, and therefore the fracture toughness is several orders of magnitude lower than the fracture toughness of the 0° plies.

Using equations (3.11) and (3.12) in equation (3.10), the relation between the tensile fracture toughness of sublaminate (i) and the tensile fracture toughness of the 0° plies is given as,

$$K_T^{(i)} = \frac{\chi^{(i)}\Omega_0^{(i)}}{\chi^0} K_T^0 \tag{3.14}$$

Note that this methodology is not able to predict the fracture toughness of laminates whose main failure mechanism is delamination. However, according to the review described in chapter 2, this is not the case for thin-ply laminates.

3.6.2. Notched compression

The purpose of the notched compression (NC) test is to measure the laminate compressive fracture toughness. Later in this thesis, based in a work of Camanho et al. [119], this property is used in a closed-form design tool to predict size effects on thin-ply laminates when subjected to compressive efforts (see chapter 5). However, the assessment of the laminate compressive fracture toughness is more complex than when dealing with tensile conditions. As in the compressive plain strength tests, a special test rig developed to minimize out-of-plane bending (buckling) is used. Table 3.5 shows the notched compression test matrix, where w is the specimens nominal width, $2a$ is the nominal length of the notch, and L is the specimens nominal length. The width to notch length ratio used in this experimental program is $w/(2a) = 7.5$. The central notch was obtained using a milling machine, ensuring a distance of 2 mm between the notch faces. In NC testing, a sharpened notch tip is not required.

Tab. 3.5. Notched compression test matrix.

Laminate	# specimens	w [mm]	$2a$ [mm]	L [mm]	Speed [mm/min]	Acquisition [Hz]
Lay-up 1	3	30	4	305	2.0	5
Lay-up 2	3	30	4	305	2.0	5

All tests were performed under displacement control in a servo-hydraulic MTS 810 testing machine (*Load Unit* 318.25, *Service Manifold* 298.12 C), using a force transducer (661.20 F-03) of 100 kN. One specimen per laminate was instrumented with two strain gages placed in the longitudinal direction, but in opposite faces of the specimen, as shown in figure 3.5. With this configuration, one is able to assess if non-negligible out-of-plane bending occurs. A Spider data acquisition system was used, with a sample frequency set to 50 Hz. Figure 3.5a also shows the in-plane nominal dimensions of the specimens.

During the experimental procedure, the dimensions of each specimen were recorded to determine the applied stress. The alignment of the longitudinal axis of the gripped specimen with the test direction is made using two guiding pins with a diameter of 6 mm in the ends of the specimen (see figure 3.5a). The compression rig was clamped with a bolt torque of 8 Nm. Each specimen was tested until failure occurs, recording afterwards the maximum load and laminate's failure mode and location.

The laminate remote compressive stress at failure, $\bar{\sigma}_C^\infty$, is determined as,

$$\bar{\sigma}_C^\infty = \frac{P_{max}}{A} \tag{3.15}$$

where P_{max} is the maximum load before rupture occurs and A is the mean cross-sectional area of the specimen.

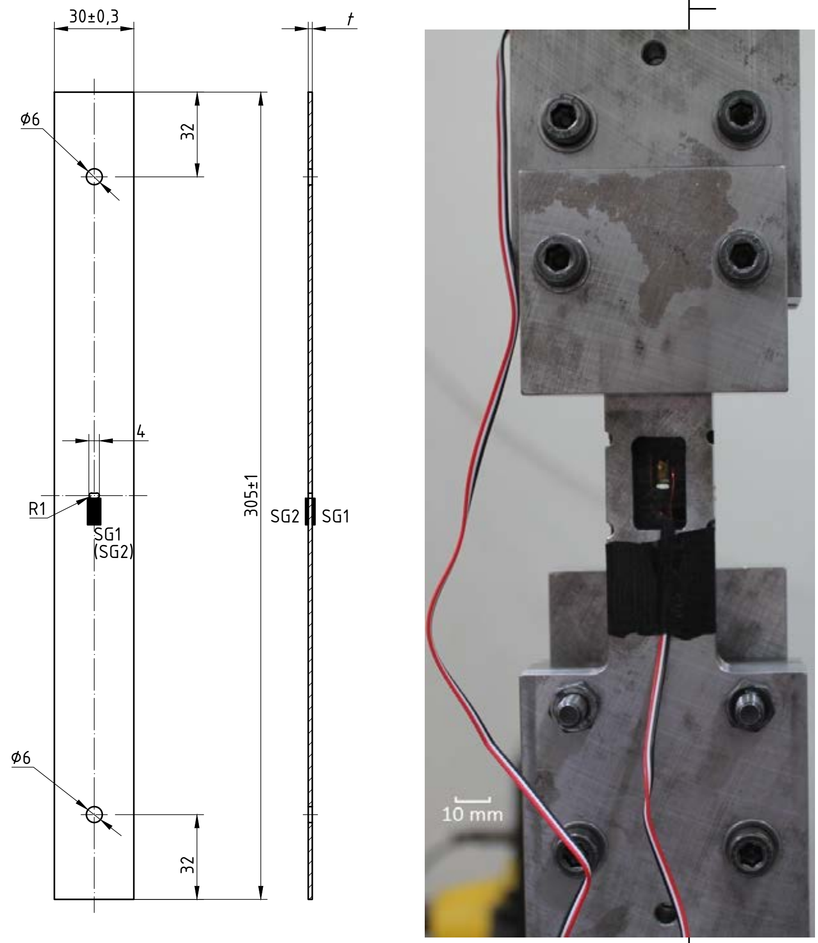

(**a**) Schematic drawing (*t* is the laminate thickness). Dimensions in mm.

(**b**) Test assembly before testing.

Fig. 3.5. Notched compression test specimen.

Neglecting the three-dimensional stress field that occurs at the vicinity of a notch in a composite laminate, the laminate compressive fracture toughness, K_C^L, is obtained using the laminate remote compressive stress at failure, $\bar{\sigma}_C^\infty$, according to the following equation [110],

$$K_C^L = \chi Y \bar{\sigma}_C^\infty \sqrt{\pi a} \tag{3.16}$$

where the geometric factor Y, the orthotropy parameter χ, and the parameter ρ are given by equations (3.7), (3.8) and (3.9), respectively. As mentioned in section 3.6.1, for the thin-ply laminates studied in this experimental program $\rho = 1$, and consequently $\chi = 1$. It should be noted, however, that equations (3.8) and (3.9) were derived for unidirectional test specimens and are used here in the analysis of multidirectional composite laminates.

Following the methodology proposed by Camanho and Catalanotti [110] for the tensile fracture toughness, the laminate compressive fracture toughness, K_C^L, is used to estimate the compressive fracture toughness of the 0° plies, K_C^0. As described in section 3.6.1, this methodology is an analytical closed-form solution based on fracture mechanics and lamination theory, and was originally developed for symmetric, balanced laminates in tension, though applied to asymmetric laminates in compression here. The three-dimensional nature of the stress field in the vicinity of the notch is neglected, which means that all possible damage mechanisms that result from the three-dimensional stress field, such as delamination, are lumped into a through-the-thickness macrocrack. So, considering a notched laminate under compressive loading, take $\Omega_0^{(i)}$ as the ratio between the mean remote compressive failure stress of a group of plies that represent the balanced sublaminate (i) and the remote compressive failure stress of the 0° sublaminate, given as,

$$\Omega_0^{(i)} = \frac{\bar{\sigma}^{(i)}}{\bar{\sigma}^0} \tag{3.17}$$

which is easily calculated from lamination theory [120], since it only depends on the elastic properties of the plies and on the lay-up of the laminate. The mean remote compressive failure stress of the balanced sublaminate (i), $\bar{\sigma}^{(i)}$, and that of the 0° plies, $\bar{\sigma}^0$, can also be calculated from linear elastic fracture mechanics as,

$$\bar{\sigma}^{(i)} = \frac{K_C^{(i)}}{\chi^{(i)} Y \sqrt{\pi a}} \tag{3.18}$$

$$\bar{\sigma}^0 = \frac{K_C^0}{\chi^0 Y \sqrt{\pi a}} \tag{3.19}$$

where $K_C^{(i)}$ and K_C^0 are the compressive fracture toughness of sublaminate (i) and of the 0° plies, respectively. Note that, assuming self-similar crack propagation along all the sublaminates considered, the laminate compressive fracture toughness is,

$$K_C^L = \frac{\sum_{(i)}^N K_C^{(i)} t^{(i)}}{t^L}, \quad (i) \neq 90\ ° \tag{3.20}$$

where $t^{(i)}$ is the thickness of the sublaminate (i), N is the number of sublaminates considered, and t^L is the total thickness of the laminate. Note that, in equation (3.20), the tensile fracture toughness of the 90° plies can be neglected, since fiber kinking do not occur in these plies, and therefore the compressive fracture toughness is several orders of magnitude lower than the compressive fracture toughness of the 0° plies.

Using equations (3.18) and (3.19) in equation (3.17), the relation between the compressive fracture toughness of sublaminate (i) and the compressive fracture toughness of the 0° plies is given as,

$$K_C^{(i)} = \frac{\chi^{(i)} \Omega_0^{(i)}}{\chi^0} K_C^0 \tag{3.21}$$

Note that this methodology is not able to predict the compressive fracture toughness of laminates whose main failure mechanism is other than transverse fiber kinking, which is the case for thin-ply laminates.

3.7. Open-hole tests

Composite laminates are characterized by a decrease of the ultimate strength when structural dimensions increase. This effect is known as *size effect*, and it can occur at different material and structural levels. At the mesomechanical level (ply level), it is observed that the transverse tensile and in-plane shear strengths of a ply constrained by sublaminates depend on the ply thickness, the so-called in-situ effect. This in-situ effect can be accounted by defining the in-situ strengths, which depend on the ply elastic properties and fracture energies. At the macromechanical level (structural level), it is observed that, at constant width to diameter ratios, the strength of notched composite laminates decreases for increasing notch sizes when thin plies are used [53, 82]. This effect is caused by the development and propagation of noncritical ply-level damage mechanisms that occur in the vicinity of the hole before the final collapse of the laminate. Such noncritical ply-level damage can be regarded as a fracture process zone that develops before final failure of the laminate. For very small specimens, the fracture process zone affects the entire width of the laminate, and the notched strength tends to the unnotched strength. On the other hand, the size of the fracture process zone in large specimens is negligible when compared to the characteristic dimensions of the specimen. This relative dimension of the fracture process zone with respect to the specimen size justifies the different strengths observed in small and large specimens [53].

Open-hole tests are typically used to study the behavior of composite laminates with stress concentrations and to assess the effect of size in composite materials. In addition, these tests are important for the definition of material/lay-up and geometric parameters, namely the *characteristic distance*, used in semi-empirical closed-form models, such as the point stress and average stress methods, for the prediction of the mechanical behavior of notched composite laminates.

3.7.1. Open-hole tension

The purpose of the open-hole tension (OHT) tests is to evaluate the mechanical behavior in the presence of stress concentrations and the effects of size in thin-ply laminates when subjected to tensile efforts. Later in this thesis, these tests are used to determine the characteristic distances of these laminates and validate the predictions of the closed-form design tools used to predict size effects on thin-ply laminates (see chapter 5).

Table 3.6 shows the OHT test matrix, where w is the specimens nominal width, d is the nominal diameter of the open hole, and L is the specimens nominal length. Due to constraints in the dimensions of the grips, a width to diameter ratio $w/d = 4$ is used in this experimental program, unlike the $w/d = 6$ recommended by the ASTM D 5766/D 5766M - 02a test standard [121]. The central open-hole was obtained using a drilling machine.

Tab. 3.6. Open-hole tension test matrix.

Laminate	# specimens	w [mm]	d [mm]	L [mm]	Speed [mm/min]	Acquisition [Hz]
Lay-up 1	3	12	3	250	2.0	5
	3	24	6	250	2.0	5
	3	40	10	250	2.0	5
Lay-up 2	3	12	3	250	2.0	5
	3	24	6	250	2.0	5
	3	40	10	250	2.0	5

All tests were performed under displacement control in a servo-hydraulic MTS 810 testing machine (*Load Unit* 318.25, *Service Manifold* 298.12 C), using a force transducer (661.20 F-03) of 100 kN. One specimen per laminate and per geometry was instrumented with one strain gage placed in the longitudinal direction, as shown in figures 3.6, 3.7

and 3.8. A Spider data acquisition system was used, with a sample frequency set to 50 Hz. Figures 3.6a, 3.7a and 3.8a also show the in-plane nominal dimensions of the specimens.

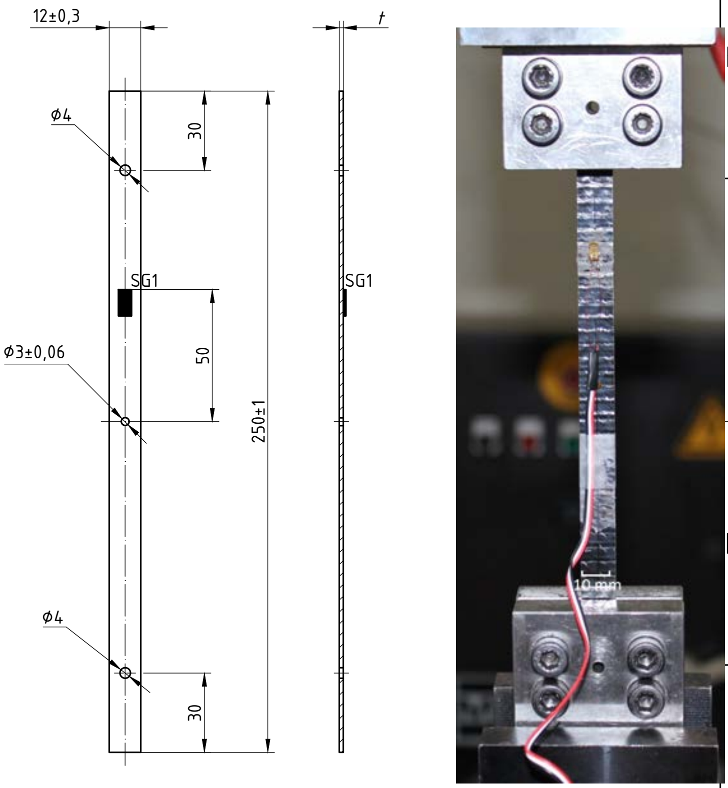

(**a**) Schematic drawing (*t* is the laminate thickness). Dimensions in mm.

(**b**) Gripped specimen before testing.

OHT1 - lay-up 1
quantity: 3
length: 250 mm
thickness: about 1.5 mm
width: 12 mm
diameter: 3 mm

Fig. 3.6. Open-hole tension test specimen ($d = 3$ mm).

FILE NAME OHT1 lay-up1	DEMec - FEUP	SHEET 1/1	SCALE 1:2
DRAWN Albertino Arteiro	Specimen for open-hole tension test	DWG NO	
APPR.	lay-up 1		

The DIC technique was used to assess transverse cracking formation in the specimens with hole diameters of 3 mm and 10 mm. One specimen per laminate and per hole size was analysed. For the specimens with a hole diameter of 3 mm, a 200 mm Nikkon lens was used together with two extension tubes of 20 mm. The working distance (defined between the specimen's surface and the support of the camera) was set to 90 mm (62 mm from the specimen to the front of the lens and 28 mm from the front of the lens to the camera), and the lens was adjusted to be in focus with regard to the surface of interest. The shutter time was set to 6 ms. The captured region was of approximately 13×18 mm^2, which defines a conversion factor of about 0.0109 mm/pixel. For the specimens with a hole diameter of 10 mm, one extension tube of 20 mm was used together with the 200 mm Nikkon lens. The working distance was set to 1760.7 mm (1735 mm from the specimen to the front of the lens and 25.7 mm from the front of the lens to the camera), and the lens was adjusted to be in focus with regard to the surface of interest. The shutter time was set to 16 ms. The captured region was of approximately 43×56 mm^2, which defines a conversion factor of about 0.0346 mm/pixel.

During the experimental procedure, the dimensions of each specimen were recorded to determine the applied stress. Coarse-grain sandpaper strips (IMPERIAL CRD 40) were inserted between each specimen and the grips to avoid sliding. The alignment of the lon-

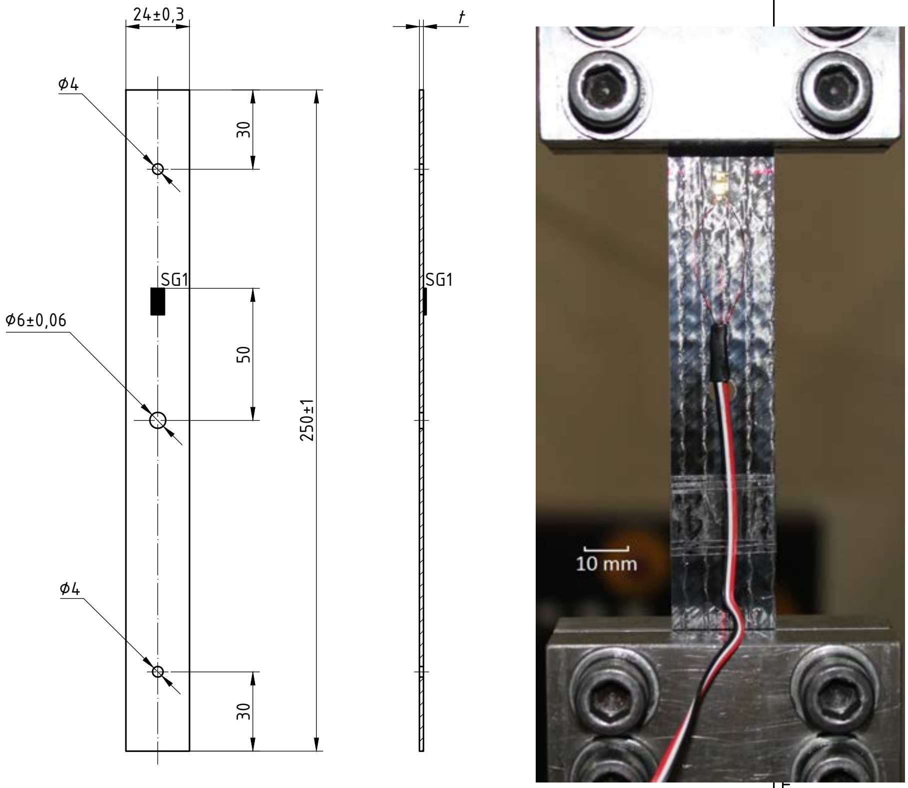

(**a**) Schematic drawing (t is the laminate thickness). Dimensions in mm.

(**b**) Gripped specimen before testing.

Fig. 3.7. Open-hole tension test specimen (d = 6 mm).

OHT3 - lay-up 1
quantity: 3
length: 250 mm
thickness: about 1.5 mm
width: 24 mm
diameter: 6 mm

FILE NAME OHT3 lay-up1	DEMec - FEUP	SHEET 1/1	SCALE 1:2
DRAWN Albertino Arteiro	Specimen for open-hole tension test	DWG NO 3	
APPR.	Lay-up 1		

gitudinal axis of the gripped specimen with the test direction is made using two guiding pins with a diameter of 4 mm in the ends of the specimen (see figures 3.6, 3.7 and 3.8). For the open-hole specimens with a 3 mm hole diameter, the grips were clamped with a bolt torque of 35–40 Nm; however, it was reduced to 25 Nm in one specimen of the thinner lay-up 2 (specimen AAOHT123) to avoid failure within the grips. It was observed that, for these specimens, a bolt torque of 25 Nm was adequate to avoid both failure and sliding within the grips. For the open-hole specimens with a 6 mm hole diameter, the grips were clamped with a bolt torque of 45–50 Nm, and for the open-hole specimens with a 10 mm hole diameter, the grips were clamped with a bolt torque of 55–60 Nm. Each specimen was tested until failure occurs, recording afterwards the maximum load and laminate's failure mode and location.

The laminate tensile notched strength, $\bar{\sigma}_T^{\infty}$, is determined as,

$$\bar{\sigma}_T^{\infty} = \frac{P_{max}}{A} \tag{3.22}$$

where P_{max} is the maximum load before rupture occurs and A is the mean cross-sectional area of the specimen.

3.7.2. Open-hole compression

The purpose of the open-hole compression (OHC) tests is to evaluate the mechanical behavior in the presence of stress concentrations and the effects of size in thin-ply lami-

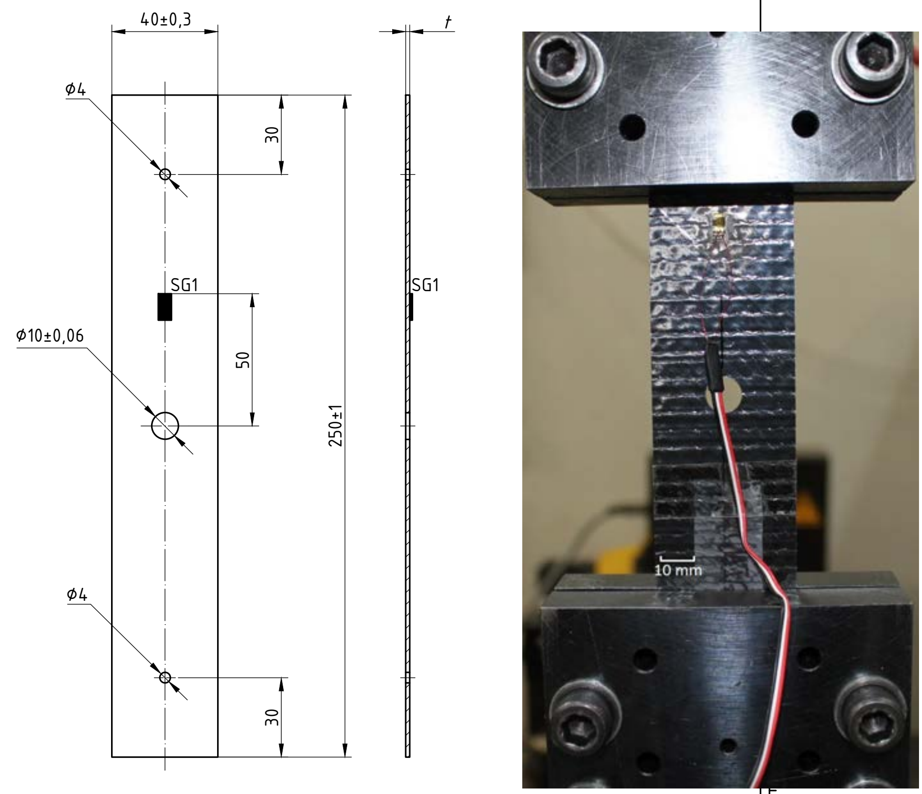

(**a**) Schematic drawing (t is the laminate thickness). Dimensions in mm.

(**b**) Gripped specimen before testing.

Fig. 3.8. Open-hole tension test specimen (d = 10 mm).

nates when subjected to compressive efforts. Later in this thesis, these tests are used to determine the characteristic distances of these laminates in compression and validate the predictions of the closed-form design tools used to predict size effects on thin-ply laminates (see chapter 5).

Because the assessment of the laminate compressive notched strength is more complex than when dealing with tensile conditions, as in the previous compressive tests, a special test rig developed to minimize out-of-plane bending (buckling) is used. Table 3.7 shows the open-hole compression test matrix, where w is the specimens nominal width, d is the nominal diameter of the open hole, and L is the specimens nominal length. The width to diameter ratio used in this experimental program is $w/d = 4$. The central open-hole was obtained using a drilling machine.

All tests were performed under displacement control in a servo-hydraulic MTS 810 testing machine (*Load Unit* 318.25, *Service Manifold* 298.12 C), using a force transducer (661.20 F-03) of 100 kN. One specimen per laminate was instrumented with two strain gages placed in the longitudinal direction, but in opposite faces of the specimen, as shown in figures 3.9, 3.10 and 3.11. With this configuration, one is able to assess if non-negligible out-of-plane bending occurs. A Spider data acquisition system was used, with a sample frequency set to 50 Hz. Figures 3.9a, 3.10a and 3.11a also show the in-plane nominal dimensions of the specimens.

The DIC technique was used to assess transverse cracking propagation in the specimens

Tab. 3.7. Open-hole compression test matrix.

Laminate	# specimens	w [mm]	d [mm]	L [mm]	Speed [mm/min]	Acquisition [Hz]
Lay-up 1	3	8	2	305	2.0	5
	3	20	5	305	2.0	5
	3	28	7	305	2.0	5
Lay-up 2	3	8	2	305	2.0	5
	3	20	5	305	2.0	5
	3	28	7	305	2.0	5

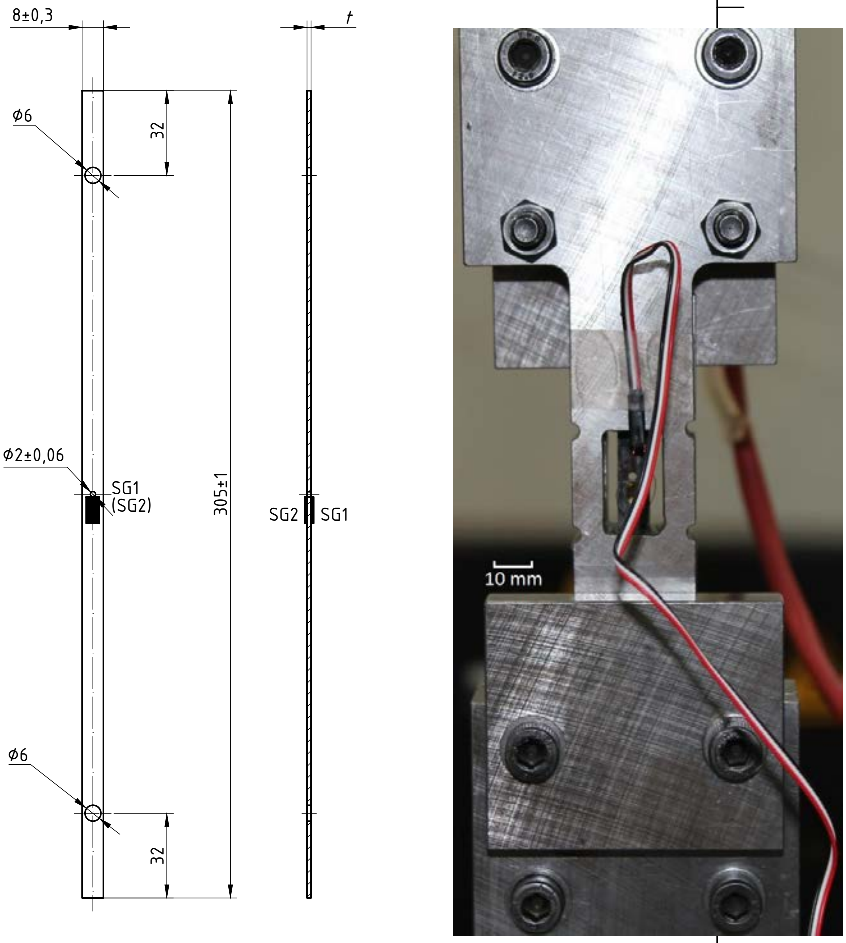

(**a**) Schematic drawing (t is the laminate thickness). Dimensions in mm.

(**b**) Test assembly before testing.

Fig. 3.9. Open-hole compression test specimen ($d = 2$ mm).

with hole diameters of 2 mm and 7 mm. One specimen per laminate and per hole size was analysed. For the specimens with a hole diameter of 2 mm, a 200 mm Nikkon lens was used together with two extension tubes of 20 mm. The working distance (defined between the specimen's surface and the support of the camera) was set to 564 mm (536 mm from the specimen to the front of the lens and 28 mm from the front of the lens to the camera), and the lens was adjusted to be in focus with regard to the surface of interest. The shutter

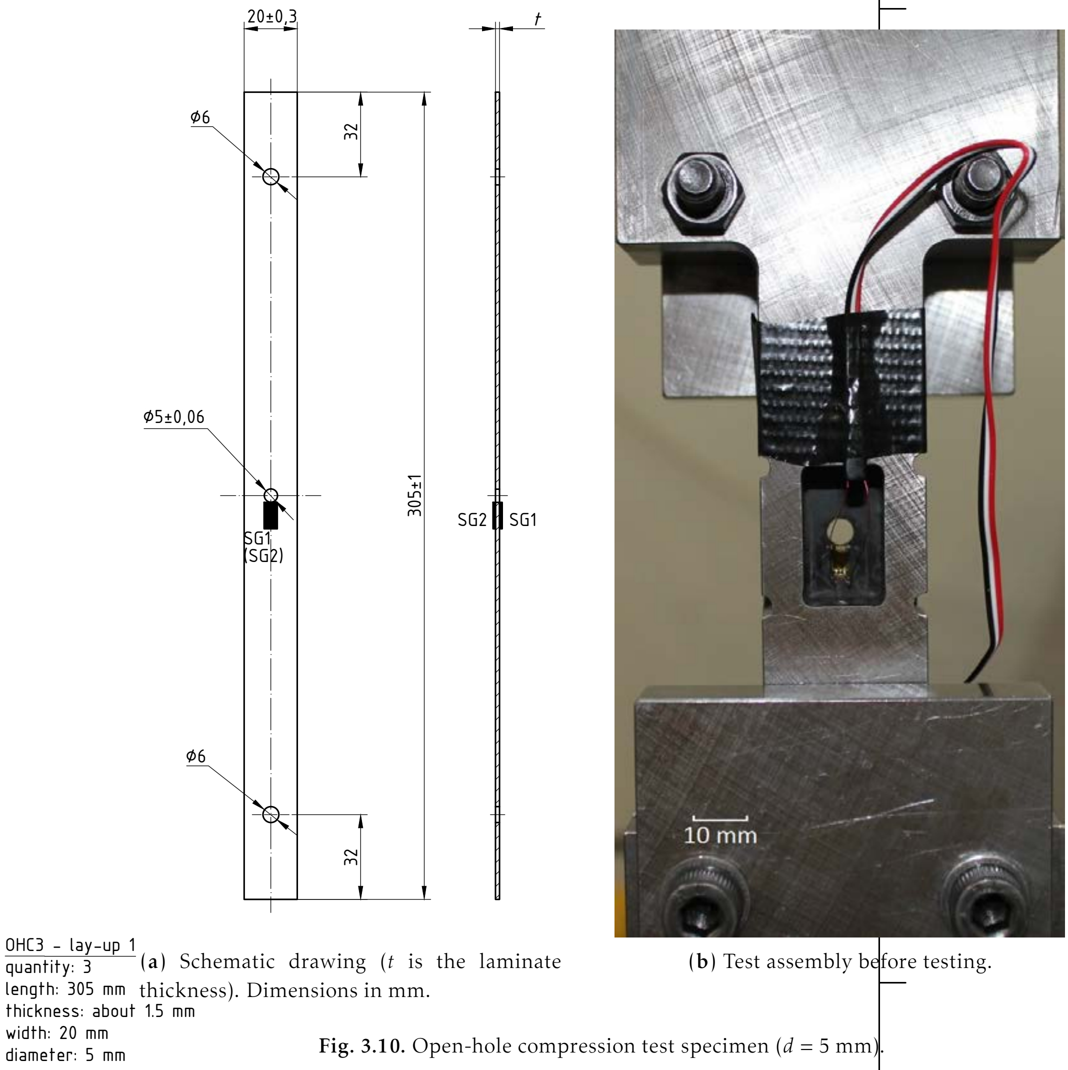

(**a**) Schematic drawing (t is the laminate thickness). Dimensions in mm.

(**b**) Test assembly before testing.

Fig. 3.10. Open-hole compression test specimen (d = 5 mm).

time was set to 4 ms for lay-up 1 and 2.5 ms for lay-up 2. The captured region was of approximately 11×15 mm^2, which defines a conversion factor of about 0.0090 mm/pixel. For the specimens with a hole diameter of 7 mm, two extension tubes of 20 mm were also used. The working distance was set to 646 mm (618 mm from the specimen to the front of the lens and 28 mm from the front of the lens to the camera), and the lens was adjusted to be in focus with regard to the surface of interest. The shutter time was set to 6 ms. The captured region was of approximately 15×19 mm^2, which defines a conversion factor of about 0.0117 mm/pixel.

During the experimental procedure, the dimensions of each specimen were recorded to determine the applied stress. The alignment of the longitudinal axis of the gripped specimen with the test direction is made using two guiding pins with a diameter of 6 mm in the ends of the specimen (see figures 3.9a, 3.10a and 3.11a). The compression rig was clamped with a bolt torque of 8 Nm. Each specimen was tested until failure occurs, recording afterwards the maximum load and laminate's failure mode and location.

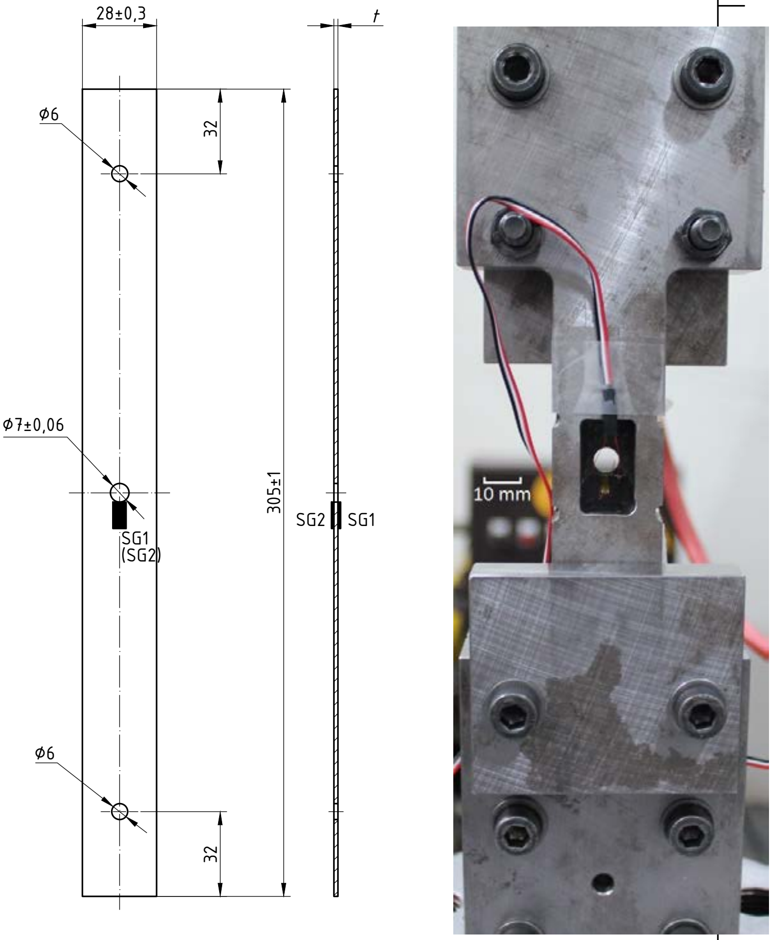

OHC2 - lay-up 1
quantity: 3
length: 305 mm
thickness: about 1.5 mm
width: 28 mm
diameter: 7 mm

(**a**) Schematic drawing (*t* is the laminate thickness). Dimensions in mm.

(**b**) Test assembly before testing.

Fig. 3.11. Open-hole compression test specimen (d = 7 mm).

FILE NAME OHC2.lay-up1	DEMec - FEUP	SHEET 1/1	SCALE 1:2
DRAWN Albertino Arteiro	Specimen for open-hole compression test Lay-up 1	DWG NO	
APPR.			

The laminate compressive notched strengh, $\bar{\sigma}_C^\infty$, is determined as,

$$\bar{\sigma}_C^\infty = \frac{P_{max}}{A} \tag{3.23}$$

where P_{max} is the maximum load before rupture occurs and A is the mean cross-sectional area of the specimen.

3.8. Bearing tests

Virtually every large-scale composite structure, particularly for application in the aircraft and spacecraft industries, contains joints. The reasons that justify their use are well known, but manufacturing constraints and requirements related to accessibility to the structure, quality control, structural integrity assessment, and part replacement are the main ones. Among the types of joints used in large-scale composite structures, mechanically fastened joints are particularly common [122]. They are used in composite structures since the 1960's, when high modulus, high strength composites first came into use [113]. Mechanically fastened joints are used mainly because they are relatively inexpensive to manufacture and can be disassembled. However, due to the stress concentrations created, mechanically fastened joints are a source of weakness and compliance [122].

The behavior of composites in bolted joints differs considerably from that of metallic materials. The quasi-brittle nature of composite materials requires more detailed analysis to quantify the level of various stress peaks. In composites, stress concentrations dictate components static strength to a larger extent than in metals due to the absence of yielding, conducting to less efficient joints. Therefore, when designing composite joints, the brittleness of the composite laminate, the possibility of using highly orthotropic laminates that promote high stress concentrations, the anisotropy in both stiffness and strength properties, and geometrical parameters such as edge distances and hole spacings need to be taken into account [113, 122]. In fact, joints are generally the critical part of a composite structure; accordingly, the soundness of the joint design procedure used is reflected on the overall weight and cost of the composite structure [122]. Since the introduction of composite structures in the aircraft and spacecraft industries, new joint design solutions had been proposed. For example, specialized fasteners featuring larger tail footprint areas to improve pull-through and bearing strengths had been introduced in composites design, whereas rivets had been eliminated due to the low through-the-thickness composite laminate strength [113]. Use of aluminum fasteners was also eliminated due to galvanic corrosion susceptibility between carbon and aluminum [113]. More recently, innovative hybrid metal-composite laminates bolted joints were proposed to increase efficiency of the bolted joints in composite structures [123].

The most common joint failure modes of composite bolted joints are bearing, net-tension and shear-out, as outlined in figure 3.12. The bearing failure mode is particularly interesting in the design of composite joints because it is a non-catastrophic failure characterized by a progressive accumulation of damage and by the subsequent permanent deformation of the hole in compression [122].

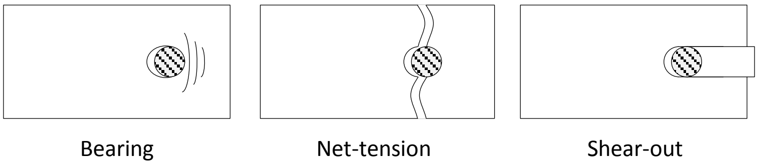

Fig. 3.12. Joint failure modes.

Because the bearing strength of a composite laminate depends on the lateral support provided in the bearing region, two different experimental configurations are possible, namely *pin-bearing tests* and *bolt-bearing tests*. In pin-bearing tests, no clamping pressure is applied in the bearing region of the laminate. In bolt-bearing tests, a "finger-tight" clamping pressure corresponding to a torque, T, of 2.2 Nm is applied [122]. In this configuration washers can be used. Note that the absence of clamping pressure in the pin-bearing tests results in lower bearing stresses than that of a bolted joint [118, 122]. Therefore, not taking into account the clamping pressure in joint design acts as a safety factor. However, most, if not all, mechanically fastened joints include clamping pressure. So, it is controversial which test is more appropriate [118].

In this experimental program, bolt-bearing tests are addressed, according to ASTM D 5961 test standard [124]. The purpose of the bolt-bearing tests is to evaluate the mechanical behavior of the thin-ply laminates when subjected to local compressive efforts, typical of mechanically fastened joints. Table 3.8 shows the bearing test matrix, where d is the nominal diameter of the hole, e/d is the edge distance ratio, w/d is the width to diameter ratio, and L is the specimens nominal length. The hole was obtained using a drilling machine. A bolt M6 is used with an applied torque $T = 2.2$ Nm.

Tab. 3.8. Bearing test matrix.

Laminate	# specimens	d [mm]	e/d	w/d	L [mm]	Speed [mm/min]	Acquisition [Hz]
Lay-up 1	3	6	6	6	215	2.0	5
Lay-up 2	3	6	6	6	215	2.0	5

All tests were performed under displacement control in a servo-hydraulic MTS 810 testing machine (*Load Unit* 318.25, *Service Manifold* 298.12 C), using a force transducer (661.20 F-03) of 100 kN. One specimen per laminate was instrumented with one strain gage placed in the longitudinal direction, as shown in figure 3.13. A Spider data acquisition system was used, with a sample frequency set to 50 Hz. Figure 3.13a also shows the in-plane nominal dimensions of the specimens.

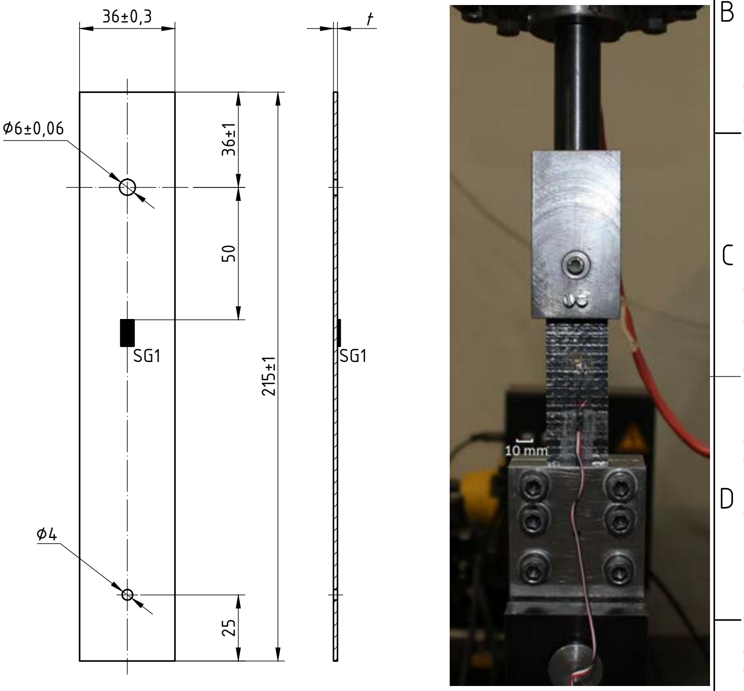

(**a**) Schematic drawing (t is the laminate thickness). Dimensions in mm.

(**b**) Gripped specimen before testing.

Fig. 3.13. Bearing test specimen.

During the experimental procedure, the dimensions of each specimen were recorded to determine the applied stress. Coarse-grain sandpaper strips (IMPERIAL CRD 40) were inserted between each specimen and the grip that supports the end opposite to the bearing region to avoid sliding (see figure 3.13b). The alignment of the longitudinal axis of the gripped specimen with the test direction is made using a guiding pin with a diameter of 4 mm at the end opposite to the bearing region (see the test assembly in figure 3.13). This

Bearing - lay-up 1
quantity: 3
length: 215 mm
thickness: about 1.5 mm
width: 36 mm
end distance: 36 mm
diameter: 6 mm

FILE NAME Bearing lay-up1	DEMec - FEUP	SHEET 1/1	SCALE 1:2
DRAWN Albertino Arteiro	Specimen for bearing test	DWG NO 1	
APPR.	Lay-up 1		

grip, placed at the end opposite to the bearing region, was clamped with a bolt torque of 55–60 Nm. Each specimen was tested until failure occurs, recording afterwards the maximum load and laminate's failure mode and location.

The laminate bearing stress, σ^b, is defined as [124],

$$\sigma^b = \frac{P}{dt} \tag{3.24}$$

where P is the test load, d is the diameter of the hole, and t is the mean thickness of the specimen. Three definitions of the bearing strength are considered, namely the maximum bearing stress ($\bar{\sigma}^b_{\text{max}}$), the bearing stress at the first load drop ($\bar{\sigma}^b_{\text{1st load drop}}$), and the bearing stress corresponding to an offset bearing strain of 2% ($\bar{\sigma}^b_{\text{offset 2\%}}$).

3.9. Over-height compact tension tests

Fracture in a composite laminate can appear either between two plies or within a lamina. In the first case, termed interlaminar fracture or delamination, the crack causes separation of two adjacent plies, generally involving matrix failure and fiber/matrix debonding, and sometimes failure by fiber bridging. In the second case, termed intralaminar fracture, the crack is located within the lamina, either parallel to the fibers (the so-called intralaminar matrix fracture), or at an angle, which includes translaminar fiber fracture. Although the energy consumed in fiber fracture is usually much larger than in matrix cracking or fiber/matrix debonding, experimental determination of the translaminar fiber fracture toughness is important for accurate numerical modeling of composite components failure [125].

In most cases, the compact tension (CT) test, where tensile load is applied through pins located above and below the notch, is employed to assess the translaminar fracture toughness of composite laminates, particularly by means of an R-curve [125]. CT testes are usually devised such that extraneous damage modes are minimized and that a brittle type crack progresses from the pre-machined notch [108]. However, in some cases, different damage mechanisms can occur in addition to, or instead of, the intended translaminar crack propagation, so invalidating the fracture toughness measurement [125].

In this experimental program, the mechanical behavior of two different thin-ply laminates, lay-up 1 and lay-up 2, with thicknesses of approximately 2.0 and 1.3 mm, respectively, are under study. Such thin laminates may easily induce different damage mechanisms during classical CT tests, particularly fiber fracture due to longitudinal compressive stress at the edge opposed to the one containing the notch (figure 3.14a) and overall specimen buckling (figure 3.14b). Therefore, in this experimental program, the **over-height compact tension** (OCT) test, adapted from the one developed at the University of British Columbia [107], is used together with an anti-buckling support, as proposed by Li et al. [108], in order to avoid both undesirable damage mechanisms, as previously mentioned.

Using the OCT test, the behavior of laminates typical of large structures can be captured since it is large enough so that the boundaries do not greatly affect the damage zone, and a stable process zone ahead of the crack tip is formed under displacement control, facilitating the post-test investigation of the damage evolution by means of a stable R-curve [107, 108]. To prevent buckling, Li et al. [108], which tested OCT specimens with thicknesses ranging from 2.0 mm to 4.0 mm, proposed a stiffening support with a width of

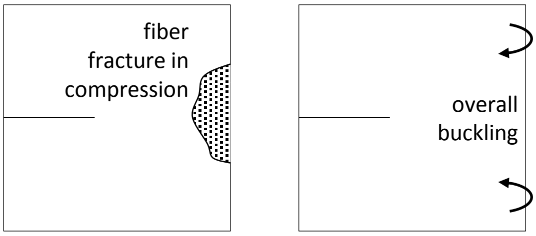

(a) Fiber fracture due to longitudinal compressive stress.

(b) Overall specimen buckling.

Fig. 3.14. Draft of the possible different damage mechanisms induced in thin CT specimens (adapted from [125]).

10 mm to be attached to the back edge of the OCT specimen. According to the authors, such anti-buckling support had little effect on the response of the specimen.

Table 3.9 shows the OCT test matrix, where w is the nominal width of the region of interest, a_0 is the nominal length of the pre-machined notch, and d is the nominal diameter of the holes for the loading pins, as shown in figure 3.15a. The 4 mm notch was created using a vertical mill equipped with a milling cutter with a radius of 2 mm. After machining the notch, a sharp crack tip location was created using a 0.4 mm thick razor blade. The holes for the pin loading were obtained also using a milling machine.

Tab. 3.9. Over-height compact tension test matrix.

Laminate	# specimens	w [mm]	a_0 [mm]	d [mm]	Speed [mm/min]	Acquisition [Hz]
Lay-up 1	3	81	30–31	25	2.0	5
Lay-up 2	3	81	30–31	25	2.0	5

A 10 mm wide anti-buckling support is used to avoid the overall specimens buckling. Such anti-buckling support is tightened to the back edge of the OCT specimen using two screw/nut M5 assemblies. Figure 3.15b shows a draft of the anti-buckling support used in this experimental program. Note that the in-plane dimensions of the OCT specimens used in this experimental work were initially constrained by the dimensions of the test rig. However, later it was found that using some extension bars together with the traditional CT test rig, the specimens nominal height could be as high as necessary (up to the 208 mm used by Li et al. [108]). However, the nominal diameter of the holes for the pin loading must be 25 mm (instead of the 20 mm used by Li et al. [108]), and the distance between holes must increase too (a minimum of 59 mm must be used instead of the 38 mm used by Li et al. [108]). If the available anti-buckling support is to be used, specimens with a nominal height up to 180 mm can be tested using the test assembly proposed in this thesis, shown in figure 3.15c. No constraints are imposed to the specimens nominal width.

All tests were performed under displacement control in a servo-hydraulic MTS 810 testing machine (*Load Unit* 318.25, *Service Manifold* 298.12 C), using a force transducer (661.20 F-03) of 100 kN. The DIC technique was used in order to quantify the crack length, without requiring any visual inspection, as proposed by Catalanotti et al. [109]. With such quantification, the evaluation of the J-integral and the measurement of the crack resistance

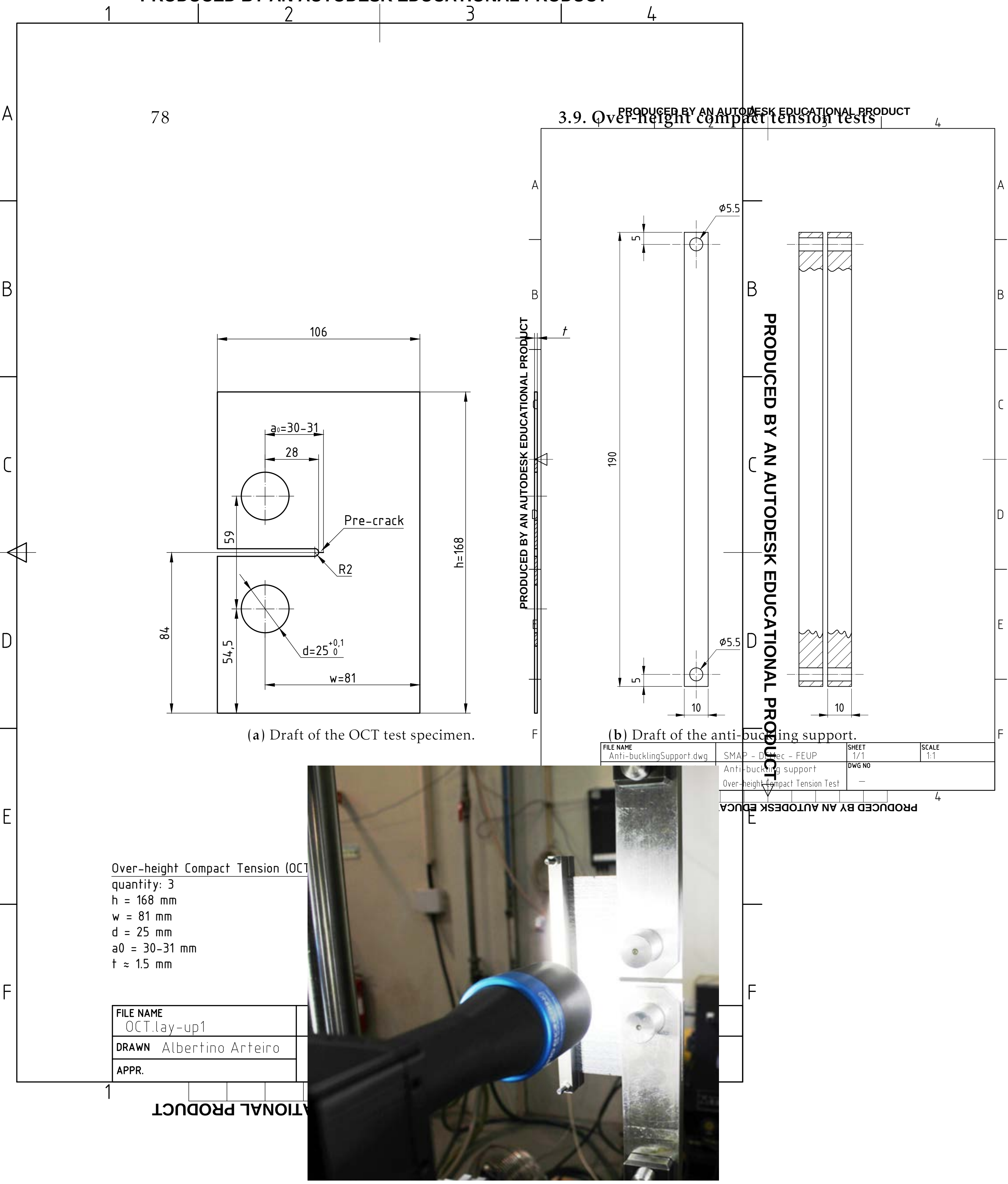

(**a**) Draft of the OCT test specimen.

(**b**) Draft of the anti-buckling support.

(**c**) Photo of the OCT test assembly.

Fig. 3.15. Over-height compact tension test specimen and anti-buckling support.

curve can be easily performed, based on the surface displacement and strain fields obtained from the DIC technique. This method is implemented in a Matlab® code, obviating the need of any complex pre- or post-processing of the test data, and enabling the real-time generation of R-curves during tests.

The Opto Engineering® TC 23 36 bi-telecentric lens used in the OCT tests has a constant working distance of 103.5±3 mm. Because it is coupled a 1/1.8" detector type camera, the field of view is constant and equal to 29.3×22.1 mm^2, which defines a conversion factor of about 0.0180 mm/pixel. The shutter time was set to 0.4–0.6 ms, and the acquisition frequency to 0.4–05 Hz.

In addition to the DIC technique, two other alternative data reduction methodologies were used. The first one is based on the linear elastic fracture mechanics solution proposed by Aronsson and Bäcklund [126] for a quasi-isotropic compact tension specimen. According to this solution, the laminate stress intensity factor, K_I^L, is given as,

$$K_I^L = P/w\sqrt{\pi a}Y(a/w) \tag{3.25}$$

where P is the load per unit thickness, w is the dimension from the load line to the edge opposite to the one containing the pre-crack (see figure 3.15a), a is the crack length, and $Y(a/w)$ is a finite width correction factor given as,

$$Y(a/w) = \frac{2+a/w}{(1-a/w)^{3/2}}\frac{1}{\sqrt{a/w}}\left[0.881 - 0.185(a/w) + 0.038(a/w)^2\right] \tag{3.26}$$

The laminate energy release rate, G_I^L, can be related with the laminate stress intensity factor, K_I^L, as,

$$G_I^L = \frac{\left(K_I^L\right)^2}{\sqrt{2E_yE_x}}\sqrt{\sqrt{\frac{E_y}{E_x}} + \frac{E_y}{2G_{xy}} - \nu_{yx}} \tag{3.27}$$

where E_x and E_y are the Young moduli in the longitudinal and transversal directions, respectively, G_{xy} is the shear modulus, and ν_{xy} is the laminate Poisson ratio, which can be obtained from the ply properties (table 3.1) using classical lamination theory [120].

Alternatively, a finite element method (FEM) based data reduction technique developed by Pinho et al. [104] is also used here. This method consists in the generation of a set of shell finite element (FE) models of the OCT specimen with unit thickness (1 mm) and with variable crack lengths that are used to calculate the corresponding values of the J-integral for a unit load (1 N). With this information, it is possible to obtain the normalized energy release rate $f(a)$, defined as,

$$f(a) = J \cdot \left(\frac{1\text{ mm}}{1\text{ N}}\right)^2 \tag{3.28}$$

which can be correlated with the experimental results (load and crack length) to obtain the laminate energy release rate as,

$$G_I^L = \left(\frac{P}{t}\right)^2 f(a) \tag{3.29}$$

where t is the thickness of the laminate. With these results, one is able to finally generate the corresponding R-curve.

According to Pinho et al. [104], the differences observed in the calculation of the J-integral for FE models with elements of 1 mm, 0.5 mm and 0.2 mm long are scarce, and therefore relatively coarse meshes can be used and still obtain accurate values of the energy release rate. In this thesis, the FE package Abaqus® is used to calculate the J-integral of the OCT specimen with unit thickness (1 mm) and subjected to a unit load (1 N). Because the specimen is symmetric, only half OCT specimen is modeled, using a structured mesh of uniform square CPS4R 4-noded reduced integration elements, with sides 1 mm long. Figure 3.16 shows the deformed mesh of the FEM model used in this analysis.

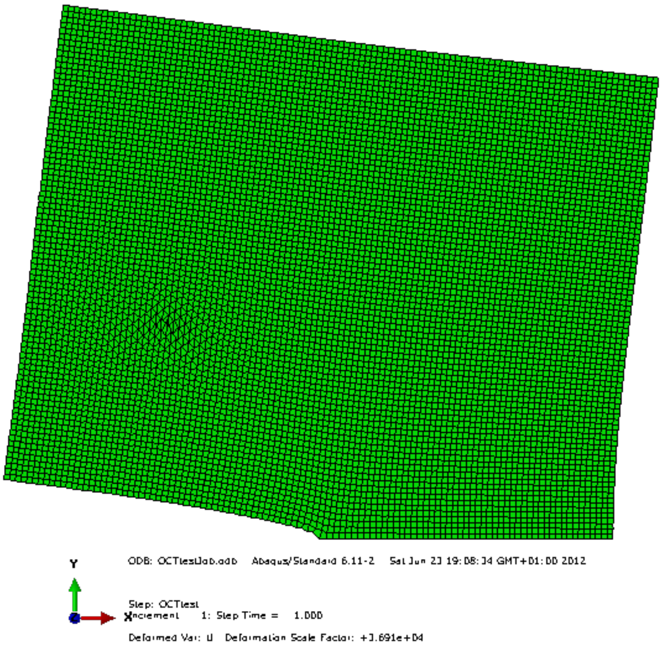

Fig. 3.16. Deformed finite element mesh of a half over-height compact tension specimen.

Chapter 4

Experimental results

A set of experimental tests were performed during the development of the present work to study some of the most relevant mechanical properties of thin-ply laminates, with particular emphasis on size effects, notched strengths, bearing strengths, and fracture toughness of such materials. In this chapter, the results of the experimental program are shown and discussed in detail. Additionally, the results obtained for the thin-ply laminates are compared with other carbon/epoxy systems used in aircraft applications. Such comparison is important in defining the performance of the thin-ply laminates studied in this thesis.

4.1. Introduction

With the main objective to assist in the technology development of the spread tow thin-ply technology, a set of experimental tests were performed during the development of the present work to study some of the most relevant mechanical properties of thin-ply laminates. Such experimental program gives particular emphasis to the size effects, notched strength, bearing strength, and fracture toughness of such materials. Accordingly, the results of the plain strength tension and compression, open-hole tension and compression, center-notched tension and compression, bolt bearing, and over-height compact tension tests are presented in this chapter.

In addition, the results obtained for the thin-ply laminates are compared with other carbon fiber-reinforced polymers (CFRP) typical of aircraft applications, namely the T800/M21 and the IM7-8552 carbon/epoxy systems. It should be noted, however, that IM7 and T800 carbon fibers are stronger and stiffer than the T700 used in the thin-ply laminates and that Hexcel's 8552 and M21 epoxy systems are classified as tough and very tough epoxy matrices, respectively. Therefore, such comparison is mainly performed in a qualitative basis. To better quantitatively understand the performance of the thin-ply laminates, the normalized strength values[1] of the specimens are considered for comparative purposes.

---

[1] The normalized strength values are given by the ratio between the strength value intended to be normalized, and a reference value such as the unnotched tensile strength or the unnotched compressive strength, when tensile or compressive efforts are present, respectively.

4.2. Plain strength test results

4.2.1. Tensile plain strength

Tensile plain strength (unnotched) tests were performed in order to evaluate the elastic properties of the thin-ply laminates studied in this experimental work and their mechanical behavior when subjected to tensile efforts. The unnotched tensile test results for the thin-ply $[(0/-45)/(90/45)]_{6T}$ laminate (lay-up 1) specimens and for the thin-ply $[(0/-45)/(45/0)/(90/45)/(-45/90)]_S$ laminate (lay-up 2) specimens are shown in figures 4.1 and 4.2, respectively. Both stress-displacement[2] and stress-strain[3] relations are represented. Note that the stress-strain relations (figures 4.1b and 4.2b) for the longitudinal deformation (ε_L) of the unnotched specimens end before failure because the maximum strain of the strain gages (about 5000 µm/m) was reached.

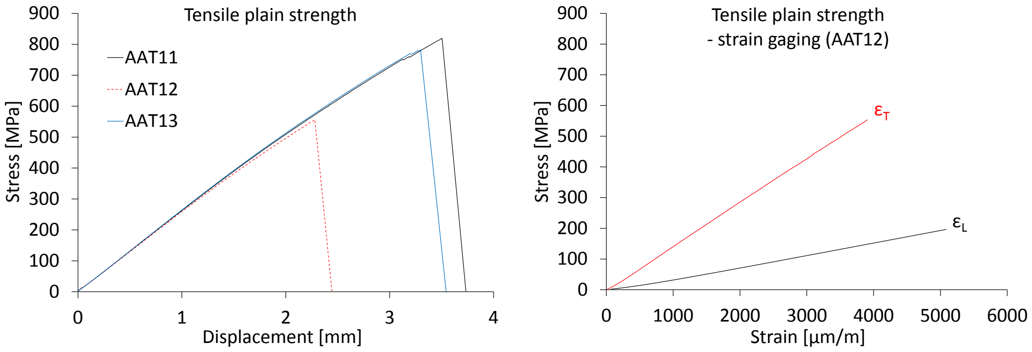

(**a**) Stress-displacement relation. (**b**) Stress-strain relation.

Fig. 4.1. Unnotched tension results for the $[(0/-45)/(90/45)]_{6T}$ specimens.

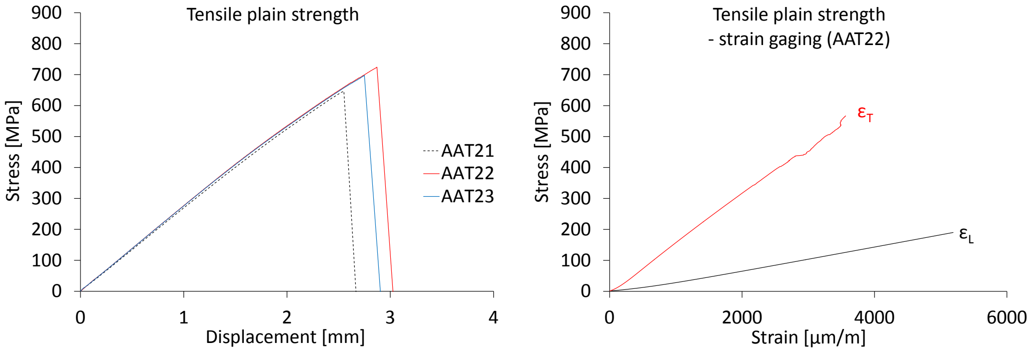

(**a**) Stress-displacement relation. (**b**) Stress-strain relation.

Fig. 4.2. Unnotched tension results for the $[(0/-45)/(45/0)/(90/45)/(-45/90)]_S$ specimens.

Before analyse these results, it should be noted that specimens AAT12 (lay-up 1) and AAT21 (lay-up 2) failed within the grip. Therefore, the testing results for these specimens

---

[2] Measured by the linear variable differential transformer (LVDT) connected to the hydraulic actuator of the test machine.

[3] Measured in one specimen (indicated in the respective figure).

are not considered in this analysis (though reported herein).

As one can see in figures 4.1a and 4.2a, both laminates exhibit a linear behavior nearly up to the ultimate failure stress, and no sudden nonlinearity is observed. These results suggest that unrecoverable severe damage, such as extensive microcracking and delamination, did not occur before failure, which was dominated by fiber breakage. Figures 4.3 and 4.4 confirm these observations.

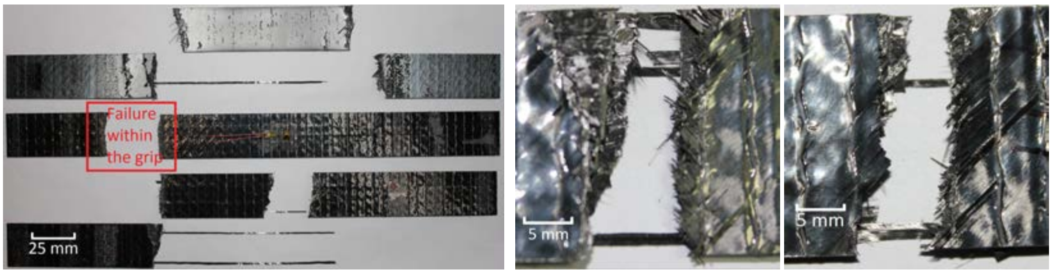

(**a**) Overview. (**b**) Close-up (specimen AAT11).

Fig. 4.3. Thin-ply $[(0/-45)/(90/45)]_{6T}$ specimens after tensile plain strength testing.

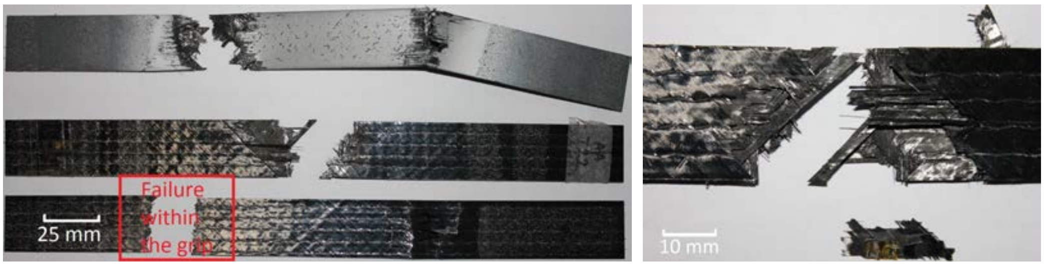

(**a**) Overview. (**b**) Close-up (specimen AAT22).

Fig. 4.4. Thin-ply $[(0/-45)/(45/0)/(90/45)/(-45/90)]_S$ specimens after tensile plain strength testing.

As one can see, except for specimen AAT22, whose failure occurred in the middle section, extensive damage can be observed in two different places for all valid specimens; particularly, for lay-up 1 specimens, failure occurred in both places. Such behavior is the result of the highly catastrophic type of failure typical of CFRP. Observing figure 4.3b, one can see that lay-up 1 specimens exhibit a brittle type of net-section failure mode, whose failure section is perpendicular to the applied tension direction. Delamination is almost nonexistent. On the other hand, figure 4.4b shows that the lay-up 2 specimens exhibit a pull-out failure mode, where some delamination can be observed.

The difference in the failure modes of the thin-ply laminates under unnotched tension is a result of the different stacking sequences. Unlike lay-up 1, which has a constant angle of 45° between interfaces (both within and between [0/−45] bi-layers), lay-up 2 has some interfaces between the [0/−45] bi-layers with an angle of 90°, conducting to higher interlaminar stress concentrations[4], and it has some interfaces between the [0/−45] bi-layers with an angle of 0°, resulting in ply clustering and conducting to higher stress concentrations in the adjacent interfaces. The combination of these two factors increases the interlaminar

---

[4] As it is well known, the higher the angle between layers, the higher the interlaminar stress concentrations.

stresses and, consequently, conducts to delamination onset during failure of the laminate. Therefore, one can conclude that the thin-ply lay-up 1 laminate has higher delamination resistance than the thin-ply lay-up 2 laminate. Still, the extent of delamination observed in the lay-up 2 specimens is far from that observed in traditional prepreg quasi-isotropic laminates.

In addition to the improved delamination resistance, both thin-ply laminates have the ability to avoid transverse cracking onset and propagation. Figures 4.5 and 4.6 show the surface longitudinal strain fields for lay-up 1 and lay-up 2, respectively, just before failure (as shown in the images in the upper right), obtained from the analysis with the digital image correlation (DIC) system. In particular, the images in the bottom right of these figures show the longitudinal strain (Eps X) along two lines near the free-edges, oriented in the loading direction.

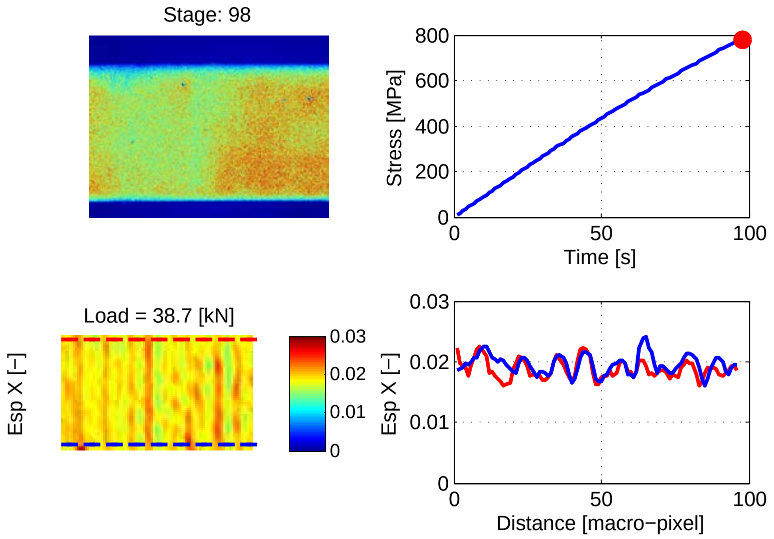

Fig. 4.5. Longitudinal strain field for the thin-ply $[(0/-45)/(90/45)]_{6T}$ unnotched specimens. The loading direction is oriented horizontally.

As one can see, although not a completely regular strain distribution as it would be in an homogeneous material, the oscillations of the longitudinal strain values are very small. Indeed, one can see that transverse cracking starting at the free-edges is almost absent, with only one exception for the lay-up 2 laminate, which, in spite of the smaller oscillations, exhibits a discontinuity on the strain field (see the blue line in the bottom right of figure 4.6) corresponding to transverse cracking onset. Note that the smaller oscillations observed for the lay-up 2 laminate, when compared with lay-up 1, are a result of having the fibers oriented in the 0° direction, unlike the lay-up 1 laminate whose strain field is measured in the surface with the fibers oriented in the 45° direction, as described in section 3.4.

The tensile unnotched strengths, X_T^L, obtained for the lay-up 1 and lay-up 2 specimens are shown in table 4.1, as well as the mean value for each laminate and the standard deviations (STDV). Table 4.2 shows the laminate modulus of elasticity, E^L, and the laminate major Poisson ratio, ν_{12}^L, for each laminate, obtained with the corresponding instrumented specimens (AAT12 for lay-up 1 and AAT22 for lay-up 2). Note that, because they are invalid tests, the tensile unnotched strength test results for specimens AAT12 (lay-up 1) and

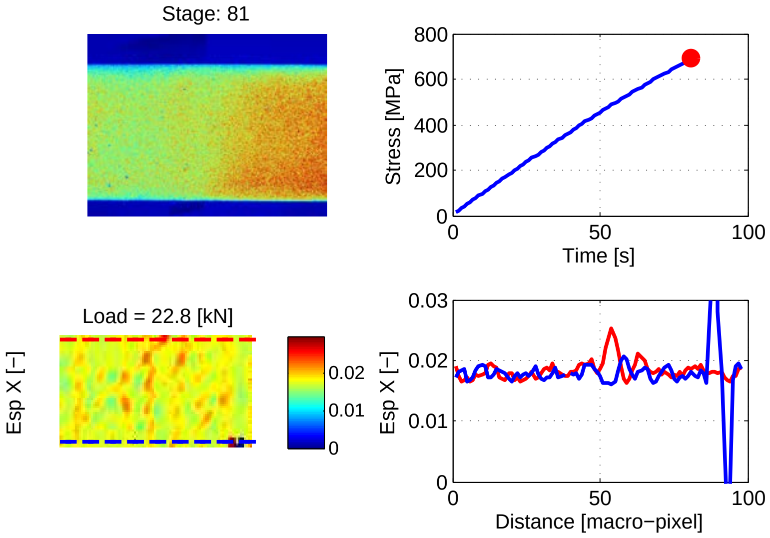

Fig. 4.6. Longitudinal strain field for the thin-ply $[(0/-45)/(45/0)/(90/45)/(-45/90)]_S$ unnotched specimens. The loading direction is oriented horizontally.

AAT21 (lay-up 2) are not considered for the calculation of the mean values and standard deviations.

Tab. 4.1. Tensile unnotched strength results for the thin-ply $[(0/-45)/(90/45)]_{6T}$ (lay-up 1) laminate and for the thin-ply $[(0/-45)/(45/0)/(90/45)/(-45/90)]_S$ (lay-up 2) laminate.

Laminate	Property		Test results			Mean value	STDV
Lay-up 1	X_T^L	[MPa]	819.1	(553.4)	781.2	800.2	19.0
Lay-up 2	X_T^L	[MPa]	(646.5)	723.8	696.9	710.3	13.4

Tab. 4.2. Elastic properties for the thin-ply $[(0/-45)/(90/45)]_{6T}$ (lay-up 1) laminate and for the thin-ply $[(0/-45)/(45/0)/(90/45)/(-45/90)]_S$ (lay-up 2) laminate.

Laminate		E^L [GPa]	ν_{12}^L
Thin-ply	$[(0/-45)/(90/45)]_{6T}$	39.7	0.27
Thin-ply	$[(0/-45)/(45/0)/(90/45)/(-45/90)]_S$	37.8	0.22

The tensile unnotched strength of lay-up 1 is 12.7% higher than that of lay-up 2. Therefore, one can conclude that the brittle type of net-section failure mode exhibited by lay-up 1, dominated by fiber breakage, is beneficial with respect to the laminate's tensile unnotched strength, whereas a pull-out failure mode, accompanied with delamination, precipitates failure of the unnotched specimens. Such results may be a consequence of the higher delamination resistance exhibited by the thin-ply lay-up 1 laminate, as previously discussed, or, in other words, it may be a consequence of the higher interlaminar stresses that occur in the interfaces of the thin-ply lay-up 2 laminate.

Regarding the elastic properties of the thin-ply laminates, one can see that the laminate moduli of elasticity for the thin-ply laminates are very similar. Indeed, lay-up 1 has a laminate modulus of elasticity 5% higher than that of lay-up 2. In order to evaluate if these values differ from those calculated by lamination theory [120] using the ply properties shown in table 3.1, the software ESAComp 4.3.1 was used in the calculation of the laminate extensional, coupling, and bending stiffness matrices, $[A]$, $[B]$, and $[D]$, respectively, later used in the calculation of the laminates Young moduli and Poisson ratios. Note that, because these thin-ply laminates are not symmetric, the coupling stiffness matrices are not necessarily zero. Accordingly, the Young modulus and the Poisson ratio of an arbitrary composite laminate may be calculated as [120, 127],

$$E^L = \frac{1}{A'_{11} \cdot t} \tag{4.1}$$

$$\nu_{12}^L = -A'_{12} \cdot t \cdot E^L \tag{4.2}$$

where t is the laminate thickness, and,

$$[A'] = [A]^{-1} + [A]^{-1}[B][D^*]^{-1}[B][A]^{-1} \tag{4.3}$$

$$[D^*] = [D] - [B][A]^{-1}[B] \tag{4.4}$$

For the lay-up 1 laminate this calculation yields $E^L = 41.9$ GPa, and $\nu_{12}^L = 0.30$, a difference with respect to the experimental results of 5.2% and 10.3%, respectively. For the lay-up 2 laminate this calculation yields $E^L = 42.57$ GPa, and $\nu_{12}^L = 0.31$, a difference with respect to the experimental results of 11.2% and 26.9%, respectively. As one can see, the differences obtained for the laminates Young moduli are common regarding the scatter typical in the experimental results. The same can be concluded for the laminate Poisson ratio, since, in spite of the errors substantially higher, such large scatter is typical in the determination of this elastic property, particularly in this case, where just one specimen per laminate was used to obtain them. Still, since figures 4.1 and 4.2 indicate that the linear behavior of the specimens of each laminate before ultimate failure is almost coincident, one can admit that the instrumented specimens reasonably represent the overall elastic behavior of these laminates. Naturally, for more accurate measurements, a large number of instrumented specimens would be needed.

4.2.2. Compressive plain strength

Compressive plain strength (unnotched) tests were performed in order to evaluate the mechanical behavior of the thin-ply laminates when subjected to compressive efforts. The unnotched compressive test results for the thin-ply lay-up 1 and lay-up 2 specimens are shown in figures 4.7 and 4.8, respectively. Both stress-displacement and stress-strain relations are represented. Note that the stress-strain relations (figures 4.7b and 4.8b) of the unnotched specimens end before failure because the maximum compressive strain of the strain gages (about -7000 μm/m) was reached. Because one of the strain gages installed in the lay-up 2 instrumented specimen (AAC22) did not work, just one stress-strain relation can be observed in figure 4.8b.

As one can see in figures 4.7a and 4.8a, the stress-displacement relations for both thin-ply laminates exhibit a nonlinear behavior, suggesting that permanent damage such as matrix cracking and/or fiber kinking is developing. Observing figure 4.7b, one can see that the stress-strain relations of both strain gages in the lay-up 1 specimen have very similar behaviors, and therefore no out-of-plane bending occurred during unnotched compression testing. Based in the similarity between the stress-strain relations for the lay-up 1 specimen and that shown for the lay-up 2 specimen (figure 4.8b), it can be assumed that out-of-plane bending also did not occur in the lay-up 2 specimens.

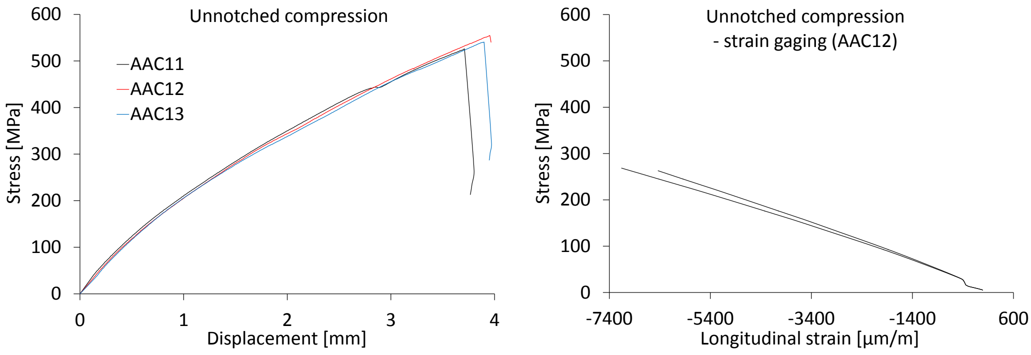

(**a**) Stress-displacement relation. (**b**) Stress-strain relation.

Fig. 4.7. Unnotched compression results for the $[(0/-45)/(90/45)]_{6T}$ specimens.

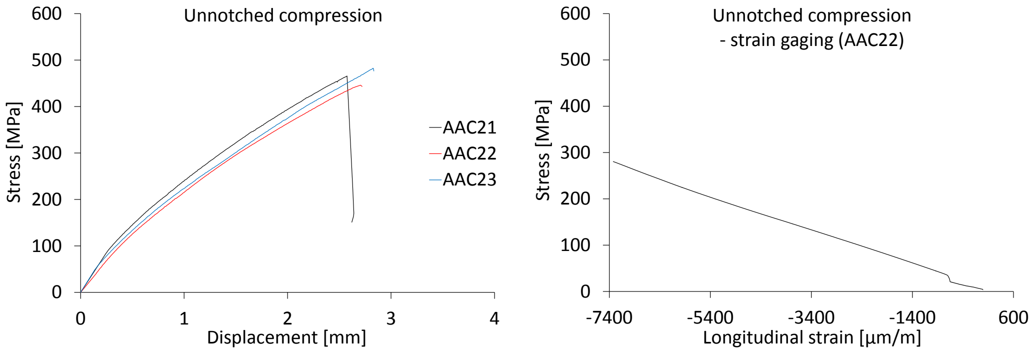

(**a**) Stress-displacement relation. (**b**) Stress-strain relation.

Fig. 4.8. Unnotched compression results for the $[(0/-45)/(45/0)/(90/45)/(-45/90)]_S$ specimens.

Figures 4.9 and 4.10 show the unnotched compression specimens after testing. Both laminates exhibit a net-section failure mode, whose failure section is perpendicular to the applied compression direction. No specimen failed in the middle section; instead, they failed between the middle section and the constrained region of the compression test rig. These results are usual when testing unnotched heterogeneous materials such as composite laminates, because the weaker section, generally characterized by a defect, where the laminate will fail, in unknown a priori.

Observing figures 4.9b and 4.10b, one can see that the fracture planes of both laminates are inclined with respect to the laminate plane, where some fiber kinking can be observed. However, the lay-up 1 laminate exhibits a more brittle failure plane, since an almost clean failure surface dominated by fiber failure can be observed in two of its specimens, including separation of the two parts of the specimens. On the other hand, the lay-up 2 specimens exhibit more irregular failure planes, dominated by fiber kinking and matrix fracture, with some fibers still connecting the two parts of the broken specimens. Such different failure behaviors result from the different lay-ups, as discussed in section 4.2.1 regarding the tensile plain strength tests. Indeed, the higher angle between layers and the ply clustering in lay-up 2 conducts to higher interlaminar stresses that precipitate failure of the laminate by other damage modes than fiber breakage, namely matrix cracking and fiber kinking, resulting in lower compressive strength, as one can see in figures 4.7a and 4.8a.

(**a**) Overview. (**b**) Close-up.

Fig. 4.9. Thin-ply $[(0/{-45})/(90/45)]_{6T}$ specimens after compressive plain strength testing.

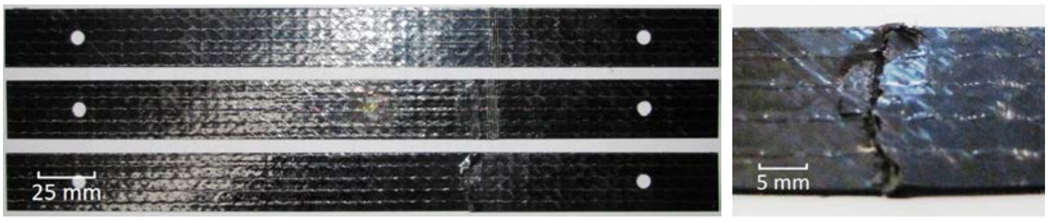

(**a**) Overview. (**b**) Close-up (specimen AAC21).

Fig. 4.10. Thin-ply $[(0/{-45})/(45/0)/(90/45)/({-45}/90)]_S$ specimens after compressive plain strength testing.

The compressive unnotched strength results, X_C^L, for the lay-up 1 and lay-up 2 specimens, and the mean values and standard deviations (STDV) for each laminate are shown in table 4.3. The compressive unnotched strength of lay-up 1 is 16.3% higher than that of lay-up 2. Therefore, one can conclude that the brittle type failure mode exhibited by lay-up 1, dominated by fiber breakage, is beneficial with respect to the laminate's compressive unnotched strength.

Tab. 4.3. Compressive unnotched strength results for the thin-ply $[(0/{-45})/(90/45)]_{6T}$ (lay-up 1) laminate and for the thin-ply $[(0/{-45})/(45/0)/(90/45)/({-45}/90)]_S$ (lay-up 2) laminate.

Laminate	Property		Test results			Mean value	STDV
Lay-up 1	X_C^L	[MPa]	525.7	554.4	540.4	540.2	11.7
Lay-up 2	X_C^L	[MPa]	465.5	445.9	482.2	464.5	14.8

4.3. Center-notched test results

4.3.1. Notched tension

The tensile fracture toughness of the thin-ply laminates under study were measured by means of notched tension (NT) testing. Figures 4.11 and 4.12 show the NT test results for both thin-ply lay-up 1 and lay-up 2 laminates. Both remote stress-displacement and remote stress-strain relations are represented. Note that the remote stress-strain relations (figures 4.11b and 4.12b) for the longitudinal deformation (ε_L) of the NT specimens end before failure because the maximum strain of the strain gages (generally around 5000 μm/m) was reached.

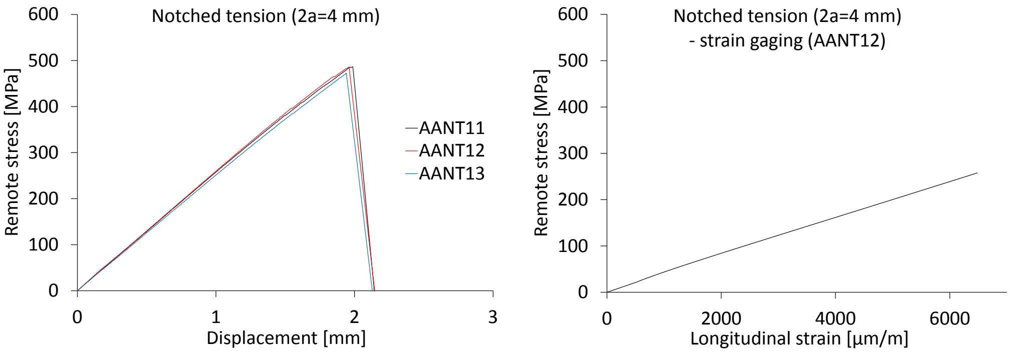

(**a**) Remote stress-displacement relation.

(**b**) Remote stress-strain relation.

Fig. 4.11. Notched tension results for the $[(0/{-45})/(90/45)]_{6T}$ specimens.

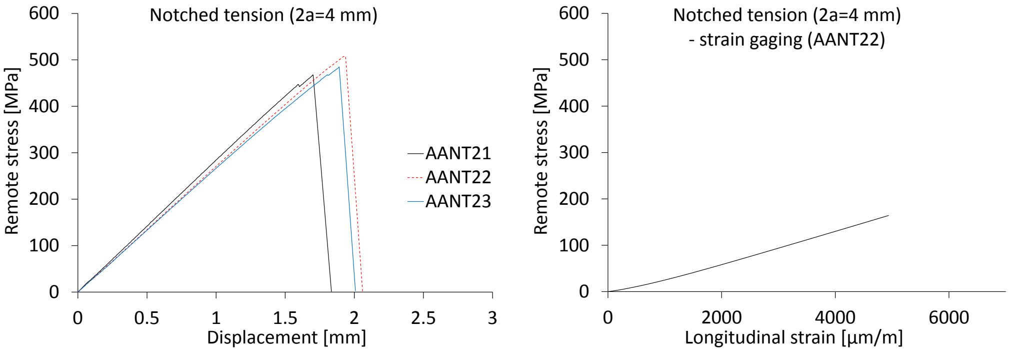

(**a**) Remote stress-displacement relation.

(**b**) Remote stress-strain relation.

Fig. 4.12. Notched tension results for the $[(0/{-45})/(45/0)/(90/45)/({-45}/90)]_S$ specimens.

Before analyse these results, it should be noted that specimen AANT22 (lay-up 2) did not fail in the notched plane. Instead it failed within both grips, and therefore its testing results are not considered in this analysis (though reported herein).

As one can see in figures 4.11a and 4.12a, the remote stress-displacement relations are approximately linear up to failure for both thin-ply laminates. Small load drops can be seen close to the peak loads (more visible for lay-up 2 specimens), with negligible effect on the stiffness of the thin-ply specimens. These small load drops indicate the development of a fracture process zone in the vicinity of the crack tip, later resulting in crack propagation and failure of the specimen. Figure 4.13 shows the lay-up 1 and lay-up 2 NT specimens in the moment before failure (image captured by the digital camera of the DIC system), where a fracture process zone is evident in the vicinity of the crack tip.

As one can see, the fracture process zone of the lay-up 2 specimen (figure 4.13b) is clearly more extensive than that of the lay-up 1 specimen (figure 4.13a). One can also note that, unlike the lay-up 1 specimen, where the fracture process zone is characterized by a small crack approximately perpendicular to the loading direction (or, in other words, parallel to the central notch), the lay-up 2 specimen exhibit a much more complex fracture process zone, with extensive fiber and matrix damage, spreading in different directions.

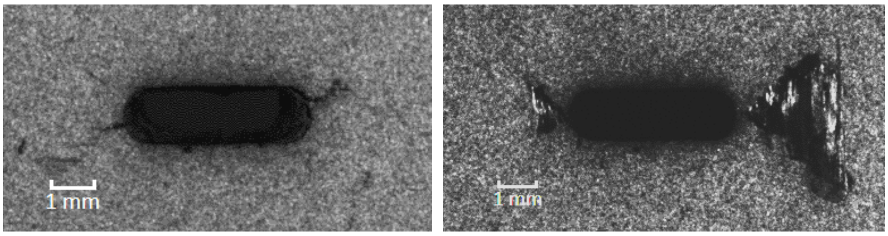

(**a**) Lay-up 1 (specimen AANT13). (**b**) Lay-up 2 (specimen AANT23).

Fig. 4.13. Thin-ply specimens in the moment before failure (images captured by the digital camera of the DIC system).

The extent of damage, in particular transverse cracking, can be further evaluated observing figures 4.14 and 4.15, where the surface longitudinal strain fields for the lay-up 1 and lay-up 2 laminates, respectively, are represented. These surface longitudinal strain fields were obtained with the DIC technique, and correspond to the moment just before failure (as shown in the images in the upper right of figures 4.14a and 4.15a). Particularly interesting are the images in the bottom right of figures 4.14a and 4.15a, which show the longitudinal strain (Eps X) along two lines near the notch tips, oriented in the loading direction. Figures 4.14b and 4.15b show the local stress-strain relation near the notch tip, as would be obtained by a strain gage.

For the lay-up 1 laminate (figure 4.14), a high strain concentration can be observed in a region confined to the notch tip, including a discontinuity in one side of the notch (blue line in the bottom right of figure 4.14a), indicating transverse cracking onset. Such discontinuity can also be observed in the local stress-strain relation near the crack tip in that side of the notch (figure 4.14b). For the lay-up 2 laminate (figure 4.15), the strain concentrations observed previously do not appear since transverse cracking already propagated beyond the reference lines, since large discontinuities can be observed in the bottom right of figure 4.15a. Due to such damage development, in figure 4.15b a stress relaxation is observed near the notch tip before failure (sudden increase of the longitudinal strain in the stress-strain relation). Such stress relaxation justifies the similar remote stress at failure observed in figures 4.11 and 4.12 for both thin-ply laminates, in spite of the higher unnotched strength exhibited by the thin-ply lay-up 1 laminate (as discussed in section 4.2.1).

The remote tensile stress at failure, $\bar{\sigma}_T^{\infty}$, and the tensile fracture toughness, K_T^L, for the lay-up 1 and lay-up 2 specimens are shown in table 4.4, as well as the mean values for each laminate and the respective standard deviations (STDV). Note that, because it is an invalid test, the remote tensile stress at failure and the tensile fracture toughness results for specimen AANT22 (lay-up 2) are not considered for the calculation of the mean values and standard deviations.

Observing table 4.4, one can see that the average remote tensile stress at failure and the average laminate tensile fracture toughness for lay-up 1 are only 1.1% higher than those of lay-up 2. As mentioned before, such results may be a consequence of the damage developed in the vicinity of the central notch before unstable crack propagation in the lay-up 2 specimens (see figure 4.13b), which is suppressed in the lay-up 1 specimens (see figure 4.13a). With the development of such damage, stresses in the vicinity of the central notch are re-

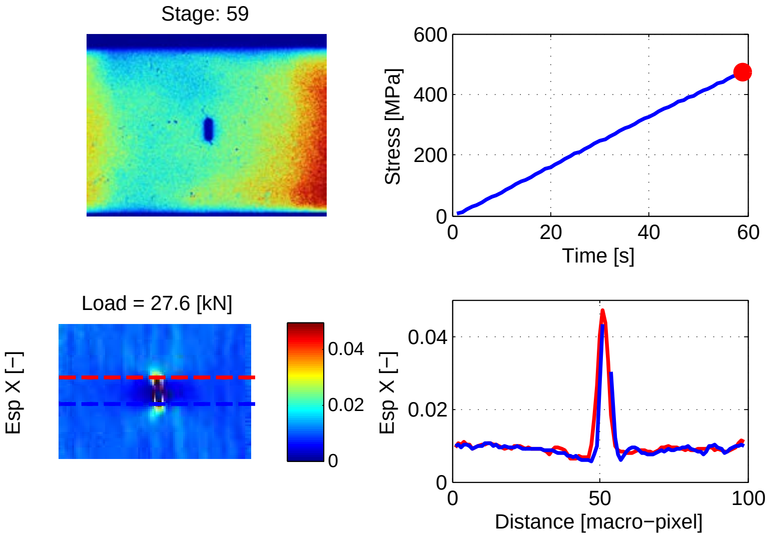

(a) Onset and propagation of transverse cracking.

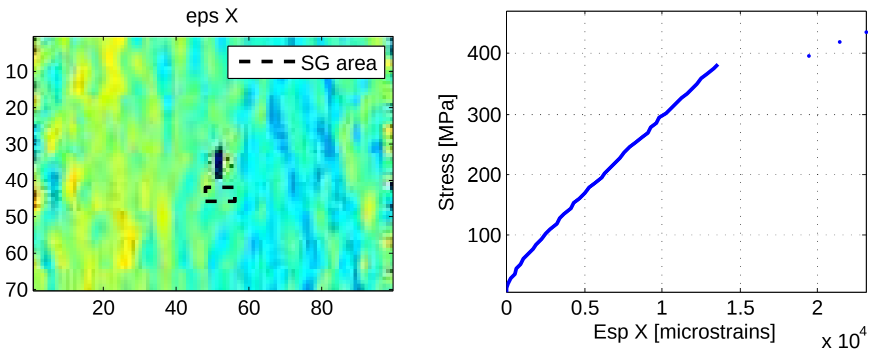

(b) Local stress-strain relation near the notch tip.

Fig. 4.14. Longitudinal strain field for the thin-ply $[(0/-45)/(90/45)]_{6T}$ center-notched specimens. The loading direction is oriented horizontally.

Tab. 4.4. Remote tensile stress at failure and tensile fracture toughness for the thin-ply $[(0/-45)/(90/45)]_{6T}$ and $[(0/-45)/(45/0)/(90/45)/(-45/90)]_S$ laminates (lay-up 1 and lay-up 2, respectively).

Laminate	Property		Test results			Mean value	STDV
Lay-up 1	$\bar{\sigma}_T^{\infty}$	[MPa]	485.9	485.7	472.0	481.2	6.5
	K_T^L	[MPa$\sqrt{\text{m}}$]	38.6	38.6	37.5	38.2	0.5
Lay-up 2	$\bar{\sigma}_T^{\infty}$	[MPa]	467.3	(507.9)	484.5	475.9	8.6
	K_T^L	[MPa$\sqrt{\text{m}}$]	37.1	(40.3)	38.5	37.8	0.7

distributed, dissipating energy and decreasing the stress concentrations, resulting in an increase of the notched strength and fracture toughness of the lay-up 2 specimens.

The mean values of the laminate tensile fracture toughness and critical energy release rate (obtained from equation (3.27)), respectively K_T^L and G_T^L, and the predictions of the tensile fracture toughness and critical energy release rate of the 0° ply calculated following

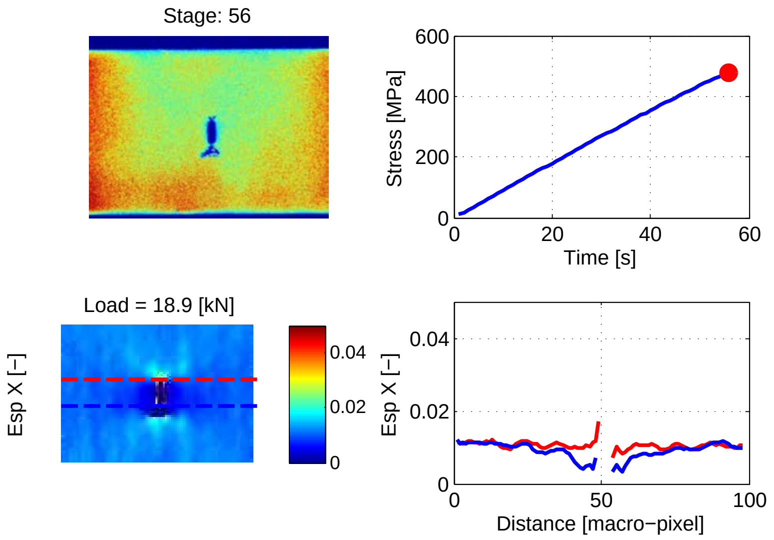

(**a**) Onset and propagation of transverse cracking.

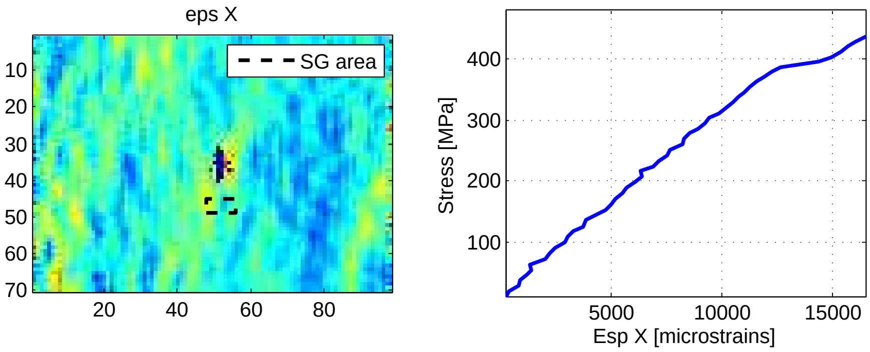

(**b**) Local stress-strain relation near the notch tip.

Fig. 4.15. Longitudinal strain field for the thin-ply $[(0/{-45})/(45/0)/(90/45)/({-45}/90)]_S$ center-notched specimens. The loading direction is oriented horizontally.

the methodology proposed by Camanho and Catalanotti [110] (see section 3.6.1), respectively K_T^0 and G_T^0, for the lay-up 1 and lay-up 2 laminates are shown is table 4.5.

Tab. 4.5. Tensile fracture toughness and critical energy release rate results for the $[(0/{-45})/(90/45)]_{6T}$ and $[(0/{-45})/(45/0)/(90/45)/({-45}/90)]_S$ (lay-up 1 and lay-up 2) thin-ply laminates, and predicted values for the 0° ply.

Laminate	K_T^L [MPa$\sqrt{\text{m}}$]	G_T^L [kJ/m^2]	K_T^0 [MPa$\sqrt{\text{m}}$]	G_T^0 [kJ/m^2]
Lay-up 1	38.2	34.3	68.3	122.2
Lay-up 2	37.8	33.6	67.5	119.7

The predictions of the tensile fracture toughness and critical energy release rate of the 0° ply for the thin-ply laminates are not far from those typically obtained for the carbon/epoxy systems used in the aircraft industry. Indeed, Camanho and Catalanotti [110], by means of compact tension tests on Hexcel IM7-8552 prepreg cross-ply laminates, obtained an initiation value of the fracture toughness of the 0° ply of G^0_{Ic} = 94.1 kJ/m^2 (K^0_{Ic} = 71.2 MPa$\sqrt{\text{m}}$), whereas the propagation value was G^0_{Ic} = 134.7 kJ/m^2 (K^0_{Ic} = 85.2 MPa$\sqrt{\text{m}}$). Note that the laminate tensile fracture toughness calculated from the center-notched tensile tests is obtained for conditions of unstable crack propagation, and therefore it may be between the laminate initiation and propagation fracture toughness, if an R-curve effect exists in the thin-ply laminates. So, since the fracture toughness of the 0°ply for the thin-ply laminates tested herein are very close or in between the initiation and propagation values obtained for the IM7-8552 carbon/epoxy system, this means that the fracture performance of these laminates is similar, and no severe notch sensitivity is observed in the thin-ply laminates, in spite of the brittle type of net-section failure mode.

The failure sections and failure modes of each specimen can be observed in figures 4.16 and 4.17, which show the failed specimens after the NT tests. Observing figure 4.16, one can see that the lay-up 1 specimens exhibit a brittle type of net-section failure mode, whose failure section is perpendicular to the applied tension direction, except for one specimen (AANT11), whose failure section is at approximately 45°. Figure 4.17 shows that the lay-up 2 specimens exhibit a failure mode characterized by some pull-out. In this case, the failure section is not so evident, since one specimen (AANT21) failed at approximately 45°, and the other exhibited a more complex failure section, with failure propagating perpendicular to the loading direction in one side of the central notch and at ±45° in the other side (inclusively, part of the specimen broke out). The different failure sections exhibited by the specimens of the same laminate results from a combination of two factors, (i) the stacking sequence (ply angles), and (ii) the unstable type of fracture typical of the NT specimens. In spite of the quasi-isotropic nature of these laminates, unstable fracture may occur predominantly in the ±45° plies and propagate in one of these directions. On the other hand, the different failure modes exhibited by the two thin-ply laminates is a result of the different stacking sequences of these laminates; in particular, it is a result of the 90° and 0° interfaces between the [0/−45] bi-layers of the lay-up 2 laminate, that originates higher interlaminar stresses and, therefore, more damage development before ply failure.

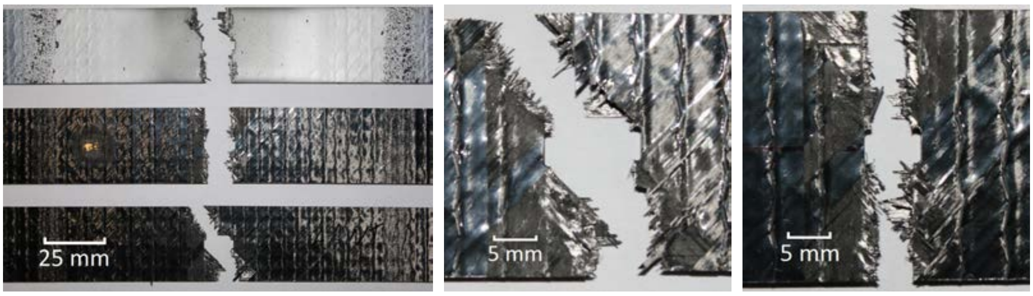

(**a**) Overview. (**b**) Specimen AANT11. (**c**) Specimen AANT12.

Fig. 4.16. Thin-ply $[(0/-45)/(90/45)]_{6T}$ specimens after center-notched tensile testing.

4.3.2. Notched compression

The compressive fracture toughness of the thin-ply laminates under study were measured by means of notched compression (NC) testing. Figures 4.18 and 4.19 show the center-notched compressive test results for both thin-ply lay-up 1 and lay-up 2 laminates. Both remote stress-displacement and remote stress-strain relations are represented.

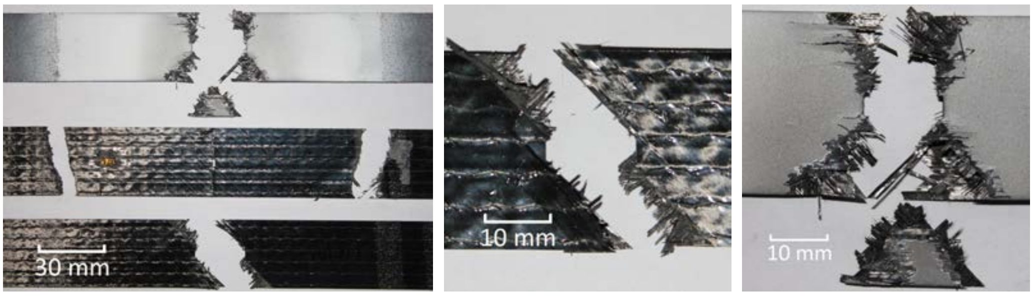

(**a**) Overview. (**b**) Specimen AANT21. (**c**) Specimen AANT23.

Fig. 4.17. Thin-ply $[(0/-45)/(45/0)/(90/45)/(-45/90)]_S$ specimens after center-notched tensile testing.

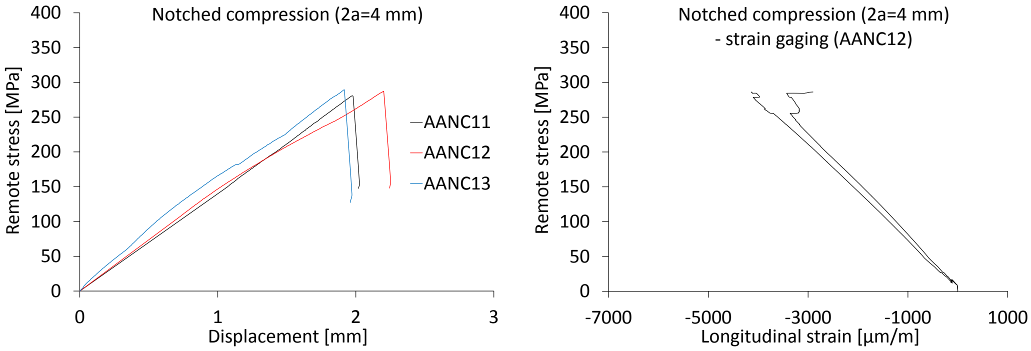

(**a**) Remote stress-displacement relation. (**b**) Remote stress-strain relation.

Fig. 4.18. Notched compression results for the $[(0/-45)/(90/45)]_{6T}$ specimens.

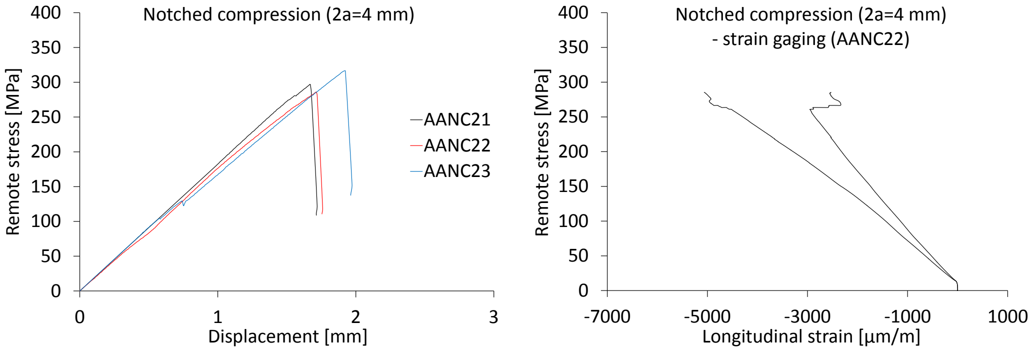

(**a**) Remote stress-displacement relation. (**b**) Remote stress-strain relation.

Fig. 4.19. Notched compression results for the $[(0/-45)/(45/0)/(90/45)/(-45/90)]_S$ specimens.

The remote stress-displacement relations are approximately linear up to failure for both thin-ply laminates. However, small load drops and some nonlinearities can be seen, in particular close to the peak loads, and generally with negligible effect on the stiffness of the thin-ply specimens. These small load drops and nonlinearities indicate the development of damage, mainly in the vicinity of the crack tip, later resulting in crack propagation and failure of the specimen.

The failure sections and failure modes of each specimen can be observed in figures 4.20 and 4.21, which show the failed specimens after the NC tests. Both thin-ply laminates exhibit a net-section failure mode, whose failure section is perpendicular to the applied compression direction. The fracture planes of both thin-ply laminates are inclined with respect to the laminate plane, as it was observed for the unnotched specimens (figures 4.9 and 4.10). Fiber kinking was observed in both laminates, though lay-up 1 exhibited a more clean fracture surface, where sometimes fiber kinking cannot be identified.

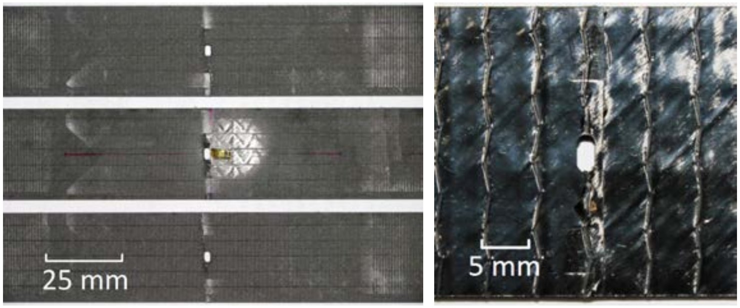

(**a**) Overview. (**b**) Specimen AANC11.

Fig. 4.20. Thin-ply $[(0/-45)/(90/45)]_{6T}$ specimens after center-notched compressive testing.

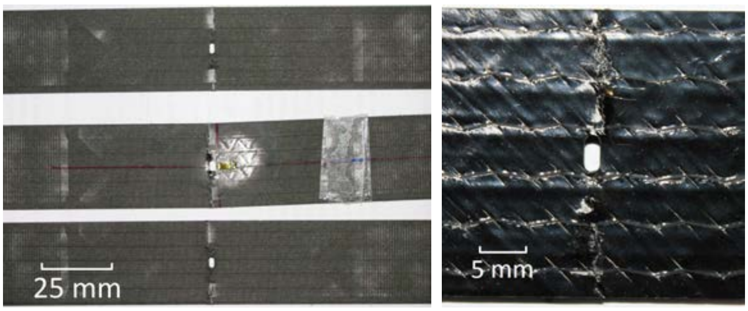

(**a**) Overview. (**b**) Specimen AANC21.

Fig. 4.21. Thin-ply $[(0/-45)/(45/0)/(90/45)/(-45/90)]_S$ specimens after center-notched compressive testing.

Table 4.6 shows the test results for the remote compressive stress at failure, $\bar{\sigma}_C^{\infty}$, and the compressive fracture toughness, K_C^L, of the lay-up 1 and lay-up 2 specimens. The mean values of the remote compressive stress at failure and compressive fracture toughness for each thin-ply laminate, and the respective standard deviations (STDV), are shown too.

Tab. 4.6. Remote compressive stress at failure and tensile fracture toughness for the thin-ply $[(0/-45)/(90/45)]_{6T}$ and $[(0/-45)/(45/0)/(90/45)/(-45/90)]_S$ laminates (lay-up 1 and lay-up 2, respectively).

Laminate	Property		Test results			Mean value	STDV
Lay-up 1	$\bar{\sigma}_C^{\infty}$	[MPa]	280.7	287.1	289.3	285.7	3.6
	K_C^L	[MPa$\sqrt{\text{m}}$]	22.3	22.8	23.0	22.7	0.3
Lay-up 2	$\bar{\sigma}_C^{\infty}$	[MPa]	296.8	285.9	316.3	299.7	12.6
	K_C^L	[MPa$\sqrt{\text{m}}$]	23.6	22.7	25.1	23.8	1.0

In spite of the higher unnotched compressive strength exhibited by lay-up 1 (see section 4.2.2), the average remote compressive stress at failure and the average laminate compressive fracture toughness for the lay-up 2 laminate are 4.9% higher than those for the lay-up 1 laminate. Such results may be a consequence of the more brittle behavior of the lay-up 1 laminate. In fact, as previously discussed, lay-up 1 exhibits a brittle failure surface, indicating that, before failure, the extent of matrix cracking and fiber kinking was very reduced, unlike lay-up 2. Note that damage mechanisms such as matrix cracking and fiber kinking are energy dissipating mechanisms, that accommodate the stresses developed before failure, increasing the compressive fracture toughness of the laminates. Precluding such damage mechanisms, as in lay-up 1, results in lower fracture toughness and, consequently, lower resistance to crack propagation (notched strength).

Following the same approach as for the NT tests, the compressive fracture toughness and critical energy release rate of the 0° ply were estimated using the methodology proposed by Camanho and Catalanotti [110] (see section 3.6.2). Table 4.7 shows the mean values of the laminate compressive fracture toughness and critical energy release rate (obtained from equation (3.27)), respectively K_C^L and G_C^L, and the predictions of the tensile fracture toughness and critical energy release rate of the 0° ply, respectively K_C^0 and G_C^0, for the lay-up 1 and lay-up 2 laminates.

Tab. 4.7. Compressive fracture toughness and critical energy release rate results for the $[(0/-45)/(90/45)]_{6T}$ and $[(0/-45)/(45/0)/(90/45)/(-45/90)]_S$ (lay-up 1 and lay-up 2) thin-ply laminates, and predicted values for the 0° ply.

Laminate	K_C^L [MPa$\sqrt{\text{m}}$]	G_C^L [kJ/m^2]	K_C^0 [MPa$\sqrt{\text{m}}$]	G_C^0 [kJ/m^2]
Lay-up 1	22.7	12.1	40.6	43.2
Lay-up 2	23.8	13.3	42.5	47.4

4.4. Open-hole test results

4.4.1. Open-hole tension

The mechanical behavior in the presence of stress concentrations and the effects of size in the thin-ply laminates when subjected to tensile efforts was evaluated by means of open-hole tension (OHT) testing. Open-hole specimens with hole diameters (d) of 3 mm, 6 mm and 10 mm were tested. The width to diameter ratio (w/d) was constant and equal to 4. Figures 4.22 to 4.27 show the OHT test results for both thin-ply lay-up 1 and lay-up 2 laminates. Both remote stress-displacement and remote stress-strain relations are represented. Note that the remote stress-strain relations (figures 4.22b to 4.27b) for the longitudinal deformation (ε_L) of the OHT specimens end before failure because the maximum strain of the strain gages (around 5000 μm/m) was reached.

Before analyse these results, it should be noted that specimen AAOHT122 (lay-up 2) did not fail in the notched plane. Instead it failed within the fixed grip, and therefore its testing results are not considered in this analysis (though reported herein).

Observing figure 4.22a, one can see that the remote stress-displacement relations for the lay-up 1 specimens with a 3 mm diameter hole are almost linear up to failure. The same can be observed for the specimens with hole diameters of 6 mm (figures 4.23a and 4.26a) and 10 mm (figures 4.24a and 4.27a). In addition, no load drops are visible in the results for these test configurations.

However, observing figure 4.25a, one can see that, for the lay-up 2 specimens with a

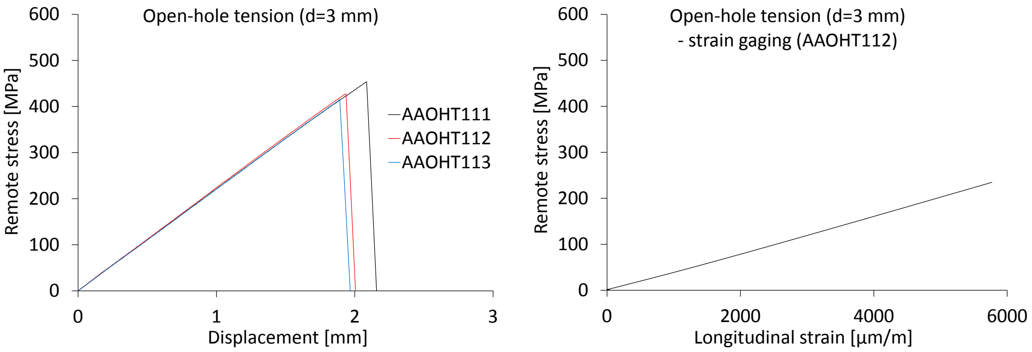

(**a**) Remote stress-displacement relation.

(**b**) Remote stress-strain relation.

Fig. 4.22. Open-hole tension results for the thin-ply $[(0/-45)/(90/45)]_{6T}$ specimens with a 3 mm diameter hole.

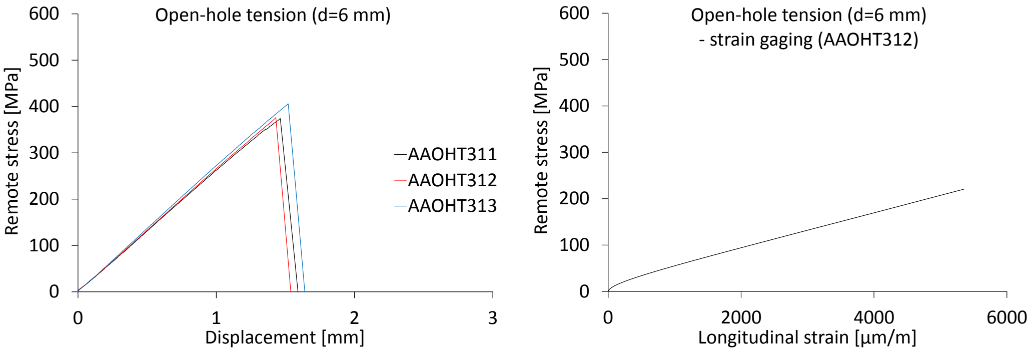

(**a**) Remote stress-displacement relation.

(**b**) Remote stress-strain relation.

Fig. 4.23. Open-hole tension results for the thin-ply $[(0/-45)/(90/45)]_{6T}$ specimens with a 6 mm diameter hole.

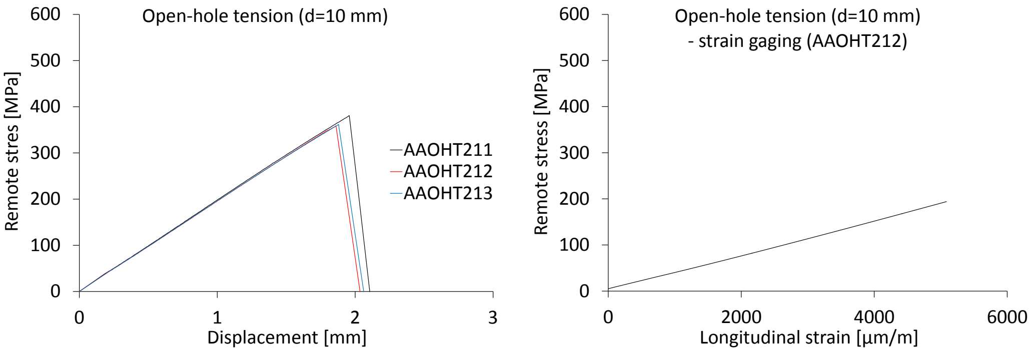

(**a**) Remote stress-displacement relation.

(**b**) Remote stress-strain relation.

Fig. 4.24. Open-hole tension results for the thin-ply $[(0/-45)/(90/45)]_{6T}$ specimens with a 10 mm diameter hole.

3 mm diameter hole, despite the approximately linear behavior up to failure of the remote stress-displacement relations, small load drops occur close to the peak loads, with negligible effect on the stiffness. These small load drops indicate the development of a fracture

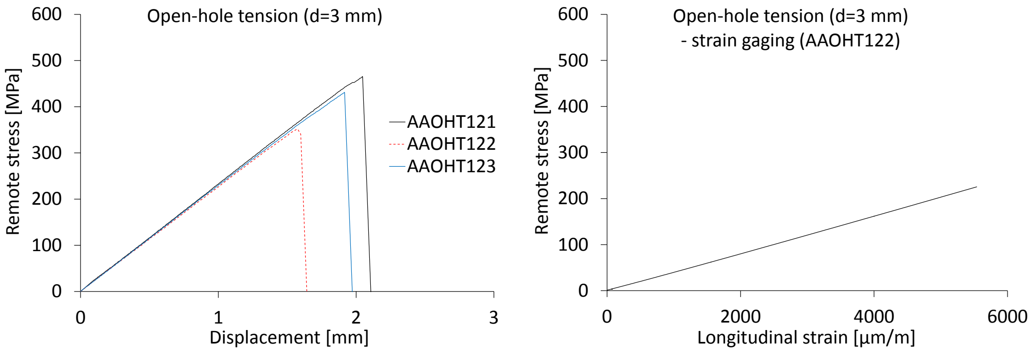

(**a**) Remote stress-displacement relation.

(**b**) Remote stress-strain relation.

Fig. 4.25. Open-hole tension results for the thin-ply $[(0/-45)/(45/0)/(90/45)/(-45/90)]_S$ specimens with a 3 mm diameter hole.

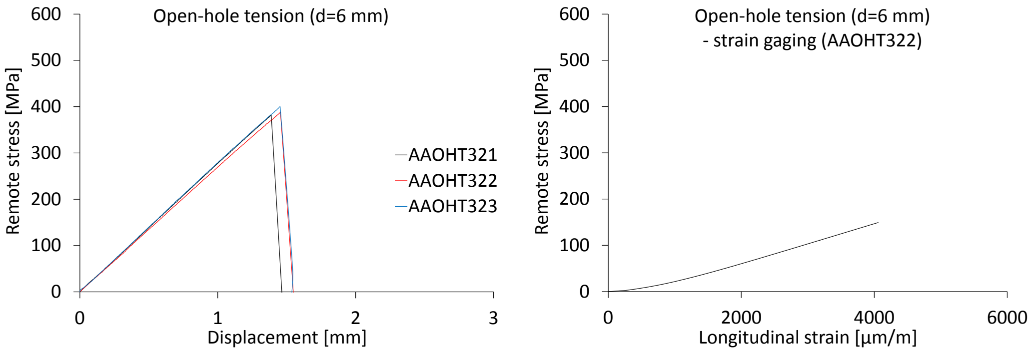

(**a**) Remote stress-displacement relation.

(**b**) Remote stress-strain relation.

Fig. 4.26. Open-hole tension results for the thin-ply $[(0/-45)/(45/0)/(90/45)/(-45/90)]_S$ specimens with a 6 mm diameter hole.

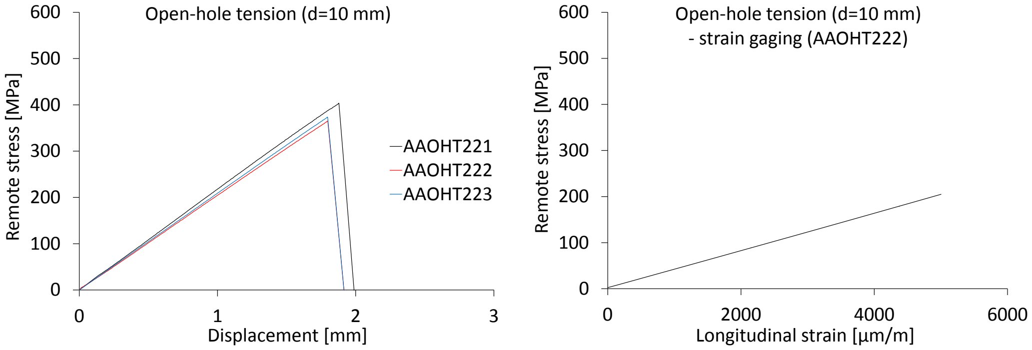

(**a**) Remote stress-displacement relation.

(**b**) Remote stress-strain relation.

Fig. 4.27. Open-hole tension results for the thin-ply $[(0/-45)/(45/0)/(90/45)/(-45/90)]_S$ specimens with a 10 mm diameter hole.

process zone near the hole (as one can see in figure 4.29a).

Figures 4.28 and 4.29 show the open-hole region of the OHT specimens in the moment before failure (images captured by the digital camera of the DIC system). For the lay-up 1 specimens (figure 4.28), no damaged zone or crack onset is visible before failure. On the other hand, for the lay-up 2 specimen with a 10 mm diameter hole, a small damaged zone, with respect to the specimen's in-plane dimensions, can be identified on the right-hand edge of the hole, as shown in figure 4.29b. However, a fracture process zone clearly developed near the hole can be observed for the lay-up 2 specimen with a 3 mm diameter hole, propagating towards the left-hand edge of the specimen (figure 4.29a). The development of such considerable damage before failure (with respect to the in-plane dimensions and hole size of the specimen) is the answer to the small load drops that occur close to the peak loads in the remote stress-displacement relations of the lay-up 2 specimens with the 3 mm diameter hole.

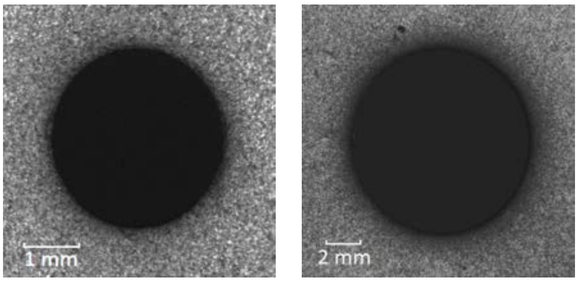

(**a**) d = 3 mm (AAOHT113). (**b**) d = 10 mm (AAOHT213).

Fig. 4.28. Open-hole thin-ply $[(0/-45)/(90/45)]_{6T}$ specimens in the moment before failure (images captured by the digital camera of the DIC system).

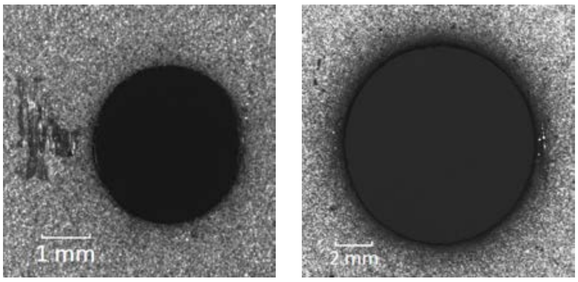

(**a**) d = 3 mm (AAOHT123). (**b**) d = 10 mm (AAOHT223).

Fig. 4.29. Open-hole thin-ply $[(0/-45)/(45/0)/(90/45)/(-45/90)]_S$ specimens in the moment before failure (images captured by the digital camera of the DIC system).

The development of damage near the holes can be further evaluated observing figures 4.30 to 4.33, where the surface longitudinal strain fields for the lay-up 1 and lay-up 2 open-hole specimens with hole diameters of 3 mm and 10 mm, obtained with the DIC technique, are represented. These results were obtained for the moment just before failure (as shown in the images in the upper right of figures 4.30a to 4.33a). Particularly interesting are the images in the bottom right of figures 4.30a to 4.33a, which show the longitudinal strain (Eps X) along two lines near the holes oriented in the loading direction. Figures 4.30b to 4.33b show the local stress-strain relation near the hole, as would be obtained by a strain gage.

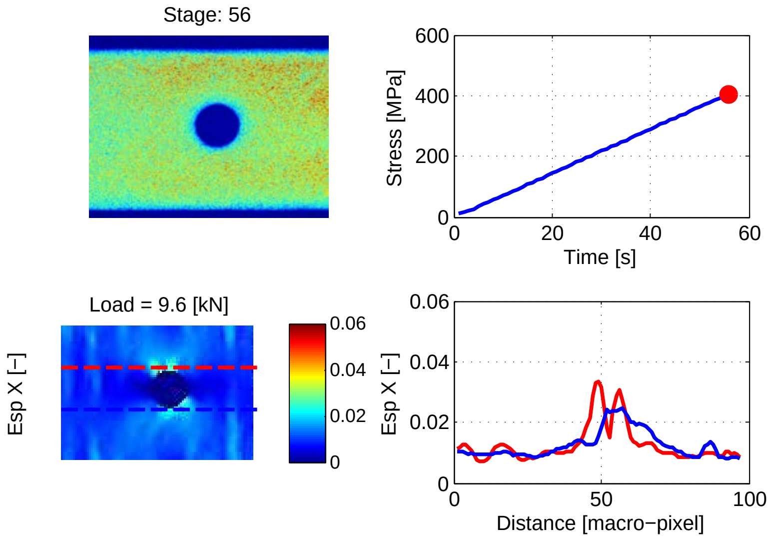

(**a**) Onset and propagation of transverse cracking.

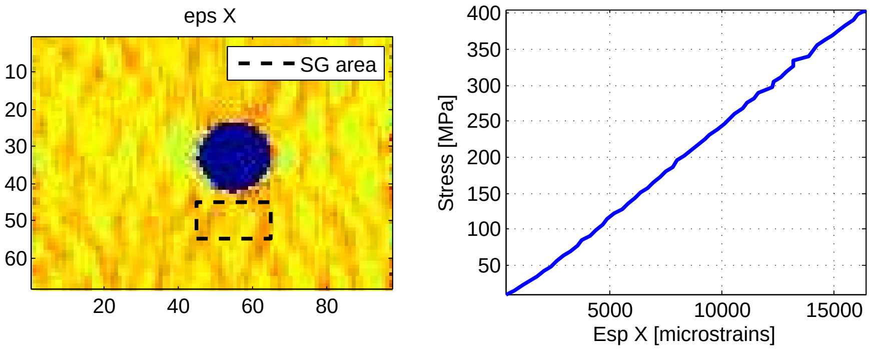

(**b**) Local stress-strain relation near the notch tip.

Fig. 4.30. Longitudinal strain field for the thin-ply $[(0/-45)/(90/45)]_{6T}$ open-hole specimens, with a 3 mm diameter hole. The loading direction is oriented horizontally.

As one can see in figures 4.30a and 4.31a (lay-up 1 and lay-up 2, respectively), the thin-ply specimens with the 3 mm diameter hole behave differently, since a substantially higher strain concentration can be observed near the hole for the lay-up 2 open-hole specimen, including a discontinuity in the strain field, associated with transverse cracking onset and propagation (as observed in figure 4.29a). Such transverse cracking near the hole is precluded by the lay-up 1 open-hole specimen with the 3 mm diameter hole. Such difference can be emphasized observing figures 4.30b and 4.31b, where, unlike the lay-up 1 open-hole specimen which exhibits an approximately linear local stress-strain relation near the hole up to failure, the lay-up 2 open-hole specimen exhibits local stress relaxation near the hole, since a sudden increase in the local strain is observed.

On the other hand, figures 4.32a and 4.33a indicate that the behavior of the thin-ply lay-up 1 and lay-up 2 specimens with the 10 mm diameter hole is not so different since

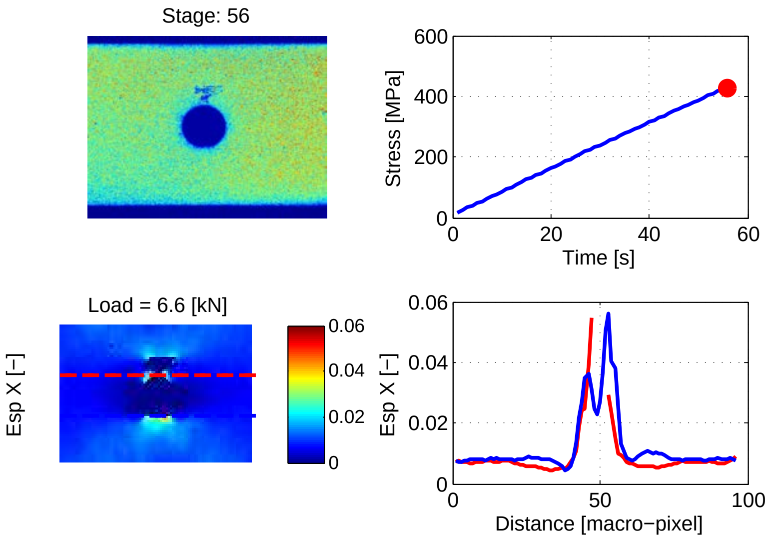

(a) Onset and propagation of transverse cracking.

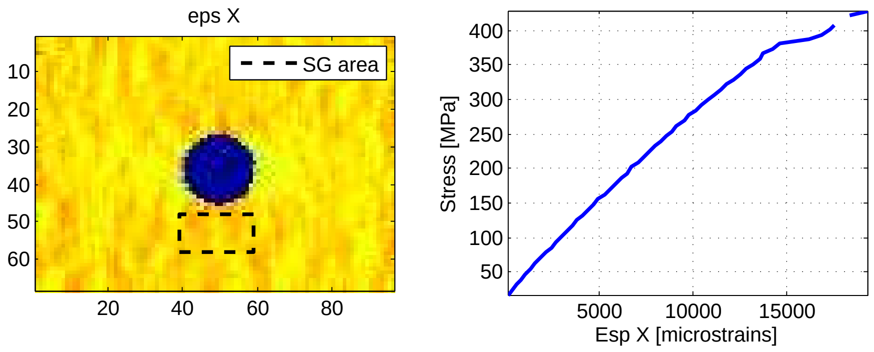

(b) Local stress-strain relation near the notch tip.

Fig. 4.31. Longitudinal strain field for the thin-ply $[(0/-45)/(45/0)/(90/45)/(-45/90)]_S$ open-hole specimens, with a 3 mm diameter hole. The loading direction is oriented horizontally.

strain concentrations are only slightly higher for the lay-up 2 open-hole specimen. Both open-hole specimens with the 10 mm diameter hole exhibit a small discontinuity in the strain field near the hole, indicating onset of transverse cracking. However, no substantial stress relaxation is observed in figures 4.32b and 4.33b for the thin-ply lay-up 1 and lay-up 2 specimens with the 10 mm diameter hole, respectively. The only thing noticeable in these local stress-strain relations is some instability near the failure stress for the lay-up 2 open-hole specimen due to the proximity of the damage zone developed near the hole before failure, as observed in figure 4.29b.

Comparing the results for the open-hole specimens with different diameter holes, one can see that the strain concentrations near the hole can be substantially higher for the smaller hole diameters. In addition, focusing in the images of the bottom left of figures 4.30 to 4.33, one can see that, though no transverse cracking was observed emanating from the free-edges, the strain field indicates that higher strain concentrations near the free-

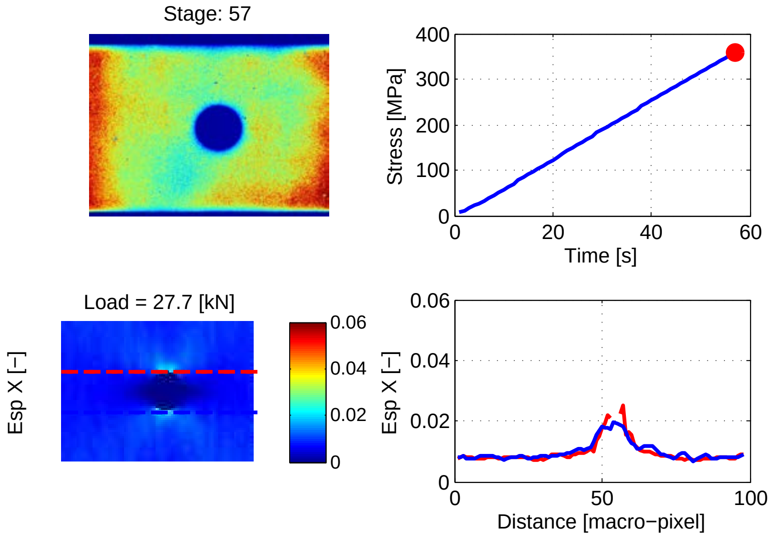

(**a**) Onset and propagation of transverse cracking.

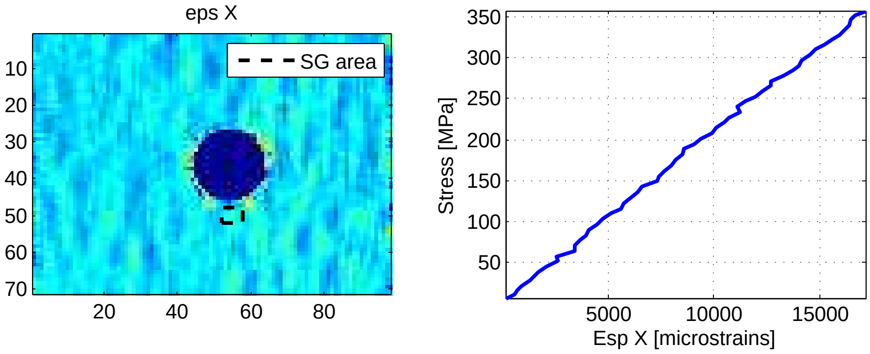

(**b**) Local stress-strain relation near the notch tip.

Fig. 4.32. Longitudinal strain field for the thin-ply $[(0/-45)/(90/45)]_{6T}$ open-hole specimens, with a 10 mm diameter hole. The loading direction is oriented horizontally.

edges are more likely to occur in the smaller specimens. Indeed, such higher strain concentrations observed in the smaller specimens are the result of their reduced dimensions. Note that, in the case of the smaller specimens, the damaged zone dimensions cannot be neglected, unlike the larger specimens, whose dimensions are generally substantially higher than those of the damaged zone.

Figures 4.34 and 4.35 show the failed OHT specimens. As one can see, both laminates exhibit a brittle type of net-section failure mode, whose failure section is perpendicular to the applied tension direction. Some pull-out is also observed in the lay-up 2 specimens, originating more irregular fracture surfaces. In practical terms, delamination is absent in both thin-ply laminates.

The remote tensile stresses at failure, $\bar{\sigma}_T^{\infty}$, for the lay-up 1 and lay-up 2 specimens are shown in table 4.8, as well as the mean values and the standard deviations (STDV). Note that, because it is an invalid test, the result for the remote tensile stress at failure for spec-

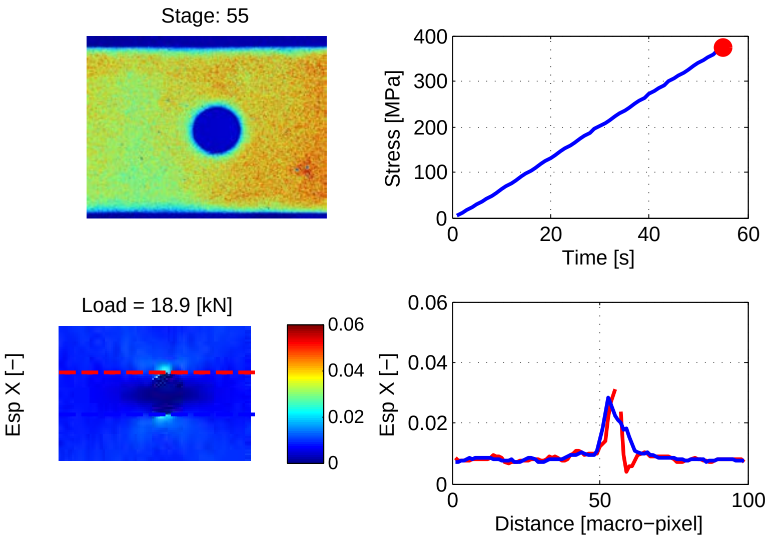

(**a**) Onset and propagation of transverse cracking.

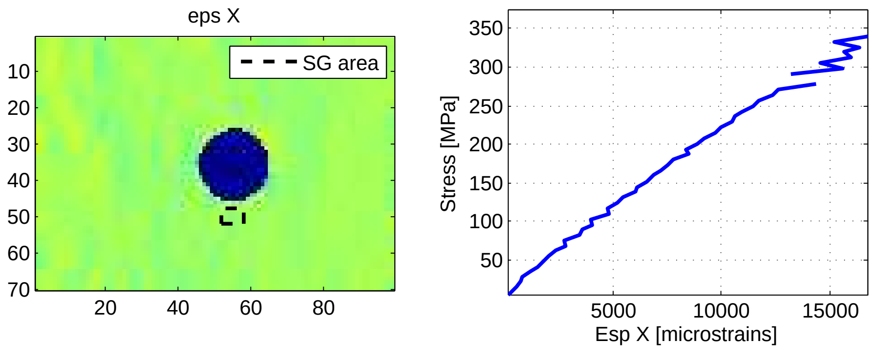

(**b**) Local stress-strain relation near the notch tip.

Fig. 4.33. Longitudinal strain field for the thin-ply $[(0/-45)/(45/0)/(90/45)/(-45/90)]_S$ open-hole specimens, with a 10 mm diameter hole. The loading direction is oriented horizontally.

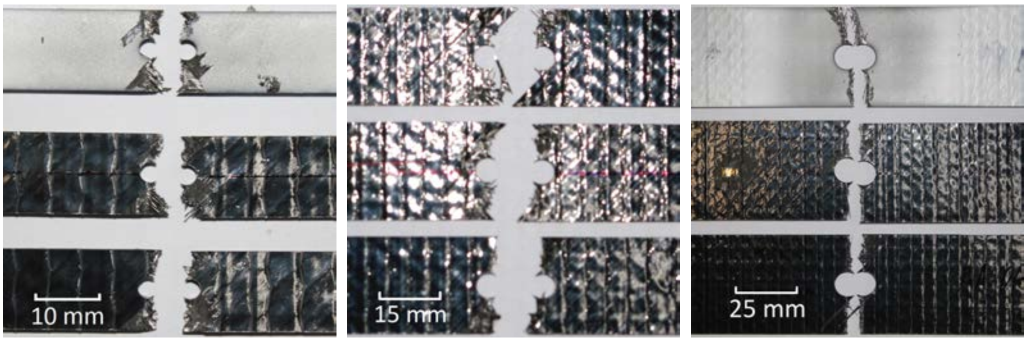

(**a**) $d = 3$ mm. (**b**) $d = 6$ mm. (**c**) $d = 10$ mm.

Fig. 4.34. Thin-ply $[(0/-45)/(90/45)]_{6T}$ (lay-up 1) specimens after the open-hole tension tests.

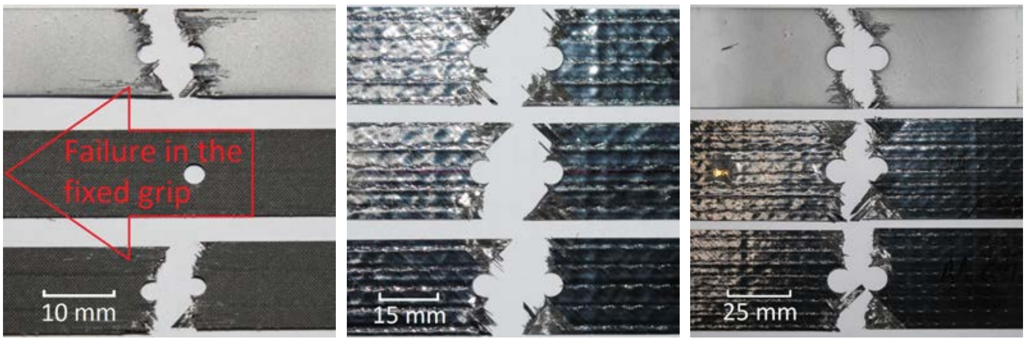

(**a**) $d = 3$ mm. (**b**) $d = 6$ mm. (**c**) $d = 10$ mm.

Fig. 4.35. Thin-ply $[(0/-45)/(45/0)/(90/45)/(-45/90)]_S$ (lay-up 2) specimens after the open-hole tension tests.

imen AAOHT122 (lay-up 2) is not considered in the calculation of the respective mean value and standard deviation.

Tab. 4.8. Remote tensile stress at failure for the thin-ply open-hole specimens.

Laminate	d [mm]	Property		Test results			Mean value	STDV
Lay-up 1	3	$\bar{\sigma}_T^\infty$	[MPa]	453.4	427.1	414.9	431.8	16.1
	6	$\bar{\sigma}_T^\infty$	[MPa]	373.7	375.6	405.5	384.9	14.6
	10	$\bar{\sigma}_T^\infty$	[MPa]	380.4	358.3	361.6	366.8	9.7
Lay-up 2	3	$\bar{\sigma}_T^\infty$	[MPa]	465.2	(351.6)	431.0	448.1	17.1
	6	$\bar{\sigma}_T^\infty$	[MPa]	382.0	387.8	399.8	389.9	7.4
	10	$\bar{\sigma}_T^\infty$	[MPa]	403.4	364.7	373.2	380.4	16.6

Unlike the tensile unnotched strength, which is 10% higher for lay-up 1 than for lay-up 2, the OHT test results show that the tensile notched strength for lay-up 2 is 1% to 4% higher than that for lay-up 1. The main cause of the opposite results observed in the unnotched and notched laminates is due to the damage developed near the hole edge of the lay-up 2 specimens before final failure, as one can see in figure 4.29. This premature damage tends to occur near the hole, mainly because of the stress concentrations at the edge of the hole. Unlike lay-up 2, where this larger fracture process zone relaxes the stress near the hole, decreasing the stress concentration, lay-up 1 suppresses such initial damage, increasing stress concentration until complete catastrophic failure.

The experimental results presented in table 4.8 also clearly identify a decrease of the tensile notched strength with the increase of the hole diameter, an effect known as "*size effect*". Increasing the hole diameter from 3 mm to 10 mm results in a decrease of the tensile notched strength of 15.1% for both thin-ply laminates. The observed size effect is caused by the development of the fracture process zone, which redistributes stresses and dissipates energy. In small specimens, the size of the fracture process zone is non-negligible when compared with the in-plane dimensions of the specimen (see, for instance, figure 4.29a), and the average stress at the fracture plane will tend to the unnotched strength of the laminate. On the other hand, in larger specimens, the relative size of the fracture process zone is very small and it is confined to the vicinity of the hole (see, for instance, figure 4.29b), resulting in a more brittle behavior.

In order to better characterize the size effect in the thin-ply laminates under study, table 4.9 shows the normalized tensile notched strengths, defined as $\bar{\sigma}_N = \bar{\sigma}_T^{\infty}/X_T^L$, where $\bar{\sigma}_T^{\infty}$ is the laminate tensile notched strength and X_T^L is the laminate unnotched strength, for both thin-ply laminates. The normalized tensile notched strengths for the T800/M21 and IM7-8552 carbon/epoxy systems, both typical of the aeronautical industry, are also presented. Two different lay-ups are considered for each alternative carbon/epoxy system.

Tab. 4.9. Identification of the size effects in the thin-ply open-hole specimens and comparison with carbon/epoxy systems typical of the aeronautical industry.

Laminate	W [mm]	d [mm]	W/d	$\bar{\sigma}_N$
Thin-ply (lay-up 1)	12	3	4	0.540
$[(0/-45)/(90/45)]_{6T}$	24	6	4	0.481
	40	10	4	0.458
Thin-ply (lay-up 2)	12	3	4	0.631
$[(0/-45)/(45/0)/(90/45)/(-45/90)]_S$	24	6	4	0.549
	40	10	4	0.536
T800/M21 (L1)	12	3	4	0.642
$[90/45/0/-45]_{3S}$	20	5	4	0.611
	28	7	4	0.573
T800/M21 (L2)	12	3	4	0.582
$[90_2/0_2/45_2/90_2/0/45/-45]_S$	20	5	4	0.552
	28	7	4	0.542
	12	2	6	0.658
IM7-8552 (L1)	24	4	6	0.569
$[90/0/45/-45]_{3S}$	36	6	6	0.519
	48	8	6	0.445
	60	10	6	0.442
	15.875	3.175	5	0.515
IM7-8552 (L2)	31.75	6.35	5	0.466
$[45/90/-45/0]_{4S}$	63.5	12.7	5	0.403
	127	25.4	5	0.356

As previously mentioned, the effect of hole size on the thin-ply laminates is very similar, with a decrease of 15.1% in the tensile notched strength when the hole diameter increases from 3 mm to 10 mm for both laminates. On the other hand, the T800/M21 L1 laminate exhibits a decrease of 10.7% in the tensile notched strength when the hole diameter increases from 3 mm to 7 mm, whereas the T800/M21 L2 laminate is the one less susceptible to the effect of size on the tensile notched strength, since a decrease of 6.8% in the tensile notched strength is observed when the hole diameter increases from 3 mm to 7 mm.

The IM7-8552 laminates seem to exhibit a pronounced hole size effect on the tensile notched strength, at least when compared with the thin-ply laminates under study and the T800/M21 laminates. For the IM7-8552 L1 laminate, a decrease of 22.3% in the tensile notched strength is observed when the hole diameter increases from 4 mm to 10 mm. Similarly, for the IM7-8552 L2 laminate, a decrease of 21.7% in the tensile notched strength is observed when the hole diameter increases from 3.175 mm to 12.7 mm. However, it should be noted that the IM7-8552 laminates were evaluated considering higher width to diameter ratios ($w/d = 6$ and $w/d = 5$, respectively), where the size effects are more pronounced.

The size effects can be further evaluated observing figure 4.36, which shows the normalized tensile notched strength as a function of the hole diameter, in both linear and logarithmic scales. The hole size effects for the thin-ply and for the T800/M21 laminates, both with a constant width to diameter ratio $w/d = 4$, can be observed. According to the available experimental data, the T800/M21 L2 laminate is the one that reveals less sensitivity to notch size changes, since the tensile notched strength decreases slightly with increasing notch size, tending to a constant value. An asymptotic behavior is also observed for both thin-ply laminates, however characterized by a more pronounced decrease of the normalized tensile notched strengths for the smaller hole diameters. On the other hand, the experimental results available for the T800/M21 L1 laminate do not evidence such asymptotic behavior, and an approximately linear decrease of the normalized tensile notched strength with increasing hole diameters is observed. Further understanding of the relations between the normalized tensile notched strengths and the hole diameters will be the main focus of chapter 5, where closed-form semi-empirical and analytical models will be used to assess the size effects on these laminates.

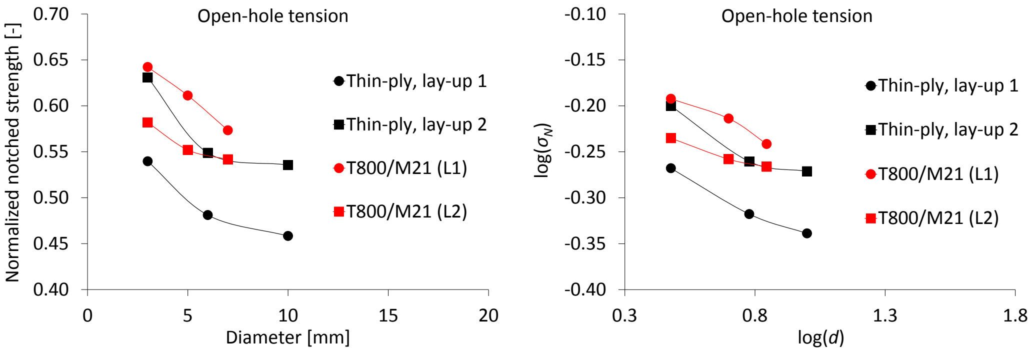

(**a**) Linear scale. (**b**) Logarithmic scale.

Fig. 4.36. Identification of the size effects in the thin-ply open-hole specimens and comparison with the T800/M21 laminates.

Observing table 4.9 and figure 4.36, one can also conclude about the notch sensitivity of these laminates. Since the normalized notched strength directly relates the tensile notched and unnotched strengths of a laminate, the lower this parameter is, the higher the notch sensitivity of the laminate. So, since the thin-ply lay-up 1 laminate exhibits, for the same hole diameter and for the same width to diameter ratio, lower normalized notched strengths than the thin-ply lay-up 2 laminate and than both T800/M21 laminates, the thin-ply lay-up 1 laminate is considered to be the most notch sensitive of these laminates. In turn, the thin-ply lay-up 2 laminate shows higher normalized notched strengths than the T800/M21 L2 laminate, and therefore it is less notch sensitive than the last one. Finally, one can see that the T800/M21 L1 laminate is the least notch sensitive of these laminates.

To further evaluate the notch sensitivity of these laminates, figure 4.37 shows the normalized tensile notched strength, $\bar{\sigma}_N$, as a function of the d/w ratio. This figure also includes the boundaries for a notch-sensitive material, whose normalized strength is a function of the stress concentration factor K_T ($\bar{\sigma}_N = 1/K_T$), and the predictions for a notch-insensitive material, whose normalized strength is a function of the geometry, particularly of the width to hole diameter ratio ($\bar{\sigma}_N = 1 - d/W$) (for more details, see chapter 5). The data points closer to the notch sensitive boundary are the corresponding to the larger hole diameters (as indicated).

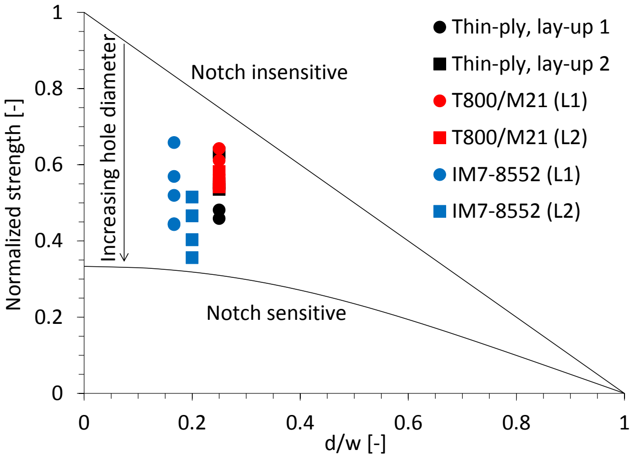

Fig. 4.37. Analysis of the notch sensitivity of the thin-ply laminates, and comparison with the T800/M21 and IM7-8552 alternative laminates.

Indeed, the IM7-8552 L2 laminate exhibits the highest notch sensitivity, followed by the IM7-8552 L1 laminate, and by the thin-ply lay-up 1 laminate. The T800/M21 L1 laminate is the less notch sensitive one, followed closely by the thin-ply lay-up 2 laminate, and by the T800/M21 L2 laminate.

However, two aspects should be noted. The first one is that, for the same hole diameter, increasing the d/w ratio should decrease the normalized notched strength of a given laminate. Therefore, when analysing the notch sensitivity, the IM7-8552 laminates take advantage of a lower d/w ratio (or higher w/d ratio). On the other hand, a second aspect persists, since in this analysis, the laminate thickness effect is not taken into account. According to Green et al. [82], independently of the laminate stacking sequence, an increase in the laminate thickness with constant hole diameter leads to a decrease in failure stress, which approaches a constant value as thickness increases. Therefore, careful must be taken when analysing these results. For instance, lay-up 2 may be benefiting of its lower laminate thickness, whereas the high notch sensitivity of the IM7-8552 L2 laminate may result from its higher laminate thickness. Nevertheless, in the following analyses carried out in this thesis, these results will be taken as preliminary reference values, since no other results are available in the literature regarding size effects on thin-ply laminates, always keeping in mind that further investigations may be conducted in order to clarify these preliminary results.

4.4.2. Open-hole compression

Open-hole compression (OHC) tests were carried out with the purpose to evaluate the mechanical behavior of thin-ply laminates when subjected to compressive efforts in the presence of stress concentrations, and quantify the size effects. Open-hole specimens with hole diameters (d) of 2 mm, 5 mm and 7 mm were tested. The width to diameter ratio (w/d) was constant and equal to 4. Figures 4.38 to 4.43 show the OHC test results for both thin-ply $[(0/-45)/(90/45)]_{6T}$ (lay-up 1) and $[(0/-45)/(45/0)/(90/45)/(-45/90)]_{S}$ (lay-up 2) specimens. Both remote stress-displacement and remote stress-strain relations are represented. Note that the two remote stress-strain relations shown for each laminate and specimen geometry were obtained by two strain gages both oriented in the load direction but installed in opposite faces of the specimen (as described in section 3.7.2). This configuration was adopted to assess the occurrence of out-of-plane bending during the compression tests.

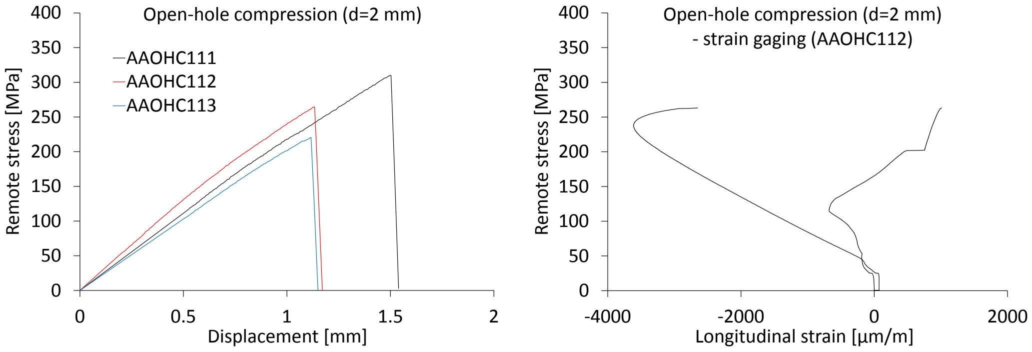

(**a**) Remote stress-displacement relation. (**b**) Remote stress-strain relation.

Fig. 4.38. Open-hole compression results for the thin-ply $[(0/-45)/(90/45)]_{6T}$ specimens (lay-up 1) with a 2 mm diameter hole.

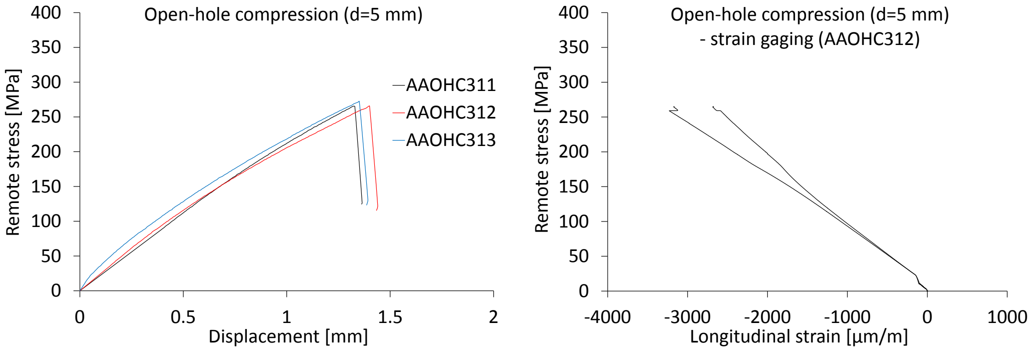

(**a**) Remote stress-displacement relation. (**b**) Remote stress-strain relation.

Fig. 4.39. Open-hole compression results for the thin-ply $[(0/-45)/(90/45)]_{6T}$ specimens (lay-up 1) with a 5 mm diameter hole.

As one can see, the remote stress-displacement relations for the lay-up 1 specimens (figures 4.38a to 4.40a) show a nonlinear behavior. For the lay-up 2 specimens (figures 4.41a to 4.43a), nonlinearity is also observed in the remote stress-displacement relations, particularly just before failure. These nonlinear responses exhibited by both thin-ply laminates may result from the development of damage such as matrix cracking and/or fiber kinking (see an example in figure 4.44 for the lay-up 1 specimen AAOHC213), and also from overall buckling phenomena.

On the other hand, observing figures 4.38a to 4.40a, no load drops can be identified in the remote stress-displacement relations of the lay-up 1 specimens. However, observ-

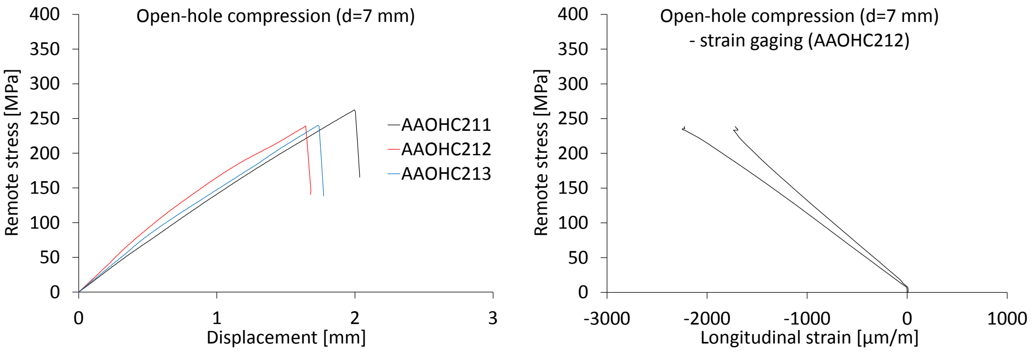

(a) Remote stress-displacement relation.

(b) Remote stress-strain relation.

Fig. 4.40. Open-hole tension results for the thin-ply $[(0/-45)/(90/45)]_{6T}$ specimens (lay-up 1) with a 7 mm diameter hole.

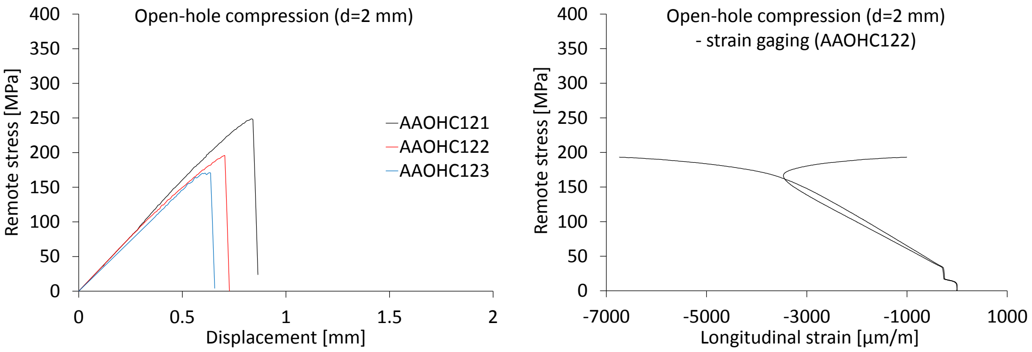

(a) Remote stress-displacement relation.

(b) Remote stress-strain relation.

Fig. 4.41. Open-hole tension results for the thin-ply $[(0/-45)/(45/0)/(90/45)/(-45/90)]_S$ specimens (lay-up 2) with a 2 mm diameter hole.

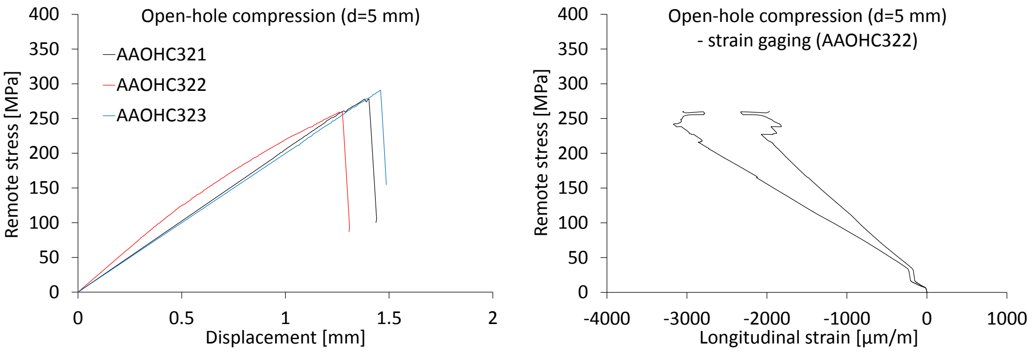

(a) Remote stress-displacement relation.

(b) Remote stress-strain relation.

Fig. 4.42. Open-hole tension results for the thin-ply $[(0/-45)/(45/0)/(90/45)/(-45/90)]_S$ specimens (lay-up 2) with a 5 mm diameter hole.

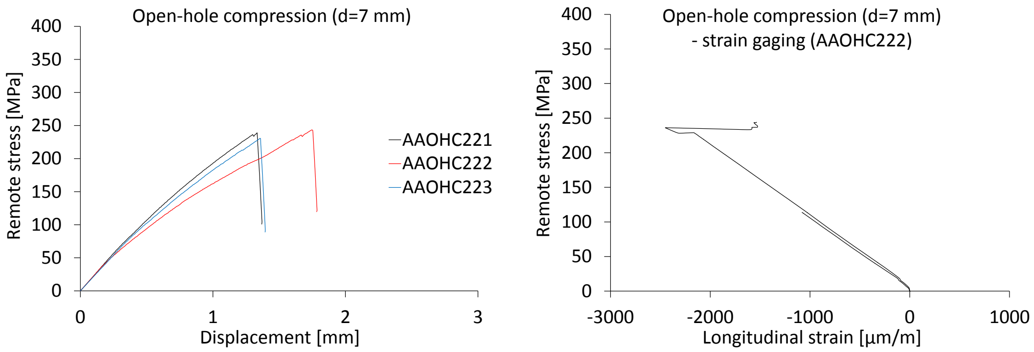

(**a**) Remote stress-displacement relation. (**b**) Remote stress-strain relation.

Fig. 4.43. Open-hole tension results for the thin-ply $[(0/-45)/(45/0)/(90/45)/(-45/90)]_S$ specimens (lay-up 2) with a 7 mm diameter hole.

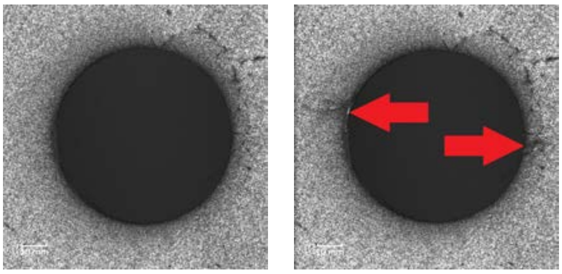

(**a**) Before OHC testing. (**b**) Moment before failure.

Fig. 4.44. Open-hole thin-ply $[(0/-45)/(90/45)]_{6T}$ (lay-up 1) AAOHC213 specimen in the beginning of the OHC test and in the moment before failure (images captured by the digital camera of the DIC system).

ing figures 4.41a to 4.43a, small load drops can be clearly identified in the remote stress-displacement relations of the lay-up 2 specimens, for all test configurations (hole sizes). As one can see, such load drops occur close to the peak loads, with negligible effect on the stiffness of the lay-up 2 specimens, indicating that damage is developing, particularly in the vicinity of the notch. Since lay-up 1 does not exhibit such small load drops, at this stage one can assume that noncritical damage, such as matrix cracking and fiber kinking, appears earlier in the lay-up 2 laminate, being almost nonexistent in the lay-up 1 laminate (it may develop just before failure). These different behaviors result in a higher compressive toughness for the lay-up 2 laminate, as discussed previously (section 4.3.2), and may conduct to a higher notch sensitivity for the lay-up 1 specimen.

The development of damage near the holes can be further evaluated observing figures 4.45 to 4.48, where the surface longitudinal strain fields for the lay-up 1 and lay-up 2 open-hole specimens with hole diameters of 2 mm and 7 mm, obtained with the DIC technique, are represented. These results were obtained for the moment just before failure (as shown in the images in the upper right of figures 4.45 to 4.48). Particularly interesting are the images in the bottom right of these figures, which show the longitudinal strain (Eps X) along two lines near the holes oriented in the loading direction.

Figures 4.45 and 4.46 show that the thin-ply open-hole specimens with the 2 mm di-

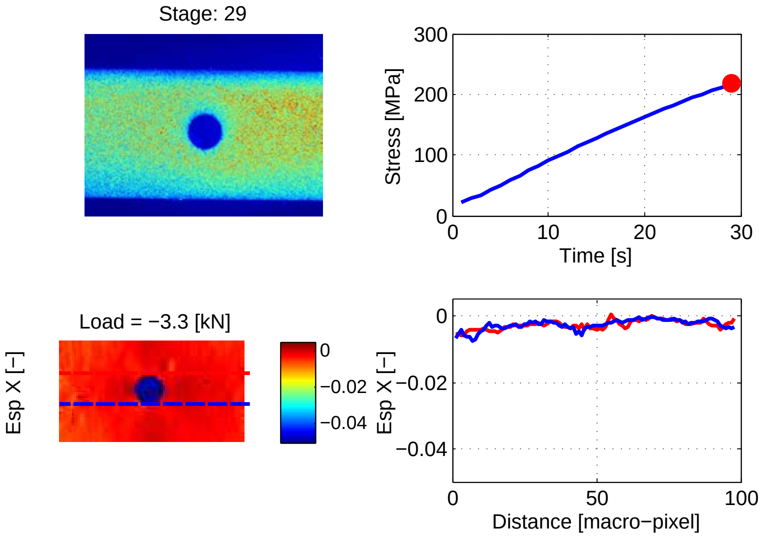

Fig. 4.45. Longitudinal strain field for the thin-ply $[(0/-45)/(90/45)]_{6T}$ open-hole specimens, with a 2 mm diameter hole. The compressive loading direction is oriented horizontally.

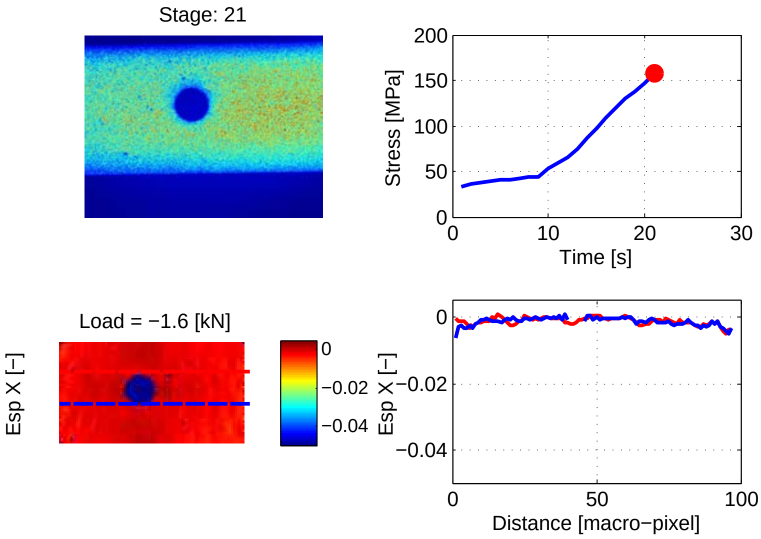

Fig. 4.46. Longitudinal strain field for the thin-ply $[(0/-45)/(45/0)/(90/45)/(-45/90)]_S$ open-hole specimens, with a 2 mm diameter hole. The compressive loading direction is oriented horizontally.

ameter hole virtually do not exhibit damage near the hole before failure. On the other hand, observing figures 4.47 and 4.48, one can see that the thin-ply open-hole specimens with the 7 mm diameter hole exhibit strain concentrations near the hole, as it would be expected. In particular, the lay-up 1 open-hole specimen with the 7 mm diameter hole shows a discontinuity in the strain field near the hole, indicating transverse damage onset (as shown in figure 4.44). As it will be discussed, the absence of damage in the smaller open-hole specimens is the result of premature failure due to out-of-plane bending (overall buckling phenomenon), invalidating any comparison between the damage development in

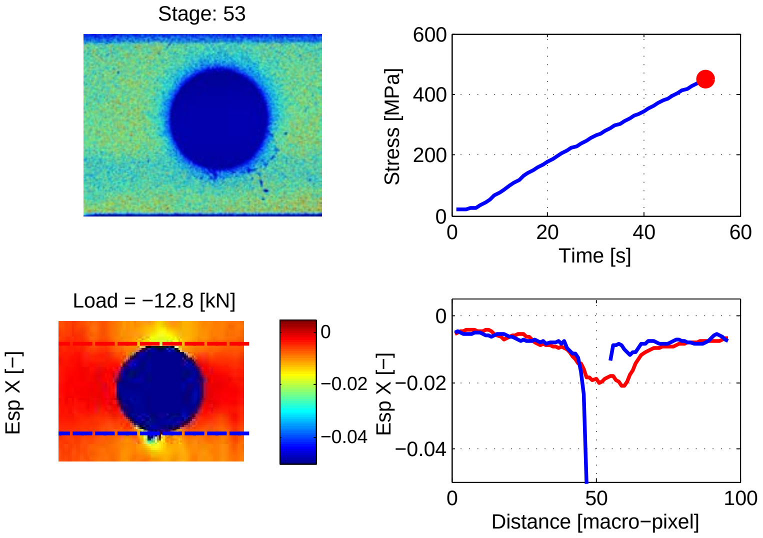

Fig. 4.47. Longitudinal strain field for the thin-ply $[(0/-45)/(90/45)]_{6T}$ open-hole specimens, with a 7 mm diameter hole. The compressive loading direction is oriented horizontally.

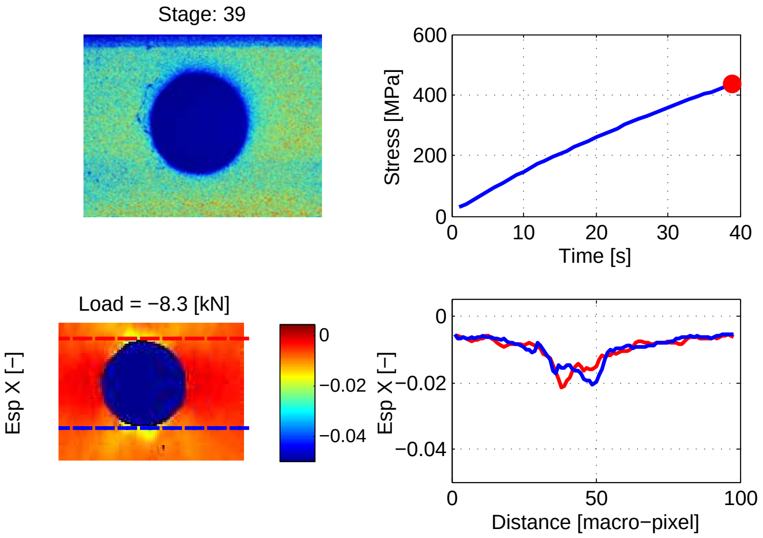

Fig. 4.48. Longitudinal strain field for the thin-ply $[(0/-45)/(45/0)/(90/45)/(-45/90)]_S$ open-hole specimens, with a 7 mm diameter hole. The compressive loading direction is oriented horizontally.

the smaller specimens and in the larger specimens.

Figures 4.49 and 4.50 show the failed OHC specimens. As one can see, in all thin-ply specimens the failure section is perpendicular to the applied compressive load direction, and no relevant difference is observed. Both thin-ply laminates show some splitting, and delamination is almost absent.

Observing the remote stress-strain relations, one can see that, for the lay-up 1 laminate (figure 4.38b), the results for the two strain gages, placed longitudinally in opposite faces of the specimen, show substantially different paths. In fact, the remote stress-strain

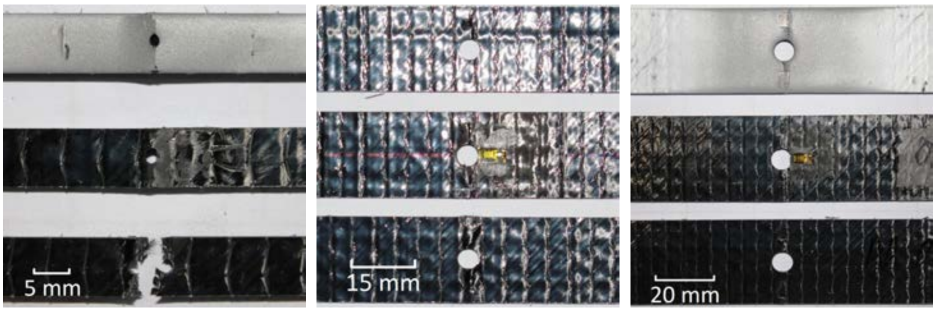

(**a**) $d = 2$ mm. (**b**) $d = 5$ mm. (**c**) $d = 7$ mm.

Fig. 4.49. Thin-ply $[(0/-45)/(90/45)]_{6T}$ (lay-up 1) specimens after the open-hole compression tests.

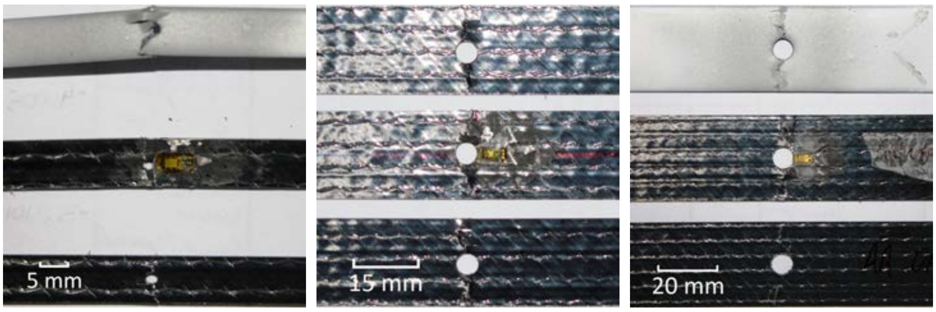

(**a**) $d = 2$ mm. (**b**) $d = 5$ mm. (**c**) $d = 7$ mm.

Fig. 4.50. Thin-ply $[(0/-45)/(45/0)/(90/45)/(-45/90)]_S$ (lay-up 2) specimens after the open-hole compression tests.

relation for one of the strain gages shows positive strain values, whereas the other shows negative strain values, a clear sign of the introduction of out-of-plane bending (buckling) in the window area of the anti-buckling rig, virtually since the beginning of the OHC test. For the lay-up 2 laminate (figure 4.41b), one can see that, in spite of the initial similarity of the remote stress-strain relations (which means that pure compressive efforts were occurring), there is a sudden variation of the strain values of the two strain gages, in opposite directions, just before failure. Such behavior is also a clear sign of the occurrence of out-of-plane bending in the window area of the anti-buckling rig, conducting to early failure of the specimen.

Note that the occurrence of out-of-plane bending in the window area of the anti-buckling rig in the specimens with a 2 mm diameter hole is the result of two factors. The first one is the small thickness of the thin-ply laminates under study (about 2.0 mm and 1.3 mm thick for the lay-up 1 and lay-up 2 laminates, respectively), which promotes instabilities during compressive loading resulting in buckling phenomena. The second factor is the small width of these specimens, whose sides are not supported by the anti-buckling rig (see figure 3.9b), making it ineffective to completely avoid out-of-plane bending.

On the other hand, the results for the specimens with hole diameters of 5 mm and 7 mm do not indicate the occurrence of buckling phenomena. The remote stress-strain relations for these hole sizes keep the negative strain values throughout the tests. Note, however, that one of the strain gages of the lay-up 2 specimen (AAOHC222, figure 4.43b) failed earlier than expected, around the −1000 μm/m, and no results until failure were available; still, one can assume that its path would not change substantially, and that out-of-plane bending did not occur.

The overall buckling phenomena that occurred in the specimens with a 2 mm diameter hole naturally has consequences in the results of the OHC tests. Such consequences are visible in table 4.10, which shows the remote compressive stresses at failure, $\bar{\sigma}_C^\infty$, for the lay-up 1 and lay-up 2 specimens, as well as the mean values and the standard deviations (STDV).

Tab. 4.10. Remote compressive stress at failure for the thin-ply open-hole specimens.

Laminate	d [mm]	Property		Test results			Mean value	STDV
Lay-up 1	2	$\bar{\sigma}_C^\infty$	[MPa]	(309.6)	(264.1)	(220.2)	(264.6)	(36.5)
	5	$\bar{\sigma}_C^\infty$	[MPa]	265.5	265.6	272.3	267.8	3.2
	7	$\bar{\sigma}_C^\infty$	[MPa]	262.3	239.0	240.0	247.1	10.8
Lay-up 2	2	$\bar{\sigma}_C^\infty$	[MPa]	(248.7)	(195.5)	(171.0)	(205.1)	(32.4)
	5	$\bar{\sigma}_C^\infty$	[MPa]	277.9	259.7	290.5	276.0	12.6
	7	$\bar{\sigma}_C^\infty$	[MPa]	238.8	243.5	230.4	237.6	5.4

According to these results, for the thin-ply lay-up 1 laminate, increasing the hole diameter from 2 mm to 7 mm results in a decrease of the compressive notched strength of 6.6%. And, unlike what would be expected, for the thin-ply lay-up 2 laminate, increasing the hole diameter from 2 mm to 7 mm results in an increase of the compressive notched strength of 15.8%. Notoriously, the compressive notched strengths of the thin-ply laminates with a 2 mm diameter hole were considerably affected by the buckling phenomena that occurred, and therefore no conclusive analysis about the size effects can be made based on these results. Accordingly, the results for the thin-ply laminates with a 2 mm diameter hole are considered invalid in this analysis.

Taking into account the test results for the specimens with hole diameters of 5 mm and 7 mm, one can see that increasing the hole diameter from 5 mm to 7 mm results in a decrease of the compressive notched strength of 7.8% and 14.0%, for the lay-up 1 and lay-up 2 laminates, respectively. Therefore, the hole size effect under compression appears to be more pronounced in the lay-up 2 laminate than in the lay-up 1 laminate, contrary to what was observed for the hole size effect under tension, where no relevant difference was observed (see section 4.4.1).

Observing table 4.10, one can also see that, for a hole diameter of 5 mm, the compressive notched strength for lay-up 1 is 3.0% lower than that of lay-up 2, whereas for a hole diameter of 7 mm, the compressive notched strength for lay-up 1 is 3.8% higher than that of lay-up 2. Note that the compressive unnotched strength for lay-up 1 was 16.3% higher than that for lay-up 2. So, in spite of the higher compressive unnotched strength observed for the lay-up 1 laminate, these thin-ply laminates may behave similarly under compressive efforts when in the presence of a notch, and therefore lay-up 1 may be considered more notch sensitive than lay-up 2.

In order to better characterize the effect of hole size in the notched compressive behavior of the thin-ply laminates under study and their notch sensitivity, table 4.11 shows the normalized compressive notched strengths, defined as $\bar{\sigma}_N = \bar{\sigma}_C^\infty / X_T^L$, where $\bar{\sigma}_C^\infty$ is the laminate compressive notched strength and X_C^L is the laminate compressive unnotched strength, for both thin-ply laminates, and for the the T800/M21 and the IM7-8552 carbon/epoxy systems. The results for two T800/M21 laminates (L1 and L2) and for one IM7-8552 laminate (L1) are presented.

Tab. 4.11. Identification of the size effects in the notched compressive behavior of thin-ply open-hole specimens and comparison with carbon/epoxy systems typical of the aeronautical industry.

Laminate	W [mm]	d [mm]	W/d	$\bar{\sigma}_N$
Thin-ply (lay-up 1)	8	2	4	(0.490)
$[(0/-45)/(90/45)]_{6T}$	20	5	4	0.496
	28	7	4	0.457
Thin-ply (lay-up 2)	8	2	4	(0.441)
$[(0/-45)/(45/0)/(90/45)/(-45/90)]_S$	20	5	4	0.594
	28	7	4	0.511
T800/M21 (L1)	12	3	4	0.620
$[90/45/0/-45]_{3S}$	20	5	4	0.516
	28	7	4	0.481
T800/M21 (L2)	12	3	4	0.646
$[90_2/0_2/45_2/90_2/0/45/-45]_S$	20	5	4	0.596
	28	7	4	0.563
	12	2	6	0.719
IM7-8552 (L1)	18	3	6	0.700
$[90/0/45/-45]_{3S}$	24	4	6	0.685
	30	5	6	0.668

As one can see, for a width to diameter ratio equal to 4 and for hole diameters of 5 mm and 7 mm, the thin-ply lay-up 2 laminate seems to be the one that exhibits the most pronounced hole size effect, with a decrease of the compressive notched strength of 14.0% when the hole diameter increases from 5 mm to 7 mm (as mentioned before). For the T800/M21 L1 laminate, increasing the hole diameter from 5 mm to 7 mm results in a decrease of the compressive notched strength of 7.3% (similar to that of the thin-ply lay-up 1 laminate, 7.8%), whereas for the T800/M21 L2 laminate increasing the hole diameter from 5 mm to 7 mm results in a decrease of the compressive notched strength of 5.5% (laminate less sensitive to variations of the hole size). Regarding the IM7-8552 L1 laminate, a decrease of the compressive notched strength of 7.1% is observed when the hole diameter increases from 2 mm to 5 mm. Since the available test data refers to hole diameters between 2 mm and 5 mm, and no experimental results are available for a hole diameter of 7 mm, it is difficult to understand if the IM7-8552 L1 laminate is more or less sensitive to variations of the hole size. In addition, the available test data is for a width to diameter ratio equal to 6, instead of 4 as the previous laminates.

The size effects can also be visually identified observing figure 4.51, which shows the normalized compressive notched strength as a function of the hole diameter, in both linear and logarithmic scales. The results for the thin-ply and for the T800/M21 laminates, both with a constant width to diameter ratio $w/d = 4$, are represented. As one can see, the T800/M21 L2 laminate is the one that reveals less sensitivity to the size of the notch, with the lowest decrease of the compressive notched strength with increasing hole diameters. Then, at least for hole diameters of 5 mm and 7 mm, the T800/M21 L1 laminate shows approximately the same behavior of the thin-ply lay-up 1 laminate. Finally, one can see that, for hole diameters of 5 mm and 7 mm, the thin-ply lay-up 2 laminate shows the highest decrease of the compressive notched strength with increasing hole diameters, i.e., the more pronounced size effect. Further understanding of the relations between the normalized compressive notched strengths and the hole diameters will be the main focus of chapter 5, where closed-form semi-empirical and analytical models will be used to assess the size effects on these laminates.

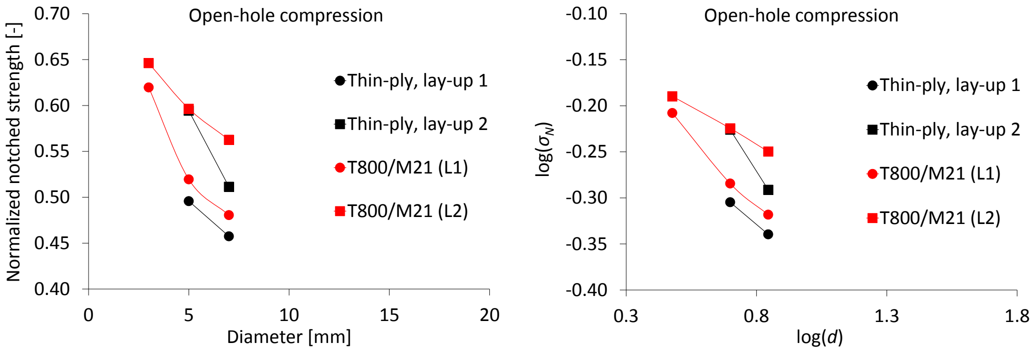

(**a**) Linear scale. (**b**) Logarithmic scale.

Fig. 4.51. Identification of the size effects in the thin-ply open-hole specimens subjected to compressive efforts, and comparison with the T800/M21 laminates.

Regarding the notch sensitivity, observing table 4.11 and figure 4.51 one can see that, for the same hole diameter and width to diameter ratio, the thin-ply lay-up 1 laminate exhibits lower normalized compressive notched strengths than the thin-ply lay-up 2 laminate and than both T800/M21 laminates. Therefore it is considered the most notch sensitive of these four laminates. In turn, the thin-ply lay-up 2 laminate shows higher normalized compressive notched strengths than the T800/M21 L1 laminate, and therefore it is less notch sensitive than the last one. Finally, one can see that the T800/M21 L2 laminate is the least notch sensitive of these laminates.

To further evaluate the notch sensitivity of these laminates, figure 4.52 shows the normalized compressive notched strength, $\bar{\sigma}_N$, as a function of the d/w ratio. This figure also includes the boundaries for a notch-sensitive material, whose normalized strength is a function of the stress concentration factor K_T ($\bar{\sigma}_N = 1/K_T$), and the predictions for a notch-insensitive material, whose normalized strength is a function of the geometry, particularly of the width to hole diameter ratio ($\bar{\sigma}_N = 1 - d/W$) (for more details, see chapter 5). The data points closer to the notch sensitive boundary are the corresponding to the larger hole diameters (as indicated).

In spite of the higher width to diameter ratio (or lower d/w ratio), figure 4.52 indicates that the IM7-8552 L1 laminate is the less notch sensitive of the analysed laminates, when subjected to compressive efforts. A more detailed analysis is performed in chapter 5, where the relations between the normalized notched strength and the d/w ratio for different hole diameters are predicted using closed-form semi-empirical and analytical models. The notch sensitivity of these laminates is assessed in detail through the construction of design charts with such relations.

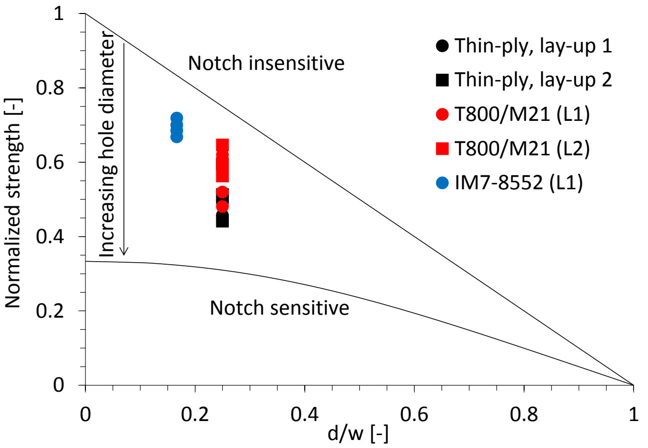

Fig. 4.52. Analysis of the notch sensitivity of the thin-ply laminates subjected to compressive efforts, and comparison with the T800/M21 and IM7-8552 alternative laminates.

4.5. Bearing test results

Bolt-bearing tests were performed according to ASTM D 5961 standard [124] to evaluate the mechanical behavior of the thin-ply laminates when subjected to local compressive efforts, typical of mechanically fastened joints. This local compressive strength, or bearing strength, is extremely important when studying the structural integrity of a composite laminate, due to the extensive use of this kind of joints, particularly in the aircraft industry.

For the bolt-bearing tests performed in this thesis, and as it would be expected, the bearing failure mode was observed in all specimens, as one can see in figure 4.53. A close-up to the bearing hole after testing is shown in figure 4.54, where no relevant difference between failure modes on both thin-ply laminates is observed.

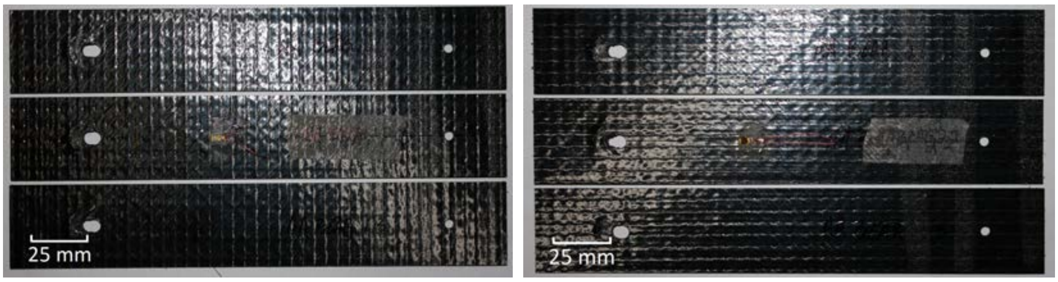

(**a**) Thin-ply $[(0/-45)/(90/45)]_{6T}$ specimens.

(**b**) Thin-ply $[(0/-45)/(45/0)/(90/45)/(-45/90)]_S$ specimens.

Fig. 4.53. Bearing test specimens after testing.

The bearing test results for the lay-up 1 and lay-up 2 specimens are shown in figures 4.55 and 4.56, respectively. Both bearing stress-displacement and bearing stress-strain relations for each thin-ply laminate are represented. A good repeatability of the bearing tests can be observed.

Figures 4.55a and 4.56a show that the bearing stress-displacement relations are ap-

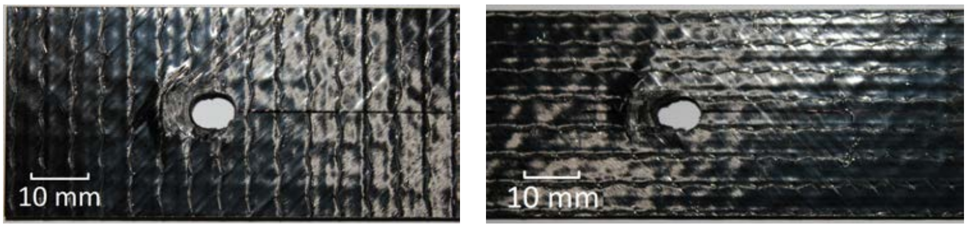

(**a**) Thin-ply $[(0/{-45})/(90/45)]_{6T}$ specimen (AABEAR12).

(**b**) Thin-ply $[(0/{-45})/(45/0)/(90/45)/({-45}/90)]_S$ specimen (AABEAR22).

Fig. 4.54. Close-up to the bearing hole of two specimens after testing.

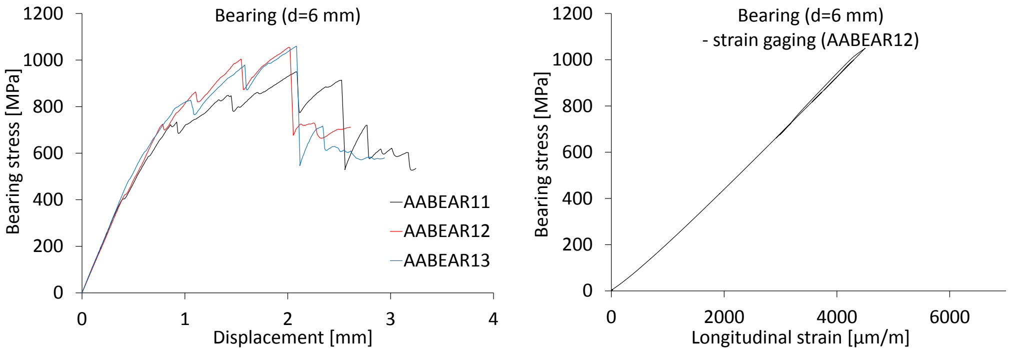

(**a**) Bearing stress-displacement relation.

(**b**) Bearing stress-strain relation.

Fig. 4.55. Bearing results for the thin-ply $[(0/{-45})/(90/45)]_{6T}$ specimens (lay-up 1).

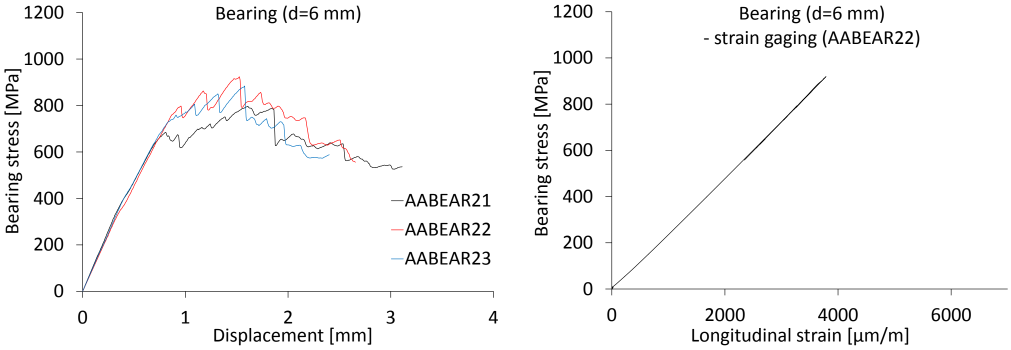

(**a**) Bearing stress-displacement relation.

(**b**) Bearing stress-strain relation.

Fig. 4.56. Bearing results for the thin-ply $[(0/{-45})/(45/0)/(90/45)/({-45}/90)]_S$ specimens (lay-up 2).

proximately linear only up to around 50% of the maximum bearing stress, exhibiting a nonlinear behavior after that point. Indeed, such nonlinear behavior was also observed in the compression tests discussed previously, and it is related with the onset of noncritical damage before permanent damage occur. On the other hand, a linear behavior can be observed in the bearing stress-strain relations shown in figures 4.55b and 4.56b for both thin-ply laminates, even during remote loading-unloading caused by damage evolution in the bearing hole. These results mean that the specimens regions far from the bearing hole show a linear-elastic behavior, independently of the damage observed in the bearing hole.

The bearing strengths obtained for lay-up 1 and lay-up 2 specimens are shown in table 4.12, as well as the mean values for each laminate and the standard deviations (STDV). As previously mentioned in section 3.8, three definitions of the bearing strength are considered, namely the maximum bearing stress ($\bar{\sigma}^b_{\text{max}}$), the bearing stress at the first load drop ($\bar{\sigma}^b_{\text{1st load drop}}$), and the bearing stress corresponding to an offset bearing strain of 2% ($\bar{\sigma}^b_{\text{offset 2\%}}$).

Tab. 4.12. Bearing strengths for the thin-ply laminates.

Laminate	Property		Test results			Mean value	STDV
Lay-up 1	$\bar{\sigma}^b_{\text{max}}$	[MPa]	949.9	1054.7	1059.2	1021.3	50.5
	$\bar{\sigma}^b_{\text{1st load drop}}$	[MPa]	733.5	724.3	827.1	761.6	46.5
	$\bar{\sigma}^b_{\text{offset 2\%}}$	[MPa]	508.7	604.3	614.6	575.8	47.7
Lay-up 2	$\bar{\sigma}^b_{\text{max}}$	[MPa]	796.7	923.1	883.3	867.7	52.8
	$\bar{\sigma}^b_{\text{1st load drop}}$	[MPa]	684.4	797.2	805.3	762.3	55.2
	$\bar{\sigma}^b_{\text{offset 2\%}}$	[MPa]	539.5	592.5	595.0	575.7	25.6

As one can see, these three definitions give considerably different bearing strength values. It can be observed that the mean maximum bearing stress is 34% and 14% greater than the mean bearing stress at the first load drop for the lay-up 1 and lay-up 2 laminates, respectively. This difference is typical of bolt bearing tests due to the lateral support imposed by the bolt/nut assembly. However, this definition, also called *ultimate bearing stress* [124], is scarcely used for design.

On the other hand, the mean bearing stress at the first load drop, or *initial peak bearing strength* [124], is 32% greater than the mean bearing stress corresponding to an offset bearing strain of 2% for both thin-ply laminates. These two definitions can be associated to the initiation of irreversible damage in the bearing hole, and therefore both are typically used in composite joints design. The difference observed in these values is due to the nonlinearity of the upper region of the bearing stress-displacement relation before the first load drop (see figures 4.55a and 4.56a). Such nonlinearity is generally related with onset of matrix cracking and fiber kinking in the bearing region. However, these damage mechanisms only start to interact for bearing stresses greater than the initial peak bearing strength, forming through-the-thickness shear cracks whose propagation, after this point, conducts to sudden load drops [122]. Therefore, the bearing stress at the first load drop is considered, in this analysis, as the design bearing strength.

Table 4.12 also shows that the mean values of the bearing strength when calculated as the bearing stress at the first load drop, $\bar{\sigma}^b_{\text{1st load drop}}$, or as the bearing stress corresponding to an offset bearing strain of 2%, $\bar{\sigma}^b_{\text{offset 2\%}}$, for both laminates are very similar (they differ less than 0.1%), whereas when calculated as the maximum bearing stress, $\bar{\sigma}^b_{\text{max}}$, it is higher for lay-up 1; indeed, all specimens of the thicker lay-up 1 exhibited higher maximum bearing stress than the specimens of the thinner lay-up 2. Such results mean that, before and during onset of permanent damage in the bearing hole, both thin-ply laminates behave very similarly, and therefore they exhibit the same damage resistance. However, the thicker lay-up 1 exhibit higher resistance to damage propagation in the bearing region than the thinner lay-up 2, and consequently higher ultimate bearing strength. This may be a consequence of the different thicknesses between this two laminates; because lay-up 2 is thinner, after damage onset the reduction of stiffness is more relevant, conducting to higher instabilities in the damaged bearing region and, consequently, resulting in a resistance to damage propagation lower than that of the thicker lay-up 1.

In order to compare the bearing behavior of the thin-ply laminates with that exhibited by a laminate typically used in aeronautical construction, figure 4.57 shows the relations between the normalized bearing stress, defined as $\sigma_N^b = \sigma^b / X_C^L$, where σ^b is the bearing stress and X_C^L is the compressive unnotched strength, and the displacement for both thin-ply laminates tested during this work and for the IM7-8552 carbon/epoxy $[90/0/45/\text{-}45]_{3S}$ laminate.

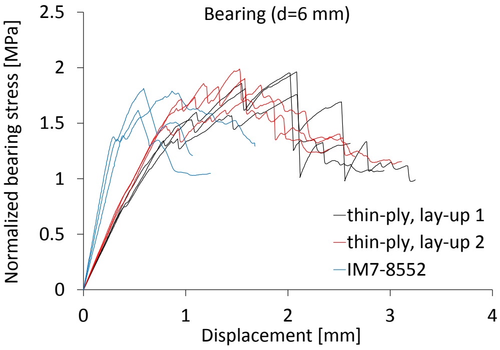

Fig. 4.57. Normalized bearing stress-displacement relations for the thin-ply laminates and for the IM7-8552 $[90/0/45/\text{-}45]_{3S}$ laminate.

Table 4.13 shows the mean maximum normalized bearing stress, the mean normalized bearing stress at the first load drop, and the mean normalized bearing stress corresponding to an offset bearing strain of 2% for both thin-ply laminates and for the IM7-8552 carbon/epoxy $[90/0/45/\text{-}45]_{3S}$ laminate.

Tab. 4.13. Normalized bearing strengths for both thin-ply laminates and for the IM7-8552 $[90/0/45/\text{-}45]_{3S}$ laminate.

Laminate		$\bar{\sigma}^b_{N\,\mathrm{max}}$	$\bar{\sigma}^b_{N\,\mathrm{1st\ load\ drop}}$	$\bar{\sigma}^b_{N\,\mathrm{offset\ 2\%}}$
Thin-ply	$[(0/-45)/(90/45)]_{6T}$	1.891	1.410	1.066
Thin-ply	$[(0/-45)/(45/0)/(90/45)/(-45/90)]_S$	1.868	1.641	1.239
IM7-8552	$[90/0/45/\text{-}45]_{3S}$	1.738	1.372	1.367

Observing figure 4.57 and table 4.13, one can see that the differences between the maximum bearing stresses of the thin-ply laminates is mainly due to the higher compressive unnotched strength of the lay-up 1 laminate, since very similar normalized maximum bearing stresses are obtained. However, the normalized bearing stress at the first load drop is clearly higher for the thin-ply lay-up 2 laminate (16.4% grater than that for the lay-up 1 laminate), indicating that this laminate has substantial better performance than the thin-ply lay-up 1 laminate.

Regarding the IM7-8552 laminate, one can see that its bearing behavior is worst than that exhibited by both thin-ply laminates. The thin-ply lay-up 1 laminate shows a normalized bearing stress at the first load drop 2.8% greater than that exhibited by the IM7-8552 laminate, whereas the thin-ply lay-up 2 laminate shows a normalized bearing stress at the first load drop 19.6% greater than that exhibited by the IM7-8552 laminate. Even with respect to the normalized maximum bearing stress, one can see that the thin-ply laminates are superior to the IM7-8552 laminate, since the normalized maximum bearing stress values are 8.8% and 7.4% higher than that of the IM7-8552 laminate. This improved performance of the thin-ply laminates comparatively to the IM7-8552 laminate may result from the ability of the thin-ply laminates to block onset and propagation of damage mechanisms such as delamination, fiber kinking, matrix cracking, and through-the-thickness shear cracking.

Note also that, generally, there is a size effect related with the bearing strength of composite laminates. Indeed, with increasing laminate thickness, the bearing strength tends to increase too. So, taking into account that the IM7-8552 laminate is thicker that the thin-ply laminates studied in this thesis, it is clear that, for the same thickness, the differences in these results would be even more pronounced. Therefore, such results, in particular the results obtained for the thin-ply lay-up 2 laminate, are very interesting, because clearly highlight an advantage of using thin-ply laminates in composites structural design. However, with respect to possible future works to validate this preliminary results, the effect of ply thickness on the bolt-bearing resistance can only be objectively evaluated by means of an experimental program on laminates with the same fiber/matrix system, the same laminate thickness, and different ply thicknesses, which was not the case in this work.

4.6. Over-height compact tension test results

Over-height compact tension (OCT) tests, based on the work developed at the University of British Columbia [107], and complemented with an anti-buckling support, as proposed by Li et al. [108], were employed to assess the translaminar fracture toughness of the thin-ply $[(0/-45)/(90/45)]_{6T}$ (lay-up 1) and $[(0/-45)/(45/0)/(90/45)/(-45/90)]_S$ (lay-up 2) composite laminates. Although this test configuration was chosen to avoid extraneous failure modes, in particular overall buckling of the specimens during testing, all lay-up 2 specimens considerably buckled, and no crack propagation was observed. Figure 4.58 shows a typical specimen of each laminate during OCT testing.

Crack propagation can be clearly identified in the lay-up 1 specimen (figure 4.58a), whereas significant overall buckling is shown for the lay-up 2 specimen, despite the use of the anti-buckling support (figure 4.58b). This buckling phenomenon results from the low thickness of the lay-up 2 laminate (about 1.3 mm), that easily promotes such instabilities. Still, this phenomenon also indicates that the fracture toughness of the lay-up 2 laminate is not so low as it would be for a material with severe notch sensitivity, since in that case the crack would propagate.

Figure 4.59 shows the load-displacement relations for both thin-ply laminates. For the thin-ply lay-up 1 specimens, figure 4.59a, the load-displacement relations are approximately linear up to the point of first load drop, at approximately 90% of the peak load. Crack propagation across the width occurs in discrete jumps. However, for the lay-up 2 specimens, figure 4.59b, substantially nonlinear load-displacement relations are observed, which tend to an approximately constant value. Such nonlinear response is a result of the nonlinear buckling phenomenon that occurred in these specimens, as previously mentioned.

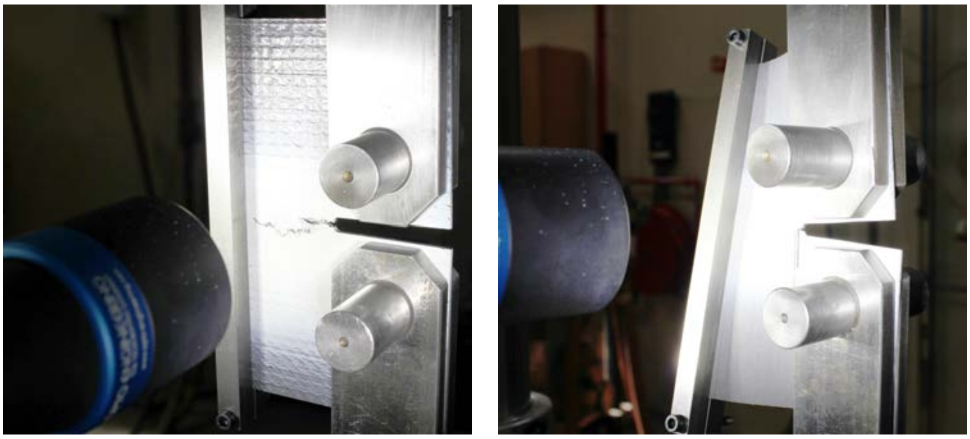

(**a**) Thin-ply $[(0/{-45})/(90/45)]_{6T}$ specimen (AAOCT13).

(**b**) Thin-ply $[(0/{-45})/(45/0)/(90/45)/({-45}/90)]_S$ specimen (AAOCT21).

Fig. 4.58. Thin-ply specimens during over-height compact tension testing.

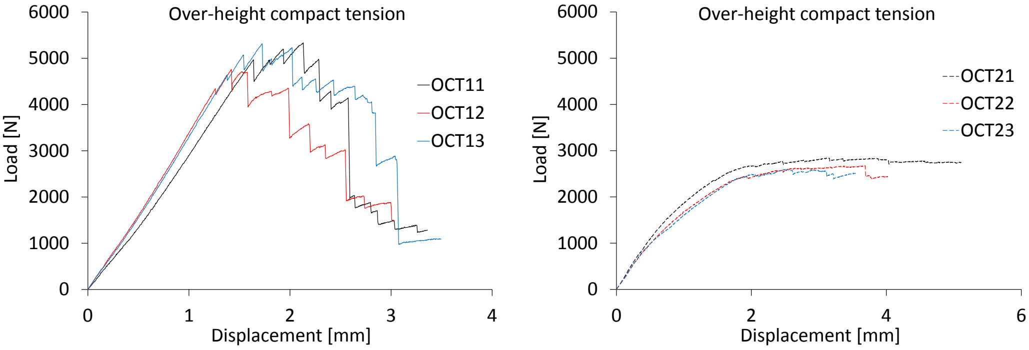

(**a**) Thin-ply $[(0/{-45})/(90/45)]_{6T}$ laminate.

(**b**) Thin-ply $[(0/{-45})/(45/0)/(90/45)/({-45}/90)]_S$ laminate.

Fig. 4.59. Load-displacement relations for the thin-ply specimens.

Figure 4.60[5] shows the typical failure modes of a thin-ply lay-up 1 specimen. Both faces of the specimen are shown (note that this is an asymmetric laminate). As one can see, the failure of these laminates is characterized by development of fiber breakage along the center of the specimen towards the back face. This translaminar crack propagates in small sudden jumps, which resulted in the load drops of figure 4.59a. Substantial splitting of the surface 0° ply is also observed (figure 4.60a). Interesting to note that splitting only occurred in the 0° ply, separating the two layers of the $[0/{-45}]$ NCF bi-layer, since the $-45°$ ply is visible where the 0° ply split.

Observing figure 4.60b, one can also see that, in spite of the stable crack propagation, its path is not clearly along the centerline of the specimen. Indeed, although crack propagation initiates at the pre-crack tip, as it would expected, it does not continue along the

---

[5] Note that the holes for the loading pins have an oval shape because the testing setup was changed after specimens preparation, and therefore they needed to be adapted by performing new holes for the loading pins, with a diameter of 25 mm and more distant from each other, according to the drawing of figure 3.15a.

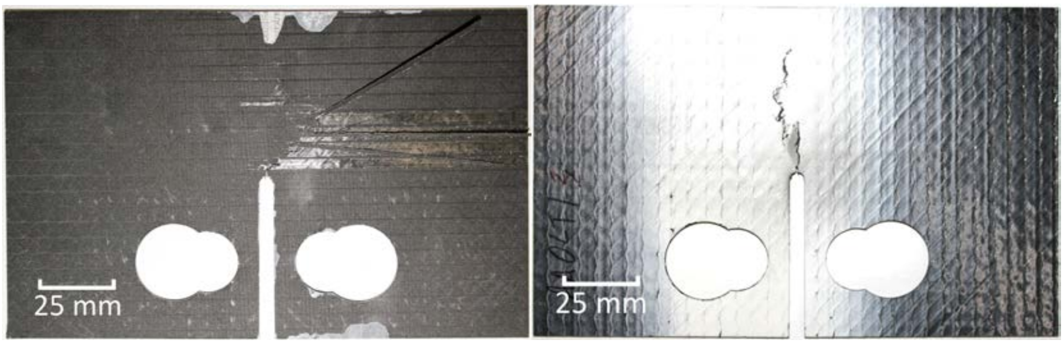

(**a**) Surface with a 0° ply.

(**b**) Surface with a 45° ply.

Fig. 4.60. Thin-ply $[(0/-45)/(90/45)]_{6T}$ specimen (AAOCT13) after over-height compact tension testing.

pre-crack direction. This behavior can be observed in figure 4.61, which shows the surface strain field in the loading direction obtained from the DIC analysis for a typical lay-up 1 specimen.

Just before initiation of crack propagation (figure 4.61a), a high strain concentration is observed in the pre-crack tip, and crack propagation initiates approximately parallel to the pre-crack direction (figure 4.61b). After initiation, the crack continues propagating in the same direction, approximately parallel to the pre-crack, but at a certain point (figure 4.61c), the highest stress concentration is no longer at the crack tip, but away a few millimeters, and the crack path changes considerably (figure 4.61d). Unlike the cross-ply laminates, typically used in compact tension testing, since this is a quasi-isotropic laminate, interaction between damage mechanisms, particularly along the different fiber directions, is likely to occur, resulting in this irregular crack path instead of the linear, centered crack propagation required for this kind of tests.

Therefore, at this point, it is impossible to evaluate the J-integral and measure the R-curve based on the surface displacement and strain fields obtained from the DIC technique using the method proposed by Catalanotti et al. [109]. So, only the linear elastic fracture mechanics (LEFM) solution proposed by Aronsson and Bäcklund [126] and the finite element method (FEM) technique developed by Pinho et al. [104], previously described in chapter 3 (section 3.9), will be used to assess the initiation fracture toughness of the thin-ply lay-up 1 laminate. Because it is not possible to accurately measure the crack length after propagation due to the irregular translaminar crack path, using either the DIC technique or the traditional visual methods, the R-curve cannot be measured, and consequently the propagation fracture toughness cannot be calculated.

Using the LEFM solution for quasi-isotropic compact tension specimens proposed by Aronsson and Bäcklund [126], the mean laminate initiation fracture toughness, calculated using the first load drop as the initiation load, yields $K_T^L = 57.7\ \text{MPa}\sqrt{\text{m}}$. On the other hand, following the FEM technique developed by Pinho et al. [104], the initiation value of the normalized energy release rate, obtained using the FE model described in section 3.9, is $f(a) = 1.21881 \times 10^{-5}$, and the laminate initiation fracture toughness yields $K_T^L = 53.7\ \text{MPa}\sqrt{\text{m}}$ ($G_T^L = 67.7\ \text{kJ/m}^2$). The difference in the laminate initiation fracture toughness obtained from these two data reduction techniques is 7.5%. Such difference may result from the inherent simplicity of the method proposed by Aronsson and Bäck-

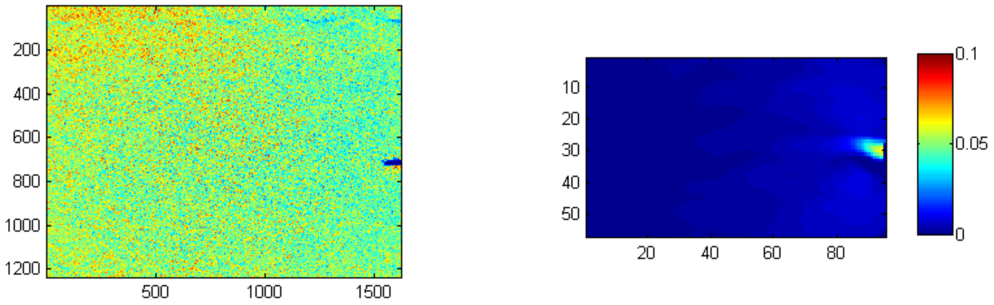

(**a**) Just before initiation of crack propagation.

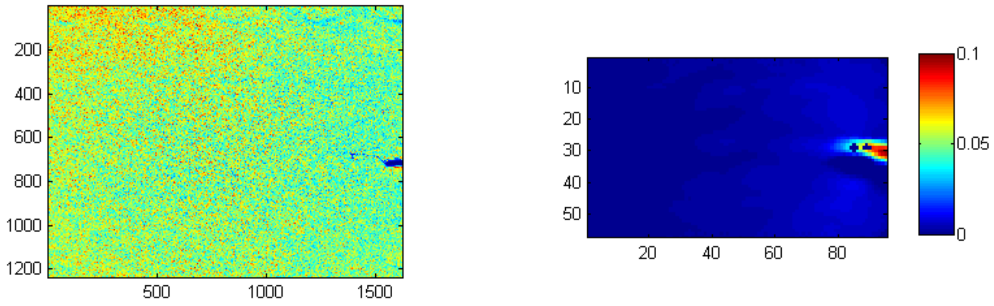

(**b**) Just after initiation of crack propagation.

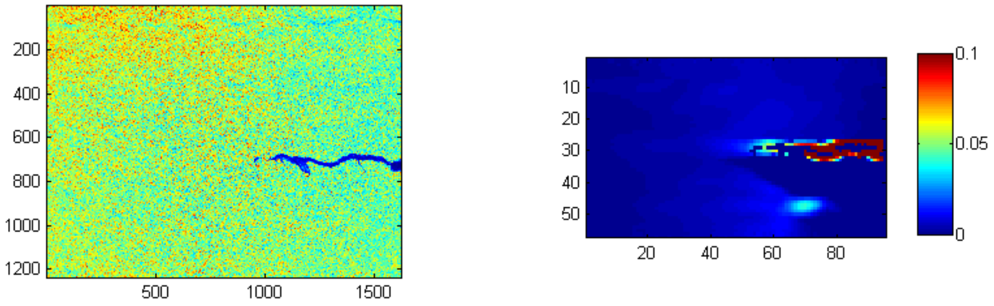

(**c**) Just before crack propagates is a different location.

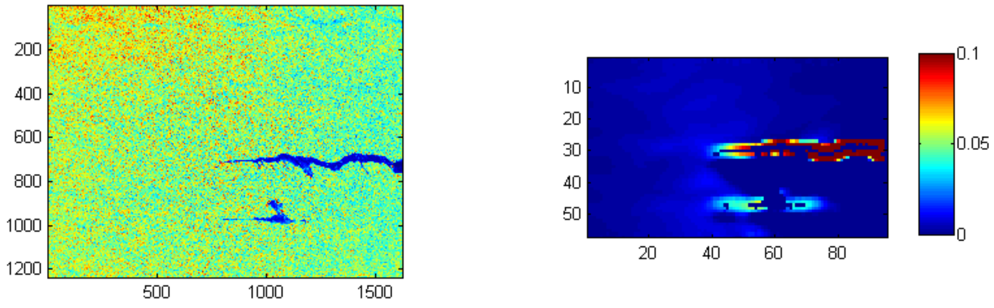

(**d**) Just after crack propagates is a different location.

Fig. 4.61. Surface strain field in the loading direction for different moments of crack propagation in a typical thin-ply $[(0/-45)/(90/45)]_{6T}$ specimen (AAOCT13), obtained from the DIC analysis. The loading direction is vertically oriented.

lund [126], based on LEFM assumptions, and from the fact that, although balanced, this thin-ply laminate is asymmetric, which results in slightly different elastic properties in the orthotropic axes, limiting the validity of the LEFM solution developed for isotropic materials. In spite of the added complexity, performing the J-integral in the FE model of the OCT specimen, both geometry and material properties are taken into account, rendering better results.

Comparing with the results for the laminate fracture toughness obtained from the NT tests (section 4.3.1), one can see that the laminate initiation fracture toughness values obtained from the OCT tests using the solution proposed by Aronsson and Bäcklund [126] and the FEM technique developed by Pinho et al. [104] are, respectively, 51.0% and 40.5% higher than that obtained from the NT tests. Such huge difference may be a consequence of two factors. The first one is that, instead of a sharp crack, a notch tip width of 0.4 mm was used, which may contribute to increase the initiation fracture toughness values. The second factor, maybe the preponderant one, is that, unlike what is expected in a compact tension test, the crack growth was not straight, along the 90° fibers direction (perpendicular to the loading direction), towards the back face of the OCT specimen; instead, crack propagation followed an irregular path, sometimes propagating along the ±45° directions (even backwards — see figures 4.60 and 4.61), indicating occurrence of multiple damage mechanisms, and precluding a completely translaminar crack propagation. Therefore, the fracture toughness values measured are not the translaminar fracture toughness of the laminate, but the fracture toughness associated with a set of damage mechanisms interacting in the crack tip.

The crack growth behavior observed in the thin-ply lay-up 1 specimens may be a consequence of the laminate stacking sequence, raising some questions about the reliability of the compact tension tests to measure the laminate fracture toughness of composite laminates with other stacking sequences than cross-ply. On the other hand, the NT specimens discussed in section 4.3.1 exhibited a brittle type of net-section failure mode, with the failure section perpendicular to the loading direction, as it is expected for translaminar fracture, resulting in valid tests for the measurement of the laminate translaminar fracture toughness. In order to further understand the behavior of the thin-ply laminates under compact tension testing and the influence of the stacking sequence, more studies need to be conducted.

4.7. Concluding remarks

The results previously discussed show that, when subjected to tensile efforts, thin-ply laminates exhibit an approximately linear behavior up to final failure. Such behavior indicates that unrecoverable severe damage, such as extensive transverse cracking and delamination, are virtually absent in thin-ply laminates. This behavior is particularly evident for the laminates with more reduced relative ply orientations and without ply clustering, which exhibit a brittle type of net-section failure mode, whose failure section is perpendicular to the applied tension load. On the other hand, pull-out can be observed in thin-ply laminates with relative ply orientations of 90° and ply clustering. Accordingly, the brittle type of net-section failure mode, dominated by fiber breakage, seems to be beneficial with respect to the laminate's tensile unnotched strength, since improving delamination resistance and precluding transverse cracking (both achievable using thin plies) result in stronger laminates, delaying first-ply-failure for the moment just before final failure.

However, this ability to suppress damage development before failure has consequences regarding the fracture toughness and the notched strength of the thin-ply laminates less susceptible to delamination and transverse cracking onset and growth, such as the $[(0/-45)/(90/45)]_{6T}$ (lay-up 1) laminate. Indeed, the development of a more extensive damaged zone, for example near the notch tip of a center-notched specimen or near the hole of an open-hole specimen, as it was observed, for example, in the thin-ply $[(0/-45)/(45/0)/(90/45)/(-45/90)]_S$ (lay-up 2) laminate, redistributes stresses and decreases stress concentrations, ultimately resulting in a tougher material. Consequently, the notch sensitivity of those laminates that suppress damage onset and growth tends to increase. Still, no substantial difference was found either in the effects of hole size or in the notch sensitivity of the thin-ply laminates when compared with other carbon/epoxy systems designed for aircraft structural applications.

On the other hand, when subjected to compressive efforts, thin-ply laminates exhibit a clear nonlinear behavior, resulting from the development of damage dominated by fiber kinking. Slightly differences were observed in the thin-ply laminates, once again resulting from the different stacking sequences. Although both laminates exhibit a net-section type of failure mode, the higher angle between layers and the ply clustering in the lay-up 2 laminate conduct to higher interlaminar stresses that precipitate failure of the laminate by other damage modes than fiber breakage, namely matrix cracking and extensive fiber microbuckling, resulting in lower unnotched compressive strengths. However, in the presence of a notch or an open-hole, such damage mechanisms redistribute the stresses, and decrease the stress concentrations, ultimately resulting in a tougher material, as in the tensile case. Still, no atypical size effects or notch sensitivity were observed for the thin-ply laminates studied in this thesis.

With respect to the translaminar fracture toughness of the thin-ply laminates, taken in the literature as the main potential problem of these composite materials, it was observed that, in spite of the slightly lower laminate fracture toughness, the fracture toughness of the 0° ply was predicted as very similar to that of other carbon/epoxy systems used in the aircraft industry. Therefore, despite the brittle type of net-section failure mode typical of these laminates, the test results shown in this chapter indicate that a severe notch sensitivity is not observed in these materials. Note, however, that further studies may be conducted in order to accurately validate these preliminary results, namely regarding the fracture toughness of the 0° ply, e.g. by means of compact tension testing of cross-ply laminates made of tow-spread thin plies, and the R-curve effect, which was not quantified in this work, taking particular attention on the proper geometry and lay-ups to be tested.

Another relevant aspect studied in this experimental program is the ability of the thin-ply laminates to resist local compressive efforts, i.e., the effect of the ply thickness on the bearing strength. According to the preliminary study conducted in this work, very interesting results were obtained, since the thin-ply laminates exhibited a superior performance over a carbon/epoxy system typically used in aircraft structural construction. This superior performance was attributed to the ability of the thin-ply laminates to block onset and propagation of damage mechanisms such as delamination, fiber kinking, matrix cracking, and through-the-thickness shear cracking.

However, there is a set of factors that must be taken into account in future works that were not considered here, since this is a preliminary study and the amount of material and laminate configurations were scarce. One of these factors is the absence of an equivalent laminate material to perform accurate comparisons with respect to the effect of ply thickness on size effects and notch sensitivity. Taking the results discussed in this chapter, one is only able to qualitatively evaluate the thin-ply laminates tested here comparing them with other composite systems made of traditional prepreg layers. So, no objective conclusions can be made regarding the effect of ply thickness on the structural integrity of composite laminates. Another important factor is the effect of the laminate thickness. As previously mentioned in this chapter, independently of the laminate stacking sequence, an increase in the laminate thickness with constant hole diameter leads to a decrease in failure stress. However, the thin-ply NCF laminates studied here are 30% to 50% thinner than those used for comparison, and this difference may have some influence in the results showed and discussed previously.

Chapter 5

Analysis method for notched laminates

For the aircraft and aerospace industries, a key aspect to ensure that a damaged structure can continue in service safely until the damage can be detected by scheduled maintenance inspection is residual strength. It is well known that, in the presence of a hole or other discontinuity, high local stresses, or local stress concentrations, can result in initial localized failure. Therefore, the development of accurate, physically-based and fast strength prediction methods for composite laminates with stress concentrations is extremely important, particularly for preliminary sizing and for optimization of composite structures. In this chapter, fast design tools based on closed-form solutions, derived from models such as the inherent flaw model, the point stress and average stress models, and the recently proposed finite fracture mechanics model, are presented. Then, these models are used in the analysis of the thin-ply laminates studied in this work and a comparison with other material systems is presented. Finally, the accuracy and reliability of the analyses based on the presented models are discussed.

5.1. Introduction

Damage tolerance provides a measure of the ability of a structure to sustain design loads with a level of damage or defect and be able to perform its operating functions [113]. There are two main approaches regarding the analysis of the damage tolerance of composite structures: residual strength analysis and *safe-life* analysis. The first one is particularly important when analyzing the effect of defects such as cuts, scratches and impact damage in a laminated composite structure. The residual strength of these types of damage may be predicted using closed-form solutions, such as linear elastic fracture mechanics (LEFM) models, the inherent flaw model, the point stress model, the average stress model, or the recently proposed finite fracture mechanics model, or using finite element analysis (FEA). On the other hand, when damage in a laminated composite structure is likely to grow under fatigue-type loading, its damage tolerance assessment requires the consideration of *safe-life* analysis, based either on closed-form or FEA solutions for damage propagation [91]. In this work, the main focus is the prediction of the residual strength of notched composite laminates, and therefore only the first approach will be considered.

The presence of a hole or other discontinuity in a structure introduces high local stresses, or local stress concentrations, that can result in initial localized failure. So, the residual strength of a notched composite structure is a key aspect to ensure that such structure can continue in service safely until the damage can be detected by scheduled maintenance inspection, in particular for the aircraft industry. However, the analysis of failure due to cracking, or fracture, resulting from stress concentrations is complicated for composite materials because of material heterogeneity at the microscale (constituent scale) and at the ply scale [113].

In the design of composite structures, particularly for the aircraft and aerospace industries, the development of accurate, physically-based and fast strength prediction methods for composite laminates with stress concentrations is extremely important [119]. Camanho et al. [53] demonstrated that, in spite of their simplicity, strength prediction methods uniquely based on stress or strain failure criteria are unable to predict the size effects observed in notched specimens, resulting in the same strength prediction for different hole diameters when the width to hole diameter ratio is held constant, contradicting the experimental observations. On the other hand, the accurate and physically-based numerical methods available for strength prediction of composite laminates need for finite element (FE) implementation, most of the times in explicit non-linear FE models, resulting in long computing times unacceptable for preliminary sizing and for optimization of composite structures [119]. In order to satisfactorily combine accuracy and celerity, fast design tools suitable for preliminary sizing and optimization of composite notched structures have been developed. Such tools are based on closed-form solutions, derived from models such as the inherent flaw model, the point stress and average stress models, or the recently proposed finite fracture mechanics model. These models will be the focus of the analyses presented in the next sections.

5.2. Inherent flaw model

The **inherent flaw model** (IFM) was originally developed by Waddoups et al., in the early 1970's, for predicting the residual strength of notched laminates with infinite width under tensile load, and later extended to finite width by introducing a finite-width correction factor [53, 91]. The IFM is based on LEFM, arguing that a composite laminate containing a notch is analogous to a crack in an isotropic material [126]. According to this model, the noncritical damage mechanisms occurring before ultimate failure of a composite laminate can be lumped into a constant "region of intense energy", or "inherent flaw", of length a [53]. The critical value of the stress intensity factor of a plate with a hole radius R is given by,

$$K_{Ic} = f(a,R)\bar{\sigma}^{\infty}\sqrt{\pi a} \tag{5.1}$$

where $f(a,R)$ is the Bowie's solution for the calculation of the stress intensity factor of two cracks emanating from a circular hole, given as,

$$f(a,R) = 0.5\left(3 - \frac{a}{R+a}\right)\left[1 + 1.243\left(1 - \frac{a}{R+a}\right)^3\right] \tag{5.2}$$

Considering that the strength of an unnotched specimen can be predicted by taking into account that the hole radius tends to zero, in which case the Bowie's solution $f(a,R)$

tends to one, then,

$$K_{Ic} = X_T^L \sqrt{\pi a} \tag{5.3}$$

where X_T^L is the laminate tensile unnotched strength. Combining equations (5.1) and (5.3) results in,

$$\bar{\sigma}^{\infty} = \frac{X_T^L}{f(a, R)} \tag{5.4}$$

Accordingly, the strength of a notched laminate is predicted using two parameters, the length of the inherent flaw, a, that needs to be calculated from a baseline specimen, and the unnotched tensile strength of the laminate, X_T^L. It should be noted that equation (5.4) is only valid when finite width effects are negligible, otherwise a finite-width correction factor must be used. Although a simple approach, since it does not require complex FE implementations, the IFM only provides reasonable predictions for specimens with hole diameters close to the diameter used to calibrate the model, whose accuracy relies upon the measurement of the length of the inherent flaw for each material/lay-up and geometry [53].

5.3. Point stress and average stress models

The **point stress** (PS) and the **average stress** (AS) semi-empirical models, proposed by Whitney and Nuismer in the 1970's, are the most widely used design methods for composite laminates with stress concentrations and for calculation of macromechanical size effects [53, 119]. Both models require the knowledge of the finite stress distribution in the vicinity of the notch [126].

The PS model predicts final failure when the stress σ_{yy} at a given distance r_{ot} from the notch boundary, the so-called *"characteristic distance"*, reaches the unnotched strength of the laminate X_T^L, i.e.,

$$\sigma_{yy}\big|_{x=R+r_{ot}} = X_T^L \tag{5.5}$$

On the other hand, the AS model predicts final failure when the laminate stress averaged over a characteristic distance r_{ot} is equal to the unnotched strength of the laminate X_T^L, i.e.,

$$\frac{1}{r_{ot}} \int_{R}^{R+r_{ot}} \sigma_{yy}(x, 0)\mathrm{d}x = X_T^L \tag{5.6}$$

Both PS and AS models are based on simple closed-form solutions, which require two additional properties besides the ply elastic properties, namely r_{ot} and X_T^L. So, the strength prediction can be performed in a short amount of time, requiring a small effort to obtain such results. However, the characteristic distance is not a material property, needing to be identified from a test in a notched laminate with a given geometry (width and hole diameter) every time the material/lay-up or the geometry are modified. Consequently, these models only provide reasonable predictions for hole diameters close to that used for the model calibration. Therefore, what appeared to be economic strength prediction methods, in reality require a large amount of empirical data from expensive experimental programmes to account for the different geometries and lay-ups that are typically used in the aerospace and aircraft industries [53, 110, 119].

5.4. Finite fracture mechanics model

A new economic, fast and accurate strength prediction method for open-hole composite laminates based on the concept of **finite fracture mechanics** (FFM) was recently proposed by Camanho et al. [119], resulting in improvements over the traditional strength prediction methods. FFM models assume that crack propagation occurs when a stress-based criterion and an energy-based criterion are simultaneously satisfied, and consider that failure occurs by the propagation of kinematically admissible cracks with finite sizes. Indeed, the crack propagates when the stress σ ahead of a crack tip averaged over a distance l reaches the material unnotched strength X_T^L (stress-based criterion), i.e.,

$$\int_a^{a+l} \sigma(x)\mathrm{d}x = X_T^L l \tag{5.7}$$

and when the energy available to propagate the crack a finite distance l is equal to a critical value that is defined by the mode I fracture toughness K_{Ic} of the material (energy-based criterion), i.e.,

$$\int_a^{a+l} K_I^2(a)\mathrm{d}a = K_{Ic}^2 l \tag{5.8}$$

where K_I is the stress intensity factor.

Now consider a composite laminate with a central circular hole with a diameter d, radius R, and width W, loaded by a remote stress. Assuming that the propagation of the macrocrack that leads to final failure occurs along the x-direction, and for the particular case of a specimen with an uncracked central circular hole, fracture occurs when the following system of equations is satisfied,

$$\begin{cases} \dfrac{1}{l}\displaystyle\int_R^{R+l} \sigma_{yy}(x,0)\mathrm{d}x = X_T^L \\[2ex] \dfrac{1}{l}\displaystyle\int_R^{R+l} K_I^2(a)\mathrm{d}a = K_{Ic}^2 \end{cases} \tag{5.9}$$

where X_T^L is the laminate unnotched strength, K_{Ic} is the mode I fracture toughness of the laminate, and l is the crack extension at failure. As one can see, the first equation in (5.9) corresponds to the AS model (equation (5.6)). This means that the proposed FFM model enriches the AS model using a second equation that represents an energy balance that must be satisfied during crack propagation. Taking into account that the system of equations (5.9) results in two unknowns, namely the remote notched strength and the crack extension at failure, there is no need to use an empirical *"characteristic distance"* identified from one notched specimen [119].

The stress distribution along the x-axis, $\sigma_{yy}(x,0)$, is obtained as,

$$\sigma_{yy}(x,0) = R_K \frac{\sigma^\infty}{2}\left[2+\xi^2+3\xi^4-(K_T^\infty-3)\left(5\xi^6-7\xi^8\right)\right], \quad \xi = \frac{R}{x} \tag{5.10}$$

where σ^∞ is the remote stress, K_T^∞ is the stress concentration factor of an infinite plate containing a circular hole, and R_K is the finite width correction factor. These parameters are defined as,

$$K_T^\infty = 1 + \sqrt{\frac{2}{A_{22}}\left(\sqrt{A_{11}A_{22}} - A_{12} + \frac{A_{11}A_{22} - A_{12}^2}{2A_{66}}\right)} \tag{5.11}$$

$$R_K = \frac{K_T}{K_T^\infty} = \left\{\frac{3(1-2R/W)}{2+(1-2R/W)^3} + \frac{1}{2}\left(\frac{2R}{W}M\right)^6 (K_T^\infty - 3)\left[1 - \left(\frac{2R}{W}M\right)^2\right]\right\}^{-1} \tag{5.12}$$

where A_{ij} are the components of the laminate in-plane stiffness matrix that are calculated using classical lamination theory [120]. The parameter M is calculated as,

$$M^2 = \frac{\sqrt{1 - 8\left[\frac{3(1-2R/W)}{2+(1-2R/W)^3} - 1\right]} - 1}{2\left(\frac{2R}{W}\right)^2} \tag{5.13}$$

The stress intensity factor K_I corresponding to two symmetric cracks emanating from a plate with a central circular hole is given for an isotropic plate as,

$$K_I = \sigma^\infty F_h F_w \sqrt{\pi a} \tag{5.14}$$

with,

$$F_h = \sqrt{1 - \frac{R}{a}} f_n \tag{5.15}$$

$$f_n = 1 + 0.358\lambda + 1.425\lambda^2 - 1.578\lambda^3 + 2.156\lambda^4, \quad \lambda = \frac{R}{a} \tag{5.16}$$

and,

$$F_w = \sqrt{\sec\left(\frac{\pi R}{W}\right)\sec\left(\frac{\pi a}{W}\right)} \tag{5.17}$$

As one can see in equations (5.9), (5.10) and (5.14), the geometric terms included in the solution for the stress distribution, equation (5.10), and for the stress intensity factor, (5.14), imply that the solutions of the system (5.9) are functions of both the geometry and the material properties. That is why the "*characteristic distance*" used in the PS and AS models, equations (5.5) and (5.6), respectively, cannot be a material property, needing to be identified from one notched specimen [119].

Using equations (5.10) and (5.14) in (5.9), and dividing the second equation of (5.9) by the square of the first one yields a nonlinear equation with only one unknown, the crack extension at failure l,

$$\frac{4l\pi \int_R^{R+l} (F_h F_w)^2 a \,\mathrm{d}a}{R_K^2 \left\{\int_R^{R+l} \left[2 + \xi^2 + 3\xi^4 - (K_T^\infty - 3)\left(5\xi^6 - 7\xi^8\right)\right] \mathrm{d}x\right\}^2} = \left(\frac{K_{Ic}}{X_T^L}\right)^2 \tag{5.18}$$

The integral in the denominator of equation (5.18) can be solved analytically, whereas the integral in the numerator cannot. Using the Simpson's rule to numerically integrate the numerator of equation (5.18), the resulting nonlinear equation can be solved for l. Once l is known, it is possible to calculate the remote stress at failure, $\bar{\sigma}^\infty$, using one of the equations of the system (5.9). Therefore, the strength predictions using the FFM model are based on independently measured material properties, namely the ply elastic properties, and the laminate unnotched strength and fracture toughness. No empirical calibration parameters are required for different hole sizes or specimen widths. So, the predictions can be obtained in a few seconds, without the need to use FEA or complex computational methods, using only the ply elastic properties and two independent material properties, and consequently the FFM model can be considered a fast and economic prediction tool [119].

It should be noted that the correction factors applied to the stress intensity factor should account for the orthotropy of the composite material. However, for quasi-isotropic laminates, which is approximately the case of the laminates studied in this thesis, the stress intensity factor calculated using equation (5.14) is accurate and no additional correction factors are required [119]. In addition, for quasi-isotropic laminates, the stress concentration factor for the infinite plate containing a circular hole, K_T^{∞} (equation (5.11)), is equal to 3 (also valid for the thin-ply laminates studied herein), simplifying considerably equations (5.10), (5.12), and (5.18).

It should also be noted that the FFM model is applicable to notched composite laminates that mainly exhibit translaminar fracture. The strength prediction of laminates whose main failure mechanism is delamination requires appropriate FEA, and the FFM model is not appropriate for that type of laminates [119].

Because there are no standard test methods to measure the fracture toughness of the laminate, the FFM model can also be used to calculate it using specimens with a central notch. These specimens are particularly suitable due to the simplicity of the geometry and of the data reduction method [119]. For sufficiently large W/a ratios, the stress distribution used in the system of equations (5.9) reads,

$$\sigma_{yy}(x,0) = \frac{\sigma^{\infty} x}{\sqrt{x^2 - a^2}} \tag{5.19}$$

and the stress intensity factor is given by,

$$K_I = \sigma^{\infty}\sqrt{\pi a} \tag{5.20}$$

According to Camanho et al. [119], it is interesting to note that the results obtained for the laminate fracture toughness using this approach are quite close to those obtained from the direct application of LEFM, which means that it is possible to use models that relate the fracture toughness of the 0° ply to the fracture toughness of a multidirectional laminate in the FFM model without incurring in significant errors. Therefore, in some cases, the properties required for the FFM model are the ply elastic properties, the unnotched strength and the fracture toughness of the 0° ply.

5.5. Results analysis

5.5.1. Notched strength predictions

Figures 5.1 to 5.4 and tables 5.1 to 5.4 show the comparisons between the predictions of the models previously described and the experimental open-hole tensile (OHT) and open-hole compressive (OHC) results obtained for the thin-ply carbon NCF C-Ply™ T700/AR-2527 epoxy laminates, where $\bar{\sigma}_N = \bar{\sigma}^{\infty}/X^L$ is the normalized notched strength, $\bar{\sigma}^{\infty}$ are the laminate tensile ($\bar{\sigma}_T^\infty$) or compressive ($\bar{\sigma}_C^\infty$) notched strengths, X^L are the laminate tensile (X_T^L) or compressive (X_C^L) unnotched strengths, and d is the hole diameter. Both linear and logarithmic scales are represented. The test results of the OHT specimens with a 6 mm diameter hole and the test results of the OHC specimens with a 5 mm diameter hole were used to calibrate the IFM, the PS model and the AS model and calculate the corresponding length of the inherent flaw (a) and characteristic distances (r_{ot}). The tensile and compressive fracture toughness required in the FFM model were calculated using the remote stress at failure measured in the experimental center-notched tests, by solving the system of equations (5.9) for K_{Ic} and for l (crack extension at failure), taking into account equations (5.19) and (5.20) (as described in section 5.4). These experimental results were discussed in detail in chapter 4. Note that, as discussed in chapter 4, the experimental OHC results for the specimens with the 2 mm diameter hole were not valid due to non-negligible buckling phenomena during testing, and therefore they are not considered in this analysis.

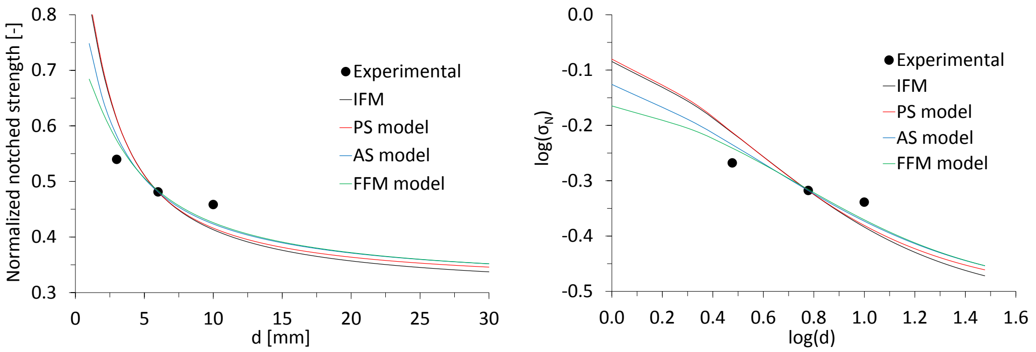

(**a**) Normalized notched strength vs. hole diameter. (**b**) Normalized notched strength vs. hole diameter (log scale).

Fig. 5.1. Predictions and experimental open-hole tensile results for the thin-ply NCF C-Ply™ T700/AR-2527 $[(0/-45)/(90/45)]_{6T}$ laminate. The length of the inherent flaw (a) is 1.025 mm. The characteristic distances (r_{ot}) for the PS and AS models are 0.754 mm and 1.838 mm, respectively. The laminate fracture toughness (K_{Ic}) and the crack extension at failure (l) predicted by the FFM model are 47.7 MPa$\sqrt{\text{m}}$ (24.9% greater than that obtained in the NT tests) and 2.266 mm, respectively.

Tab. 5.1. Predictions and experimental open-hole tensile results for the thin-ply NCF C-Ply™ T700/AR-2527 $[(0/-45)/(90/45)]_{6T}$ laminate. The length of the inherent flaw (a) is 1.025 mm. The characteristic distances (r_{ot}) for the PS and AS models are 0.754 mm and 1.838 mm, respectively. The laminate fracture toughness (K_{Ic}) and the crack extension at failure (l) predicted by the FFM model are 47.7 MPa$\sqrt{\text{m}}$ (24.9% greater than that obtained in the NT tests) and 2.266 mm, respectively.

d [mm]	$\bar{\sigma}_T^\infty$ (exp.) [MPa]	$\bar{\sigma}_T^\infty$ (IFM) [MPa]	Error [%]	$\bar{\sigma}_T^\infty$ (PS) [MPa]	Error [%]
3	432	489	13.4	490	13.6
6	385	385	n/a	385	n/a
10	367	331	9.8	333	9.2

d [mm]	$\bar{\sigma}_T^\infty$ (exp.) [MPa]	$\bar{\sigma}_T^\infty$ (AS) [MPa]	Error [%]	$\bar{\sigma}_T^\infty$ (FFM) [MPa]	Error [%]
3	432	466	7.9	459	6.4
6	385	385	n/a	387	0.4
10	367	339	7.6	341	7.1

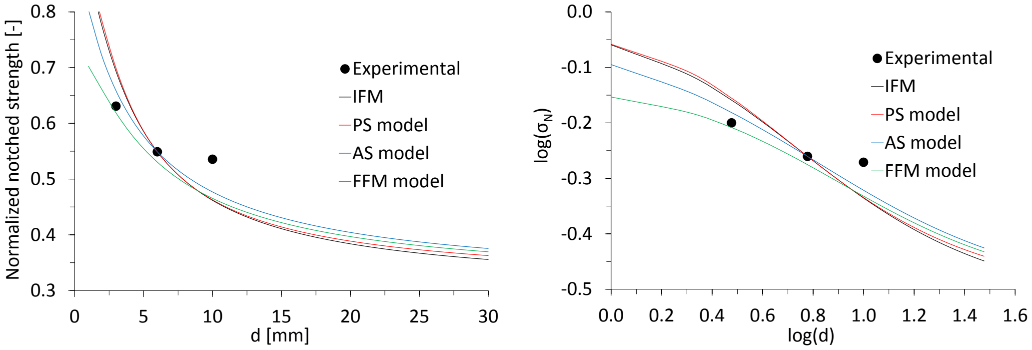

(**a**) Normalized notched strength vs. hole diameter. (**b**) Normalized notched strength vs. hole diameter (log scale).

Fig. 5.2. Predictions and experimental open-hole tensile results for the thin-ply NCF C-Ply™ T700/AR-2527 $[(0/{-45})/(45/0)/(90/45)/({-45}/90)]_S$ laminate. The length of the inherent flaw (a) is 1.506 mm. The characteristic distances (r_{ot}) for the PS and AS models are 1.110 mm and 2.968 mm, respectively. The laminate fracture toughness (K_{Ic}) and the crack extension at failure (l) predicted by the FFM model are 50.8 MPa$\sqrt{\text{m}}$ (34.4% greater than that obtained in the NT tests) and 3.258 mm, respectively.

Tab. 5.2. Predictions and experimental open-hole tensile results for the thin-ply NCF C-Ply™ T700/AR-2527 $[(0/{-45})/(45/0)/(90/45)/({-45}/90)]_S$ laminate. The length of the inherent flaw (a) is 1.506 mm. The characteristic distances (r_{ot}) for the PS and AS models are 1.110 mm and 2.968 mm, respectively. The laminate fracture toughness (K_{Ic}) and the crack extension at failure (l) predicted by the FFM model are 50.8 MPa$\sqrt{\text{m}}$ (34.4% greater than that obtained in the NT tests) and 3.258 mm, respectively.

d [mm]	$\bar{\sigma}_T^\infty$ (exp.) [MPa]	$\bar{\sigma}_T^\infty$ (IFM) [MPa]	Error [%]	$\bar{\sigma}_T^\infty$ (PS) [MPa]	Error [%]
3	448	492	9.9	497	10.8
6	390	390	n/a	390	n/a
10	380	328	13.8	329	13.6
d [mm]	$\bar{\sigma}_T^\infty$ (exp.) [MPa]	$\bar{\sigma}_T^\infty$ (AS) [MPa]	Error [%]	$\bar{\sigma}_T^\infty$ (FFM) [MPa]	Error [%]
3	448	468	4.4	440	1.9
6	390	390	n/a	377	3.4
10	380	339	10.9	331	13.1

Tab. 5.3. Predictions and experimental open-hole compressive results for the thin-ply NCF C-Ply™ T700/AR-2527 $[(0/{-45})/(90/45)]_{6T}$ laminate. The length of the inherent flaw (a) is 0.935 mm. The characteristic distances (r_{ot}) for the PS and AS models are 0.689 mm and 1.713 mm, respectively. The laminate fracture toughness (K_{Ic}) and the crack extension at failure (l) predicted by the FFM model are 26.7 MPa$\sqrt{\text{m}}$ (17.6% greater than that obtained in the NC tests) and 1.553 mm, respectively.

d [mm]	$\bar{\sigma}_C^\infty$ (exp.) [MPa]	$\bar{\sigma}_C^\infty$ (IFM) [MPa]	Error [%]	$\bar{\sigma}_C^\infty$ (PS) [MPa]	Error [%]
5	268	268	n/a	268	n/a
7	247	240	2.7	241	2.4
d [mm]	$\bar{\sigma}_C^\infty$ (exp.) [MPa]	$\bar{\sigma}_C^\infty$ (AS) [MPa]	Error [%]	$\bar{\sigma}_C^\infty$ (FFM) [MPa]	Error [%]
5	268	268	n/a	249	7.2
7	247	245	0.8	229	7.3

Observing figures 5.1 and 5.2 and tables 5.1 and 5.2 one can see that all proposed models reasonably predict the tensile notched behavior of the thin-ply NCF laminates under

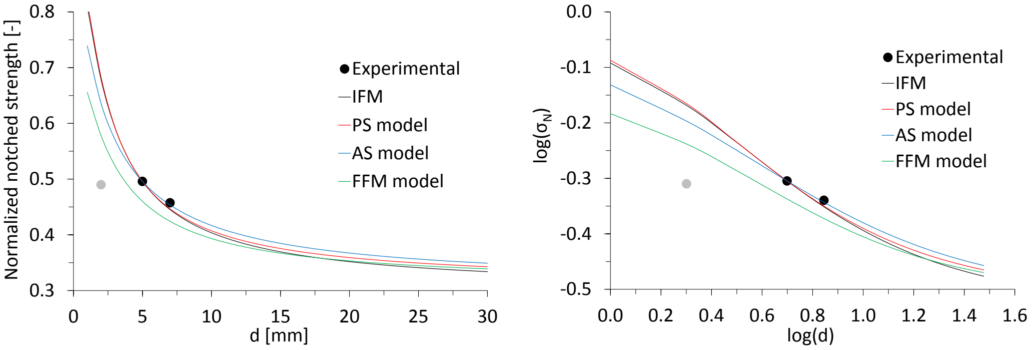

(**a**) Normalized notched strength vs. hole diameter. (**b**) Normalized notched strength vs. hole diameter (log scale).

Fig. 5.3. Predictions and experimental open-hole compressive results for the thin-ply NCF C-Ply™ T700/AR-2527 $[(0/-45)/(90/45)]_{6T}$ laminate. The length of the inherent flaw (a) is 0.935 mm. The characteristic distances for the PS and AS models are 0.689 mm and 1.713 mm, respectively. The laminate fracture toughness (K_{Ic}) and the crack extension at failure (l) predicted by the FFM model are 26.7 MPa$\sqrt{\text{m}}$ (17.6% greater than that obtained in the NC tests) and 1.553 mm, respectively.

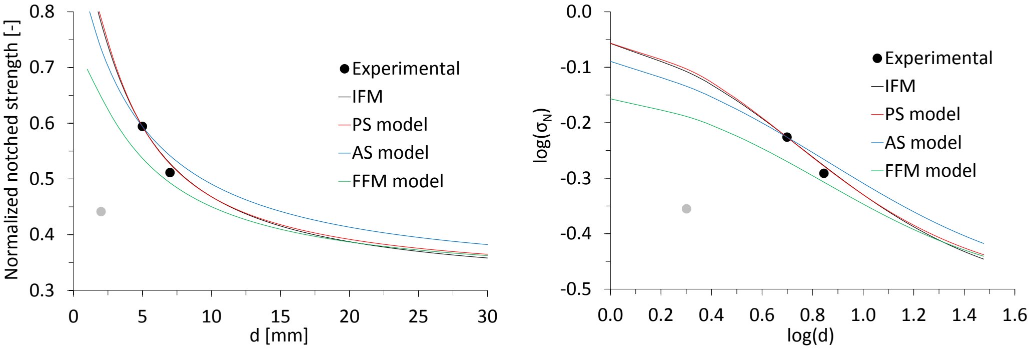

(**a**) Normalized notched strength vs. hole diameter. (**b**) Normalized notched strength vs. hole diameter (log scale).

Fig. 5.4. Predictions and experimental open-hole compressive results for the thin-ply NCF C-Ply™ T700/AR-2527 $[(0/-45)/(45/0)/(90/45)/(-45/90)]_S$ laminate. The length of the inherent flaw (a) is 1.572 mm. The characteristic distances (r_{ot}) for the PS and AS models are 1.152 mm and 3.303 mm, respectively. The laminate fracture toughness (K_{Ic}) and the crack extension at failure (l) predicted by the FFM model are 31.1 MPa$\sqrt{\text{m}}$ (30.6% greater than that obtained in the NC tests) and 2.853 mm, respectively.

study. Comparing with the experimental results, all predictions show errors below 14%. As one can see, the FFM model provides more accurate predictions than the alternative models. On the other hand, the predictions obtained using the AS model are more accurate than those obtained with the IFM and the PS model. Remember that the FFM model enriches the AS model using a second equation that represents an energy balance that must be satisfied during crack propagation, instead of an inverse identification from one of the OHT tests.

Observing figures 5.3 and 5.4 and tables 5.3 and 5.4 one can see that all proposed models also reasonably predict the compressive notched behavior of the thin-ply NCF laminates

Tab. 5.4. Predictions and experimental open-hole compressive results for the thin-ply NCF C-Ply™ T700/AR-2527 $[(0/{-45})/(45/0)/(90/45)/({-45}/90)]_S$ laminate. The length of the inherent flaw (a) is 1.572 mm. The characteristic distances (r_{ot}) for the PS and AS models are 1.152 mm and 3.303 mm, respectively. The laminate fracture toughness (K_{Ic}) and the crack extension at failure (l) predicted by the FFM model are 31.1 MPa$\sqrt{\text{m}}$ (30.6% greater than that obtained in the NC tests) and 2.853 mm, respectively.

d [mm]	$\bar{\sigma}_C^{\infty}$ (exp.) [MPa]	$\bar{\sigma}_C^{\infty}$ (IFM) [MPa]	Error [%]	$\bar{\sigma}_C^{\infty}$ (PS) [MPa]	Error [%]
5	276	276	n/a	276	n/a
7	238	245	3.2	245	3.0

d [mm]	$\bar{\sigma}_C^{\infty}$ (exp.) [MPa]	$\bar{\sigma}_C^{\infty}$ (AS) [MPa]	Error [%]	$\bar{\sigma}_C^{\infty}$ (FFM) [MPa]	Error [%]
5	276	276	n/a	249	9.6
7	238	252	5.9	229	3.6

under study. Comparing with the experimental results, all predictions show errors below 10%. One can see that the predictions of the FFM model are not so accurate as the predictions of the alternative models. However, unlike the alternative models which use an inverse calibration from one of the OHC tests (hole diameter of 5 mm, in this case), resulting in good predictions for hole diameters around that used for calibration, the FFM model, besides the compressive unnotched strength, simply requires the compressive fracture toughness of the laminate, whose accurate evaluation is very difficult, even from center-notched compression testing. Nevertheless, one can see that the errors are still very reasonable, in the same range of those obtained for the tensile notched strength.

From the previous discussion, regarding the results shown in figures 5.1 to 5.4 and tables 5.1 to 5.4, and due to the promising generality and versatility of this model, it is valid to assume that the FFM model is better suited to evaluate the macroscopic size effects on carbon fiber reinforced polymers (CFRP) than the IFM, the PS model, or the AS model. To further validate such assumption, figure 5.5 shows the comparison between the experimental results and the predictions of the finite fracture mechanics model for the T800/M21 $[90/45/0/{-45}]_{3S}$ laminate and for the IM7-8552 $[90/0/45/{-45}]_{3S}$ laminate, both typical of the aircraft and aerospace industries.

As one can see, the macroscopic size effects on the T800/M21 and the IM7-8552 carbon/epoxy systems are also well predicted by the FFM model proposed by Camanho et al. [119]. Therefore, in order to analyse the mechanical performance of the thin-ply carbon NCF C-Ply™ T700/AR-2527 epoxy laminates studied in this thesis, with respect to the size effects exhibited when subjected to either tensile or compressive efforts, in the following paragraphs, the predictions of the FFM model for these four laminates are compared. Such analysis will help to understand the effect of increasing the hole diameter in these laminates without limiting it to the available experimental data, which does not always allow a direct comparison.

Figure 5.6 shows the predictions of the FFM model for the thin-ply NCF C-Ply™ T700/AR-2527 $[(0/{-45})/(90/45)]_{6T}$ (lay-up 1) and $[(0/{-45})/(45/0)/(90/45)/({-45}/90)]_S$ (lay-up 2) laminates, for the T800/M21 $[90/45/0/{-45}]_{3S}$ laminate, and for the IM7-8552 $[90/0/45/{-45}]_{3S}$ laminate, considering $w/d = 4$. The predictions for both tensile and compressive notched strengths are represented, in both linear and logarithmic scales.

The predictions shown in figure 5.6 for the normalized tensile notched strengths (5.6a and b) indicate that the hole size effect is more pronounced in the IM7-8552 laminate, fol-

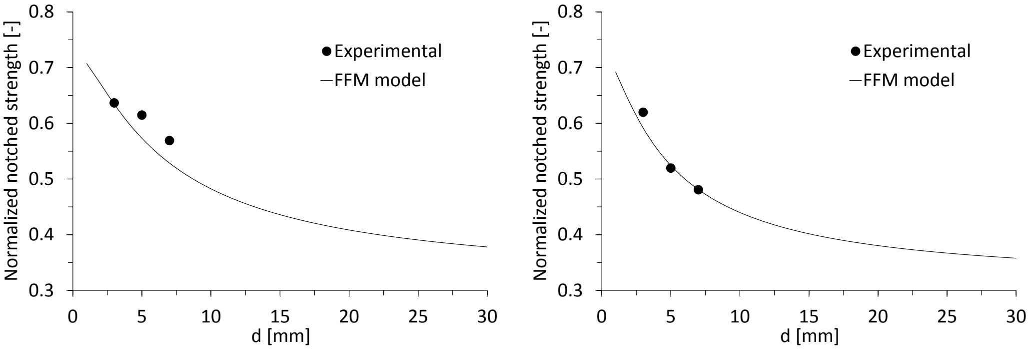

(**a**) T800/M21 $[90/45/0/-45]_{3S}$ laminate (tension). (**b**) T800/M21 $[90/45/0/-45]_{3S}$ laminate (compression).

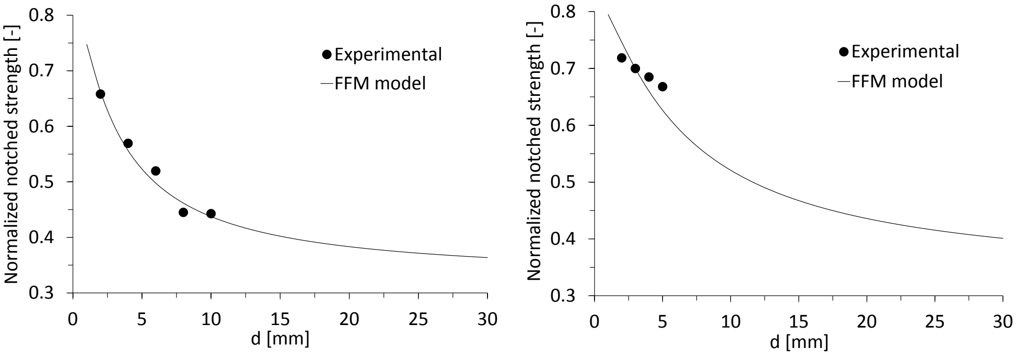

(**c**) IM7-8552 $[90/0/45/-45]_{3S}$ laminate (tension). (**d**) IM7-8552 $[90/0/45/-45]_{3S}$ laminate (compression).

Fig. 5.5. Comparison between the predictions of the FFM model and the experimental results for two alternative carbon/epoxy systems.

lowed closely by the thin-ply NCF lay-up 1 laminate. The T800/M21 laminate exhibits the least pronounced hole size effect, however followed closely by the thin-ply NCF lay-up 2 laminate. On the other hand, with respect to the normalized compressive notched strengths (figures 5.6c and d), one can see that, contrary to what is observed for the tensile case, the IM7-8552 laminate clearly exhibits the least pronounced hole size effect, whereas the thin-ply NCF lay-up 1 laminate shows the most pronounced strength reductions with increasing hole diameters. The thin-ply NCF lay-up 2 laminate and the T800/M21 laminate show a very similar hole size effect under compression, with a slight advantage for thin-ply NCF lay-up 2 laminate.

Remembering figures 4.36 and 4.51, and now observing figure 5.6, one can see how easier becomes the analysis of the size effects on the thin-ply NCF laminates when considering the (reliable) predictions of closed-form models such as the FFM model. However, as it was already discussed in chapter 4 (section 4.4), this analysis do not take into account the laminate thickness effect. The lower laminate thickness of the thin-ply NCF lay-up 2 may be resulting in a virtual improvement of the effect of the hole size in the notched strength of the laminate that, otherwise, would be inferior. In addition, and because the T800/M21 and the IM7-8552 laminates were made of traditional unidirectional prepreg, they are thicker than the thin-ply NCF lay-up 1 laminate too. Therefore, the results for the thin-ply NCF lay-up 1 laminate may also be affected by the laminate thickness. Still,

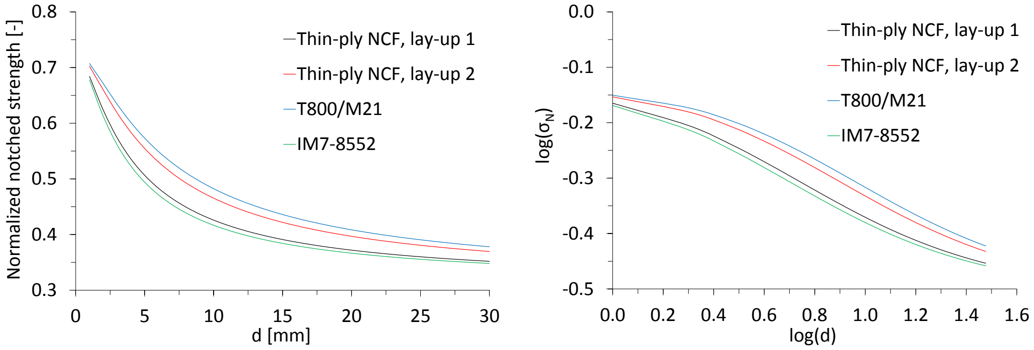

(**a**) Tension. (**b**) Tension (log scale).

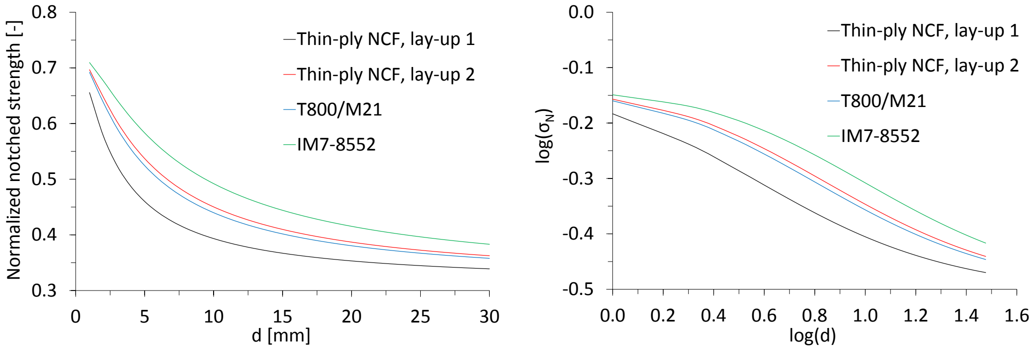

(**c**) Compression. (**d**) Compression (log scale).

Fig. 5.6. Predictions of the FFM model for the thin-ply NCF C-Ply™ T700/AR-2527 $[(0/-45)/(90/45)]_{6T}$ (lay-up 1) and $[(0/-45)/(45/0)/(90/45)/(-45/90)]_S$ (lay-up 2) laminates, for the T800/M21 $[90/45/0/-45]_{3S}$ laminate, and for the IM7-8552 $[90/0/45/-45]_{3S}$ laminate.

and because no other results are available, these will be considered as preliminary ones, showing that the size effects observed in traditional prepreg CFRP and not substantially different from those exhibited by the thin-ply NCF laminates.

5.5.2. Design charts

Taking into account that the FFM model provides predictions of notched strength in a few of seconds, it can be used to generate design charts for notched laminates [119]. In such design charts, the predicted normalized notched strength, defined as $\bar{\sigma}_N = \bar{\sigma}^{\infty}/X_T^L$, is represented as a function of the d/W ratio for different hole sizes. This design chart must also include the predictions obtained for a notch-sensitive material, whose normalized strength is a function of the stress concentration factor K_T ($\bar{\sigma}_N = 1/K_T$), and the predictions for a notch-insensitive material, whose normalized strength is a function of the geometry ($\bar{\sigma}_N = 1 - d/W$).

Figures 5.7 and 5.8 show the design charts for the thin-ply carbon NCF C-Ply™ T700/AR-2527 epoxy laminates, for the T800/M21 $[90/45/0/-45]_{3S}$ laminate, and for the IM7-8552 $[90/0/45/-45]_{3S}$ laminate, regarding their tensile and compressive notched responses, respectively. In addition to the predicted normalized notched strength values, the experimental results available for these materials are also represented. Note that the experimental data points closer to the notch sensitive boundary are the corresponding to the larger hole diameters.

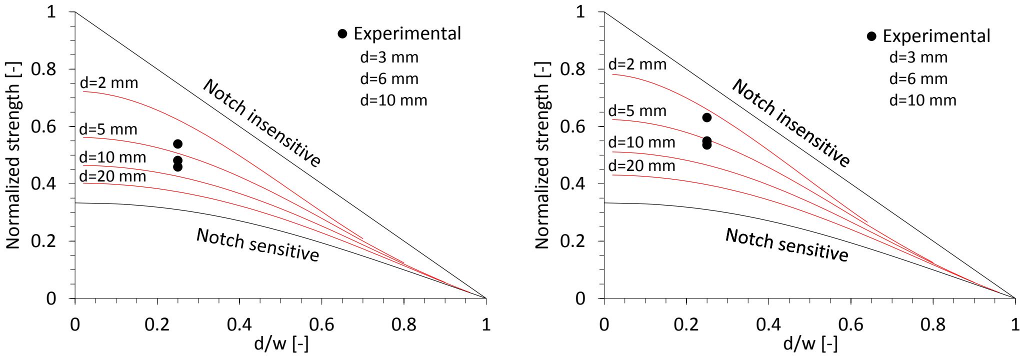

(**a**) Thin-ply $[(0/-45)/(90/45)]_{6T}$ laminate.

(**b**) Thin-ply $[(0/-45)/(45/0)/(90/45)/(-45/90)]_S$ laminate.

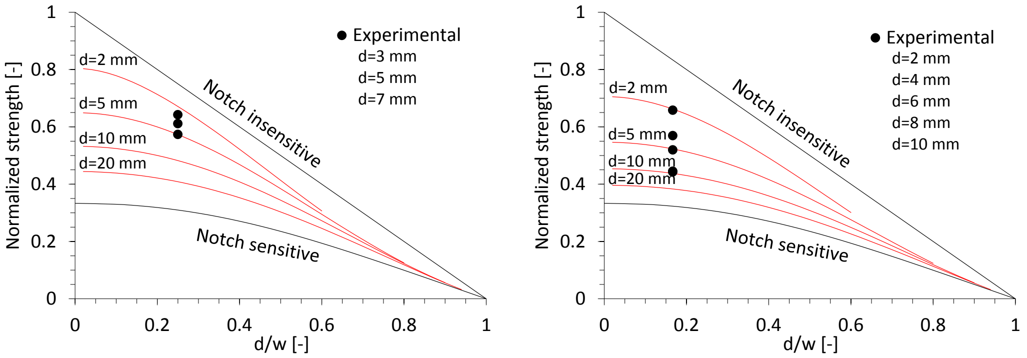

(**c**) T800/M21 $[90/45/0/-45]_{3S}$ laminate.

(**d**) IM7-8552 $[90/0/45/-45]_{3S}$ laminate.

Fig. 5.7. Design charts of the tensile notched responses for the thin-ply and alternative laminates.

Observing the predicted curves, one can see that, for a constant d/W ratio, the FFM model predicts that the mechanical response of a notched composite laminate moves from notch sensitivity to notch insensitivity for decreasing hole diameters, confirming the experimental evidence. In addition, the FFM model predicts that for large hole diameters (d) and d/W ratios the notched responses become brittle and a simple analysis based on stress concentration factors would yield sufficiently accurate predictions.

Regarding the different laminates under analysis, with respect to the the tensile notched responses (figure 5.7), one can see that the T800/M21 $[90/45/0/-45]_{3S}$ laminate, followed by the thin-ply NCF $[(0/-45)/(45/0)/(90/45)/(-45/90)]_S$ (lay-up 2) laminate, exhibits the lowest notch sensitivity. In fact, the predicted curves for the thin-ply lay-up 2 and T800/M21 laminates (figures 5.7b and c) are closer to the notch insensitive boundary than those showed for the thin-ply NCF $[(0/-45)/(90/45)]_{6T}$ (lay-up 1) and IM7-8552 $[90/0/45/-45]_{3S}$ laminates (figures 5.7a and d). The last one is the most notch sensitive of these composite materials.

On the other hand, with respect to the compressive notched responses (figure 5.8), one can see that the IM7-8552 $[90/0/45/-45]_{3S}$ laminate is the least notch sensitive of the

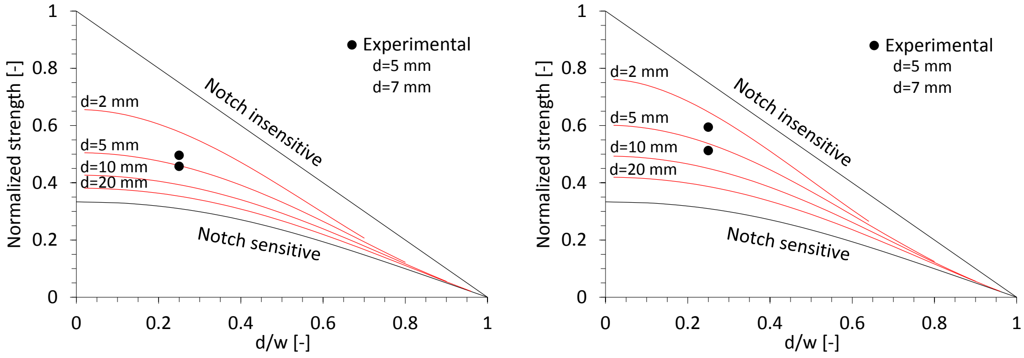

(a) Thin-ply $[(0/-45)/(90/45)]_{6T}$ laminate.

(b) Thin-ply $[(0/-45)/(45/0)/(90/45)/(-45/90)]_S$ laminate.

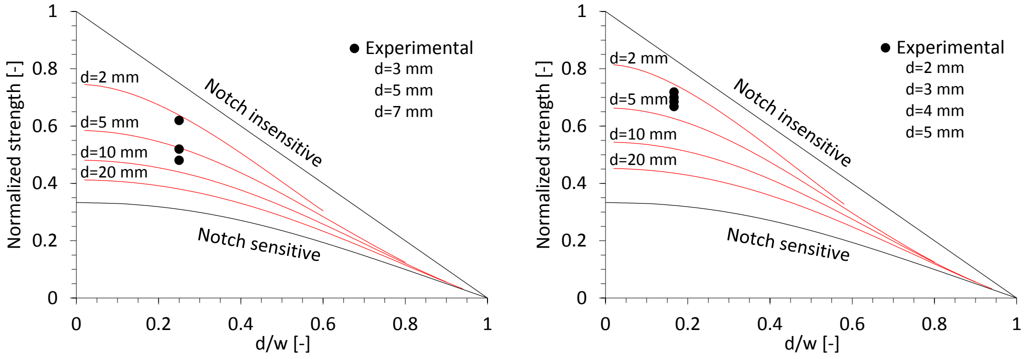

(c) T800/M21 $[90/45/0/-45]_{3S}$ laminate.

(d) IM7-8552 $[90/0/45/-45]_{3S}$ laminate.

Fig. 5.8. Design charts of the compressive notched responses for the thin-ply and alternative laminates.

analysed laminates, whose predicted curves (figure 5.8d) are clearly closer to the notch insensitive boundary than those of the other laminates. The thin-ply lay-up 2 laminate follows it, as well as the T800/M21 laminate (figures 5.7b and c, respectively). Finally, one can see that the thin-ply lay-up 1 laminate (figure 5.8a) clearly shows the highest notch sensitivity, since its predicted curves are considerably below those showed for the other laminates.

Comparing the predicted notched responses with the experimental data, one can see that the use of the design charts proposed by Camanho et al. [119] conducts to reliable predictions of the notched behavior of composite laminates, obtained in a fraction of a minute, whose results can be very useful for preliminary sizing and optimization of composite notched structures. Note that the calculation of such design charts is only possible because the FFM model does not require any inverse identification from an open-hole test. Indeed, it would be unreliable to calculate these design charts using any of the alternative closed-form models previously described, since to do so, a set of open-hole tests would be necessary for inverse identification of the length of the inherent flaw (in the IFM) or the characteristic distances (in the PS and AS models) for each d/W ratio, which would be impracticable.

5.5.3. Notch sensitivity factor

The FFM model can also be used to assess the inherent brittleness of different combinations of materials and geometries [119]. To do so, Camanho et al. [119] introduced a dimensionless parameter, designated *notch sensitivity factor*, defined as,

$$\eta_N = \frac{d}{l} \tag{5.21}$$

where l is the crack extension at failure, given by the nonlinear equation (5.18), and d is the hole diameter.

Camanho et al. [119] demonstrated that the notch sensitivity factor increases with the hole size specially for materials with a low fracture toughness. For open-hole carbon/epoxy laminates that exhibit either brittle or pull-out failure modes (i.e., laminates whose main failure mechanism in not delamination), it is reasonable to admit that when $\eta_N \geq 22.5$ the material/structure is brittle. In this case, it is possible to predict the notched strength with a good accuracy simply using the stress concentration factor as $\bar{\sigma}^\infty = X^L/K$, where X^L is the laminate tensile (X_T^L) or compressive (X_C^L) unnotched strength, and K is the tensile (K_T) or compressive (K_C) fracture toughness. In such conditions, the FFM prediction tends to the solution obtained for a perfectly brittle, notch sensitive material. On the other hand, when $\eta_N \leq 0.4$ the material/structure is considered to be ductile. So, it is possible to predict the notched strength simply using the geometry of the specimen as $\bar{\sigma}^\infty = X^L(1 - d/W)$, where X^L is the laminate tensile (X_T^L) or compressive (X_C^L) unnotched strength and W is the width of the laminate. For the intermediate quasi-brittle response, more complex analyses are required.

Figure 5.9 shows the relations between the notch sensitivity factor (η_N), calculated using FFM, and the hole diameter (d) for the thin-ply carbon NCF C-Ply™ T700/AR-2527 epoxy laminates, for the T800/M21 $[90/45/0/-45]_{3S}$ laminate, and for the IM7-8552 $[90/0/45/-45]_{3S}$ laminate, for both tensile and compressive notched responses.

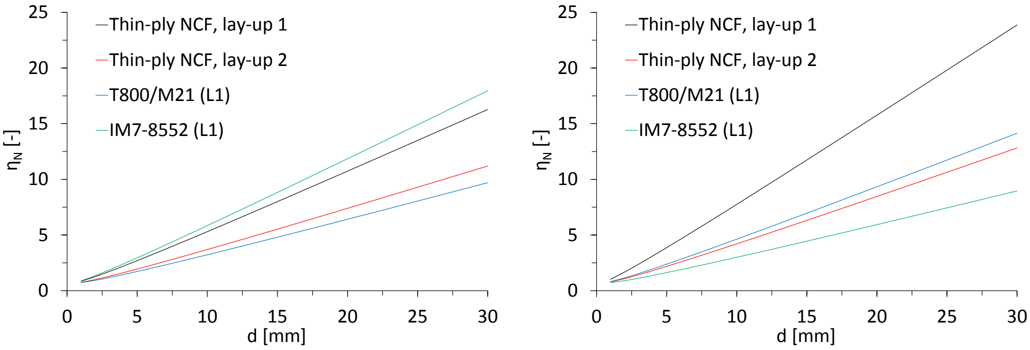

(**a**) Tensile notched response.

(**b**) Compressive notched response.

Fig. 5.9. Relation between the notch sensitivity factor and the hole diameter for the thin-ply NCF $[(0/-45)/(90/45)]_{6T}$ and $[(0/-45)/(45/0)/(90/45)/(-45/90)]_S$ (lay-up 1 and lay-up 2, respectively), T800/M21 $[90/45/0/-45]_{3S}$, and IM7-8552 $[90/0/45/-45]_{3S}$ laminates.

As it was observed in the experimental results discussed in chapter 4, the thin-ply carbon NCF C-Ply™ T700/AR-2527 epoxy laminates exhibit either brittle or pull-out failure modes, where delamination is almost absent. Therefore, the conclusions of Camanho et al. [119] with respect to the limits for brittle and ductile materials assessed by means of the notch sensitivity factor may also be reasonable for both thin-ply NCF laminates studied in this thesis. It is also assumed that the T800/M21 $[90/45/0/-45]_{3S}$ and IM7-8552 $[90/0/45/-45]_{3S}$ laminates verify such assumptions (indeed, the work of Camanho et al. [119] is based in the IM7-8552 $[90/0/45/-45]_{3S}$ laminate).

Regarding the tensile notched responses (figure 5.9a), the results presented herein show that the T800/M21 and the thin-ply lay-up 2 laminates are less notch sensitive than both thin-ply lay-up 1 and IM7-8552 laminates, since the notch sensitivity factors for the last ones are substantially higher, mainly for larger hole diameters, confirming the results previously discussed in section 5.5.2. However, at least for hole diameters lower than 30 mm, one can see that any of the considered laminates shows a notch sensitivity factor greater than 22.5. Indeed, the notch sensitivity factor is always lower or equal to 18, meaning that these laminates do not exhibit a brittle type of notched response for the hole diameters considered in this analysis.

With respect to the compressive notched response (figure 5.9b), these results show that the IM7-8552 laminate is the least notch sensitive composite material. These results also show that the thin-ply lay-up 2 and T800/M21 laminates exhibit similar notch sensitivity, whereas the thin-ply lay-up 1 laminate is clearly the most notch sensitive composite material, confirming the results previously discussed in section 5.5.2. Indeed, for hole diameters greater than 28 mm, and unlike the results for the tensile notched response of these laminates, one can see that the thin-ply lay-up 1 laminate has a notch sensitivity factor greater than 22.5, meaning that it is considered to exhibit a brittle type of notched response. Still, for hole diameters lower than 28 mm, its notched response is not considered a brittle one. Regarding the other laminates, for hole diameters lower than 30 mm, one can see that the notch sensitivity factor is always lower than 14, and a quasi-brittle response is expected for this range of hole diameters.

5.6. Discussion and concluding remarks

In addition to the ease of use, the closed-form models presented in this chapter were able to reasonably predict both tensile and compressive notched responses of the thin-ply NCF laminates experimentally investigated in this thesis, as well as the notched responses of the two alternative laminates typical of aircraft and aerospace industries. However, because it does not require any inverse identification from a notched experimental test, and due to its promising generality and versatility, the FFM model was considered to be the best suited one to evaluate the macroscopic size effects on CFRP, as well as the notch sensitivity by means of design charts and a recently introduced dimensionless parameter, designated *notch sensitivity factor*.

With respect to the thin-ply carbon NCF C-Ply™ T700/AR-2527 epoxy laminates investigated herein, despite the brittle type of fracture mode exhibited by these laminates, and despite some concerns regarding this issue, these predictions indicate that these composite materials do not exhibit inherent brittleness. Indeed, the previous analyses showed that the notched responses in both tension and compression are not so different from those exhibited by the alternative T800/M21 and IM7-8552 carbon/epoxy systems, both designed for the aircraft industry.

However, there are a set of factors that may influence the analyses carried out in this chapter, that should be taken into account in future works. One obvious drawback of this analysis is the absence of an equivalent laminate material to perform accurate comparisons with respect to the effect of ply thickness on size effects and notch sensitivity, and eventually regarding the effect of stitching. The possibility to carry out an apple to apple comparison between laminates of the same carbon/epoxy system (the T700/AR-2527, eventually), with different ply thicknesses and stacking sequences, and for instance with and without stitching, would greatly enhance the previous analyses. Another important factor, not so obvious but already mentioned in this thesis, is the effect of the laminate thickness. If these analyses aim to establish the in-plane size effects on notched thin-ply laminates and their notch sensitivity, it is important to guarantee that the comparisons are made with laminates of the same thickness, since, as mentioned before, independently of the laminate stacking sequence, an increase in the laminate thickness with constant hole diameter leads to a decrease in failure stress. However, the thin-ply NCF laminates studied here are 30% to 50% thinner than those used for comparison, and this difference may have some influence in the results showed and discussed previously. Therefore, in future works, it is important to minimize such differences, and possibly seek for more reliable results.

Chapter 6

Numerical modeling of damage in composite materials — An overview

The process of substantiating the structural performance and durability of composite components generally consists of a complex mix of testing and analysis. While testing alone is prohibitively expensive and time consuming, analysis techniques alone are usually not sophisticated enough to adequately predict results under every set of conditions. So, the development of accurate analytical and numerical tools that are able to predict the response of composites under general loading conditions and geometries is extremely important, because in the absence of such tools, the design process will rely on costly matrices of mechanical tests based on a large number of test specimens and empirical knockdown factors. Due to the more complex damage behavior of composite materials, the models used to predict initiation and growth of damage may take into account the progressive loss of stiffness and strength typical of these materials, generally conducting to too simplistic analytical models and/or computationally costly numerical models. However, the recent computational advances allowed numerous published demonstrations of successful representations of the initiation and propagation of damage in composite materials. In this chapter, an overview of the most common numerical modeling techniques employed in the prediction of damage onset and evolution in composite materials is presented, including a description of the composite damage mechanisms, the importance of damage scale, and the basic theories behind crack initiation and propagation in composite materials. The different approaches used when modeling damage, namely the micromechanics approach, the continuous damage mechanics approach, and the discrete damage mechanics approach (the last two on the basis of mesomechanics), and their application to composite materials are briefly described.

6.1. Introduction

When composites are to be used in structural components, a design development program is generally initiated during which the performance of the structure is assessed prior to use. This process of substantiating the structural performance and durability of composite components generally consists of a complex mix of testing and analysis. Testing alone is prohibitively expensive and time consuming because of the number of specimens needed to verify every geometry, loading, environment, and failure mode. However, in spite of the lower costs associated, analysis techniques alone, with analytical or numerical basis, are usually not sophisticated enough to adequately predict results under every set of conditions [113]. So, in order to reduce the cost of the overall effort while maintaining, or even increasing reliability, the development of accurate analytical and numerical tools that are able to predict the thermo-mechanical response of composites under general loading conditions and geometries is extremely important, whether the interest is to asses the structural integrity of composites or to quantify their energy absorption capability, particularly in the development and introduction of advanced composite materials in new applications [53, 128, 129]. In the absence of such tools, the design process will rely on costly matrices of mechanical tests based on a large number of test specimens and empirical knockdown factors [53].

The potential benefit of augmenting current design and certification processes with high-fidelity analysis methods to reduce empiricism and extensive structural testing is, therefore, well recognized. Indeed, quantification of the structural fracture resistance under various loading conditions is fundamental for evaluating the residual strength and life of composite structures [130]. The aim of damage mechanics, the mathematical science dealing with quantitative descriptions of the physical events that irreversibly alter a material when it is subjected to loads, is to develop a framework that describes the material response caused by the evolving damage state and its consequences for the mechanical behavior of the structure, i.e., a framework that describes initiation and evolution of damage up to and including rupture [5, 46, 59]. The greatest difficulty in the development of an accurate and computationally efficient numerical procedure to predict damage growth has to do with how to analyse the material micro-structural changes and how to relate those changes to the material response [46, 48].

The onset and evolution of damage in composite materials is different, and generally more complex than that of metals both in the involved mechanisms and in the effects on the mechanical properties [8, 91, 131]. In fact, the damage previous to failure in composites with non-ductile matrices involves a loss of stiffness and strength which is more relevant than in metals [131, 132]. Therefore, a damage model to predict initiation and growth of damage and calculate the intensity of each damage mechanism in composites should take this behavior into account, leading to the so-called progressive damage models [131, 133, 134]. However, even in the case of laminated composites (the most studied and, therefore, the best understood ones), the prediction of damage initiation and propagation, including final fracture, remains a major challenge in modern mechanics of composite materials [134].

In the last years, the advances in computational methods and the numerous published demonstrations of successful representations of the initiation and propagation of damage in composite materials have been remarkable. However, due to these rapid developments and the apparent diversity of the proposed approaches, it is necessary to formulate under what conditions a given model can be expected to work and when it will cease to be adequate, something that sometimes is difficult given the complexity of these methods [44].

6.2. Damage mechanisms in composite materials

Macroscopic fracture in composite materials is a result of the evolution of discrete damage events during the loading process, namely fiber/matrix debonding and subsequent pull-out, matrix cracking and yielding, delamination between plies, fiber breakage (longitudinal tension) or fiber kinking/buckling (longitudinal compression), and fiber splitting [1, 8, 44, 48, 51, 58, 59, 129, 131, 135, 136]. These damage mechanisms can be divided into intralaminar and interlaminar damage. Intralaminar damage mechanisms correspond to different underlying micromechanical failure modes, such as fiber fracture/buckling, matrix cracking and fiber/matrix debonding and pull-out. Interlaminar damage mechanisms correspond to interfacial separation of the plies, i.e., delamination [44, 137].

In composite materials, there are some primary differences between the failure mechanisms in tension and compression. Tensile failure in most commonly due to fiber breakage and matrix cracking or yielding. However, depending on the laminate lay-up, failure can also involve delamination. For compressive failure the primary failure mechanisms are kink banding, i.e., formation of matrix cracking or yielding and fiber rotation in plies having their reinforcement aligned with the loading direction, along with delamination and off-axis matrix cracking [128].

Additionally, due to the presence of different constituents, namely fiber and matrix, and due to the anisotropy in both stiffness and strength properties, in composites the damage mechanisms develop at different levels, acting together under different combinations [44]. Such combinations of damage depend on the stacking sequence and ply thicknesses and cause redistributions of stress in the fractured composite. While some combinations may reduce local stress concentrations, others may conduct directly to a structural collapse [44, 129]. Therefore, a methodology capable of predicting structural strength must take into account damage initiation and propagation. However, the idealization of the individual constituent responses and their interactions is still an extremely complex task. Accordingly, the details of the complex mechanisms that lead to failure of a composite structure are not fully understood [44].

6.3. Damage scale

The ability of damage models to predict physical phenomena, such as the initiation and propagation of damage, strongly depends on the scale (or resolution) at which the (failure) mechanisms under consideration are modeled [44, 58]. In fact, the conceptual idealization of damage process, i.e., the identification, characterization and formulation of the governing physical principles of damage evolution, may span from molecular dynamics scales to structural mechanics scales, including the intermediate micro and mesomechanics scales [44]. In the case of composite laminates, where the in-plane dimensions exceed the length scale at which delamination, matrix cracking and fiber debonding take place by one to several orders of magnitude, the proper definition of the modeling scale has particular importance [58].

At lower structural scales, damage idealizations have higher resolution, higher kinematic freedom and are able to recreate all kinds of damage mechanisms, each of these captured with separate damage laws [5, 44, 134]. **Micromechanical scale models**, based in the constituent level, represent what is normally the smallest scale of composite damage idealization [5, 44, 138]. At this scale, experimental data on the properties of the fibers and matrix materials, which are seen as individual homogeneous materials, are used to predict the properties of the individual laminae, then the laminate and finally the structure [4, 5, 138]. Detailed matrix damage mechanisms, such as matrix plasticity and damage, and fiber/matrix interface cracking can be easily represented, typically based on a reduction of the material stiffness [44]. Hence, fracture is represented as a band of localized volumetric stiffness reduction, referred to as a “soft discontinuity” (material domain in which the damage had become critical, i.e., where the material cannot sustain stress anymore [133]), as opposed to a “hard discontinuity”, in which voids are represented by displacement discontinuities in the model, as in classical computational fracture mechanics [44]. If successful, this approach has the potential of allowing the designer to predict the effects of material changes before lamina test data is available [5, 138], and the influence of the geometry and spatial distribution of the phases (i.e., size, shape, clustering, connectivity, etc.) on the mechanical behavior of the lamina [139]. However, although precise estimations of the onset and propagation of damage and accurate prediction of the failure strength may be achieved [139], micromechanical models are far from being complete for the prediction of damage and final fracture localization [134]. Furthermore, these models introduce an additional set of calculations, with the associated possibility of introducing inaccuracies into predicted lamina properties, and, due to computational constraints, it is typically limited to two-dimensional (2D) models, which represent domains much smaller than a ply thickness [44, 138, 140].

Mesomechanical scale approaches take the laminate layers or the sublaminates as the basic homogeneous building blocks and use the orthotropic material properties related to the directions of the fibers, determined from lamina-level characterization tests, to predict the behavior of the whole laminate, disregarding imperfections and variabilities that must be considered at lower scales [5, 44, 50, 136, 138]. For example, this is the scale level used for the analysis of delamination [58]. Mesomechanical scale is typically divided into two different approaches, the *continuum damage mechanics* (CDM) approach and the *discrete damage mechanics* (DDM) approach, both with several computational advantages compared to micromechanical models. To account for micromechanical effects such as fiber/matrix debonding, some mesomechanical methods perform concurrent analysis on idealized unit-cell models that represent typical distribution patterns of fibers in matrix. Other mechanisms, such as transverse matrix cracking or fiber kinking, which depend on meso-scale data such as ply thickness, are usually taken into account with failure criteria and in-situ strengths. These failure criteria are used in conjunction with material degradation schedules to soften the material properties associated with a particular mode of failure. The delamination failure mechanism is represented at the meso-scale level as a hard discontinuity between plies, which is generally modeled using either cohesive elements or nonlinear springs [44].

The most common idealizations for composite damage are **CDM models** at the meso-scale level, one of the most used approaches to evaluate the damage initiation and propagation in structural components [44]. Continuum approaches to fracture regard crack initiation and growth as the ultimate consequences of a gradual, local loss of material integrity, and are defined in the framework of the thermodynamics of irreversible processes, without requiring calibration and, consequently, potentially providing the means for a truly predictive methodology of damage onset and propagation [53, 133]. CDM models assume that plies are composed of a homogeneous material with orthotropic properties (in the case of composite laminates), and damage modes, such as fiber fracture, fiber kinking and delamination, are represented as a reduction in the corresponding stiffnesses, using a set of continuous damage variables and interacting activation functions which explicitly describe the local loss of material integrity, directly or indirectly representing the density and/or redistribution of the microscopic defects that characterize damage [44, 53, 114, 133, 141, 142]. In CDM models, localizing damage is therefore represented as a "soft discontinuity", as opposed to the "hard discontinuities" used in DDM models [44]. Redistribution of stresses results in the concentration of deformation and damage growth in a relatively small region in front of the crack tip, the so-called process zone, which determines in which direction and at which rate the crack will propagate. Thus, crack initiation and growth follow naturally from the standard continuum mechanics theory, instead of from separate fracture criteria [133]. However, the diffused representation of damage in the CDM approach may lack sufficient resolution to capture some important damage interactions at the micromechanical scale. Particularly, meso-scale CDM models have difficulty in predicting the correct propagation of matrix cracks parallel to the fibers, and the damage models for intralaminar damage may not interact correctly with the delamination models [44].

DDM models represents a new class of analysis methods in which the plies are represented at the meso-scale level, i.e., the material is assumed to be homogeneous with orthotropic properties, but where displacement discontinuities, such as cracks, are regarded as a zero-thickness cohesive process zones. Alternatively, embedded discontinuity models, such as the extended finite element method (X-FEM), are used to insert cracks and delaminations in locations that are independent of the mesh orientation and without the need of remeshing [44, 143]. DDM models can be used to represent complex networks of transverse matrix cracks and delaminations using a single simple cohesive law [44].

In **structural-level (macromechanical) damage models**, performing analyses is easier and the computational effort required is more reduced. The material is assumed homogeneous and the effects of the constituent materials are represented only by averaged apparent properties of the composite material. These models allow designers to study stress patterns and stress concentration regions in a component assuming the composite to be an homogeneous material [5]. Cracks are represented as hard discontinuities and prediction of the propagation of the crack could be based on a strain-softening law or a criterion based on the critical energy release rate. However, all structural-level crack propagation criteria are strongly dependent on the material system and laminate configuration; consequently, these criteria must be determined for each new material system and laminate stacking sequence. In addition, structural-level semi-empirical fracture models cannot address the characteristics of the crack-tip damage zone nor the complex interactions between micro and macro-failures associated with the crack-extension process. Instead, the crack-tip damage zone is simulated as some "effective" notch-tip damage zone that is assumed to grow in a self-similar manner. In many cases, self-similar crack growth is not observed, and the lack of resolution in the damage mechanisms often renders structural-level damage models inaccurate after a short propagation damage [44].

Alternatively, **multi-scale approaches** consider the various aspects of the entire structural problem at different levels of observation, each of them characterized by a well-defined *length-scale*. The different levels at which analyses are carried out are connected either through *length scale transitions*, in which the structural behavior at a given level is homogenized to arrive at mechanical properties at a next higher level, or through finite element analysis (FEA) which are conducted at two different levels simultaneously, connected by matching the boundary conditions at both levels, usually invoking periodicity to reduce the amount of computations that need to be performed [50, 58]. Therefore, multi-scale analyses can be performed by using the best out of each level of analysis [5]. For instance, in an information-passing multi-scale approach, analyses on unit cells on micro-scale can determine the stiffnesses and strengths of unidirectional fiber bundle material through homogenization techniques, the mesomechanical unit cell describes the fiber architecture of the composite, providing stiffnesses and strengths for computations on macro-scale [5, 11].

6.4. Crack initiation and propagation in composites

6.4.1. Fracture mechanics

Fracture initiation is associated with defects such as voids, machining irregularities, stress concentrating design features, damage from impacts, etc., which can propagate and progressively reduce residual strength [1, 8]. **Linear elastic fracture mechanics** (LEFM) characterizes crack behavior by means of the *crack-tip stress intensity factor* (SIF), K. Although routinely used to predict the residual strength of cracked metallic structures since the 1970s, the ability to predict crack initiation and propagation in composites based on LEFM only emerged with the development of computational methods, in particular the modified *virtual crack closure technique* (VCCT) and the implementation of the *J-integral* in the finite element method (FEM) [44, 91]. The VCCT, proposed by Rybicki and Kanninen [144], is a straightforward computational method to calculate the energy release rate, G, for each mode of fracture, based in a modified crack closure integral. The J-integral, first introduced by Rice [145], later implemented in a *virtual crack extension method* [146–148], and further extended to domain integral methodologies for general FEA [149–153], is a measure of the intensity crack tip fields that can be applied to both quasistatic and dynamic problems with elastic, plastic, or viscoplastic material responses (surpassing LEFM conditions[1]), as well as thermal loading.

Unfortunately, the implementation of such methods only successfully simulates single one-dimensional (1D) crack propagation, with the fracture mechanics scaling procedure generally occurring outside of the finite element (FE) code. If multiple crack tips exist, multiple computer runs are required to propagate the cracks, each of these runs corresponding to a different crack length, requiring tedious postprocessing of multiple FE solutions [154].

According to LEFM theory, when the energy release rate (or the SIF) exceeds the corresponding critical value, G_c (or fracture toughness, K_c), the crack should propagate. However, LEFM assumes that the material response is elastic and that the mechanisms that consume the fracture energy act at the crack tip. So, LEFM theory is limited to applications

---

[1] Note that, when LEFM conditions are valid, the *J-integral* equals the energy release rate, i.e., $J = G$. Otherwise, J represent an extension of the definition of G (valid for linear-elastic conditions) to nonlinear behavior.

in which the fracture process zone is confined to the immediate neighborhood of the crack tip, and it cannot be applied to a number of important cracking problems involving some of the tougher, more ductile materials that fracture after extensive nonlinear deformation. This is the case of many composite materials and structures, where the fracture process zone may be relatively large compared to other structural dimensions [44]. Furthermore, if nonlinear behaviors exist in a model, difficulties arise when using the previously mentioned LEFM computational methods in determining the load at which the crack tip energy release rate equals its critical value [154].

In order to avoid some of these problems, a set of *fracture interface finite elements* have been proposed that take advantage of the LEFM theory and combines it with the ease of use of interface based FEM. Particularly, these elements allow the simulation of initiation and propagation of interlaminar cracks (delaminations) or debonding in layered materials using LEFM procedures without many separate analysis. These fracture elements are based on the mixed-mode modified VCCT, and utilize common mixed-mode delamination growth, fatigue crack onset and fatigue crack growth criteria. However, the discussion regarding the accuracy of the VCCT is also applicable to these elements (elastic material response, confined fracture process zone, and difficulties when nonlinear behavior occurs in the model), and maintaining accuracy of the analysis during the propagation phase is a challenging task [154].

Some criteria, such as Sun and Qian's two parameter model [155], were devised for extending the classical LEFM theory to situations where it cannot be directly applied. However, these criteria can easily be supplanted by **nonlinear fracture mechanics** (NLFM), which provides a framework for characterizing crack growth resistance and for analysing initial amounts of stable crack growth. NLFM was initiated by Irwin with a model for ductile solids based on an elastic/perfectly plastic material response to describe the effect of plastic material behavior in the vicinity of the crack-tip on the fracture propagation. By assuming that plasticity affects the stress field only in the vicinity of the crack tip, the size of the plastic region may be estimated by equating the yield strength to the stress of the elastic field ahead of the leading crack tip (see figure 6.1) [44].

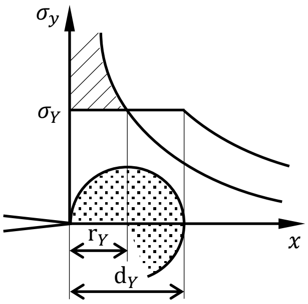

Fig. 6.1. Estimated size of the plastic region, assuming plane stress conditions, according to Irwin's model (after Branco et al. [156]).

An alternative, simple NLFM model, based on LEFM considerations, was proposed in 1960 by Dugdale [157]. According to Dugdale's model, yielding in an ideal elastic-plastic infinite plate subjected to an uniform tensile stress σ must occur over some length $c - a$ ($c > a$) measured from the crack tip, as shown in figure 6.2. It is assumed that the plate may deform elastically under the action of the external stress together with a tensile stress distributed over the yielded (plastic) region. Assuming that plastic deformation occurs when the yield strength, σ_Y, is reached, this tensile stress distributed over part of an hypothetical crack may be equal to the yield strength, as shown in figure 6.2. Accordingly, the size of the plastic region may be estimated assuming that the stress singularity in the hypothetical crack tip, $|x| = c$, ceases to exist, i.e., $K_{|x|=c} = 0$.

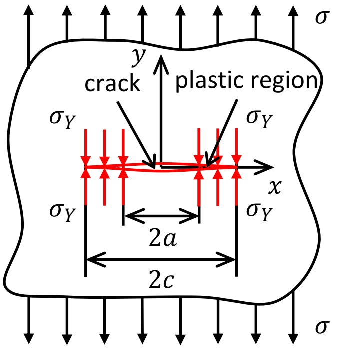

Fig. 6.2. Draft of Dugdale's model.

Another NLFM approach with particular interest is the *cohesive zone model* (see section 6.4.2), a methodology that simulates the nonlinear fracture response near the crack tip. Unlike LEFM models, where an initial crack must be defined and the simulation of crack growth may require complex moving mesh techniques to advance the crack front when the local energy release rate reaches a critical value, cohesive zone models can be applied to initially uncracked structures and describe the entire fracture process, including crack initiation, crack growth and complete structure failure [44, 65].

6.4.2. Cohesive zone models

Cohesive zone models (or cohesive crack models) are based on kinematic descriptions of the fracture process that use strong discontinuities in the displacement field and constitutive models that account for the different loading modes [44, 158, 159]. These models have the ability to be numerically implemented, namely in *cohesive* (*decohesion*) *elements*, such as the one formulated by Camanho et al. [65], which use failure criteria that combine aspects of strength-based analysis to predict the onset of the softening process, and fracture mechanics to predict damage propagation. For example, when simulating delamination, interfacial cohesive elements are placed between composite layers, modeling the plies as continua, and delamination onset and propagation are simulated by softening of the cohesive element without previously knowledge of the location, size and propagation direction of the delaminations [58, 65, 91, 160]. This approach shows excellent performance in simulation of nonlinear progressive failure analyses where both ply damage and delaminations are present [91, 159], and it is considered to be the most feasible approach when the goal is to simulate large three-dimensional (3D) structures with multiple delamination onsets and propagation fronts [161].

Cohesive elements can be divided into two main groups, continuous interface elements and point cohesive (decohesion) elements. Different types of continuous cohesive elements include zero-thickness volumetric elements connecting solid elements, finite-thickness volumetric elements connecting shell elements and line elements. Point cohesive elements are identical to nonlinear spring elements connecting nodes [65].

Cohesive zone models are based in the so-called *cohesive interfacial laws* (or *traction-separation laws*), phenomenological mechanical relations between the tractions, σ, and the interfacial separations, δ, such that, with increasing interfacial separation, the tractions across the interface reach a maximum, and then decrease and vanish when complete decohesion occurs [44, 158].

Complete representation of fracture in a continuum requires an ability to model both the initiation and growth of fracture, whose principles can be illustrated by considering a quasi-brittle bar of length L and cross-section A, as shown in figure 6.3a. To model the fracture of the bar, a cohesive interface is introduced. The crack is assumed to open according to the softening law shown in figure 6.3b. Initially, the crack is assumed to be elastic, and the crack closing forces are related to the interfacial displacement jump, δ_{coh}, by a high penalty stiffness k. If the displacement jump exceeds a critical value, δ_i, the crack closing forces are assumed to soften linearly such that the area under the traction-displacement curve is equal to the fracture toughness, G_c. Complete separation is achieved when the displacement jump exceeds δ_f. Therefore, the bilinear cohesive law can be expressed in two parts,

$$\sigma = \begin{cases} k\delta, & \delta < \delta_i \\ (1-d)k\delta, & \delta_i \leq \delta < \delta_f \end{cases} \tag{6.1}$$

where the damage variable d is a function of the displacement jump and accounts for the reduction in load-carrying ability of the material as a result of damage [44].

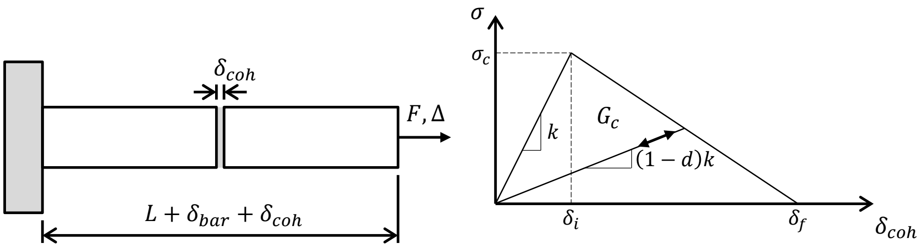

(**a**) Elastic bar with a cohesive crack. (**b**) Bilinear cohesive law.

Fig. 6.3. Quasi-brittle bar of length L and cross-section A with a cohesive interface (after Dávila et al. [44]).

In composite materials, however, more than one physical phenomenon is often involved in the fracture process. Some phenomena act at small opening displacements, which are confined to correspondingly small distances from the crack tip, and others act at higher displacements, which extend further into the crack growth response. For example, when fiber bridging or friction effects are present, a softening law may have a peak at low crack displacements, to represent the tip process zone, and a long tail at high crack displacements to represent the bridging in the wake of the crack. In this case, multilinear softening laws can be obtained by combining two or more bilinear cohesive laws, as illustrated in figure 6.4 [44].

To describe a trilinear cohesive law, such as shown in figure 6.4, it is convenient to consider the superposition of two bilinear cohesive laws that peak at the same displacement jump. The two underlying linear responses may be seen as representing different phenomena, such as quasi-brittle delamination fracture characterized by a short critical opening displacement, δ_{c1}, and fiber bridging, characterized by a lower peak stress and a

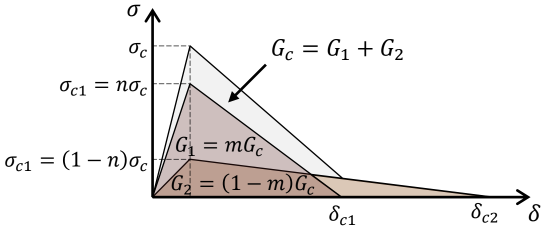

Fig. 6.4. Trilinear cohesive law obtained by superposing two bilinear laws (after Dávila et al. [44]).

longer critical opening displacement, δ_{c2}. However, note that the two bilinear softening responses are used for convenience and do not necessarily correspond to two distinct failure modes which could peak at different displacement jumps. In fact, the bridging strength does not typically contribute to the peak strength, which is associated with the intrinsic fracture process prior to the bridging process. Consequently, a trilinear cohesive law can be described by the proportions $\sigma_{c1} = n\sigma_c$, $\sigma_{c2} = (1-n)\sigma_c$, $G_1 = mG_c$ and $G_2 = (1-m)G_c$, with $0 \leq n, m \leq 1$, so that,

$$G_c = G_1 + G_2 \quad \text{and} \quad \sigma_c = \sigma_{c1} + \sigma_{c2} \tag{6.2}$$

A procedure for determining the strength ratio n and the toughness ratio m that approximate an experimentally-determined R-curve can be seen, for instance, in reference [162]. As one can expect, a multilinear cohesive law can provide a more accurate approximation of the process zone length, as well as a more accurate approximation of an experimentally determined R-curve [44].

Additionally, in structural applications of composites, crack growth is likely to occur under mixed-mode loading. Therefore, a general formulation for cohesive laws must address mixed-mode fracture. A mixed-mode cohesive law can be illustrated in a single 3D map by representing the bilinear material responses in pure mode I and pure mode II on normal planes, as shown in figure 6.5. Under mixed-mode, damage initiates at δ^0, and complete fracture is reached at δ^F. Consequently, the tractions (σ) for mode I and mode II under mixed-mode loading follow the reduced curves O–N^M–δ_I^{FM} and O–S^M–δ_{II}^{FM}, respectively. The areas under these two curves represent the fracture energies under mixed-mode.

In a model proposed by Turon et al. [56], the initial strength σ_c (initiation criterion) and the critical value of the energy release rate G_c (propagation criterion) in the mixed-mode cohesive interface damage may be expressed as functions of a mixed-mode parameter B, defined as,

$$B = \frac{G_{II}}{G_T} = \left(\frac{\delta_{II}}{\delta}\right)^2 = 1 - \left(\frac{\delta_I}{\delta}\right)^2 \tag{6.3}$$

where $G_T = G_I + G_{II}$, δ_I and δ_{II} are the displacement jumps in mode I and in mode II, respectively, and δ is the total mixed mode relative displacement ($\delta = \sqrt{\delta_I^2 + \delta_{II}^2}$). The initial strength σ_c and the critical value of the energy release rate G_c are defined as,

$$\sigma_c^2 = N^2 + (S^2 - N^2)B^\eta \tag{6.4}$$

$$G_c = G_I + (G_{II} - G_I)B^\eta \tag{6.5}$$

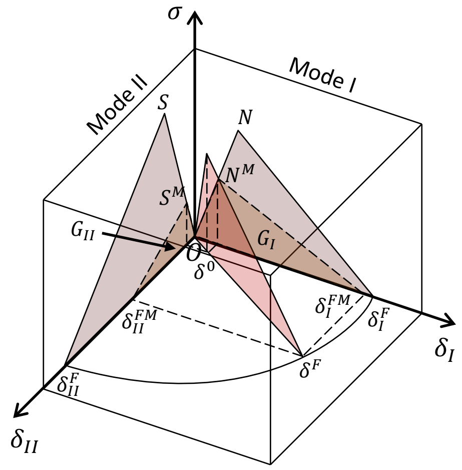

Fig. 6.5. Mixed-mode cohesive law (after Dávila et al. [44]).

where N and S are the transverse tensile and shear strengths, respectively, of a composite ply, G_I and G_{II} are the mode I and mode II critical energy release rate values, respectively, and the parameter η can be obtained applying a least squares fit to the experimental data obtained, for instance, from mixed-mode bending (MMB) tests at different mode ratios[2].

Despite the maturity of cohesive laws, according to Dávila et al. [44], some issues regarding the prediction of crack propagation under mixed mode conditions remain unresolved. In particular, the mode ratio is rarely, if ever, constant during fracture, even in MMB specimens, where, from an LEFM point of view, the mode ratio is constant during propagation. It was observed that the opening displacements at damage initiation are dominated by mode I, and that immediately before complete separation the displacement jumps are mostly in mode II. Turon et al. [163] showed that when delamination grows under pure mode I or pure mode II loading, there is no effect of the interface strength on the energy dissipated during delamination propagation. However, if the mixed-mode ratio varies as the damage grows, the mixed-mode interface strength and fracture toughness of the material varies according to equations (6.4) and (6.5). Therefore, it must be assured by the model that the time derivative of the damaged area is always non-negative, otherwise the model predicts healing of the material. By enforcing this condition, a unique relation between interlaminar strengths and fracture toughnesses can be obtained,

$$\tau_0 = \sigma_0 \sqrt{\frac{G_{IIc}}{G_{Ic}}} \tag{6.6}$$

---

[2] If mode III loading occurs, the model proposed by Turon et al. [56] may be expressed as,

$$B = \frac{G_{shear}}{G_T} = \left(\frac{\delta_{shear}}{\delta}\right)^2 = 1 - \left(\frac{\delta_I}{\delta}\right)^2$$

with $G_{shear} = G_{II} + G_{III}$, $G_T = G_I + G_{shear}$, $\delta_{shear} = \sqrt{\delta_{II}^2 + \delta_{III}^2}$ and $\delta = \sqrt{\delta_I^2 + \delta_{shear}^2}$,

$$\sigma_c^2 = N^2 + (S^2 - N^2)B^\eta$$

where $S = T$ are the in-plane and out-of-plane shear strengths, respectively, and finally,

$$G_c = G_I + (G_{II} - G_I)B^\eta$$

where τ_0 is the interlaminar shear strength and σ_0 is the peel strength. As shown by Turon et al. [163], the load-displacement curves obtained when the shear strength is set according to equation (6.6) are independent of the interlaminar strengths used and they are in agreement with the LEFM solution for any mixed-mode ratio considered. However, relation (6.6) is only useful for problems where LEFM applies. For tougher materials, which have non-negligible fracture process zones ahead of a crack tip, both the strength and the shape of the cohesive law define the global response, and the modification of the interlaminar strengths would not be appropriate [163]. An alternative solution, also proposed by Turon et al. [163], consists on adjusting the penalty stiffness, which is a non-physical parameter for undamaged material points, taking the interlaminar strengths as the measured material constants. According to this solution, the following relation between the mode I and shear mode interface stiffness, k_I and k_{shear}, respectively, is obtained,

$$k_{shear} = k_I \frac{G_{Ic}}{G_{IIc}} \left(\frac{\tau^0_{shear}}{\tau^0_I} \right)^2 \tag{6.7}$$

where τ^0_{shear} and τ^0_I are the shear mode and mode I interlaminar shear strengths, respectively. The use of different penalty stiffness for mode I and for shear mode loading requires the re-formulation of the constitutive model, something not regarded by Turon et al. [163]. Therefore, further research is needed for a full understanding of mixed-mode crack propagation.

Finally, note that in notch-ductile parts, the load-carrying capability is dictated by strength, while in notch-brittle parts it is dictated by fracture toughness. For the range in between these extremes, both strength and toughness play a role. However, because cohesive laws are defined in terms of strength and fracture toughness (G_c), they can represent equally well the propagation of cracks as the softening of a material, which gives them the capability to deal with the entire scope of material responses [44].

6.4.3. Length of the fracture process zone

Most failure processes in materials are characterized by the development of a process zone where deformations start to localize and from which all failure events will originate [114]. In composites, the **fracture process zone** (or cohesive zone) is a nonlinear zone characterized by plastic deformations and progressive material softening due to nonlinear material deformations, such as micro-cracking, void formation and fiber/matrix pullout [44, 114]. The propagation of the process zone results in a global decrease of the load carrying capacity of the structure, denoted as structural softening. Further propagation finally triggers the total fracture or failure of the structure [114].

The **length of the fracture process zone** is generally considered to represent an intrinsic characteristic of a material response, since it mainly depends on the microscopic material interaction [44, 114]. In many situations of crack growth in composite structures, it may be relatively large compared to other structural dimensions. However, when the structural dimensions are small, the boundary conditions can influence the stress distribution ahead of the crack tip, while in notched specimens whose height is less than the crack length, the non-singular stresses become significant and induce a larger process zone [44].

The size of the process zone is dependent on the type of material softening and it must be considered in many situations of crack growth, since development of a process zone gives rise to stable growth and crack growth resistance. In fact, the apparent fracture toughness increases with crack growth until the process zone is fully developed, an effect denoted as the *resistance curve* (or the *R-curve*). In the presence of an R-curve, the toughness measured during crack propagation typically increases monotonically until reaching a steady-state value. In the case of delamination, the increase in toughness with crack growth is attributed mostly to fiber bridging across the delamination plane. In the through-the-thickness fracture of composite laminates, the R-curve effect is caused by a combination of damage mechanisms leading the process zone, and fiber bridging in the trailing region of the process zone. This R-curve response makes it difficult to predict the effect of structural size on strength using LEFM, since experimental results for notched laminated composites of different sizes indicate that their strength cannot normally be predicted using a constant fracture toughness [44].

The knowledge of the length of the process zone is also useful for determining the FE mesh requirements for a given material, since it is necessary to use more than three elements in the simulation of the process zone. On the other hand, the development of analytical expressions for predicting accurately the length of the process zone for general configurations is the subject of ongoing research [44].

6.5. Micromechanics approach

Computational micromechanics is emerging as an accurate tool to study the mechanical behavior of composites due to the sophistication of the modeling tools and to the ever-increasing power of digital computers. Within this framework, the macroscopic properties of a composite lamina can be obtained by means of the numerical simulation of the deformation and failure of a representative volume element (RVE) of the microstructure. Indeed, by using the appropriate constitutive equations for the fiber, matrix and interfaces, computational micromechanics can assess the mechanical behavior of engineering composites, providing a detailed picture of deformation and fracture mechanisms at microscopic level, including the effect of nonlinear processes and of their interaction [139, 164, 165].

A RVE can be defined as the smallest volume fraction of the material whose properties are representative of the global mechanical performance of the system [17, 18]. Therefore, an important issue when using computational micromechanics is the minimum size of the RVE, which cannot be too large, as this would endanger the possibility to numerically analyse it, but it cannot be too small, since it should contain all the necessary information about the statistical description of the microstructure, so that the average properties of this volume element are independent of its size and position within the material [5, 139, 166]. This critical RVE size depends on the phase and interface properties, and on the spatial distribution [139]. In addition to the size of the RVE, other important issues are fiber size distribution, volume fraction and spatial arrangement of reinforcements in the matrix. This spatial arrangement is usually not periodic and is highly dependent upon the manufacturing process [5, 166]. In fact, in order to reproduce the onset and evolution of damage in the matrix, it is important to represent properly the transverse randomness of the fiber distribution (distance to first neighbors, occurrence of clusters of fibers, etc.) [166, 167].

However, in the computational analysis of composite materials, periodic RVE are often employed, assuming that the material has a deterministic and ordered distribution of fibers, mainly because this assumption leads to lower computational costs [167, 168]. In order to understand if this type of assumption conducts to worse results than when using

RVE with randomly distributed fibers, Trias et al. [168] compared the stress and strain distributions between a periodic and a random model for a carbon fiber reinforced polymer, established in [167]. This comparison showed that periodic models can be used for the simulation of effective properties when the accuracy required is not so high (the difference in the Young modulus was about 12% and in the Poisson ratio about 6%); however, for any statistical analysis or for the simulation of local phenomena such as local damage or matrix cracking, random models must be considered.

Using computational micromechanics, Ng et al. [169] presented a procedure to determine the nonlinear in-plane lamina shear response and the full nonlinear response of the in-situ matrix of laminated composites. The accuracy of the nonlinear response of the in-situ matrix was determined using the nonlinear shear stress-shear strain response of the composite, measured using experimental data, and the in-situ matrix equivalent stress-strain response, calculated with some simplifying assumptions, by means of a micromechanics-based 3D FE model. To perform such analysis, a RVE of the ±45° symmetric laminate tensile test was used. In this model, each lamina consisted of three layers of fibers (+45° and −45°), packed using an hexagonal (periodic) scheme, surrounded by the matrix. No periodic boundary conditions were imposed, since the authors admitted that the errors incurred in such relaxation were minimal for the proposed RVE geometry. According to the authors, the numerical results were found to match experimental results well.

Romanowicz [170] investigated the effect of damage due to interfacial debonding on the post initial failure (softening) behavior of unidirectional fiber reinforced polymers subjected to transverse tension using a micromechanics FE model. The RVE contained fibers randomly distributed over the transverse cross-section with inhomogeneous, radially graded interphase layers. According to the author, the proposed micromechanics model could be used to predict reduction in stiffness and final failure of a unidirectional lamina embedded in a composite laminate, since the computational results of the transverse strains and stresses at failure had shown good agreement with experimental results for different fiber volume fractions; in addition, it was able to correctly simulate the evolution of damage, explain the softening mechanism, and evaluate the post initial failure behavior of unidirectional lamina under transverse tension, which was mainly controlled by the interface strength and interphase stiffness.

González, Llorca and co-authors [139, 164, 165, 171] studied the effect of fiber, matrix and interface properties on the mechanical behavior of fiber reinforced composites under transverse compression, and in-plane, out-of-plane and longitudinal shear. The authors performed FE analyses on RVE of the microstructure, idealized as a random and homogeneous dispersion of parallel, circular fibers embedded in the continuous polymeric matrix. Interface decohesion was included, by means of cohesive elements, whose behavior is controlled by a cohesive zone model, as well as matrix shear yielding damage mechanisms, represented by an isotropic, elasto-plastic solid following the Mohr-Coulomb yield criterion. According to the authors, these simulations reliably showed the role played by the two dominant damage mechanisms (decohesion at the interfaces between fibers and matrix and shear band formation in the matrix) in controlling the transverse compressive strength of the lamina. These simulations were also in excellent agreement with previously reported experimental data for laminated composites under different biaxial compressive/shear loadings. The results also showed that the strategy adopted by the authors was able to accurately reproduce the physical fracture mechanisms experimentally observed, and predict the macroscopic properties of composite lamina from the properties and spatial distribution of the constituents. Accordingly, such results were able to evidence the potential to reproduce very complex stress states with well-defined boundary conditions, and showed the ability to carry out systematic parametrical studies to optimize composite materials without costly and time consuming mechanical tests. However, the authors assumed that further validation of this technique is necessary to gain confidence and to assess its limitations, since no estimations regarding the critical RVE analysed by the authors were available. To surpass this difficulty, their analyses were based on the average value of the results obtained from six different distributions in a RVE which included 30 fibers. To ensure that the number of fibers included in the RVE did not influenced significantly the model predictions, in selected cases these results were compared with those obtained with RVE containing over 70 fibers.

Vaughan and McCarthy [172, 173] presented a micromechanics damage model used to evaluate the effect of fiber/matrix debonding, cyclic loading and thermal residual stress on the transverse damage behavior of carbon fiber/epoxy laminates, as well as the influence of intraply properties (fiber/matrix interface strength, interfacial toughness, local fiber distribution, etc.) on the transverse shear deformation of these materials. Cohesive elements, based on a cohesive zone model, were used to predict the onset of fiber/matrix debonding, and the nonlinear behavior in the matrix was modeled using the Mohr-Coulomb plasticity theory. The RVE was generated using an algorithm previously developed by the authors [174], that can accurately reproduce a statistically equivalent fiber distribution for the high volume fraction composites. According to the authors, the micromechanical model developed produced failure patterns very similar to those observed in in-situ scanning electron microscope (SEM) experiments, and could prove to be useful in determining optimum constituent properties, allowing for increased interlaminar shear strength of composite laminates. Additionally, when subjected to a multiple loading cycle (i.e., tension-compression-tension), the micromechanical model provided novel insight into the microscopic damage accumulation that forms prior to ultimate failure, clearly highlighting the different roles that fiber/matrix debonding and matrix plasticity play in forming the macroscopic response of composite laminates. Such information may be useful in the development of accurate CDM models, which often smear those effects using damage variables. Finally, the results from the micromechanical model highlighted the influence of the manufacturing conditions on the overall fracture behavior as the cure temperature would affect the magnitude of thermal residual stresses.

Melro et al. [5, 166] presented a new algorithm to generate a random distribution of fibers, in which periodic boundary conditions can be applied. A statistical analysis was performed on the generated arrangements to demonstrate their correspondence to the random distributions of reinforcements. However, the inter-ply matrix-rich areas were not considered. A mechanical analyses was also performed, in order to demonstrate that the transversal isotropy typical of these materials is fully captured, and good agreement between independently calculated material properties in different loading schemes was found to exist. This algorithm was used by Melro et al. [5, 175] to quickly and efficiently reproduce a RVE with a random distribution of fibers, and predicted the elastic properties of composite materials departing from the properties of the individual constituents, performing volumetric homogenization of the results from micromechanical analyses. The influence of different geometrical parameters used in the generation of random distribution of fibers was also analysed, namely the dimensions of the RVE, the fiber radius, and the interval between neighboring fibers. According to the authors, although fiber radius does not have an influence on the mechanical properties of the composites, the longitudinal and transversal dimensions of the RVE and the minimum acceptable distance between neighboring fibers had considerable influence on the transverse properties and on the longitudinal shear modulus, while the thickness of the RVE influenced the estimated longitudinal properties. In future analyses, the authors intend to implement a nonlinear constitutive model for the matrix, as well as interfacial and fiber damage, and residual thermal stresses.

In a parallel work, Melro et al. [5, 176] modeled the mechanical behavior of 5-harness satin weave-reinforced epoxy using a micromechanical approach in which each of its constituents was characterized by a constitutive damage model. The epoxy matrix was modeled using an isotropic elasto-plastic damage law and the yarns, considered as homogenized material with a fiber volume fraction of 65%, whose properties were determined with micromechanical analyses as outlined in [5, 166], were modeled using a transversely isotropic damage law. A RVE of a 5-harness satin weave was generated and a set of in-plane periodic boundary conditions implemented in order to run the FE micromechanical analyses. Volumetric homogenization was performed on the obtained micro-stress and -strain fields to study stiffness degradation and damage evolution of the satin weave under different in-plane multiaxial loading conditions. According to the authors, for the uniaxial tensile case, a good qualitative agreement is obtained with experimental data regarding damage activation regions of the material as well as damage progression. In-plane shear, biaxial tension and a combination of uniaxial tension with in-plane shear load cases were also simulated and results provided an interesting insight on the triggering sequence of different damage mechanisms for this type of textile composites.

Canal et al. [177] studied the intraply fracture behavior parallel to the fibers of an E-glass/epoxy unidirectional laminate by means of three-point tests of notched beams. These tests were carried out within a SEM to ascertain the damage and fracture micromechanisms upon loading. The mechanical behavior of the notched beam was simulated within the framework of the embedded cell model, in which the whole notched beam is included in the numerical model but just the actual composite microstructure in front of the notch tip was represented, where all the fracture process occur (the remainder of the beam was assumed to be a homogeneous solid and the displacement field was continuous across the interface between both regions). In addition, this methodology was exploited to ascertain the influence of matrix and interface properties on the intraply fracture toughness. Glass fibers were assumed to behave as linear elastic, isotropic solids and the epoxy matrix was modeled as an isotropic elasto-plastic solid (plastic deformation and fracture was included by means of a continuum plasticity-damage model). The fiber/matrix interface was modeled as a cohesive crack. According to the authors, the macroscopic response of the composite, and the damage development and crack growth in front of the notch tip were very accurately predicted by the numerical simulations, demonstrating the ability of the embedded cell approach to simulate the fracture behavior of heterogeneous materials.

6.6. Continuum damage mechanics

6.6.1. Continuum mechanics approach

All materials exhibit irreversible nonlinearities, such as plasticity, damage, and fracture, which can be identified by comparing the unloading paths to the loading paths (see figure 6.6). Due to these nonlinearities, hardening and softening may occur. The first is a macroscopic, distributed and irreversible material response that smears the stress concentrations and eliminates any stress singularities, while the latter corresponds to the development and coalescence of voids and microcracks, conducting to damage localized along a fracture surface and elastic unload adjacent to the fracture surface [44].

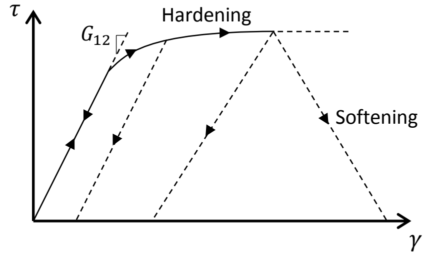

Fig. 6.6. Typical shear stress-strain response exhibiting multiple nonlinearities (after Dávila et al. [44]).

A large number of models have been proposed to represent material nonlinearities. Hardening of composites can be modeled with local constitutive models, i.e., models described by differential equations in which the stress at a given point uniquely depends on the history of the deformation gradient at that point only, relying on the implicit assumption that the material can be treated as a continuum at any arbitrary small scale [44].

Alternatively, the constitutive response of a material can be approximated using spatially periodic RVE to represent the micromechanical response of individual constituents and their interaction by means of a representative sample of damage variables [44, 178]. Assuming that each RVE deforms in a repetitive way, periodic boundary conditions are imposed in order to ensure compatibility of the deformation field along the boundaries. In order to reflect the stochastic fluctuations of material properties on the pertinent scale, the RVE needs to be as large as possible. However, computational requirements call for an RVE to be as small as possible. Furthermore, even when the RVE is large, if the analysis is extended to highly nonlinear material response that leads to localization of damage, the periodicity in the boundary conditions and, consequently, the RVE approach becomes unsatisfactory [44].

In addition to the drawbacks already enumerated, CDM models based in RVE when implemented in FE codes result in numerical solutions that are not objective. In other words, with successive mesh refinement, damage localizes into a zone of zero dimensions and the numerical results fail to converge to a unique solution [114, 128]. In the limit of an infinite spatial resolution, damage localizes in a zero thickness region where no work is needed to complete the fracture process, and the crack growth becomes instantaneous (perfectly brittle response) [133, 141]. This problem may be solved considering an alternative approach, which has been applied with higher success: the *crack band theory*, as described by Bažant and Oh [179]. This fracture theory was developed for materials that exhibit gradual strain softening due to microcracking, based in the hypothesis that this kind of fracture can be modeled as a blunt smeared band of parallel microcracks, instead of a line crack, in which the material undergoes progressive microcracking characterized by a stress-strain relation that exhibits strain-softening. Computationally, the crack is modeled by changing the matrix isotropic elastic moduli to orthotropic ones, reducing the material stiffness in the direction normal to the cracks in the band, which can be easily implemented in a FE program [179]. According to Bažant and Oh [179], the post-peak material response may be adjusted using a characteristic element length. This technique consists of ensuring that the computed dissipated energy due to the fracture process is constant and equal to the product between the fracture energy, G_c, and the crack surface, A [44, 179]. Another important aspect is that damage localizes into a layer of FE (one element in height), and therefore there exists a maximum size of the FE that can be used in the simulation of a crack band, in order to avoid snapback in the constitutive model (i.e., avoid having $\delta_f < \delta_i$, figure 6.3b) [44, 128, 130, 158, 179]. Moreover, because cracking and damage tend to grow parallel to the mesh orientation, this theory requires one to know the crack path a priori and design a mesh accordingly. In situations where a well-defined path for the crack propagation does not exist, i.e., where the fracture process zone rotates significantly during the passage of the fracture front, or the damage pattern is rather diffused (e.g., in scenarios involving dynamic loading, or quasi-static loading of unnotched specimens), the crack band theory ceases to apply [128, 179].

To overcome the above limitations, the so-called *nonlocal techniques* emerged and, unlike previous continuum mechanics models, proved to be suitable to resolve spurious mesh sensitivity and to retain the objectivity of the numerical response [44, 128, 141, 180, 181]. In local CDM models the state of damage is evaluated at individual integration points without consideration of the state of damage at neighboring locations, originating a severe mesh dependency problem related to *strain localization* during the fracture process which occurs whenever failure is preceded by the emergence of narrow and highly strained zones [44, 130, 133, 140, 142]. Typical examples of strain localization include shear bands in metals, formation of kink bands and accumulation of damage that results in fracture in composites [142]. Accordingly, local formulations are not able to describe the localization phenomena either in a physically or mathematically appropriate way, leading to unreliable results for strain softening problems [114, 142].

Physically, the introduction of nonlocal terms can be interpreted by taking into account the heterogeneous substructure of the material [182]. Indeed, nonlocality is a consequence of long range mechanisms such as dislocation motion in metal plasticity or microcrack interactions in quasi-brittle materials [114, 182, 183]. The growth of a microcrack is not decided by the local stress or strain tensor at the continuum point corresponding to the microcrack center but by the overall energy released from a finite volume surrounding the whole microcrack, whose growth depends on the average deformation of that volume and whose size is determined by the size of the microcracks and their average spacing. Additionally, one microcrack may either amplify the SIF or act as a shield of another adjacent microcrack [158].

Most of the nonlocal CDM techniques introduce spatial interaction terms that have a smearing effect on the deformation fields and thus preclude localization in a plane [44, 133]. This smearing effect on the deformation field can be ensured applying an integral formulation that takes the nonlocal effect into account by the direct coupling of the damage variable to a nonlocal equivalent strain, which is a weighted average of a local equivalent strain over a certain volume in the vicinity of the point of consideration [114, 133, 140, 141, 181]. Physically, this weighting averaging represents long-range interactions and heterogeneities at the microstructure, which can no longer be neglected when the scale of fluctuations of the continuous damage variables approaches that of the microstructure [133]. The enhanced continuous description which is thus obtained results in smooth damage fields, in which the localization of damage is limited to the length scale introduced by the averaging; as a consequence, premature initiation of cracks is avoided and predicted crack growth rates remain finite [141]. This approach may be enhanced taking the field in the immediate vicinity of the point into account by enriching the local constitutive relations with the first or higher gradients of the strain fields, either explicitly or implicitly [133, 141, 158]. A similar smearing can be obtained in a computationally simpler technique by using material viscosity (real or artificial), rate effect or damping [44, 158], or through a gradient term, where the nonlocal quantity is introduced as independent variable [182]. The material properties necessary for crack smearing, or strain softening, are chosen such that the width of a localizing diffuse crack band in a continuum is equal to the characteristic length, which is associated with the material response [44, 158]. A salient characteristic of these nonlocal models is the presence of a characteristic length (or material length) in the constitutive relation [158].

According to Germain et al. [140], although classical nonlocal models are well suited to describe the behavior of one single layer or of a bulk composite material, some open questions remain when representing damage onset and evolution in composite laminates, particularly the interaction between layers. Accordingly, Germain et al. [140] proposed a nonlocal model for composite layered materials where it was assumed that damage remains confined in each layer, so that nonlocal damage variables must be defined for each individual layer. Consequently, the authors defined two sets of nodal damage variables at the nodes in the interfaces between two layers. Additionally, in order to take into account anisotropic damage evolution, an internal length was defined for each material direction and damage variable. Other CDM models have been proposed and applied to composite materials in the last years. Some of them will be summarized in section 6.6.3.

6.6.2. Idealization of damage mechanisms in composite materials

The complex damage mechanisms occurring in advanced composite materials result in additional difficulties in the numerical simulation of failure. While some intralaminar damage mechanisms such as transverse matrix cracking occur in easily identifiable fracture planes that are parallel to the fiber direction, others such as fiber breakage (or fiber failure) are more difficult to idealize. These complexities make the representation of intralaminar damage using a kinematic description based on strong discontinuities a challenging task [44].

Some of the CDM models proposed in the literature are exclusively based on thermodynamic restrictions of the constitutive model and on some adjusting functions for damage onset and evolution. Other models, besides satisfying the thermodynamic restrictions, are based on the failure mechanisms, i.e., the damage activation functions are related to the physics of the different failure mechanisms, and the damage variables are related to the orientation of the ply failure planes experimentally observed, allowing the prediction of damage onset, the extent and type of noncritical damage mechanisms and simulating the effect of crack closure under load reversal cycles [53].

A computationally tractable approach to include the damage modes in the CDM model consists of using failure criteria based on the homogenized stress or strain state to idealize the mechanisms of failure [44]. Many failure criteria have been proposed to predict the onset of matrix cracking and fiber fracture, as described in the world wide failure exercise (WWFE) [138, 184–190], which provided a good assessment of the status of available theoretical methods for predicting material failure in fiber reinforced polymer composites [44, 46, 47]. However, due to an inadequate understanding of the damage mechanisms and the difficulties in developing tractable models of the failure modes, few criteria represent satisfactorily several relevant aspects of the failure process of laminated composites, e.g. the increase on apparent shear strength when applying moderate values of transverse compression, or the detrimental effect of the in-plane shear stresses in failure by fiber kinking [44, 47, 48]. Some recent phenomenological, physically based and interactive failure criteria, particularly the *LaRC03 criteria* [46, 47], subsequent proposed corrections [142, 191], and their general 3D extensions (*LaRC04 criteria*) [48], address some of the limitations of other failure criteria as identified from the WWFE, namely the effect of ply thickness (in-situ effect), fiber misalignment in compression, and the effect of shear nonlinearity on fiber kinking and in-situ strength. Unlike curve-fitting based criteria, LaRC03 and LaRC04 criteria are based on a physical model for each failure mechanism which predict matrix and fiber failure accurately without requiring curve-fitting parameters and without any restriction regarding loading combinations [44, 46, 47, 191]. These physical models, implemented in such criteria, may establish when failure takes place, and also describe the post-failure behavior of a certain composite structure [48].

For typical ply thicknesses, it can be assumed that defects exist in a ply, which span the thickness of the ply. Cracking of the ply can be assumed to occur when the ply is loaded above the load required to propagate the slit crack in the fiber direction, a mechanism known as tunneling. The stress required for tunneling is the in-situ strength [44].

In multidirectional composite laminates, cracks accumulate in the transverse plies during the loading process. As the loading on an individual transverse ply is increased, new cracks suddenly appear, initially at rather random locations, and then with a progressively mode uniform crack spacing. At some load, the crack density reaches a saturation value at which a different event occurs, such as delamination or fiber failure in an adjacent ply. Particularly, as the density of cracks in each ply of the laminate increases, networks of cracks are formed which can link up through the thickness of the laminate by inducing delaminations [44].

6.6.3. Continuum damage mechanics models applied to composite materials

To predict the ultimate strength of composite structures, it is necessary to have an accurate numerical representation of all damage modes and their interaction. When using continuum damage mechanics models to predict the behavior of such structures, a distinction is made between the different failure modes, especially between fiber and matrix failure. These models include a progressive softening of the material response, with internal damage variables describing the softening of the material response [44]. However, a softening response causes a localization of the strains along a surface known as the failure surface and a singularity of the damage rate at the crack tip. Furthermore, these strain-softening models typically do not include a characteristic length. Therefore, they exhibit pathological mesh sensitivity in numerical computations. Upon reducing the element size to zero, such analyses would predict failure to occur with zero energy dissipation. These localization instabilities, damage rate singularities and lack of objectivity with respect to element size can be avoided by the introduction of a characteristic length (nonlocality — see section 6.6.1) in the constitutive relations [44, 133, 141, 158]. The use of continuous representation of cracks renders CDM and related models particularly suitable for numerical simulations. Indeed, CDM formulations can be implemented in nonlinear FE codes with relative ease, without relying on special discretization and remeshing techniques [133, 141].

The evolution of intralaminar damage in laminated composites can be represented by softening laws described by a maximum traction and a critical energy release rate that define the evolution of damage in terms of the fracture energy dissipated in each damage mode. When a damage activation function (F_M) of a certain type of damage mechanism (M) is satisfied, the associated damage variable (d_M) takes on a positive, nonzero value less than or equal to one, and the ply compliance tensor (H) is affected by the presence of damage. In addition, it is necessary to define the evolution laws for the damage variables (d_M), which need to assure that the computed energy dissipated is independent of the refinement of the mesh [44].

Camanho and Mathews [9] implemented a FE model based on a 3D failure criterion and a progressive damage model to predict the final failure of mechanically fastened joints in composite laminates. This model related the material elastic properties with internal state variables associated with the different damage mechanisms, accurately predicting failure modes, joint stiffness and strength. Furthermore, using the information available with the proposed model, the damage progression is satisfactorily predicted. However, in bearing failures, the model was not able to accurately simulate damage growth developed in regions lying outside the washer edge. It was considered that delamination simulation should be included in the analysis by means of cohesive elements.

In order to avoid non-progressive fiber failure or non-realistic complete material collapse due to fiber breakage, Turon et al. [131] presented a physically-based and thermodynamically consistent mechanistic (based on a rule of mixtures) progressive damage model for unidirectional composite laminates based on the fiber fragmentation, able to simulate the stiffness-loss under static, sustained (creep), and fatigue loads. In this work, a degradation model which allows the evaluation of the apparent stress for a unidirectional ply is proposed, by taking into account a low density of breaks (valid at the initial stages of damage), assuming the absence of local load sharing in the vicinity of a broken fiber, and assuming a parallel behavior between fiber and matrix. The proposed formulation was considered to be flexible in order to join other degradation process, like the glass fiber degradation under moisture (developed on a subsequent work [192]). According to Turon et al. [131], this damage model represented an improvement over traditional models, where fibers were considered as pure elastic constituents until reach a nominal strength, reproducing the nonlinear behavior of fiber-dominated composites. However, this model based on fiber fragmentation still had some limitations, particularly regarding the stiffness loss due to debonding between fiber and matrix near the fiber break.

Mayugo and co-authors [51, 135] proposed a CDM model based on a micromechanical analysis of cracked $[\pm\theta/90_n]_S$ laminates subjected to multiaxial loads. The constitutive model was based on the thermodynamics of irreversible processes. This CDM model was able to predict the onset and accumulation of transverse matrix cracks, the effect of matrix cracks on the stiffness of the laminate, as well as the ultimate failure of laminates under uniform stresses or small stress gradients, where periodic distribution of transverse matrix cracks could be assumed. The proposed model also accounted for the effect of the ply thickness on the ply strength (i.e. in-situ strengths).

Later, Maimí et al. [50, 52, 193] proposed a complete definition of a CDM model for the prediction of the onset and evolution of intralaminar failure mechanisms and collapse of fiber reinforced plastic laminates, whose algorithm for the integration of the damage constitutive model was implemented in an Abaqus® UMAT subroutine. This CDM model were able to simulate localized intralaminar damage (matrix cracking and fiber fracture) using strain softening constitutive models, based on four possible fracture planes related to fiber tensile fracture, fiber kinking, and matrix cracking. These fracture planes could be oriented at 0° and 53° with respect to the ply thickness direction, predicted using a simplification of the *LaRC04 failure criteria* [48]. Exponential damage evolution laws were used to represent the cohesive response of all the failure modes of the ply, except for the longitudinal tension damage evolution law. The effect of ply thickness on the onset of transverse matrix cracking was taken into account by replacing the unidirectional strengths by the in-situ strengths in the failure criteria. On the other hand, the unilaterality of damage was taken into account by the ability of the model to represent complex load histories, including crack-closure effects under tension-compression load reversals. In order to avoid mesh dependent solutions (i.e., the objectivity of the numerical solution), the regularization of the energy dissipated for each damage mechanism was taken into account using a modification of the crack band model. A viscous model was proposed to mitigate the convergence difficulties associated with the strain softening constitutive models. To avoid physically unacceptable snap-backs of the material response, the maximum allowable element size was determined using closed-form equations, functions of the fracture toughness, elastic modulus, and strengths. The computational model was able to relive the condition of maximum element size by automatically lowering the strength of the elements larger than the critical size whilst keeping the fracture toughness constant.

Camanho et al. [53] used the CDM model proposed by Maimí et al. [52, 193] to predict strength and size effects in notched carbon-epoxy laminates. Although simpler alternative approaches such as the point stress and inherent flaw models, which do not require complex FE implementations, provided reasonable predictions, the accuracy of these models relies upon the measurement of the characteristic distance and length of the inherent flaw for each lay-up. In turn, the CDM model proposed predicted with good accuracy hole size effects in notched tensile specimens, providing not only the final failure load, but also information concerning the integrity of the material during the load history. The model only required the material properties, measured at the ply level, and fracture energies measured using both standard test methods and compact tension/compact compression test methods. Furthermore, according to the authors, the FE-based CDM model proposed was not limited to simple geometries, allowing the analysis of arbitrary configurations where analytical solutions could not be developed.

Bessa [194] also used the CDM model proposed by Maimí et al. [52, 193] to predict the strength and failure modes of open-hole carbon-epoxy specimens subjected to tensile and compressive loading, and carbon-epoxy specimens subjected to off-axis loading. According to the author, this CDM model proved to be well suited to perform such analyses, although more numerical studies need to be performed to confirm the applicability of this model for simulation of off-axis tests. The author also mentioned that the accuracy of this model in predicting open-hole compressive strength can be improved because it is dependent on the longitudinal compressive fracture energy, which was difficult to measure, conducting to inaccuracies caused by an external factor and not a formulation problem. Another drawback pointed out by the author was the very high computational effort of this model, suggesting that this should be an issue to account in future implementations.

More complex CDM models incorporate the intralaminar damage modes (e.g., transverse matrix cracking and fiber breakage) and use cohesive zone models to capture delamination between ply interfaces [44]. This is the case of the progressive failure methodology developed by Goyal et al. [195], and implemented into a user-defined subroutine of the commercial FE package Abaqus® to simulate intralaminar and interlaminar failure initiation and subsequent material degradation. Simulations on a flat panel in shear and on a curved panel in compression with centrally located circular cutouts were carried out by the authors. Intralaminar failure modes included matrix cracking, fiber/matrix shear and fiber failure modes, whose initiation was predicted using Hashin's criteria. Subsequent material degradation was modeled using damage parameters for each mode. The interlaminar failure mechanism (delamination) was simulated by positioning cohesive elements between adjacent sublaminates, based on a nonlinear constitutive law that accounted for a multiaxial stress criteria for delamination initiation, a mixed-mode fracture criteria for delamination progression, and a damage parameter to prevent restoration of a previous cohesive state. According to the authors, very good agreement between the progressive failure analyses and the experimental results was achieved when the failure analyses included the interaction between intralaminar and interlaminar failures.

More recently, van der Meer and Sluys [137] presented a model for FEA consisting of separate parts for description of onset to complete local failure inside a ply (intralaminar failure) and between plies (interlaminar failure). In this model, intralaminar failure is simulated with a softening plasticity model based on an interactive Tsai-Wu criterion with viscoplastic regularization for the simulation of progressive failure. On the other hand, interlaminar failure is modeled using cohesive elements with a damage law for mixed mode delamination, as proposed by Turon et al. [56], to capture the onset and growth of delamination cracks. According to van der Meer and Sluys [137], this combined model was robust and enabled the simulation of failure processes in laminated composites involving both intra and interlaminar processes and their interaction. However, some drawbacks of the softening model were pointed out by the authors. First, in its proposed form, the direction of plastic strain was often unrealistic, resulting in spurious transverse strains. Second, the viscoplastic regularization was not clearly linked to physical phenomena. Third, both the delamination and the softening plasticity models putted serious restrictions on the maximum element size in the regions where failure occurred, since the cohesive zone in delamination and the localization band in intraply failure had to be spanned by more than one element, meaning that there was a limit to the size of the structure that could be analyzed without excessive growth of computation time.

Lopes et al. [102] developed an impact CDM/cohesive model, whose constitutive models were able to take into account the physical progressive failure behavior of fibers, matrix, and interfaces between plies. The damage model used in this work was an extension to 3D scenarios of the plane stress formulation proposed by Maimí et al. [52, 193] for in-plane behavior. The interfaces between plies were simulated by means of cohesive elements, as proposed by Turon et al. [56]. This impact model was implemented in an explicit FE code and used in the simulation of low-velocity impact events on composite laminates, resulting in reliable predictions of the impact dynamics, impact footprint, locus and size of delaminations, matrix cracks and fiber damage, as well as the amount of energy dissipated through delaminations, intraply damage and friction.

González [196, 197] also used a combination of the CDM model proposed by Maimí et al. [52, 193] and the cohesive elements proposed by Turon et al. [56] in the analysis of the low velocity impact event and subsequent compression after impact (CAI) testing. According to the author, the comparisons with experimental data showed that the impact simulations reproduced better the experimental results when fewer composite plies and interfaces were modeled. When simulating laminates with higher number of layers, besides significantly increasing the computational effort, the predictions showed a worse correlation with experimental data, according to the author due to the high number of contact constraints imposed by the cohesive elements, which degraded the numerical predictions. The author suggested that using cohesive surfaces instead of interface elements would improve those results. Still, the simulations carried out by González demonstrated the capacity of such modeling approach in describe the phenomena that occur at any moment of the impact and CAI tests, something not possible to obtain by real tests and non-destructive inspections.

Since the combined CDM/cohesive models, such as the impact models described previously, rely on extremely fine meshes with one or more elements through the thickness of a ply, other authors try to use stacks of shell elements to represent sublaminates within larger structures, without increasing too much the computational efforts [44]. This is the case of Overgaard et al. [161], which used layered continuum-based 3D shell elements, whose formulation was based in standard 8-node brick elements with tri-linear shape functions using a 3D material law, as proposed by Klinkel et al. [198], and a mixed-mode cohesive element formulation developed for variable mixed-mode loading as proposed in refs. [56, 64–66]. In their work, Overgaard et al. proposed a modeling strategy for the structural analysis of large 3D laminated composite structures undergoing geometric and material induced instability, such as in the case of composite wind turbine blades. A localized sub-plane control strategy was adopted for tracking multiple crack formations and the propagation of multiple delamination fronts. This FE formulation was implemented in an in-house FE system called *MUltidisciplinary Synthesis Tool* (MUST), developed at Aalborg University. According to the authors, the proposed solver strategy showed a good correlation with the closed-form solution and experimental values for simple delamination test specimens and excellent performance in the case of simple benchmarks. However, further improvements in the robustness of the numerical schemes were foreseen by the authors.

Song et al. [130] presented a study on the performance of a state-of-the-art CDM model for intralaminar damage coupled with cohesive elements for interlaminar damage for failure simulation of quasi-isotropic open-hole tension specimens. In this study, a modeling approach consisting of different meshes within the individual plies was proposed, such that the element edges are aligned with the ply fiber direction. Tie constraints were used to connect the individual ply meshes with the cohesive element layers. According to the authors, the delamination failure mode was successfully predicted with the proposed aligned mesh, and the predicted damage evolution qualitatively agreed with the experimentally observed damage evolution. Generally, the numerical models predicted the proper failure mechanisms and the proper trends in the failure load. However, the failure loads for specimens exhibiting delamination failure were consistently over predicted due to late onset of damage, whereas failure loads for specimens exhibiting pull-out failure were consistently under predicted due to late onset and development of subcritical damage and, consequently, early onset of fiber failure.

However, despite advances in progressive damage modeling, CDM models coupled with cohesive zone models may not always represent laminate failure sequences properly. These deficiencies are particularly evident when the observed fracture mode exhibits matrix splitting and pullouts or when the fracture is characterized by a strong coupling between transverse matrix cracking and delamination [44, 130]. Furthermore, the majority of the existing models that are able to predict matrix cracking and delamination, though excellent tools to design laminates, are not efficient in the design of large composite structures [199].

Maimí et al. [200] proposed and implemented in Abaqus®, in a user material (UMAT), a continuum plastic-damage model to determine the onset of matrix cracking and analyse the onset of delamination promoted by matrix cracks for in-plane stress states, taking into account that under in-plane shear stresses composite laminates show a nonlinear response prior to the formation of a macrocrack. In the second part of their work [199], Maimí et al. presented a model to predict the propagation of transverse cracks in polymer matrix composite laminates, analysing different possibilities for the crack pattern and comparing the different stress-strain responses. Because matrix cracking promotes delamination between the plies, the propagation of delamination was also simulated. Accordingly, a framework for a constitutive model able to predict damage and plasticity at microscale, cracking, and delamination was defined. According to this work, it was shown that without considering the presence of randomly distributed flaws in the material the crack spacing was not periodic. It was also shown that assuming a periodic crack pattern the results were similar to those considering a non-periodic crack pattern; however, the evolution of delamination was underpredicted when a periodic crack pattern was assumed. Finally, it was shown that, when the ply was sufficiently thin and the laminate sufficiently thick and stiff, the definition of a damage model at the ply level yielded very good results, which is important for the definition of a model able to be applied to large structures with non-uniform stress fields.

According to Peerlings et al. [133], it is interesting to note that a "convergence" of discrete and continuous representations of fracture can be observed not only in their numerical implementations, but also in the underlying theory. In a sense, continuum damage formulations such as the one proposed by Peerlings et al. [133] result in a discrete crack. On the other hand, strong discontinuity approaches which a priori assume a discrete crack are extended with nonlinear constitutive models and can sometimes be regarded as solutions of nonlocal formulations.

It is believed that the integration of both approaches will only intensify under the influence of the increasing demand for accurate failure predictions. This is the case of the so-called *hybrid* approaches, such as those proposed by Ladevèze, Lubineau and coauthors. In order to create more robust mesomechanics models, these authors, using hybrid formalisms, focused on the development of bridges between the micro and mesomechanics, providing more detailed information on the actual origin of the damage mechanisms [134]. Lubineau and Ladevèze [201] introduced an intralaminar model formulated within the framework of damage mechanics and based on a micromechanics reference model, previously developed by the authors [134, 202–207]. Bridging in a "pragmatic" manner the micro and mesomechanics of laminates, the adopted approach was compatible with the standard formalisms used in commercial analysis codes, in order to take advantage of commercial FE packages such as Abaqus®. The micromechanics framework was able to describe explicitly each degradation mechanism by its own optimum model, differing from classical micromechanics approaches and CDM models. This micromechanics model, written according to the damage mechanics formalism through systematic homogenization, was already used by the authors in the context of fatigue and thermo-mechanical loading [208, 209]. The adopted formalism is classified as *hybrid*, in the sense that the description of the degradation uses both damage mechanics and fracture mechanics alternatively. Thus, diffuse degradation (fiber/matrix splitting) is described through damage mechanics on the mesoscale. On the other hand, transverse cracks and associated delamination are described in a discrete manner by introducing minimum surfaces whose rupture is determined by a fracture criterion. However, in this work, the authors limited their analysis to intralaminar damage. When implemented into Abaqus®/Standard, using the user subroutine UMAT, this framework was able to predict damage by fiber rupture, diffuse damage, transverse cracking and plasticity. According to the authors, future works may extend this approach to the interlaminar interface damage and the corresponding implementation.

More recently, Violeau et al. [210], also based on a hybrid micromechanics reference model, mixing discrete and continuous approaches by introducing potential rupture surfaces and a damage continuous medium, developed a multi-scale calculation strategy with homogenization in space for the simulation of damage mechanisms in composite laminates. This calculation strategy was based on a decomposition of the domain into substructures and interfaces, and therefore requiring calculation tools unavailable in industrial analysis codes. This multi-scale in space approach enabled the simulation of complex problems with multiple cracks. However, it was not practical, since it was not able to handle with very large numbers of substructures and interfaces due to computational restrictions, needing further improvements. Another disadvantage relies in the need of defining the minimum cracking subsurfaces *a priori*, which limited the model to stacking sequences containing only four different orientations. Still, according to the authors, the first results were very promising and lead to degradation patterns which other models are incapable of producing.

6.6.4. Limitations of continuum damage mechanics models

Nonlocal damage models are less widely used due to the difficulty in implementing them within the FEM [44, 130]. So, the deficiencies of the predictive capabilities of CDM models, which include the incorrect prediction of the damage zone size normal to the fracture direction when using crack band models and the inability of local CDM models to reliably predict matrix crack paths, must be taken into account.

The premise of the crack band approach for regularizing CDM models is that damage localizes into a band with width equivalent to the element dimension. If the element size is smaller than the damage process zone, the crack band approach may not predict correctly the width of the damage zone nor the local stress field [44, 128, 130, 158, 179]. Consequently, the stress redistribution resulting from damage development may be inaccurately predicted and can potentially result in inaccurate representation of damage mode interactions and failure sequences [44].

As a result of homogenization and damage localization, CDM models have difficulties predicting crack paths. The predicted results may exhibit dependence on the shape and the orientation of the FE, due to the fact that a crack simply tends to grow following the shortest way and due to the so-called *stress locking effect*, which arises after strain localization due to softening, as described in section 6.6.1. Stress locking produces spurious stress transfer across a widely open crack, allowing the structure to stand more loading, and conducts to a strong directional bias of the crack bands that propagate aligned with the element sides of the mesh [196]. On the other hand, homogenization eliminates the distinction between fibers and matrix, and therefore CDM models cannot distinguish between cracks that propagate along fiber directions from those that cross fibers. Furthermore, in local CDM models, the direction of damage evolution is driven only by the instantaneous local stress distribution, meaning that the local direction of cracking may be predicted correctly by the failure criteria, but the sequence of failures that eventually defines the path of a crack at a macroscopic level may be predicted incorrectly [44, 130].

The inability of CDM models to determine the correct direction of propagation is evident when considering two different plies in a laminate with a notch and subjected to shear, as described in [44, 130] (see figure 6.7). In both situations illustrated in figure 6.7, the direction of the matrix microcracks is correctly predicted by the failure criterion to be at 45° to the fiber direction, resulting in an identical sequence of failures, since the stress field is identical. However, it is clearly not the same to have matrix cracking in a shear band running parallel to the fibers (figure 6.7a), which is a relatively brittle failure mechanism, as it is to have a crack band across fibers (figure 6.7b), which requires much more work to propagate.

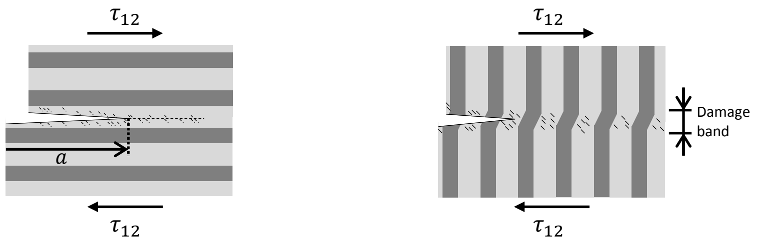

(**a**) Propagation of shear damage along fiber. (**b**) Propagation of shear damage across fiber.

Fig. 6.7. Idealized propagation of shear damage (after Song et al. [130]).

Another example of the inability of CDM models to predict crack paths is related with the particular phenomenon of splitting, as illustrated in figure 6.8 and discussed by van der Meer and Sluys [136]. In the real material, figure 6.8b, failure will be concentrated in the weaker matrix domain, while homogenized continuum material models, illustrated in figure 6.8a, do not offer this domain separation. Therefore, a discontinuous approach to modeling failure may represent more accurately the phenomenon of splitting. In such approach, a split is modeled as a discontinuity and it is possible to fix the direction of propagation, incorporating at the mesolevel the micromechanical phenomenon characterized by the tendency of ply cracks to propagate in the fiber direction [136].

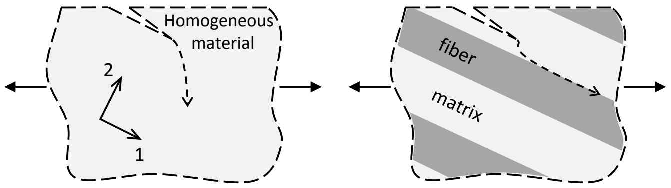

(**a**) Homogeneous orthotropic medium.

(**b**) Fiber-matrix material.

Fig. 6.8. Prediction of crack paths (after van der Meer and Sluys [136]).

6.7. Discrete damage mechanics

6.7.1. eXtended finite element method

The **extended finite element method** (X-FEM) is a local mesh enrichment technique that incorporates both discontinuous fields and near tip asymptotic fields through a partition of unity method to account for the presence of a crack independently of the mesh and without need of remeshing [70, 211–223]. Initially proposed by Belytschko and Black [224], and further improved by Möes et al. [211], this technique facilitates the introduction of displacement discontinuities, such as cracks, by the enrichment of the shape functions of a *subset of nodes* with the generalized Heaviside step function for the traction-free crack wake region, at locations and along directions that are independent of the underlying FE mesh [136, 211, 212, 214, 219, 222]. By eliminating the need to include the crack surfaces in the model, mesh generation is greatly simplified [212]. Furthermore, this technique simulates crack growth by redefining the tip location and by adding new crack segments, completely avoiding the need to remesh as the crack grows [211]. Accordingly, the X-FEM is particularly suitable to predict the location and evolution of matrix cracks in composite structures, since neither the fiber/matrix interfaces nor the crack surfaces need to conform to the mesh [44, 221].

Combined CDM/X-FEM approaches are also possible. Areias and Belytschko [225] presented a combined CDM-discrete approach for general 3D problems, assuming that *part* of the process zone energy dissipation can be adequately represented by a viscous-regularized CDM model (using a characteristic element length, resulting in a regularized crack-band model), and, after a preferred orientation is naturally formed, the remaining energy is released by a surface-oriented mechanism, through the introduction of the jump part of the displacement field in the X-FEM. According to the authors, the proposed pragmatic approach showed high level of robustness, particularly in order to extend the proposed formulation to a wider variety of constitutive laws and more flexible discontinuity surface evolution laws, and also showed successful analysis results.

A drawback of the X-FEM, pointed out by several authors [211, 226] is the need for the introduction of additional degrees of freedom into the variational formulation which solely determine the crack kinematics, i.e., the jump in the displacement field, conducting to a different number of degrees of freedom per node that increase when the crack grows. In addition, although modeling a matrix crack in a ply that propagates parallel to the fiber direction is conceptually straightforward using X-FEM, it is more difficult to model networks of matrix cracks in a laminate, whose fracture planes in individual plies intersect at common interfaces, causing delaminations that link the cracks through the thickness. Within the traditional X-FEM approach, the difficulty in modeling networks of linked matrix cracks can be addressed by developing a special enrichment for multiple crack situations or by connecting two enriched/cracked elements (*phantom node method* — see section 6.7.3) [44, 129].

In spite of the previously mentioned drawbacks, the X-FEM has been applied in the development of DDM models for composite damage analysis. For example, Kästner et al. [227] applied the X-FEM to modeling textile-reinforced composites. In the proposed model, X-elements replace the original FE when intersected by a material interface. This approach allowed for the simulation of cracks in fiber/matrix interfaces of textile-composites. However, this model was limited to linear material behavior. Huynh and Belytschko [221] developed a method to analyse both 2D and 3D composites with cracks. Both material interfaces and singularities were modeled by X-FEM, and no mesh restriction was imposed. However, the proposed methodology is only described for isotropic materials with interfaces. Still, according to the authors, the numerical examples demonstrated the accuracy and versatility of this method, which can easily integrate other failure laws, such as cohesive laws, and can be extended to anisotropic materials. Ashari and Mohammadi [70] adopted and further improved the X-FEM for modeling interfacial cracks between two orthotropic media by a new set of bimaterial orthotropic enrichment functions, derived from analytical asymptotic displacement fields around a traction-free interfacial crack. Mode I, mode II and mixed-mode SIF were numerically evaluated, and the performance of the proposed approach was examined simulating various numerical examples and comparing the results with reference solutions. According to the authors, the numerical results exhibited close agreement with the reference solutions. With these new enrichments, the authors expected to allow for full X-FEM fracture analysis of layered orthotropic composites including both layer cracking and interlaminar debonding.

6.7.2. Regularized extended finite element method

A variant of the X-FEM, the so-called **regularized extended finite element method** (RX-FEM), where the Heaviside step function used to describe the crack surface is replaced by higher order displacement shape functions to approximate the discontinuity in the displacement field, has been applied for detailed analysis of the stress field in laminates in the presence of splitting cracks [44, 129, 136, 143, 217]. An advantage of the RX-FEM is that the Gauss integration schema for element stiffness matrix computation is maintained, i.e., its implementation only involves integration of the products of the original shape functions and their derivatives and does not require modification of the integration domains, as in the X-FEM [44, 129, 217]. According to Dávila et al. [44], a kinematically powerful model of crack networks can be constructed in which transverse matrix cracks are inserted parallel to the fiber direction at locations determined using a failure criterion such as the LaRC03 criteria [46, 47, 142, 191] or the LaRC04 criteria [48].

In a RX-FEM framework, simulations of splitting in composite laminates begin without any initial matrix cracks. As the loading is increased, matrix cracks are inserted according to the chosen failure criterion. This criterion is evaluated at each integration point and, when exceeded, a matrix crack oriented in the fiber direction is added. The crack is inserted using the displacement enrichment necessary to model the displacement jump. The magnitude of the jump is initially zero and it is controlled by an interface cohesive law. The same cohesive law is used at the ply interfaces to represent potential delamination surfaces. A Newton-Raphson procedure is applied to find the equilibrium solution at each load step of the implicit incremental solution [44].

According to Iarve [217], the application of the RX-FEM to fracture mechanics problems, such as the calculation of the total energy release rate of transverse and oblique (to the loading direction) cracks in a rectangular composite plate, conducted to accurate results. The author also showed that the error of modeling the crack geometry in terms of effective length decreases with increasing order of approximation. In addition, accurate fiber stress redistribution prediction in unidirectional composites with an open hole in the presence of transverse splitting was displayed. Later, Iarve, Mollenhauer and co-authors [228, 229] numerically investigated the stress redistribution and ply cracking in open-hole composite laminates using the RX-FEM and compared the numerical results with experimental tests carried out at the same time. According to the authors, a good agreement with the experimental data was obtained. In more recent works, Iarve, Mollenhauer and co-authors [129, 230] proposed a fully 3D numerical approach based on a combination of a cohesive interface damage model for modeling delamination, as proposed by Turon et al. [56], and the RX-FEM framework proposed by Iarve [217], and applied it to the prediction of initiation and evolution of complex transverse matrix cracking and delamination networks in laminated composites and damage progression in laminated over-height compact tension (OCT) specimens, without any prior knowledge or assumptions regarding the locations of damage onset. The proposed methodology was extended to allow for multiple matrix cracks in a ply as well as connectivity and subsequent delamination between plies with arbitrary fiber and matrix cracking direction, and it includes the LaRC03 failure criteria for initiation detection [46, 47]. Additionally, for the prediction of damage progression in laminated OCT specimens, a CDM approach of the type described by Maimí et al. [50, 52, 193] was employed to account for fiber breakage. According to the authors, good agreement between this methodology and experimental observations and/or other computational techniques was observed. Simulation of delamination initiation from matrix cracks, modeling of delamination jumps from one ply interface to another, prediction of the effects of ply thickness on delamination shape and transverse crack density, examination of delamination initiation variations due to varying ply orientations, and the ability to describe the damage evolution trends were properly verified. In addition, this studies demonstrated the mesh independence of this approach. This ability to address various failure mechanisms arising in nontraditional composite laminates without modifying the analysis framework and/or mesh is, in fact, a critical advantage of the RX-FEM approach [44]. According to Mollenhauer et al. [230], the RX-FEM framework developed to simulate in detail the damage evolution process in laminated composites using discrete representations of matrix cracking and delamination showed excellent promise, although the addition of fiber damage simulation using a CDM model requires additional effort for validation.

6.7.3. Phantom node method

With the **phantom node method**, introduced by Song et al. [231], it is possible to model discontinuities, such as cracks, at an arbitrary location in the mesh by overlapping of an extra element on top of an existing element, instead of introducing additional degrees of freedom as in the original X-FEM. Although based on the X-FEM, the phantom node method uses a transformation of the nodal variables that leads to the superposed element formalism of the method of Hansbo and Hansbo [232], later coupled with cohesive zone models by Mergheim et al. [233–235] to cope with arbitrary fracture problems, which has particular advantages over the X-FEM with respect to its implementation [136, 226, 231]. In the formalism of the phantom node method, the discontinuous (cracked or sheared) element is replaced by two elements with additional phantom nodes or phantom degrees of freedom, so that little modification is needed in existing explicit FE programs to implement this formulation [231]. In other words, all degrees of freedom are physical and no additional degrees of freedom are introduced [226]. Additionally, the associated shape functions in a cracked or sheared element are identical to the shape functions of an intact element, simplifying its implementation into explicit dynamic codes and into commercial FE codes [226, 231]. These feature make the phantom node method especially useful for dynamic fracture problems [226]. However, it is only applicable to cohesive zone modeling, where the singularity in the stress field is removed due to the presence of a cohesive traction [136, 226]. Crack progression is simulated by element-by-element cracking, which conducts to some mesh dependency; indeed, according to Song et al. [231], crack tip speed decreases somewhat with mesh size, whereby element-by-element cracking requires finer meshes to match the accuracy of methods with partial element cracking.

Different approaches to the phantom node method include modeling crack growth elementwise with the tip always located at an element boundary [136], or modeling crack tips within a FE [226]. When crack tips are placed within a FE, as proposed by Rabczuk et al. [226], the crack growth in the phantom-node method became almost independent of the FE mesh, surpassing the problems reported by Song et al. [231] with respect to mesh size effects. Both approaches enable the formulation for the crack tip for 2D and 3D elements [136, 226].

Van der Meer and Sluys [136] proposed a phantom node method with mixed mode cohesive law for the simulation of splitting in composite laminates. This method was also coupled with cohesive elements in order to analyse splitting and delamination in notched cross-ply laminates. According to the authors, promising numerical results were obtained. However, it was envisioned that the model could be combined with a separate description for fiber failure to allow for complete mesoscopic analysis of progressive failure in composite laminates.

6.7.4. Augmented finite element method

The **augmented finite element method** (A-FEM), presented by Ling et al. [222], is also based on the discontinuous FEM developed by Hansbo and Hansbo [232]. The A-FEM can deal with arbitrary internal discontinuities, as in the previous methods, but maintaining the essential FEM advantage of elemental locality, i.e., without requiring local enrichment functions, so that it can be readily integrated into commercial FEM packages as a user element without access to the source code. Augmentation is implemented via separable mathematical elements that employ standard FE nodal interpolation, involving nodal information from the modified element only. In other words, a physically cracked element is represented by two separable mathematical elements possessing standard FE structure. This formulation allows the use of meshes that need not to conform to the surfaces of heterogeneities, has the ability to apply the augmented element recursively, enabling modeling of multiple discontinuities arising on different, possibly intersecting surfaces within an element, and can easily incorporate cohesive zone models of nonlinear fracture which are not activated until a failure initiation criterion is satisfied locally. According to Ling et al. [222], the A-FEM is ideally suited to modeling damage evolution in complex structural materials such as laminated or woven textile composites. However, the number of studies in the literature regarding application of this approach are still scarce.

Chapter 7

Numerical modeling of interlaminar damage

Delamination resistance is seen as one of the potential benefits of thin-ply laminates. This type of damage (interlaminar) is extremely important because it may develop during manufacturing, from impact damage, or in geometric discontinuities, with no visible visual defect, and generally conducts to a significant loss of structural integrity, including reduction of bending stiffness and reduction of the compressive load-carrying capacity due to local buckling. One way to study the resistance to delamination onset is by numerically analyse the onset of free-edge delamination. In this chapter, a decohesion element implemented as an Abaqus® user subroutine (UEL) for implicit analysis is used to simulate free-edge delamination in unnotched and open-hole specimens. The decohesion elements are placed between the non-crimp fabric bi-layers, simulating their interface. It is assumed that delamination do not occur between the layers of the non-crimp fabric. A comparative study is performed with laminates having alternative stacking sequences.

7.1. Introduction

As reported in section 2.5, delamination resistance is seen as a potential benefit of thin-ply laminates, with respect to their structural integrity. As mentioned back there, delamination (interlaminar damage) is extremely important due to the relatively weak interlaminar strengths of composite laminates. This type of damage may develop during manufacture, from impact damage, or from the interlaminar stresses that develop at geometric discontinuities, with no visible visual defect. In addition, delamination growth, under both static and dynamic loading, redistributes the stresses in the plies of a laminate and may influence residual stiffness, residual strength and fatigue life, generally conducting to a significant loss of structural integrity, including reduction of bending stiffness and reduction of the compressive load-carrying capacity due to local buckling.

One way to study the resistance to delamination onset is by numerically analyse the onset of free-edge delamination, an approach already implemented, for example, by Camanho et al. [45] to study the resistance to delamination onset in thin-ply T700/RTM6 laminates. Free-edge delamination occurs due to the high interlaminar stresses that developed due to the mismatch in Poisson contraction of the individual plies with different orientations and due to the fact that fibers are broken at the surface when the specimen is cut, which may happen even for a unidirectional composite.

In this chapter, the advantages of having laminates with thin plies in the onset of delamination is further investigated, particularly with regard to thin-ply non-crimp fabric (NCF) laminates, subject of this thesis. A decohesion element, proposed by Turon et al. [55], implemented as an Abaqus® user subroutine (UEL) for implicit analysis is used to simulate free-edge delamination in unnotched and open-hole specimens. The decohesion elements are placed between each [0/−45] NCF bi-layer, simulating their interface. As an effect of stitching, it is assumed that delamination do not occur between the layers of the NCF. A comparative study is performed with laminates having alternative stacking sequences.

It should be noted that this study is necessarily different from that performed by Camanho et al. [45], since in that study the main focus was simply understand the effect of having thinner plies in the resistance to delamination onset. Herein, the main goal is to extend this former study to thin-ply NCF laminates.

7.2. Formulation and implementation of a decohesion element

Turon et al. [55] proposed a thermodynamically consistent continuum damage model for the simulation of progressive delamination in composite materials under variable mixed-mode ratio, based on the cohesive zone approach. Cohesive damage zone models relate tractions with the displacement jump at an interface where a crack may occur. Damage initiation is related to the interfacial strength, i.e., the maximum traction on the traction-displacement jump curve. When the area under the traction-displacement jump curve is equal to the fracture toughness, the traction is reduced to zero and new crack surface formed. The advantages of cohesive zone models are their simplicity and the unification of crack initiation and growth within a single model. Furthermore, cohesive zone formulations can also be easily implemented in finite element (FE) codes using decohesion elements.

The constitutive law proposed by Turon et al. [55] follows a bilinear relationship between relative displacements and tractions at the interface, and it is defined by using a delamination onset and propagation criteria. The delamination onset criterion is based on energy terms and is proposed so the model formulation accounts for loading mode changes in a consistent thermodynamically way. The formulation also accounts for crack closure effects to avoid interfacial penetration of two adjacent layers.

This model is implemented by using an user element subroutine called UEL, as a zero-thickness decohesion element, called *DECO-UEL.V1*, for implicit analysis in the Abaqus® FE code. The main aspects of the delamination model proposed by Turon et al. [55] and its implementation in an Abaqus® user subroutine (UEL) are presented in this section. The complete formulation is described by Turon et al. [55] in full detail.

7.2.1. Interlaminar damage model theory

A constitutive equation relating the cohesive tractions τ_j at the middle surface of the decohesion element to the displacement jump Δ_i in the local coordinates is required for modeling the constitutive behavior of the material discontinuity. Such equation is represented by a bilinear relationship (figure 7.1), where the first line represents an elastic relationship, prior to damage onset, which is related to the interface strength τ^0. When the area under the traction-displacement jump curve is equal to the fracture toughness, the traction is reduced to zero and new crack surface formed. The boundary value problem and the kinematics of the interfacial surface are presented in detail by Turon et al. [55].

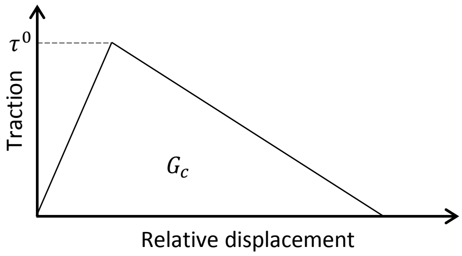

Fig. 7.1. Bilinear constitutive law.

The different relative displacements between the nodes of a surface element are shown in figure 7.2, where each displacement is directly associated with the corresponding propagation mode by assuming that the crack front is located at the indicated line. Note that, at finite element scale level, it is not possible to distinguish the shear modes II and III because their evaluation depends on the relative displacement between homologous nodes with respect to the crack front orientation, which is in fact unknown, and therefore shear modes are generally grouped together in the formulation of the cohesive zone models [196].

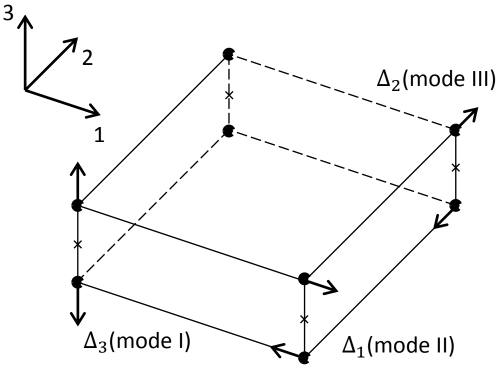

Fig. 7.2. Propagation modes.

Because negative values of Δ_3 (mode I) have no physical sense (the crack is closed and interpenetration is prevented by contact, without producing damage), the damage model has a unilateral behavior for this propagation mode, which means that the damage variable can be activated or deactivated as a function of the loading state. Therefore, negative values of Δ_3 should not have any influence in the variation of the free energy per surface unit of the interface, $\Psi(\Delta_i, d)$, which, under isothermal conditions, is defined as,

$$\Psi(\Delta, d) = (1-d)\Psi^0(\Delta_i) - d\Psi^0\left(\delta_{3i}\langle -\Delta_3\rangle\right), \quad i = 1,2,3 \tag{7.1}$$

where d is the scalar isotropic damage variable, $\langle\cdot\rangle$ is the MacAulay bracket, defined as $\langle x\rangle = \frac{1}{2}(x + |x|)$, δ_{ij} is the Kronecker delta operator, and $\Psi^0(\Delta_i)$ is a function of the relative displacement space defined as,

$$\Psi^0(\Delta) = \frac{1}{2}\Delta_i D^0_{ij}\Delta_j, \quad i,j = 1,2,3 \tag{7.2}$$

where D^0_{ij} is the initial (undamaged) stiffness tensor, defined as,

$$D^0_{ij} = \delta_{ij} K, \quad i,j = 1,2,3 \tag{7.3}$$

where K is the penalty stiffness, a scalar parameter defining the intact stiffness of the interface for the three loading modes, corresponding to the slope of the first line in the constitutive law.

The constitutive equation for the interface is obtained by differentiating the free energy with respect to the displacement jumps,

$$\tau_i = \frac{\partial\Psi}{\partial\Delta_i} = (1-d)D^0_{ij}(\Delta_j) - dD^0_{ij}\delta_{3i}\langle -\Delta_3\rangle, \quad i,j = 1,2,3 \tag{7.4}$$

To ensure the thermodynamic consistency of the model, the dissipated energy per surface unit during the damage propagation process, Ξ, has to be equal or greater than zero,

$$\Xi = -\frac{\partial\Psi}{\partial d}\dot{d} \geq 0 \tag{7.5}$$

The relative displacement components, Δ_i, are the free variables of the system (i.e., displacement driven formulation), and d is the internal variable that ensures the irreversibility of the model, whose values have to be evaluated at each time increment during the loading process. For that purpose, it is necessary to define a suitable norm of the displacement jump tensor, a damage criterion, and a damage evolution law.

The norm of the displacement jump tensor, λ, is used to compare different stages of the displacement jump state so that it is possible to define such concepts as "loading", "unloading" and "reloading". It is a non-negative and continuous function, defined as,

$$\lambda = \sqrt{\langle\Delta_3\rangle^2 + (\Delta_{shear})^2} \tag{7.6}$$

where Δ_3 is the displacement jump in mode I, i.e., normal to midplane, and Δ_{shear} is the Euclidean norm of the displacement jump in mode II and in mode III,

$$\Delta_{shear} = \sqrt{(\Delta_1)^2 + (\Delta_2)^2} \tag{7.7}$$

The damage criterion is formulated in the displacement jump space, and it is represented as,

$$F(\lambda^t, r^t) = G(\lambda^t) - G(r^t) \leq 0, \quad \forall t \geq 0 \tag{7.8}$$

where t indicates the actual time and r^t is the damage threshold for the current time. If r^0 denotes the initial damage threshold, then $r^t \geq r^0$ at every point in time. Damage initiation is produced when the displacement jump norm, λ, exceeds the initial damage threshold, r^0, which is a material property. $G(\cdot)$ represents a suitable monotonic scalar function raging from 0 to 1 that will define the evolution of the damage value.

The evolution laws for the damage threshold and the damage variable must be defined in the damage model. These laws are defined by the rate expressions,

$$\dot{r} = \dot{\mu} \tag{7.9a}$$

$$\dot{d} = \dot{\mu}\frac{\partial F(\lambda, r)}{\partial \lambda} = \dot{\mu}\frac{\partial G(\lambda)}{\partial \lambda} \tag{7.9b}$$

where $\dot{\mu}$ is a damage consistency parameter used to define loading/unloading conditions according to the Kuhn-Tucker relations,

$$\dot{\mu} \geq 0 \quad ; \quad F(\lambda^t, r^t) \leq 0 \quad ; \quad \dot{\mu}F(\lambda^t, r^t) = 0 \tag{7.10}$$

The evolution of the internal variables may be explicitly integrated to render,

$$r^t = \max\left\{r^0, \max_s \lambda^s\right\}, \quad 0 \leq s \leq t \tag{7.11a}$$

$$d^t = G\left(r^t\right) \tag{7.11b}$$

where d^t is the damage variable at time t, which is used as the threshold function. This explicit definition fully describes the evolution of the internal variables for any loading/unloading/reloading situation. The scalar function $G(\cdot)$ defines the evolution of the damage value. For a given mixed-mode ratio β, given by,

$$\beta = \frac{\Delta_{shear}}{\Delta_{shear} + \langle \Delta_3 \rangle} \tag{7.12}$$

the function $G(\lambda)$ is defined as,

$$G(\lambda) = \frac{\Delta^f\left(\lambda - \Delta^0\right)}{\lambda\left(\Delta^f - \Delta^0\right)} \tag{7.13}$$

Equation (7.13) defines the damage evolution law by means of a bilinear constitutive equation (see figure 7.3), where Δ^0 and Δ^f are the onset and final (corresponding to propagation) displacement jumps, obtained by means of the onset and propagation damage criteria, respectively.

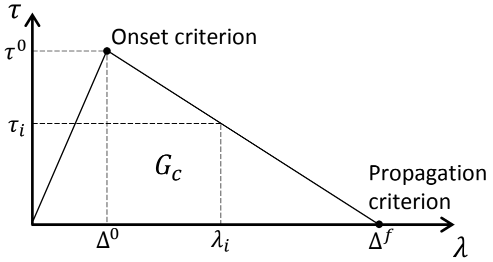

Fig. 7.3. Parameters of the bilinear constitutive equation.

The propagation criterion for delamination growth under mixed-mode loading conditions is established in terms of energy release rates and fracture toughnesses as follows,

$$G = G_{Ic} + (G_{IIc} - G_{Ic})\left(\frac{G_{shear}}{G_I + G_{shear}}\right)^{\eta} \tag{7.14}$$

where G_{Ic} and G_{IIc} are the fracture toughnesses in mode I and II, respectively, G_I and G_{II} are the energy release rates in mode I and II, respectively, and G_{shear} is the shear energy release rate, defined as,

$$G_{shear} = G_{II} + G_{III} \tag{7.15}$$

The η parameter is found by least square fit of experimental data points of the fracture toughnesses under different mixed-mode ratios.

Equation (7.15) is valid whenever the constitutive equations of modes II and III are equal. This hypothesis is very common because the fracture toughness of mode III is difficult to obtain and typically is considered equal to G_{IIc}. This fact ensures that the propagation criterion is consistent for pure mode loading cases II or III.

The propagation criterion in the displacement jump space is defined through the final displacements, which are defined from the pure mode fracture toughness (G_{Ic}, G_{IIc}, G_{IIIc}) and considering that the area under the traction-displacement jump curves is equal to the corresponding fracture toughness, i.e.,

$$G_c = \frac{1}{2}\tau^0\Delta^f = \frac{1}{2}K\Delta^0\Delta^f \quad \text{(see figure 7.3)} \tag{7.16}$$

For a given mixed mode ratio β, the energy release rates corresponding to total decohesion are obtained from,

$$G_I = \frac{1}{2}K\Delta_3^0(\beta)\Delta_3^f(\beta) \tag{7.17a}$$

$$G_{shear} = \frac{1}{2}K\Delta_{shear}^0(\beta)\Delta_{shear}^f(\beta) \tag{7.17b}$$

where $\Delta_{shear}^0(\beta)$ and $\Delta_3^0(\beta)$ are respectively the shear and normal (mode I) displacement jump corresponding to the onset of softening under mixed-mode loading, and $\Delta_{shear}^f(\beta)$ and $\Delta_3^f(\beta)$ are respectively the shear and normal (mode I) displacement jump corresponding to the total decohesion under mixed-mode loading. From equation (7.12), $\Delta_{shear}^0(\beta)$ and $\Delta_{shear}^f(\beta)$ can be written as,

$$\Delta_{shear}^0(\beta) = \Delta_3^0(\beta)\frac{\beta}{\beta+1} \tag{7.18a}$$

$$\Delta_{shear}^f(\beta) = \Delta_3^f(\beta)\frac{\beta}{\beta+1} \tag{7.18b}$$

Combining equations (7.18a) and (7.18b) with equations (7.17a) and (7.17b), the ratio between G_{shear} and $G_I + G_{shear}$, denoted B, can be written in terms of β as,

$$B = \frac{G_{shear}}{G_I + G_{shear}} = \frac{\beta^2}{1+\beta^2-2\beta} \tag{7.19}$$

Using equations (7.16) and (7.19) in equation (7.14), the propagation criterion is obtained in the displacement jump space as,

$$\Delta^f = \frac{\Delta_3^0\Delta_3^f + \left(\Delta_{shear}^0\Delta_{shear}^f - \Delta_3^0\Delta_3^f\right)[B]^\eta}{\Delta^0} \tag{7.20}$$

The parameter Δ^0 is the displacement for damage onset, which is determined by means of the damage onset criterion. Therefore, equation (7.20) shows that both criteria, for damage onset and damage propagation, are linked in this model.

The damage onset criterion is also based on energy terms. Since delamination is a fracture process, Turon et al. [55] proposed a damage onset criterion that evolves from the propagation criterion and the damage evolution law. So, considering only the elastic energy terms of the constitutive equation, the energy release rates corresponding to damage onset are defined as,

$$G_I = \frac{1}{2}K\left(\Delta_3^0\right)^2 \tag{7.21a}$$

$$G_{shear} = \frac{1}{2}K\left(\Delta_{shear}^0\right)^2 \tag{7.21b}$$

and the fracture toughness is,

$$G_c = \frac{1}{2}K\left(\Delta^0\right)^2 \tag{7.22}$$

Using equations (7.21) and (7.22) in equation (7.14), and taking into account equation (7.19), the damage onset criterion can be written as,

$$\Delta^0 = \left\{\left(\Delta_3^0\right)^2 + \left[\left(\Delta_{shear}^0\right)^2 - \left(\Delta_3^0\right)^2\right][B]^\eta\right\}^{\frac{1}{2}} \tag{7.23}$$

7.2.2. Interlaminar damage model implementation

The decohesion element proposed by Turon et al. [55] and briefly described here is implemented in a user-written element subroutine (UEL) to simulate problems in ABAQUS® implicit. Therefore, the basic requirement of the subroutine is to define the contribution of the decohesion element to the global model, i.e., the subroutine must define the contribution of the element to the tangent stiffness matrix and to the internal force vector of the decohesion element (residual vector).

The formulation of the constitutive tangent tensor is described in detail by Turon et al. [55], and no further details are presented herein. The internal force vector of the decohesion element is given by,

$$f_{Ki} = \int_{\Gamma_{d_i}} \tau_i B_{imK} \mathrm{d}\Gamma_d \tag{7.24}$$

where Γ_{d_i} is the boundary of the delamination and B_{imK} is defined as,

$$B_{imK} = \Theta_{im}\bar{N}_K \tag{7.25}$$

where Θ_{im} is the rotation tensor, which relates the global and the local coordinates, and $\bar{N}_K$ are standard Lagrangian shape functions of the K node of the element defined for the cohesive elements (see reference [65]).

The softening nature of the decohesion element constitutive equation causes difficulties in obtaining a converged solution for the nonlinear problem when using the Newton-Raphson iterative method. In particular, quadratic convergence is not assured because the residual vector is not continuously differentiable with respect to the nodal displacements. Therefore, the tangent stiffness matrix must be defined, which stems from the linearization of the internal force vector and it is obtained using Taylor's series expansion about the approximation of the displacement components at the element node K, q_{Ki}. The tangent stiffness matrix, K_{jKrZ}, for the decohesion element is therefore approximated as,

$$K_{jKrZ} \approx \int_{\Gamma_d} B_{ijK} D_{in}^{\tan} B_{nrZ} \, \mathrm{d}\Gamma_d \tag{7.26}$$

where $D_{in}^{\tan}$ is the material tangent stiffness matrix, or constitutive tangent tensor used to define the tangent stiffness matrix and depends on the interfacial constitutive model adopted.

The implementation of the damage model as a finite element stiffness was performed using the tangent as well as the secant constitutive tensors. The tangent stiffness poses convergence difficulties in the vicinity of a global instability, while the secant stiffness produces slow convergence of the solution procedure. The code initially uses the tangent stiffness tensor in the calculations. If after a certain number of iterations the convergence has not achieved, the code automatically reduces the time step. If convergence is again not achieved after a certain number of iterations, then the code switches between the tangent stiffness tensor and the secant stiffness tensor [236].

7.3. Free-edge delamination simulation

7.3.1. Finite element model

A FE model implemented in the implicit FE code Abaqus®/Standard is used to investigate the effect of using thin-ply NCF laminates in the resistance to delamination. In particular, the onset of free-edge delamination in unnotched and open-hole laminates is analysed using the decohesion elements proposed by Turon et al. [55], briefly described in the previous section. The Abaqus®/Standard FE model is generated using a parametric model implemented in Python. Such parametric model is able to quickly generate the unnotched and open-hole FE models for different geometries, lay-ups and materials by simply changing the parameters that govern these characteristics, such as the width, length and hole diameter for the geometry, the number of plies and ply angles for the lay-up, and the ply material properties for the material.

The FE model used to evaluate the onset of free-edge delamination in unnotched and open-hole laminates is 5 mm wide, 10 mm long and has a width to hole diameter ratio $w/d = 4$, as shown in figure 7.4. The thickness of the FE model, t^L, depends on the number of layers, which have a constant thickness of 0.08 mm. Each layer is modeled with one element through the thickness. Initially, a thermal step with a temperature variation $\Delta T = -150$ °C is performed to account with thermal stresses[1]. Then, an imposed displacement in the longitudinal direction, Δ, is applied to the laminate to assess the onset of free-edge delamination.

In this model, the DECO-UEL.V1 zero-thickness decohesion elements are placed between each [0/−45] NCF bi-layer of the thin-ply laminates investigated in the experimental program of this thesis (see chapter 3). The decohesion elements simulate the interface between [0/−45] NCF bi-layers, since it is assumed that delamination does not occur in the interface between the 0° and the −45° layers of the NCF, due to the effect of stitching.

---

[1] Because the thermal expansion coefficients for the thin-ply laminates studied here are not available, typical values for carbon/epoxy laminates are used, namely $\alpha_1 = -5.5 \times 10^{-6}$ /°C, $\alpha_2 = 2.58 \times 10^{-5}$ /°C, and $\alpha_3 = 2.58 \times 10^{-5}$ /°C.

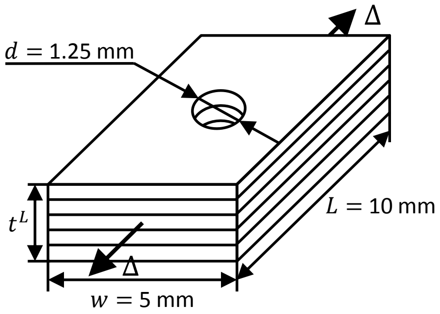

Fig. 7.4. Finite element model of the open-hole laminate for the simulation of free-edge delamination (the model of the unnotched laminate is exactly the same, but without the hole).

In other words, it is assumed that delamination only occurs between the [0/−45] NCF bi-layers. The [0/−45] interface of the NCF bi-layers is considered as a perfect one, and is modeled as a tie constraint.

Free-edge delamination is simulated along the long edges of the laminates. The decohesion elements are placed in a region corresponding to 80% of the laminate length (0.8L), as shown in figure 7.5. This approach is a simple way to take into account the clamping pressure of the grips traditionally used in tensile tests, which prevents the onset of delamination in the gripped areas.

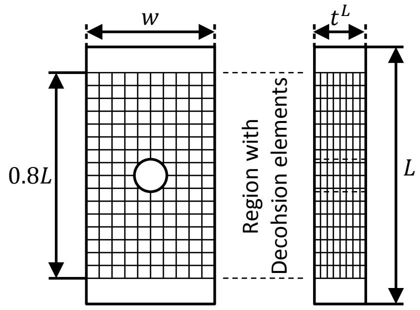

Fig. 7.5. Region of the finite element model of the open-hole laminate where the decohesion elements are placed (the model of the unnotched laminate is exactly the same, but without the hole).

Abaqus®/ C3D8R elements, with reduced integration, are used to model the material layers. Each element is 0.08 mm thick (layer thickness) and the in-plane dimensions are 0.5×0.5 mm^2. However, note that, because the decohesion element is based in a cohesive zone model, there is a minimum mesh size required to correctly capture the distribution of tractions, and therefore guarantee reasonable results. Such mesh size must be determine in order to have more than two (typically four) elements in the cohesive zone, generally conducting to very fine meshes. To maximize the time efficiency of the present analysis and minimize its computational requirements, a procedure developed by Turon et al. [68] to adapt the length of the cohesive zone to a given mesh size is taken into account. This procedure consists of determining the value $\bar{\tau}^0$ of the interlaminar strength required for a desired number of elements N_e^0 in the cohesive zone. This adjusted interlaminar strength is given by,

$$\bar{\tau}^0 = \sqrt{\frac{9\pi E G_c}{32 N_e^0 l_e}} \tag{7.27}$$

where E is the Young modulus of the material, G_c is the critical energy release rate and l_e is the mesh size in the direction of crack propagation. The interlaminar strength is chosen as,

$$T = \min\{\tau^0, \bar{\tau}^0\} \tag{7.28}$$

The interlaminar strength is computed for each loading mode by substituting the value of the fracture toughness in equation (7.27) and the value of the ultimate traction in equation (7.28) by the values corresponding to the loading mode. Note that, although variations of the maximum interlaminar strength do not have a strong influence in the predicted results, lowering the interlaminar strength can improve the convergence rate of the solution. The result of using a lower interlaminar strength is that the length of the cohesive zone and the number of elements in the cohesive zone increase. Therefore, the mechanics of energy dissipation are properly captured, and the representation of the softening response of the fracture process ahead of the crack tip is more accurate, ensuring the proper propagation of the crack front, though the stress concentrations in the bulk material near the crack tip might be altered [68].

Following this procedure developed by Turon et al. [68], the mode I interlaminar strength, τ_3^0, can be obtained as,

$$\bar{\tau}_3^0 = \sqrt{\frac{9\pi E_2 G_{Ic}}{32 N_e^0 l_e}} \tag{7.29a}$$

$$\tau_3^0 = \min\{\tau_3^0, \bar{\tau}_3^0\} \tag{7.29b}$$

Assuming that the material used in the simulations has a transverse Young modulus $E_2 = 7.4$ GPa, and a mode I fracture toughness $G_{Ic} = 0.28$ kJ/m^2, in order to have four elements of length $l_e = 0.5$ mm in the cohesive zone, $N_e^0 = 4$, the mode I interlaminar strength yields $\tau_3^0 = 42.8$ MPa. Note that these properties are not the interlaminar properties of the C-Ply™ T700 NCF/AR-2527 laminate studied in the experimental program of this thesis, since such properties are not available at the moment. Therefore, idealized properties are used in the free-edge delamination numerical simulations performed herein. Note also that this is not a problem, since this numerical analysis is a comparative (qualitative) study with regard to the advantages of using thin-ply laminates, in particular thin-ply NCF, in the resistance to delamination onset and growth. The reliability of the numerical tools used herein were already proved with the extensive work of Turon, Camanho and co-authors.

The appropriate mode II interlaminar strength, τ_{sh}^0, can be obtained using the relation proposed by Turon et al. [163],

$$\tau_{sh}^0 = \tau_3^0 \sqrt{\frac{G_{IIc}}{G_{Ic}}} \tag{7.30}$$

where G_{Ic} and G_{IIc} are the fracture toughness under mode I loading and mode II loading, respectively. According to Turon et al. [163], when linear elastic fracture mechanics applies, using the relation given by equation (7.30), the predictions obtained using decohesion finite elements are independent of the pure mode interlaminar strengths used. Therefore, using equations (7.27) to (7.30), a reliable methodology to analyse delamination onset and growth using relatively coarse meshes can be obtained. Assuming that the material used in the simulations has a mode II fracture toughness $G_{IIc} = 0.69$ kJ/m^2, the mode II interlaminar strength yields $\tau_{sh}^0 = 66.0$ MPa.

A comparative study is performed with laminates having stacking sequences similar to $[(0/{-45})/(90/45)]_{6T}$ and $[(0/{-45})/(45/0)/(90/45)/({-45}/90)]_{S}$, corresponding to the lay-up 1 and lay-up 2 laminates, respectively (see figure 7.6). A $[0/{-45}/90/45]_{3T}$ thick alternative to the lay-up 1 stacking sequence is chosen, hereafter referred to as *alternative 1* (see figure 7.6c). The alternative to the lay-up 2 is a thin alternative where the effect of stitching is not taken into account, hereafter referred to as *alternative 2*, with a stacking sequence $[0/{-45}/45/0/90/45/{-45}/90]_{S}$ (see figure 7.6d).

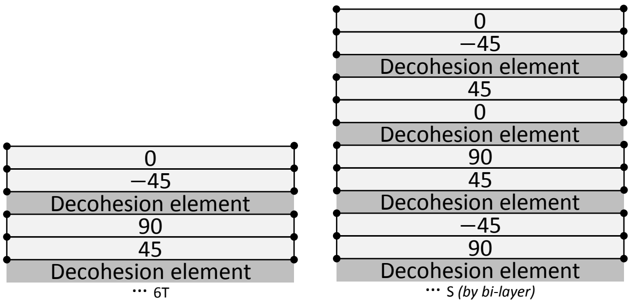

(**a**) Lay-up 1. (**b**) Lay-up 2.

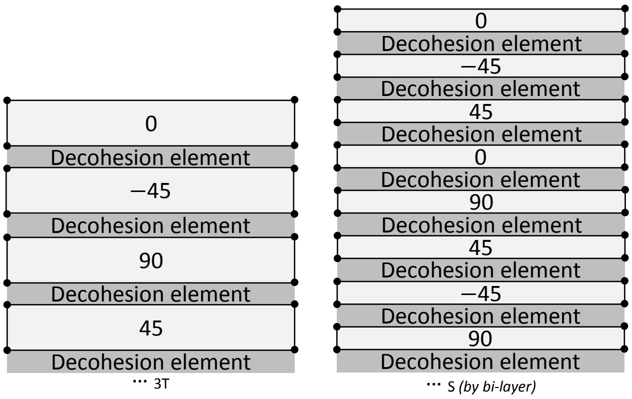

(**c**) Alternative 1. (**d**) Alternative 2.

Fig. 7.6. Stacking sequences for the comparative study of the resistance to onset and growth of free-edge delamination.

The alternative 1 stacking sequence has 12 layers, each one with a thickness of 0.16 mm. The laminate thickness is kept constant and equal to that of lay-up 1, as well as the laminate elastic properties. Decohesion elements are placed in all interfaces between layers, which means that the stitching effect is not considered (i.e., alternative 1 is not considered to be a NCF). The comparative study between the lay-up 1 and alternative 1 laminates is intended to assess the effect of ply thickness when designing a laminate using thin NCF bi-layers instead of unidirectional (UD) layers in the resistance to delamination onset. Note that both stacking sequences have the same number of overlapping plies, and therefore the design procedures associated with manufacturing using NCF bi-layers would be similar to those of the UD layers, or advantageous when using pre-forms, due to the higher dry rigidity of the NCF. In addition, the number of interfaces for delamination is the same for both stacking sequences, meaning that the difference in the through-the-thickness stress distributions will be the main driver of the difference in the results. Note that the through-the-thickness stress distribution for alternative 1 (tick-ply laminate) is considered to have higher stress concentrations at the adjacent interfaces than those of the lay-up 1 (thin-ply NCF), due to the difference in the ply thicknesses. In spite of the same number of interfaces for delamination, it is expected that the higher interlaminar stresses will conduct to earlier delamination onset in the alternative 1 stacking sequence.

The alternative 2 stacking sequence is intended to assess the effect in the overall resistance of the laminate to delamination onset caused by the reduction of interfaces for delamination due to stitching. This can be done using the lay-up 2 stacking sequence but placing decohesion elements in all interfaces, which is equivalent to consider that alternative 2 is made with UD 0.08 mm thick thin plies. Because the through-the-thickness stress distributions are similar, at least before delamination onset, if any difference in the resistance to delamination onset exists it is expected that this difference will depend on the number of interfaces for delamination, which are the double for the alternative 2. Particularly, because the number of interfaces for delamination is higher, it is expected that onset of delamination may be delayed in the alternative 2 laminate due to a more homogeneous distribution of damage in the interfaces between plies. With such results, it will be possible to evaluate the interlaminar mechanical responses, at least until delamination onset, of thin-ply laminates made with bi-layer NCF or UD layers, assuming plies of the same thickness.

7.3.2. Results

The results of the FE simulations carried out to assess the onset of free-edge delamination in unnotched and open-hole laminates subjected to tensile loading are shown in table 7.1. For each laminate (either unnotched and with an open-hole), it is shown the critical load, obtained for the moment at which the first damage variable (d) reaches 1, corresponding to the moment of complete interlaminar damage in an integration point, i.e., corresponding to delamination onset. As it would be expected, in all simulations, the onset of delamination occurred at a free-edge.

Tab. 7.1. Critical loads corresponding to onset of free-edge delamination, obtained using the finite element method.

Laminate	Critical load (unnotched) [N]	Critical load (open-hole) [N]
Lay-up 1	3941	3426
Alternative 1	3726	2573
Lay-up 2	3323	1764
Alternative 2	5338	3321

As one can see, and as it would be expected, the critical loads corresponding to free-edge delamination onset for the open-hole laminates are lower than those for the unnotched laminates, regardless of the stacking sequence. However, according to these results, the lay-up 2 and alternative 2 laminates seem to be quite more sensitive to the introduction of an open-hole than the lay-up 1 and alternative 1 laminates. This is somewhat expectable, since the introduction of the open-hole leads to an increase of the interlaminar stresses near the free-edges, that added to the higher interlaminar stresses developed in the lay-up 2 and alternative 2 laminates due to higher interlaminar relative orientations and ply clustering results in a quite earlier onset of free-edge delamination.

Comparing the predictions for the lay-up 1 and lay-up 2 laminates, one can see that the critical load corresponding to free-edge delamination onset is 15.7% and 48.5% lower, respectively, for the unnotched and open-hole lay-up 2 laminates than for the respective lay-up 1 laminates. These results indicate that the lay-up 1 laminate is clearly more resistant to delamination onset than the lay-up 2 laminate. Indeed, such results confirm those obtained during the experimental tests carried out in this thesis, where it was observed that the susceptibility of the lay-up 2 laminate to show some delamination was considerably higher than that exhibited by the lay-up 1 laminate, which always showed a brittle type of net-tension failure mode (see chapter 4). As pointed out during discussion of the experimental results, such differences on the interlaminar mechanical responses of these two laminates are a result of their stacking sequences. Unlike the lay-up 1 laminate, which has a constant angle of 45° between interfaces (both within and between $[0/-45]$ bi-layers), the lay-up 2 laminate has some interfaces between the $[0/-45]$ bi-layers with an angle of 90°, conducting to higher interlaminar stress concentrations. In addition, the lay-up 2 laminate has some interfaces between the $[0/-45]$ bi-layers with an angle of 0°, resulting in ply clustering and conducting to higher stress concentrations in the adjacent interfaces. The combination of these two factors increases the interlaminar stresses and, consequently, conducts to earlier delamination onset.

Regarding the effect of ply thickness on the resistance to delamination onset, evaluated taking into account the predictions for the lay-up 1 and alternative 1 laminates, one can see that the critical loads for the thick-ply unnotched and open-hole alternative 1 laminates are, respectively, 5.5% and 25.9% lower than those for the respective thin-ply lay-up 1 laminates. As described in section 7.3.1, these results were expected, since, despite the same number of interfaces for delamination, the interlaminar stresses in the thick-ply alternative 1 laminate are higher than those in the thin-ply lay-up 1 laminate, conducting to earlier delamination onset. These results also show that this difference is even higher when an open-hole is introduced in the laminate. Based on these predictions, it becomes clear that for decreasing ply thicknesses, the resistance to delamination onset increases, even when NCF bi-layers are used and the number of interfaces for delamination is kept constant, generalizing the results of a previous work of Camanho et al. [45].

Regarding the effect of the number of interfaces for delamination on the resistance to delamination onset, i.e. the effect of using NCF bi-layers instead of UD plies, evaluated taking into account the predictions for the lay-up 2 and alternative 2 laminates, one can see that the critical loads for the unnotched and open-hole alternative 2 laminates are, respectively, 60.6% and 88.3% higher than those for the respective lay-up 2 laminates. Such results show a huge influence of the number of interfaces for delamination, indicating that using UD thin-plies instead of thin-ply NCF would greatly enhance the delamination resistance of thin-ply laminates. As described in section 7.3.1, it was expected that onset of delamination would be delayed in the alternative 2 laminate due to a more homogeneous distribution of damage in the interfaces between plies. However, this difference is too much pronounced, whereby these results must be carefully evaluated. Indeed, it is difficult to understand the difference observed. Therefore, further studies may be conducted regarding this issue. In particular, new simulations may be carried out using the effective properties of the thin-ply laminates studied here, using geometrical models more similar to the unnotched and open-hole specimens, and using more complete numerical tools (for simulation of interlaminar as well as intralaminar damage), in order to more accurately and reliably assess the effect of stitching on the mechanical behavior of thin-ply laminates.

7.3.3. Discussion and concluding remarks

A qualitative numerical study based on the FEM was carried out in this chapter to assess the effect of ply thickness and the effect of stitching on the interlaminar mechanical response of thin-ply laminates. The DECO-UEL.V1 zero-thickness decohesion element was used to simulate delamination in FE models of unnotched and open-hole laminates with stacking sequences similar to the thin-ply laminates studied in this thesis, as well as two alternative stacking sequences, to assess the effect of ply thickness and the effect of stitching on the resistance to free-edge delamination onset.

The numerical predictions showed that the introduction of an open-hole results in a substantial decrease of the resistance to delamination onset. This was particularly true for those laminates more susceptible to interlaminar damage, such as those with higher interlaminar relative orientations and ply clustering. Indeed, these numerical simulations confirmed the results obtained during the experimental tests carried out in this thesis, where it was observed that laminates with higher interlaminar relative orientations and ply clustering are more susceptible to delamination onset.

Regarding the effect of ply thickness, the numerical predictions also showed that decreasing the ply thickness, the resistance to delamination onset increases, even when NCF bi-layers are used and the number of interfaces for delamination is kept constant. This is particularly interesting, since using thin-ply NCF laminates it is possible to enhance the mechanical performance without any additional manufacturing effort. In a matter of fact, the use of thin-ply NCF bi-layer may be advantageous in the manufacture of a laminate, particularly when using pre-forms, due to the higher dry rigidity of the NCF when compared with UD plies.

On the other hand, regarding the effect of the number of interfaces for delamination (or effect of stitching), the numerical simulations carried out in this thesis indicated that using UD thin-plies instead of thin-ply NCF would greatly enhance the delamination resistance of thin-ply laminates. However, such results were difficult to understand, and no physical explanation was found. Therefore, it is suggested that new studies with respect to this issue may be carried out in the future, namely using the effective properties of the thin-ply laminates, using geometrical models more similar to the unnotched and open-hole specimens, and using more complete numerical tools (for simulation of interlaminar as well as intralaminar damage), in order to more accurately and reliably assess the effect of stitching on the mechanical behavior of thin-ply laminates.

Chapter 8

Conclusions and future work

In this thesis, a new technology of interest, the spread tow thin-ply technology, was presented, aiming to assist in its technology development. In this chapter, the main conclusions regarding the state-of-the-art of this technology, the experimental test program and respective results, the analysis methods, and the numerical analysis performed during development of this thesis are presented. Based on these main conclusions, and because this thesis is just a first step on the understanding of the structural integrity of thin-ply laminates built of spread tow thin-ply technology, the future work that needs to be carried out in order to fully characterize the structural integrity of these promising materials is also proposed.

8.1. Conclusions

The spread tow thin-ply technology is considered to be a technology of interest, particularly in the development of new and optimized concepts for high-performance composite structures. Since the introduction of this technology, developed by the Industrial Technology Center in Fukui Prefecture, Japan, in the late 1990's, and the manufacture of the first thin-ply laminates, a few works demonstrated some of the potential advantages of these promising composite materials, namely with respect to the improved delamination resistance, first-ply-failure delay, and improved design options, regarding easier laminate homogenization, continuous stacking (asymmetric laminates), and simpler laminate mechanical optimization through anisotropy.

In addition, particularly in the last 10 years, the scientific community that has been focused on composite laminates design has centered part of their attention to the effects of having sublaminate-level (thin-ply) or ply-level (thick-ply) scaled composite laminates on the mechanical performance of these materials, namely with respect to the in-situ strengths, delamination resistance, damage resistance and tolerance, and translaminar fracture toughness. The several studies regarding these issues indicate that sublaminate-level scaling has particular advantages in the strength and damage prevention. Indeed, the strength of the sublaminate-level scaled laminates was proved to be higher than that of the ply-level scaled laminates, and irreversible subcritical damage, such as delamination or transverse cracking, was almost absent before failure of sublaminate-level scaled laminates, opposing to ply-level scaled laminates, where onset and propagation of delamination and transverse cracking typically resulted in a substantial nonlinear behavior before failure.

In notched laminates, the earlier onset and propagation of delamination and transverse cracking resulting of ply-level scaling generally conducted to higher notched strength, attributed to the reduction of the stress concentrations near the notches. Because this kind of subcritical damage is almost absent when sublaminate-level scaling is adopted, there are no mechanisms to reduce stress concentrations, and fracture of notched sublaminate-level scaled laminates generally occurs as a brittle type of net-section failure mode, ultimately resulting in a more brittle material response. However, some studies demonstrated that, before failure, for the same imposed displacement, the level of subcritical damage in notched ply-level scaled laminates was substantially higher than that of notched sublaminate-level scaled laminates, where it was virtually absent. This may be critical for applications where the laminate may be subjected to variable loading conditions, such as alternating tension-compression loading, since, as it is well known, delamination substantially reduces the compressive strength of a laminate, or mechanical fatigue, because, as some studies indicated, the fatigue behavior of a laminate is clearly lower when ply-level scaling is adopted.

Regarding the effect of ply thickness on the impact resistance and damage tolerance of composite laminates, distinct results and conclusions appear in the literature. In addition, the experimental test programs regarding damage resistance and tolerance of composite laminates built of spread tow thin-ply technology are scarce, and any of these were accompanied by reliable numerical simulations so far. Therefore, taking into account the available work, at the moment, no definitive conclusions can be made with respect to this issue.

Similarly, the available work regarding the effect of the type of lay-up scaling on the translaminar fracture toughness of composite laminates is also very scarce. Indeed, those few works did not provide sufficient data to conclude about the effect of ply thickness either in the laminate translaminar fracture toughness or in the translaminar fracture toughness of the 0° ply of composite laminates, and future work regarding this issue is essential in the assessment of the structural integrity of thin-ply laminates.

Although some work was already done regarding the mechanical characterization of thin-ply laminates, a set of relevant issues were not taken into account yet, whereas others need revision and/or further validation. Accordingly, an experimental test program was conducted in order to support the technology development of the spread tow thin-ply technology. Some of the most relevant mechanical properties regarding the structural integrity of two thin-ply carbon NCF C-Ply™ T700/AR-2527 epoxy laminates were studied, with particular emphasis in size effects, notched strength, bearing strength, and fracture toughness of such materials.

The results discussed in this thesis show that, when subjected to tensile efforts, thin-ply laminates exhibit an approximately linear behavior up to final failure. Such behavior indicates that unrecoverable severe damage, such as extensive transverse cracking and delamination, are virtually absent in thin-ply laminates. This behavior is particularly evident for the laminates with more reduced relative ply orientations and without ply clustering, which exhibit a brittle type of net-section failure mode, whose failure section is perpendicular to the applied tension load. On the other hand, pull-out can be observed in thin-ply laminates with relative ply orientations of 90° and ply clustering. Accordingly, the brittle type of net-section failure mode, dominated by fiber breakage, seems to be beneficial with respect to the laminate's tensile unnotched strength, since improving delamination resistance and precluding transverse cracking (both achievable using thin plies) result in stronger laminates, delaying first-ply-failure for the moment just before final failure.

However, the ability of thin-ply laminates to suppress damage development before failure may have some consequences regarding their fracture toughness and their notched strength, particularly for the thin-ply laminates less susceptible to delamination and transverse cracking onset and growth, such as the $[(0/-45)/(90/45)]_{6T}$ (lay-up 1) laminate. Indeed, the development of a more extensive damaged zone, for example near the notch tip of a center-notched specimen or near the hole of an open-hole specimen, as it was observed, for example, in the thin-ply $[(0/-45)/(45/0)/(90/45)/(-45/90)]_S$ (lay-up 2) laminate, redistributes stresses and decreases stress concentrations, ultimately resulting in a tougher material. Consequently, the notch sensitivity of the thin-ply laminates that suppress damage onset and growth tends to increase. Still, no substantial differences were found either in the effects of hole size or in the notch sensitivity of the thin-ply laminates when compared with other carbon/epoxy systems designed for aircraft structural applications.

On the other hand, when subjected to compressive efforts, thin-ply laminates exhibit a clear nonlinear behavior, resulting from the development of damage dominated by fiber kinking. Slightly differences were observed in the thin-ply laminates, once again resulting from the different stacking sequences. Although both laminates exhibit a net-section type of failure mode, the higher angle between layers and the ply clustering in the lay-up 2 laminate, which conduct to higher interlaminar stresses, precipitate failure of the laminate by other damage modes than fiber breakage, namely matrix cracking and fiber microbuckling, resulting in lower unnotched compressive strengths. However, in the presence of a notch or an open-hole, such damage mechanisms redistribute the stresses, and decrease the stress concentrations, ultimately resulting in a tougher material, as in the tensile case. Still, no atypical size effects or notch sensitivity were observed for the thin-ply laminates studied in the experimental work carried out in this thesis.

With respect to the experimental tests on the translaminar fracture toughness of the thin-ply laminates, taken in the literature as the main potential problem of these composite materials, it was observed that, in spite of the slightly lower laminate fracture toughness, the fracture toughness of the 0° ply was predicted as very similar to that of other carbon/epoxy systems used in the aircraft industry. Therefore, despite the brittle type of net-section failure mode typical of these laminates, the test results shown in this chapter indicate that a severe notch sensitivity is not observed in these materials.

Another relevant aspect studied in this experimental program was the ability of the thin-ply laminates to resist local compressive efforts, i.e., the effect of the ply thickness on the bearing strength. According to this preliminary study, very interesting results were obtained, since the thin-ply laminates exhibited a superior performance over a carbon/epoxy system typically used in aircraft structural construction. This superior performance was attributed to the ability of the thin-ply laminates to block onset and propagation of damage mechanisms such as delamination, fiber kinking, matrix cracking, and through-the-thickness shear cracking. However, further studies may be conducted in order to reliably understand the bearing failure mechanisms of thin-ply laminates.

Due to the importance of accurate, physically-based and fast strength prediction methods for composite laminates with stress concentrations, particularly for preliminary sizing and for optimization of aircraft composite structures, fast design tools based on closed-form solutions were used in the prediction of size effects and notch sensitivity of thin-ply laminates. In addition to the ease of use, the closed-form models used in this thesis were able to reasonably predict both tensile and compressive notched responses of the thin-ply NCF laminates experimentally investigated in this thesis, as well as the notched responses of two alternative laminates typical of aircraft and aerospace industries. However, because it does not require any inverse identification from a notched experimental test, and due to its promising generality and versatility, the finite fracture mechanics model was considered to be the best suited one to evaluate the macroscopic size effects on carbon/epoxy composite systems, as well as the notch sensitivity, by means of design charts and a recently introduced dimensionless parameter, designated *notch sensitivity factor*.

With respect to the thin-ply carbon NCF C-Ply™ T700/AR-2527 epoxy laminates investigated herein, despite the brittle type of fracture mode exhibited by these laminates, and despite some concerns regarding this issue, the predictions obtained with these closed-form models indicate that these composite materials do not exhibit inherent brittleness. Indeed, the previous analyses showed that the notched responses in both tension and compression are not so different from those exhibited by the alternative T800/M21 and IM7-8552 carbon/epoxy systems, both designed for the aircraft industry, which is in agreement with the experimental results obtained.

To assess the effect of ply thickness and the effect of stitching on the interlaminar mechanical response of thin-ply laminates, a qualitative numerical study based on the FEM was also carried out in this thesis. Zero-thickness decohesion elements were used to simulate delamination in FE models of unnotched and open-hole laminates with stacking sequences similar to the thin-ply laminates studied in this thesis, as well as two alternative stacking sequences, to assess the effect of ply thickness and the effect of stitching on the resistance to free-edge delamination onset.

These numerical predictions showed that the introduction of an open-hole results in a substantial decrease of the resistance to delamination onset. This was particularly true for those laminates more susceptible to interlaminar damage, such as those with higher interlaminar relative orientations and ply clustering, confirming the results obtained during the experimental tests. Regarding the effect of ply thickness, the numerical predictions also showed that decreasing the ply thickness, the resistance to delamination onset increases, even when NCF bi-layers are used and the number of interfaces for delamination is kept constant. This is particularly interesting, since using thin-ply NCF laminates it is possible to enhance the mechanical performance without any additional effort when manufacturing. As a matter of fact, the use of thin-ply NCF bi-layer may be advantageous in the manufacturing of a laminate, particularly when using pre-forms, due to the higher dry rigidity of the NCF when compared with UD plies. On the other hand, regarding the effect of the number of interfaces for delamination (or effect of stitching), the numerical simulations carried out in this thesis indicated that using UD thin-plies instead of thin-ply NCF would greatly enhance the delamination resistance of thin-ply laminates. However, such results were difficult to understand, and no physical explanation was found.

8.2. Future work

In spite of the efforts made previously to characterize the mechanical behavior and the structural integrity of composites built of spread tow thin-ply technology, some work still needs to be done in order to reliably accomplish this task. In particular, the assessment of the effect of ply thickness on the mechanical performance of these composite laminates is intended to be very important, and therefore, further studies may be conducted.

Regarding the development of new experimental programs, a comparison between thin-ply (for instance, obtained by tow spreading) and thick-ply laminates, with the same laminate thickness, and made of the same material system is strongly recommended. As discussed along this thesis, the absence of an equivalent laminate material to perform accurate comparisons with respect to the effect of ply thickness did not allow an effective quantitative evaluation of the structural integrity of thin-ply laminates. In addition, the results discussed in this thesis may be affected by the different laminate thicknesses, either between the thin-ply laminates studied here, and between these laminates and the T800/M21 and IM7-8552 laminates used for comparison purposes. Also, besides the effect of ply thickness, and since the material tested herein is based in a bi-layer $[0/-45]$ carbon NCF, it may also be interesting to assess the effect of stitching in the structural integrity of these laminates. Therefore, the possibility to perform an apple to apple comparison between laminates of the same carbon/epoxy system (the T700/AR-2527, eventually), with different ply thicknesses and stacking sequences, and for instance with and without stitching, would greatly enhance the analyses carried out in this thesis.

In addition, further studies may be conducted in order to accurately validate the preliminary results obtained for the tests carried out to assess the translaminar fracture toughness of thin-ply laminates. Particularly, new experimental programs need to be developed in order to accurately evaluate the fracture toughness of the 0° ply, e.g. by means of compact tension testing of cross-ply laminates made of tow-spread thin plies, and the R-curve effect, which was not quantified in this work, taking particular attention on the proper geometry and lay-ups to be tested. In this particular case, it is recommended the use of thicker laminates (around 4 mm thick), in order to avoid undesirable failure mechanisms, and with different ply thickness, in order to take into account its effect.

Further studies may also be conducted to validate the preliminary bearing test results obtained in this work. However, and unlike this preliminary work, such studies may include composite laminates with the same material system, with the same laminate thickness, and with different ply thicknesses. In addition, the new experimental program may also include post-testing through-the-thickness micrographic analysis, in order to accurately understand the effect of ply thickness on the damage development during bolt-bearing testing.

In addition to the studies already performed in this thesis, in order to fully assess the structural integrity of composite laminates, it is essential to conduct studies on the damage resistance and tolerance of thin-ply laminates, particularly by means of low velocity impact and compression after impact testing. Such studies may address a range of composite laminates with different scaling configurations in order to clarify the effect of ply thickness on the damage resistance and tolerance of thin-ply laminates.

Note also that the assessment of the structural integrity of any composite material based on experimental testing alone is not enough, since development of reliable and accurate numerical tools able to predict the response of composites under general loading conditions and geometries is more and more important. Therefore, in future works, as soon as the thin-ply composite laminates become fully characterized (which is essential to perform reliable numerical simulations), the structural integrity of these materials may also be assessed by means of numerical analysis. Particularly, the implementation of micromechanical models, as well as mesomechanical models, for instance based on the smeared crack model and continuous damage mechanics, to study the constituents micromechanical behavior, the notched behavior, and the damage tolerance of thin-ply laminates, would enhance the analysis of the structural integrity of thin-ply laminates, and greatly contribute for the knowledge regarding application and design of composite structures built of spread tow thin-ply technology.

Bibliography

[1] O. O. Ochoa and J. N. Reddy. *Finite Element Analysis of Composite Laminates*. Kluwer Academic Publishers, Dordrecht/Boston/London, 1992.

[2] Isaac M. Daniel and Ori Ishai. *Engineering Mechanics of Composite Materials*. Oxford University Press, Oxford [etc.], 2008.

[3] Daniel Gay and Suong V. Hoa. *Composite materials: design and applications*. CRC Press, Taylor and Francis Group, Boca Raton, 2^{nd} edition, 2007.

[4] Stephen W. Tsai. *Theory of Composites Design*. Composites Design Group, Department of Aeronautics & Astronautics, Stanford University, 2008.

[5] António Rui Melro. *Analytical and Numerical Modelling of Damage and Fracture of Advanced Composites*. PhD thesis, University of Porto, Porto, February 2011.

[6] W. S. Smith and C. Zweben. Properties of Constituent Materials — Introduction. In C. A. Dostal, M. S. Woods, H. J. Frissel, A. W. Ronke, D. M. Jenkins, K. L. O'Keefe, K. L. Pilarczyk, R. L. Stedfeld, K. M. J. J. J. Mills, R. T. Kiepura, and D. A. Humphries, editors, *Engineered Materials Handbook: Composites*, volume 1. ASM International, 1987.

[7] E. car, F. Zalamea, S. Oller, J. Miquel, and E. O nate. Numerical simulation of fiber reinforced composite naterials — two prodecures. *Int J Solids Struct*, 39:1967–1986, 2002.

[8] Bahram Farahmand. *Fracture Mechanics of Metals, Composites, Welds, and Bolted Joints: Application of LEFM, EPFM, and FMDM theory*. Kluwer Academic Publishers, Boston/Dordrecht/London, 2001.

[9] P. P. Camanho and F. L. Mathews. A Progressive Damage Model for Mechanically Fastened Joints in Composite Laminates. *J Compos Mater*, 33(24):2248–2280, 1999.

[10] Sangwook Sihn, Ran Y. Kim, Kazumasa Kawabe, and Stephen W. Tsai. Experimental studies of thin-ply laminated composites. *Compos Sci Technol*, 67:996–1008, 2007.

[11] Raimund Rolfes, Gerald Ernst, Matthias Vogler, and Chrstian Hühne. Material and Failure Models for Textile Composites. In Pedro P. Camanho, C. G. Dávila, S. T. Pinho, and J. J. C. Remmers, editors, *Mechanical Response of Composites*, volume 10 of *Computational Methods in Applied Sciences, E. Oñate, Series editor*, chapter 1. Springer, 2008.

[12] Stephen W. Tsai. The Science and Engineering of Bi-angle Non Crimp Fabric (NCF). Workshop presentation, Stanford University, July 13, 2011.

[13] Thomas Roure and Philippe Sanial. C-PLY™, a new structural approach to multiaxials in composites. *JEC Composites Magazine*, No68:53–54, October 2011. Special JEC Asia 2011.

[14] Stephen W. Tsai and Michel Cognet. A totally new concept of a laminated composite — The amazing bi-angle thin-ply NCF. *JEC Composites Magazine*, No68:51–52, October 2011. Special JEC Asia 2011.

[15] North Thin Ply Technology, LLC. Thin Ply Technology® from design to industrial production of composite components. Presentation, Airbus Hamburg, June 14, 2012.

[16] Kazumasa Kawabe, Tatsuki Matsuo, and Zen ichiro Maekawa. New Technology for Opening Various Reinforcing Fiber Tows. *J Soc Mat Sci Jpn*, 47(7):727–734, July 1998. (in Japanese).

[17] A. Petriccione, D. Annicchiarico, V. Antonucci, M. Giordano, A. Riccio, and F. Scaramuzzino. A stiffness volume averaging based approach to model non-crimp fabric reinforced composites. *Compos Sci Technol*, 72:360–369, 2012.

[18] Nicola Tessitore and Aniello Riccio. A novel FEM model for biaxial non-crimp fabric composite materials under tension. *Comput Struct*, 84:1200–1207, 2006.

[19] Frederick F. Saremi. First prepreg of bi-angle NCF and their mechanical properties. *JEC Composites Magazine*, No68:57–58, October 2011. Special JEC Asia 2011.

[20] Robert S. Skillen and Ajit D. Kelkar. Processing bi-angle non-crimp fabrics. *JEC Composites Magazine*, No68:64–65, October 2011. Special JEC Asia 2011.

[21] Valentin Neacsu, Jerry Fanucci, Rick Balonis, and John Stronck. Pultrusion and Resin Film Infusion (RFI) of bi-angle thin-ply NCF. *JEC Composites Magazine*, No68:59–61, October 2011. Special JEC Asia 2011.

[22] Thierry Massard, Roland Harry, Philippe Sanial, and Thierry Lorriot. Characterization of the equivalent unidirectional thin ply from NCF. *JEC Composites Magazine*, No68:55–56, October 2011. Special JEC Asia 2011.

[23] Stephen W. Tsai, editor. *Strangth & Life of Composites*, pages C–1–F–44. Composites Design Group, Department of Aeronautics & Astronautics, Stanford University, 2008.

[24] Stephen W. Tsai and Alan T. Nettles. Representative test data on bi-angle thin-ply NCF. *JEC Composites Magazine*, No68:62–63, October 2011. Special JEC Asia 2011.

[25] Stephen W. Tsai and Melih Papila. Thin-ply NCF: design for deformation through anisotropy. *JEC Composites Magazine*, No68:66–67, October 2011. Special JEC Asia 2011.

[26] S. W. Tsai. Weight and cost reduction by using unbalanced and unsymmetric laminates. In *The 18th International Conference on Composite Materials*, Jeju Island, Korea, August 21–26, 2011.

[27] C. T. Sun and S. P. Berreth. A New End Tab Design for Off-Axis Tension Test of Composite Materials. Technical Report HTMIAC Report 5, High Temperature Materials — Mechanical, Electronic and Thermophysical Properties Information Analysis

Center, Purdue University, West Lafayette, Indiana, March 1987. Operated by Center for Information and Numerical Data Analysis and Synthesis.

[28] C. T. Sun and S. P. Berreth. A new end tab design for off-axis tension test of composite materials. *J Compos Mater*, 22:766–779, 1988.

[29] C. T. Sun and Ilsup Chung. An oblique end-tab design for testing off-axis composite specimens. *Composites*, 24(8):619–623, 1993.

[30] Hannes Körber. *Mechanical Response of Advanced Composites under High Strain Rates*. PhD thesis, Faculdade de Engenharia da Universidade do Porto, Departamento de Engenharia Mecânica, 2010.

[31] M. Kawai, M. Morishita, H. Satoh, S. Tomura, and K. Kemmochi. Effects of end-tab shape on strain field of unidirectional carbon/epoxy composite specimens subjected to off-axis tension. *Compos Part A-Appl S*, 28A:267–275, 1997.

[32] Tomohiro Yokozeki, Yuichiro Aoki, and Toshio Ogasawara. Experimental characterization of strength and damage resistance properties of thin-ply carbon fiber/toughened epoxy laminates. *Compos Struct*, 82:382–389, 2008.

[33] Muhammad Ridha and T. E. Tay. Predicting the OHT strength of NCF composites. *JEC Composites Magazine*, No68:76–77, October 2011. Special JEC Asia 2011.

[34] M. Ridha and T. E. Tay. Notched vs Unnotched Failure Envelope [0/45/-45/0]s. National University of Singapore.

[35] M. J. Laffan, S. T. Pinho, P. Robinson, and L. Iannucci. Measurement of the in situ ply fracture toughness associated with mode I fibre tensile failure in FRP. Part II: Size and lay-up effects. *Compos Sci Technol*, 70:614–621, 2010.

[36] S. R. Hallett, B. G. Green, W. G. Jiang, and M. R. Wisnom. An experimental and numerical investigation into the damage mechanisms in notched composites. *Compos Part A-Appl S*, 40:613–624, 2009.

[37] Preliminary Open-Hole Compression Data on 24-ply Quasi-Isotropic Laminates Made of NCF and an Equivalent Aerospace Grade Prepreg.

[38] C. S. Lopes, O. Seresta, Y. Coquet, Z. Gürdal, P. P. Camanho, and B. Thuis. Low-velocity impact damage on dispersed stacking sequence laminates. Part I: Experiments. *Compos Sci Technol*, 69:926–936, 2009.

[39] Stephen W. Tsai and Melih Papila. Homogenization made easy with bi-angle thin-ply NCF. *JEC Composites Magazine*, No68:70–71, October 2011. Special JEC Asia 2011.

[40] Stephen W. Tsai and Melih Papila. First and last ply failure predictions by homogenized strength parameters. *JEC Composites Magazine*, No68:72–73, October 2011. Special JEC Asia 2011.

[41] T. Kim Parnel and Stephen W. Tsai. Equivalent properties for finite element analysis in composite design. *JEC Composites Magazine*, No68:74–75, October 2011. Special JEC Asia 2011.

[42] Stephen W. Tsai, editor. *Strength & Life of Composites*, pages Ai–A I–6. Composites Design Group, Department of Aeronautics & Astronautics, Stanford University, 2008.

[43] Yasuhiro Nishikawa, Kazuya Okubo, Toru Fujii, and Kazumasa Kawabe. Fatigue crack constraint in plain-woven CFRP using newly-developed spread tows. *Int J Fatigue*, 28:1248–1253, 2006.

[44] Carlos G. Dávila, Cheryl A. Rose, and Endel Iarve. Modeling fracture and complex crack networks in laminated composites. In Vladislav Mantič, editor, *Mathematical Methods and Models in Composites*. World Scientific Publishing, 2012.

[45] Pedro P. Camanho, A. Arteiro, Albert Turon, Josep Costa, and Gerard Guillamet. Structural integrity of thin-ply laminates. *JEC Composites Magazine*, No71:49–50, March 2012.

[46] Carlos G. Dávila and Pedro P. Camanho. Failure Criteria for FRP Laminates in Plane Stress. Technical Report NASA/TM-2003-212663, NASA Langley Research Center, Hampton, Virginia, November 2003.

[47] Carlos G. Dávila, Pedro P. Camanho, and Cheryl A. Rose. Failure Criteria for FRP Laminates. *J Compos Mater*, 39(4):323–345, 2005.

[48] Silvestre T. Pinho, Carlos G. Dávila, Pedro P. Camanho, Lorenzo Iannucci, and Paul Robinson. Failure Models and Criteria for FRP Under In-Plane or Three-Dimensional Stress States Including Shear Non-Linearity. Technical Report NASA/TM-2005-213530, NASA Langley Research Center, Hampton, Virginia, February 2005.

[49] Pedro P. Camanho, Carlos G. Dávila, Silvestre T. Pinho, Lorenzo Iannucci, and Paul Robinson. Prediction of in situ strengths and matrix cracking in composites under transverse tension and in-plane shear. *Compos Part A-Appl S*, 37:165–176, 2006.

[50] Pere Maimí, Pedro P. Camanho, Joan-Andreu Mayugo, and Carlos G. Dávila. A Thermodynamically Consistent Damage Model for Advanced Composites. Technical Report NASA/TM-2006-214282, NASA Langley Research Center, Hampton, Virginia, March 2006.

[51] Joan-Andreu Mayugo, Pedro P. Camanho, Pere Maimí, and Carlos G. Dávila. A Micromechanics-Based Damage Model for $[\pm\theta/90_n]_S$ Composite Laminates. Technical Report NASA/TM-2006-214285, NASA Langley Research Center, Hampton, Virginia, March 2006.

[52] P. Maimí, P. P. Camanho, J. A. Mayugo, and C. G. Dávila. A continuum damage model for composite laminates: Part I — Constitutive model. *Mech Mater*, 39:897–908, 2007.

[53] P. P. Camanho, P. Maimí, and C. G. Dávila. Prediction of size effects in notched laminates using continuum damage mechanics. *Compos Sci Technol*, 67:2715–2727, 2007.

[54] A. Parvizi, K. W. Garrett, and J. E. Bailey. Constrained cracking in glass fibre-reinforced epoxy cross-ply laminates. *J Mater Sci*, 13:195–201, 1978.

[55] Albert Turon, Pedro P. Camanho, Josep Costa, and Carlos G. Dávila. An Interface Damage Model for the Simulation of Delamination Under Variable-Mode Ratio in Composite Materials. Technical Report NASA/TM-2004-213277, NASA Langley Research Center, Hampton, Virginia, October 2004.

[56] A. Turon, P. P. Camanho, J. Costa, and C. G. Dávila. A damage model for the simulation of delamination in advanced composites under variable-mode loading. *Mech Mater*, 38:1072–1089, 2006.

[57] A. Turon, P. P. Camanho, J. Costa, and C. G. Dávila. A Damage Model for the Simulation of Delamination in Advanced Composites under Variable-Mode Loading. Technical report, NASA Langley Research Center, Hampton, Virginia, 2006. Preprint submitted to Elsevier Science (11 January 2005).

[58] René de Borst and Joris J. C. Remmers. Computational Methods for Debonding in Composites. In Pedro P. Camanho, C. G. Dávila, S. T. Pinho, and J. J. C. Remmers, editors, *Mechanical Response of Composites*, volume 10 of *Computational Methods in Applied Sciences, E. Oñate, Series editor*, chapter 1. Springer, 2008.

[59] Carl T. Herakovich. Mechanics of composites: A historical review. *Mech Res Commum*, 41:1–20, 2012.

[60] T. Kevin O'Brien. Characterization of delamination onset and growth in a composite laminate. NASA Technical Memorandum, NASA-TM-81940, NASA Langley Research Center, Hampton, Virginia, January 1981.

[61] M. F. S. F. de Moura, J. P. M. Gonçalves, A. T. Marques, and P. M. S. T. de Castro. Prediction of compressive strength of carbon-epoxy laminates containing delamination by using a mixed-mode damage model. *Compos Struct*, 50:151–157, 2000.

[62] P. P. Camanho, C. G. Dávila, and D. R. Ambur. Numerical Simulation of Delamination Growth in Composite Materials. Technical Report NASA/TM-2001-211041, NASA Langley Research Center, Hampton, Virginia, August 2001.

[63] Carlos G. Dávila and Pedro P. Camanho. Decohesion Elements using Two and Three-Parameter Mixed-Mode Criteria. In *American Helicopter Society Conference*, Williamsburg, VA, October 29–November 1, 2001.

[64] Pedro P. Camanho and Carlos G. Dávila. Mixed-Mode Decohesion Finite Elements for the Simulation of Delamination in Composite Materials. Technical Report NASA/TM-2002-211737, NASA Langley Research Center, Hampton, Virginia, June 2002.

[65] P. P. Camanho, C. G. Dávila, and M. F. de Moura. Numerical Simulation of Mixed-mode Progressive Delamination in Composite Materials. *J Compos Mater*, 37(16):1415–1438, 2003.

[66] Albert Turon, Carlos G. Dávila, Pedro P. Camanho, and Josep Costa. An Engineering Solution for using Coarse Meshes in the Simulation of Delamination With Cohesive Zone Model. Technical Report NASA/TM-2005-213547, NASA Langley Research Center, Hampton, Virginia, March 2005.

[67] A. Turon, C. G. Dávila, P. P. Camanho, and J. Costa. An Engineering Solution for solving Mesh Size Effects in the Simulation of Delamination with Cohesive Zone Models. Technical report, NASA Langley Research Center, Hampton, Virginia, 2007. Preprint submitted to Elsevier Science (16 June 2005).

[68] A. Turon, C. G. Dávila, P. P. Camanho, and J. Costa. An engineering solution for

mesh size effects in the simulation of delamination using cohesive zone models. *Eng Fract Mech*, 74:1665–1682, 2007.

[69] Michael R. Wisnom and Stephen R. Hallett. The role of delamination in strength, failure mechanisms and hole size effect in open hole tensile tests on quasi-isotropic laminates. *Compos Part A-Appl S*, 40:335–342, 2009.

[70] S. Esna Ashari and S. Mohammadi. Delamination analysis of composites by new orthotropic bimaterial extended finite element method. *Int J Numer Meth Engng*, 86:1507–1543, 2011.

[71] T. Kevin O'Brien. Analysis of local delaminations and their influence on composite laminate behavior. NASA Technical Memorandum 85728/USAAVSCOM Technical Report 83-B-6, NASA-TM-85728, NASA Langley Research Center/U.S. Army AVSCOM, Hampton, Virginia, January 1984.

[72] Carlos G. Dávila, Pedro P. Camanho, and Marcelo F. de Moura. Mixed-Mode Decohesion Elements for Analyses of Progressive Delamination. Technical Report Paper AIAA 01-1486, 42nd AIAA/ASME/ASCE/AHS/ASC Structures, Structural Dynamics and Materials Conference, Seattle, Washington, April 16–19, 2001.

[73] Carlos G. Dávila and Pedro P. Camanho. Analysis of the effects of residual strains and defects on skin/stiffner debonding using decohesion elements. Technical Report AIAA Paper 2003-1465, NASA Langley Research Center, Hampton, Virginia, 2003.

[74] M. F. S. F. de Moura, J. P. M. Gonalves, A. T. Marques, and P. M. S. T. de Castro. Modelling Compression Failure After Low Velocity Impact on Laminated Composites Using Interface Elements. *J Compos Mater*, 31(15):1462–1479, 1997.

[75] M. R. Wisnom. Size effects in the testing of fibre-composite materials. *Compos Sci Technol*, 59:1937–1957, 1999.

[76] Pedro P. Camanho, Albert Turon, Josep Costa, and Carlos G. Dávila. Simulation of delamination under high cycle fatigue in composite materials using cohesive models. Technical report, NASA Langley Research Center, Hampton, Virginia, 2006.

[77] Albert Turon, Josep Costa, Pedro P. Camanho, and Carlos G. Dávila. Simulation of Delamination Propagation in Composites Under High-Cycle Fatigue by Means of Cohesive-Zone Models. Technical Report NASA/TM-2006-214532, NASA Langley Research Center, Hampton, Virginia, December 2006.

[78] A. Turon, J. Costa, P. P. Camanho, and C. G. Dávila. Simulation of delamination in composites under high-cycle fatigue. *Compos Part A-Appl S*, 38:2270–2282, 2007.

[79] T. Kevin O'Brien. Interlaminar fracture toughness: the long and winding road to standardization. *Compos Part B-Eng*, 29B:57–62, 1998.

[80] M. R. Wisnom, B. Khan, and S. R. Hallett. Size effects in unnotched tensile strength of unidirectional and quasi-isotropic carbon/epoxy composites. *Compos Struct*, 84:21–28, 2008.

[81] R. M. O'Higgins, M. A. McCarthy, and C. T. McCarthy. Comparison of open hole tension characteristics of high strength glass and carbon fibre-reinforced composite materials. *Compos Sci Technol*, 68:2770–2778, 2008.

[82] B. G. Green, M. R. Wisnom, and S. R. Hallett. An experimental investigation into the tensile strength scaling of notched composites. *Compos Part A-Appl S*, 38:867–878, 2007.

[83] Fabrice Pierron, Ben Green, and Michael Wisnom. Full-field assessment of the damage process of laminated composite open-hole tensile specimens. Part I: Methodology. *Compos Part A-Appl S*, 38:2307–2320, 2007.

[84] F. Pierron, B. Green, M. R. Wisnom, and S. R. Hallett. Full-field assessment of the damage process of laminated composite open-hole tensile specimens. Part II: Experimental results. *Compos Part A-Appl S*, 38:2321–2332, 2007.

[85] Jim-Bum Moon, Myung-Gon Kim, Chun-Gon Kim, and Shantanu Bhowmik. Improvement of tensile properties of CFRP composites under LEO space environment by applying MWNTs and thin-ply. *Compos Part A-Appl S*, 42:694–701, 2011.

[86] Alan Nettles. C-Ply™ Bi-Angle NCF Laminate test results: Tension. Technical report, NASA — Marshall Space Center, Huntsville, Alabama, March 2012.

[87] J. Lee and C. Soutis. Thickness effect on the compressive strength of T800/924C carbon fibre-epoxy laminates. *Compos Part A-Appl S*, 36:213–227, 2005.

[88] J. Lee and C. Soutis. A study on the compressive strength of thick carbon fibre-epoxy laminates. *Compos Sci Technol*, 67:2015–2026, 2007.

[89] J. Lee and C. Soutis. Measuring the notched compressive strength of composite laminates: Specimen size effects. *Compos Sci Technol*, 68:2359–2366, 2008.

[90] C. Soutis and J. Lee. Scaling effects in notched carbon fibre/epoxy composites loaded in compression. *J Mater Sci*, 43:6593–6598, 2008.

[91] James B. Chang, Vanay K. Goyal, John C. Klug, and Jacob I. Rome. Composite Structures Damage Tolerance Analysis Methodologies. Technical Report NASA/CR-2012-217347, NASA Langley Research Center, Hampton, Virginia, March 2012.

[92] L. S. Sutherland and C. Guedes Soares. The use of quasi-static testing to obtain the low-velocity impact damage resistance of marine GRP laminates. *Compos Part B-Eng*, 2012. doi:10.1016/j.compositesb.2012.01.002.

[93] S. A. Hitchen and R. M. J. Kemp. The effect of stacking sequence on impact damage in a carbon fibre/epoxy composite. *Composites*, 26:207–214, 1995.

[94] M. O. W. Richardson and M. J. Wisheart. Review of low-velocity impact properties of composite materials. *Compos Part A-Appl S*, 27A:1123–1131, 1996.

[95] L. Reis and M. de Freitas. Damage growth analysis of low velocity impacted composite panels. *Compos Struct*, 38(1–4):509–515, 1997.

[96] M. de Freitas and L. Reis. Failure mechanisms on composite specimens subjected to compression after impact. *Compos Struct*, 42:365–373, 1998.

[97] E. V. González, P. Maimí, P. P. Camanho, C. S. Lopes, and N. Blanco. Effects of ply clustering in laminated composite plates under low-velocity impact loading. *Compos Sci Technol*, 71:805–817, 2011.

[98] Tomohiro Yokozeki, Akiko Kuroda, Akinori Yoshimura, Toshio Ogasawara, and Takahira Aoki. Damage characterization in thin-ply composite laminates under out-of-plane transverse loading. *Compos Struct*, 93:49–57, 2010.

[99] Edgar Fuoss, Paul V. Straznicky, and Cheung Poon. Effects of stacking sequence on the impact resistance in composite laminates — Part 1: parametric study. *Compos Struct*, 41:67–77, 1998.

[100] Y. Aoki, H. Suemasu, and T. Ishikawa. Damage propagation in CFRP laminates subjected to low velocity impact and static indentation. *Adv Compos Mater*, 16:45–61, 2007.

[101] Compression-After-Impact (CAI) Results of NCF Panels and "Equivalent" Aerospace Grade Laminates, January 2012.

[102] C. S. Lopes, P. P. Camanho, Z. Gürdal, P. Maimí, and E. V. González. Low-velocity impact damage on dispersed stacking sequence laminates. Part II: Numerical simulations. *Compos Sci Technol*, 69:937–947, 2009.

[103] M. J. Laffan, S. T. Pinho, P. Robinson, and L. Iannucci. Measurement of the in situ ply fracture toughness associated with mode I fibre tensile failure in FRP. Part I: Data reduction. *Compos Sci Technol*, 70:606–613, 2010.

[104] S. T. Pinho, P. Robinson, and L. Iannucci. Fracture toughness of the tensile and compressive fiber failure modes in laminated composites. *Compos Sci Technol*, 66:2069–2079, 2006.

[105] M. J. Laffan, S. T. Pinho, P. Robinson, and A. J. McMillan. Translaminar fracture toughness testing of composites: A review. *Polym Test*, 31:481–489, 2012.

[106] P. Linde. Overview of Test Prediction and Damage Simulation of Composite Aircraft Structures. In 2^{nd} *International Conference on Buckling and Postbuckling Behaviour of Composite Laminated Shell Structures*, Braunschweig, Germany, September 3–5, 2008. DLR, Institute of Composite Structures and Adaptive Systems.

[107] Ingrid Kongshavn and Anoush Poursartip. Experimental investigation of a strain-softening approach to predicting failure in notched fibre-reinforced composite laminates. *Compos Sci Technol*, 59:29–40, 1999.

[108] Xiangqian Li, Stephen R. Hallett, Michael R. Wisnom, Navid Zobeiry, Reza Vaziri, and Anoush Poursartip. Experimental study of damage propagation in Over-height Compact Tension tests. *Compos Part A-Appl S*, 40:1891–1899, 2009.

[109] G. Catalanotti, P. P. Camanho, J. Xavier, C. G. Dávila, and A. T. Marques. Measurement of resistance curves in the longitudinal failure of composites using digital image correlation. *Compos Sci Technol*, 70:1986–1993, 2010.

[110] P. P. Camanho and G. Catalanotti. On the relation between the mode I fracture toughness of a composite laminate and that of a 0° ply: Analytical model and experimental validation. *Eng Fract Mech*, 78:2535–2546, 2011.

[111] Sung Kyu Ha. Innovative design of wind turbine blades based on micromechanics of failure. *JEC Composites Magazine*, No68:78–80, October 2011. Special JEC Asia 2011.

[112] Sung Kyu Ha. Innovative design procedures for large-scale wind turbine blades. *JEC Composites Magazine*, No70:39–45, January–February 2012.

[113] MIL-HDBK-17-3F. *Composite Materials Handbook*, volume 3 of 5: Polymer Matrix Composites Materials Usage, Design and Analysis. Department of Defense Handbook, June 2002.

[114] Marc Georges Denis Geers. *Experimental Analysis and Computational Modelling of Damage Fracture.* PhD thesis, Technische Universiteit Eindhoven, Eindhoven, 1997.

[115] D. Lecompte, A. Smits, Sven Bossuyt, H. Sol, J. Vantomme, D. Van Hemelrijck, and A. M. Habraken. Quality assessment of speckle patterns for digital image correlation. *Opt Laser Eng*, 4:1132–1145, 2006.

[116] David Grégoire. *Initiation, propagation, arrêt et redémarrage de fissures sous impact.* PhD thesis, l'Institut National des Sciences Appliquées de Lyon, October 2008.

[117] GOM International AG. Bremgarterstrasse 89B, CH-8967 Widen, Switzerland.

[118] P. P. Camanho, C. M. L. Tavares, J. B. Almeida, P. M. Bandeira, P. M. Portela, and R. M. Guedes. Test plan and test procedures. Technical note ICFRP_INEGI_TN_002, INEGI, CEFAD — Structural Integrity Division, 7 November 2003.

[119] P. P. Camanho, G. H. Erçin, G. Catalanotti, S. Madhi, and P. Linde. A finite fracture mechanics model for the prediction of the open-hole strength of composite laminates. *Compos Part A-Appl S*, 43:1219–1225, 2012.

[120] Robert M. Jones. *Mechanics of Composite Materials.* Taylor & Francis, Philadelphia, PA, 2^{nd} edition, 1999.

[121] ASTM International, West Conshohocken, PA, USA. *Standard Test Method for Open Hole Tensile Strength of Polymer Matrix Composite Laminates, ASTM D 5766/D 5766M – 02a*, December 2002.

[122] P. P. Camanho and M. Lambert. A design methodology for mechanically fastened joints in laminated composite materials. *Compos Sci Technol*, 66:3004–3020, 2006.

[123] P. P. Camanho, A. Fink, A. Obst, and S. Pimenta. Hybrid tytanium-CFRP laminates for high-performance bolted joints. *Compos Part A-Appl S*, 40:1826–1837, 2009.

[124] ASTM International, West Conshohocken, PA, USA. *Standard Test Method for Bearing Response of Polymer Matrix Composite Laminates, ASTM D 5961/D 5961M–01*, November 2001.

[125] Norbert Blanco, Silvestre T. Pinho, and Paul Robinson. Design and analysis of a compact tension (CT) specimen for intralaminar fracture toughness characteriation of woven composite laminates. In *13^{th} European Conference on Composite Materials*, Stockholm, Sweden, June 2–5, 2008.

[126] Carl-Gustaf Aronsson and Jan Bäcklund. Tensile Fracture of Laminates with Cracks. *J Compos Mater*, 20:287–307, May 1986.

[127] T. K. O'Brien. Characterization of delamination onset and growth in a composite laminate. In K. L: Reifsnider, editor, *Damage in Composite Materials, ASTM STP 775*, pages 140–167. American Society for Testing and Materials, 1982.

[128] N. Zobeiry, A. Forghani, C. McGregor, R. Vaziri, and A. Poursartip. Progressive Damage Modeling of Composite Materials Under Both Tensile and Compressive Loading Regimes. In Pedro P. Camanho, C. G. Dávila, S. T. Pinho, and J. J. C. Remmers, editors, *Mechanical Response of Composites*, volume 10 of *Computational Methods in Applied Sciences, E. Oñate, Series editor*, chapter 1. Springer, 2008.

[129] Endel V. Iarve, Mark R. Gurvich, David H. Mollenhauer, Cheryl A. Rose, and Carlos G. Dávila. Mesh-independent matrix cracking and delamination modeling in laminated composites. *Int J Numer Meth Engng*, 88:749–773, 2011.

[130] Kyongchan Song, Yingyong Li, and Cheryl A. Rose. Continuum Damage Mechanics Models for the Analysis of Progressive Failure in Open-Hole Tension Laminates. Technical Report NF1676L-12382, NASA Langley Research Center, Hampton, Virginia, April 2011.

[131] A. Turon, J. Costa, P. Maimí, D. Trias, and J. A. Mayugo. A progressive damage model for unidirectional fibre-reinforced composites based on fibre fragmentation. Part I: Formulation. *Compos Sci Technol*, 65:2039–2048, 2005.

[132] A. Matzenmiller, J. Lubliner, and R. L. Taylor. A constitutive model for anisotropic damage in fiber-coposites. *Mech Mater*, 20:125–152, 1995.

[133] R. H. J. Peerlings, R. de Borst, W. A. M. Brekelmans, and M. G. D. Geers. Localisation issues in local and nonlocal continuum approaches to fracture. *Eur J Mech A-Solid*, 21:175–189, 2002.

[134] P. Ladevèze, G. Lubineau, D.Violeau, and D. Marsal. A computational damage micromodel for laminate composites. In T. Sadowski, editor, *IUTAM Symposium on Multscale Modelling of Damage and Fracture Processes in Composite Materials*, pages 1–12. Springer, 2006.

[135] Pedro P. Camanho, Joan A. Mayugo, Pere Maimí, and Carlos G. Dávila. A micromechanics-based damage model for the strength prediction of composite laminates. In C. A. Mota Soares et al., editor, *III European Conference on Computational Mechanics Solids, Structures and Coupled Problems in Engineering*, Lisbon, 5–8 June 2006.

[136] F. P. van der Meer and L. J. Sluys. A phantom node formulation with mixed mode cohesive law for splitting in laminates. *Int J Fract*, 158:107–124, 2009.

[137] F. P. van der Meer and L. J. Sluys. Interaction Between Intraply and Interply Failue Laminates. In Pedro P. Camanho, C. G. Dávila, S. T. Pinho, and J. J. C. Remmers, editors, *Mechanical Response of Composites*, volume 10 of *Computational Methods in Applied Sciences, E. Oñate, Series editor*, chapter 1. Springer, 2008.

[138] P. D. Soden, A. S. Kaddour, and M. J. Hinton. Recommendations for designers and researchers resulting from the world-wide failure exercise. *Compos Sci Technol*, 64:589–604, 2004.

[139] Carlos González and Javier Llorca. Mechanical behavior of unidirectional fiber-reinforced polymers under transverse compression: Microscopic mechanisms and modeling. *Compos Sci Technol*, 67:2795–2806, 2007.

[140] Norbert Germain, Jacques Besson, and Frédéric Feyel. Composite layered materials: Anisotropic nonlocal damage models. *Comput Method Appl M*, 196:4272–4282, 2007.

[141] Ronnie Henricus Johannes Peerlings. Enhanced damage modelling for fracture and fatigue. Technical report, Technische Universiteit Eindhoven, Eindhoven, 1999.

[142] S. T. Pinho, L. Iannucci, and P Robinson. Physically-based failure models and criteria for laminated fibre-reinforced composites with emphasis on fibre kinking. Part II: FE implementation. *Compos Part A-Appl S*, 37:766–777, 2006.

[143] E. Benvenuti. A regularized XFEM framework for embedded cohesive interfaces. *Comput Method Appl M*, 197:4367–4378, 2008.

[144] E. F. Rybicki and M. F. Kanninen. A finite element calculation of stress intensity factors by a modified crack closure integral. *Eng Fract Mech*, 9(4):931–938, 1977.

[145] J. R. Rice. A Path Independent Integral and the Approximate Analysis of Strain Concentration by Notches and Cracks. *J Appl Mech-T ASME*, pages 379–386, June 1968.

[146] D. M. Parks. A stiffness derivative finite element technique for determination of crack tip stress intensity factors. *Int J Fracture*, 10(4):487–502, December 1974.

[147] D. M. Parks. The virtual crack extension method for nonlinear material behavior. *Comput Method Appl M*, 12:353–364, 1977.

[148] James R. Rice, Robert M. McMeeking, David M. Parks, and E. Paul Sorensen. Recent finite element studies in plasticity and fracture mechanics. *Comput Method Appl M*, 17/18:411–442, 1979.

[149] F. Z. Li, C. F. Shih, and A. Needleman. A comparison of methods for calculating energy release rates. *Eng Fract Mech*, 21(2):405–421, 1985.

[150] C. F. Shih, B. Moran, and T. Nakamura. Energy release rate along a three-dimensional crack front in a thermally stressed body. *Int J Fracture*, 30:79–102, 1986.

[151] B. Moran and C. F. Shih. A general treatment of crack tip contour integrals. *Int J Fracture*, 35:295–310, 1987.

[152] B. Moran and C. F. Shih. Crack tip and associated domain integrals from momentum and energy balance. *Eng Fract Mech*, 27(6):615–642, 1987.

[153] Robert H. Dodds and Pedro M. Vargas. Numerical evaluation of domain and contour integrals for nonlinear fracture mechanics: formulation and implementation aspects. Civil Engineering Studies, Structural Research Series No. 542 UILU-ENG-88-2006, Department of Civil Engineering, University of Illinois, Urbana, Illinois, August 1988.

[154] Gerald E. Mabson, Lyle R. Deobald, Bernhard Dopker, D. M. Hoyt, Jeffrey S. Baylor, and Douglas L. Graesser. Fracture interface elements for static and fatigue analysis. In *16^{th} International Conference on Composite Materials*, Kyoto, Japan, July 8–13, 2007.

[155] C. T. Sun and Haiyang Qian. Brittle fracture beyond the stress intensity factor. *J Mech Mater Struct*, 4(4):743–753, April 2009.

[156] C. Moura Branco, A. Augusto Fernandes, and Paulo M. S. Tavares de Castro. *Fadiga de Estruturas Soldadas*. Fundação Calouste Gulbenkian, Lisboa, 2^{nd} edition, 1986.

[157] D. S. Dugdale. Yielding of steel sheets containing slits. *J Mech Phys Solids*, 8:100–104, 1960.

[158] Zdeněk Bažant and Milan Jirásek. Nonlocal Integral Formulations of Plasticity and Damage: Survey of Progress. *J Eng Mech-ASCE*, 128(11):1119–1149, November 2002.

[159] Albert Turon, Josep Costa, Pedro P. Camanho, and Pere Maimí. Analytical and Numerical Investigation of the Length of the Coehsive Zone in Delaminated Composite Materials. In Pedro P. Camanho, C. G. Dávila, S. T. Pinho, and J. J. C. Remmers, editors, *Mechanical Response of Composites*, volume 10 of *Computational Methods in Applied Sciences, E. Oñate, Series editor*, chapter 1. Springer, 2008.

[160] Carlos G. Dávila, Pedro P. Camanho, and Albert Turon. Cohesive Elements for Shells. Technical Report NASA/TM-2007-214869, NASA Langley Research Center, Hampton, Virginia, April 2002.

[161] L. C. T. Overgaard, E. Lund, and P. P. Camanho. A methodology for the structural analysis of composite wind turbine blades under geometric and material induced instabilities. *Comput Struct*, 88:1092–1109, 2010.

[162] Carlos G. Dávila, Cheryl A. Rose, and Pedro P. Camanho. A procedure for superposing linear cohesive laws to represent multiple damage mechanisms in the fracture of composites. *Int J Fract*, 158:211–223, 2009.

[163] A. Turon, P. P. Camanho, J. Costa, and J. Renart. Accurate simulation of delamination growth under mixed-mode loading using cohesive elements: Definition of interlaminar strengths and elastic stiffness. *Compos Struct*, 92:1857–1864, 2010.

[164] Essam Totry, Carlos González, and Javier Llorca. Failure locus of fiber-reinforced composites under transverse compression and out-of-plane shear. *Compos Sci Technol*, 68:829–839, 2008.

[165] Essam Totry, Carlos González, and Javier Llorca. Prediction of the failure locus of C/PEEK composites under transverse compression and longitudinal shear through computational mechanics. *Compos Sci Technol*, 68:3128–3136, 2008.

[166] A. R. Melro, P. P. Camanho, and S. T. Pinho. Generation of random distribution of fibres in long-fibre reinforced composites. *Compos Sci Technol*, 68:2092–2102, 2008.

[167] D. Trias, J. Costa, A. Turon, and J. E. Hurtado. Determination of the critical size of a statistical representative volume element (SRVE) for carbon reinforced polymers. *Acta Mater*, 54:3471–3484, 2006.

[168] D. Trias, J. Costa, J. A. Mayugo, and J. E. Hurtado. Random models versus periodic models for fiber reinforced composites. *Comp Mater Sci*, 38:316–324, 2006.

[169] Wei H. Ng, Amit G. Salvi, and Anthony M. Waas. Characterization of the in-situ non-linear shear response of laminated fiber-reinforced composites. *Compos Sci Technol*, 70:1126–1134, 2010.

[170] Marek Romanowicz. Progressive failure analysis of unidirectional fiber-reinforced

polymers with inhomogeneous interphase and randomly distributed fibers under transverse tensile loading. *Compos Part A-Appl S*, 41:1829–1838, 2010.

[171] Essam Totry, Jon M. Molina-Aldareguía, Carlos González, and Javier Llorca. Effect of fiber, matrix and interface properties on the in-plane shear deformation of carbon-fiber reinforced composites. *Compos Sci Technol*, 70:970–980, 2010.

[172] T. J. Vaughan and C. T. McCarthy. Micromechanical modeling of the transverse damage behavior in fibre reinforced composites. *Compos Sci Technol*, 71:388–396, 2011.

[173] T. J. Vaughan and C. T. McCarthy. A micromechanical study on the effect of intra-ply properties on transverse shear fracture in fibre reinforced composites. *Compos Part A-Appl S*, 42:1217–1228, 2011.

[174] T. J. Vaughan and C. T. McCarthy. A combined experimental numerical approach for generating statistically equivalent fibre distributions for high strength laminated composite materials. *Compos Sci Technol*, 70:291–297, 2010.

[175] A. R. Melro, P. P. Camanho, and S. T. Pinho. Influence of geometrical parameters on the elastic response of unidirectional composite materials. *Compos Struct*, 2012. doi: `http://dx.doi.org/10.1016/j.compstruct.2012.05.004` (in press).

[176] A. R. Melro, P. P. Camanho, F. M. Andrade Pires, and S. T. Pinho. Numerical simulation of the non-linear deformation of 5-harness satin weaves. *Comp Mater Sci*, 61:116–126, 2012.

[177] Luis Pablo Canal, Carlos González, Javier Segurado, and Javier Llorca. Intraply fracture of fiber reinforced composites: Microscopic mechanisms and modeling. *Compos Sci Technol*, 72:1223–1232, 2012.

[178] R. Talreja. Damage development in composites: mechanisms and modelling. *J Strain Anal Eng*, 24(4):215–222, 1989.

[179] Zdeněk P. Bažant and B. H. Oh. Crack band theory for fracture of concrete. *Mater Struct*, 16(93):155–177, 1983.

[180] Zdeněk P. Bažant, Yuyin Xiang, and Pere C. Prat. Microplane Model for Concrete. I: Stress-Strain Boundaries and Finite Strain. *J Eng Mech-ASCE*, 122(3):245–254, March 1996.

[181] Milan Jirásek. Nonlocal models for damage and fracture: comparison of approaches. *Int J Solids Struct*, 35(31,32):4133–4145, 1998.

[182] Ellen Kuhl, Ekkehard Ramm, and René de Borst. An anisotropic gradient damage model for quasi-brittle materials. *Comput Method Appl M*, 183:87–103, 2000.

[183] Zdeněk P. Bažant, Yuyin Xiang, Mark D. Adley, Pere C. Prat, and Stephen A. Akers. Microplane Model for Concrete. II: Data Delocalization and Verification. *J Eng Mech-ASCE*, 122(3):255–262, March 1996.

[184] M. J. Hinton and P. D. Soden. Predicting failure in composite laminates: the background to the exercise. *Compos Sci Technol*, 58:1001–1010, 1998.

[185] P. D. Soden, M. J. Hinton, and A. S. Kaddour. A comparison of the predictive capabilities of current failure theories for composite laminates. *Compos Sci Technol*, 58:1225–1254, 1998.

[186] M. J. Hinton, A. S. Kaddour, and P. D. Soden. Evaluation of failure prediction in composite laminates: background to 'part B'of the exercise. *Compos Sci Technol*, 62:1481–1488, 2002.

[187] M. J. Hinton, A. S. Kaddour, and P. D. Soden. A comparison of the predictive capabilities of current failure theories for composite laminates, judged against experimental evidence. *Compos Sci Technol*, 62:1725–1797, 2002.

[188] M. J. Hinton, A. S. Kaddour, and P. D. Soden. Evaluation of failure prediction in composite laminates: background to 'part C'of the exercise. *Compos Sci Technol*, 64:321–327, 2004.

[189] A. S. Kaddour, M. J. Hinton, and P. D. Soden. A comparison of the predictive capabilities of current failure theories for composite laminates: additional contributions. *Compos Sci Technol*, 64:449–476, 2004.

[190] M. J. Hinton, A. S. Kaddour, and P. D. Soden. A further assessment of the predictive capabilities of current failure theories for composite laminates: comparison with experimental evidence. *Compos Sci Technol*, 64:549–558, 2004.

[191] S. T. Pinho, L. Iannucci, and P Robinson. Physically-based failure models and criteria for laminated fibre-reinforced composites with emphasis on fibre kinking: Part I: Development. *Compos Part A-Appl S*, 37:63–73, 2006.

[192] J. Costa, A. Turon, D. Trias, N. Blanco, and J. A. Mayugo. A progressive damage model for unidirectional fibre-reinforced composites based on fibre fragmentation. Part II: Stiffness reduction in environment sensitive fibres under fatigue. *Compos Sci Technol*, 65:2269–2275, 2005.

[193] P. Maimí, P. P. Camanho, J. A. Mayugo, and C. G. Dávila. A continuum damage model for composite laminates: Part II — Computational implementation and validation. *Mech Mater*, 39:909–919, 2007.

[194] Miguel Bessa. Meso-mechanical model of the structural integrity of advanced composite laminates. Master's thesis, Faculty of Engineering, University of Porto, Porto, July 2010.

[195] Vinay K. Goyal, Navin R. Jaunky, Eric R. Johnson, and Damodar R. Ambur. Intralaminar and interlaminar progressive failure analyses of composite panels with circular cutouts. *Compos Struct*, 64:91–105, 2004.

[196] Emilio Vicente González Juan. *Simulation of interlaminar and intralaminar damage in polymer-based composites for aeronautical applications under impact loading*. PhD thesis, Universitat de Girona, 2010.

[197] E. V. González, P. Maimí, P. P. Camanho, A. Turon, and J. A. Mayugo. Simulation of drop-weight impact and compression after impact tests on composite laminates. *Compos Struct*, 2012. doi: `http://dx.doi.org/10.1016/j.compstruct.2012.05.015` (in press).

[198] S. Klinkel, F. Gruttman, and W. Wagner. A continuum based three-dimensional shell element for laminated structures. *Comput Struct*, 71:43–62, 1999.

[199] P. Maimí, P. P. Camanho, J. A. Mayugo, and A. Turon. Matrix cracking and delamination in laminated composites. Part II: Evolution of crack density and delamination. *Mech Mater*, 43:194–211, 2011.

[200] P. Maimí, P. P. Camanho, J. A. Mayugo, and A. Turon. Matrix cracking and delamination in laminated composites. Part I: Ply constitutive law, first ply failure and onset of delamination. *Mech Mater*, 43:169–185, 2011.

[201] G. Lubineau and P. Ladevèze. Construction of a micromechanics-based intralaminar mesomodel, and illustrations in ABAQUS/Standard. *Comp Mater Sci*, 43:137–145, 2008.

[202] P. Ladevèze and G. Lubineau. On a damage mesomodel for laminates: micro-meso relationships, possibilities and limits. *Compos Sci Technol*, 61:2149–2158, 2001.

[203] P. Ladevèze and G. Lubineau. An enhanced mesomodel for laminates based on micromechanics. *Compos Sci Technol*, 62:533–541, 2002.

[204] Pierre Ladevèze and Gilles Lubineau. On a damage mesomodel for laminates: micromechanics basis and improvement. *Mech Mater*, 35:763–775, 2003.

[205] P. Ladevèze, G. Lubineau, and D. Marsal. Towards a bridge between the micro- and mesomechanics of delamination for laminated composites. *Compos Sci Technol*, 66:698–712, 2006.

[206] Pierre Ladevèze, Gilles Lubineau, and David Violeau. A computational damage micromodel of laminated composites. *Int J Fracture*, 137:139–150, 2006.

[207] David Marsal, Pierre Ladevèze, and Gilles Lubineau. On the out-of-plane interactions between ply damage and interface damage in laminates. In T. Sadowski, editor, *IUTAM Symposium on Multscale Modelling of Damage and Fracture Processes in Composite Materials*, pages 97–104. Springer, 2006.

[208] G. Lubineau, P. Ladevèze, and D. Violeau. Durability of cfrp laminates under thermomechanical loading: A micro-meso damage model. *Compos Sci Technol*, 66:983–992, 2006.

[209] G. Lubineau, D. Violeau, and P. Ladevèze. Illustrations of a microdamage model for laminates under oxidizing thermal cycling. *Compos Sci Technol*, 69:3–9, 2009.

[210] David Violeau, Pierre Ladevèze, and Gilles Lubineau. Micromodel-based simulations for laminated composites. *Compos Sci Technol*, 69:1364–1371, 2009.

[211] Nicolas Möes, John Dolbow, and Ted Belytschko. A finite element method for crack growth without remeshing. *Int J Numer Meth Engng*, 46:131–150, 1999.

[212] N. Sukumar, N. Möes, B. Moran, and T. Belytschko. Extended finite element method for three-dimensional crack modelling. *Int J Numer Meth Engng*, 48:1549–1570, 2000.

[213] Christophe Daux, Nicolas Möes, John Dolbow, Natarajan Sukumar, and Ted Belytschko. Arbitrary branched and intersecting cracks with the extended finite element method. *Int J Numer Meth Engng*, 48:1741–1760, 2000.

[214] G. N. Wells and L. J. Sluys. A new method for modelling cohesive cracks using finite elements. *Int J Numer Meth Engng*, 50:2667–2682, 2001.

[215] Nicolas Möes and Ted Belytschko. Extended finite element method for cohesive crack growth. *Eng Fract Mech*, 69:813–833, 2002.

[216] N. Möes, A. Gravouil, and T. Belytschko. Non-planar 3D crack growth by the extended finite element and level sets — Part I: Mechanical model. *Int J Numer Meth Engng*, 53:2549–2568, 2002.

[217] E. V. Iarve. Mesh independent modelling of cracks by using higher order shape functions. *Int J Numer Meth Engng*, 56:869–882, 2003.

[218] Goangseup Zi and Ted Belytschko. New crack-tip elements for XFEM and applications to cohesive cracks. *Int J Numer Meth Engng*, 57:2221–2240, 2003.

[219] Bořek Patzák and Milan Jirásek. Process zone resolution by extended finite elements. *Eng Fract Mech*, 70:957–977, 2003.

[220] É Budyn, G. Zi, N. Möes, and T. Belytschko. A method for multiple crack growth in brittle materials without remeshing. *Int J Numer Meth Engng*, 61:1741–1770, 2004.

[221] D. B. P. Huynh and T. Belytschko. The extended finite element method for fracture in composite materials. *Int J Numer Meth Engng*, 77:214–239, 2009.

[222] Daosheng Ling, Qingda Yang, and Brian Cox. An augmented finite element method for modeling arbitrary discontinuities in composites. *Int J Fracture*, 156:53–73, 2009.

[223] Thomas-Peter Fries and Ted Belytschko. The extended/generalized finite element method: An overview of the method and its applications. *Int J Numer Meth Engng*, 84:253–304, 2010.

[224] T. Belytschko and T. Black. Elastic crack growth in finite elements with minimal remeshing. *Int J Numer Meth Engng*, 45:601–620, 1999.

[225] Pedro M. A. Areias and Ted Belytschko. Analysis of three-dimensional crack initiation and propagation using the extended finite element method. *Int J Numer Meth Engng*, 63:760–788, 2005.

[226] Timon Rabczuk, Goangseup Zi, Axel Gerstenberger, and Wolfgang A. Wall. A new crack tip element for the phantom-node method with arbitrary cohesive cracks. *Int J Numer Meth Engng*, 75:577–599, 2008.

[227] M. Kästner, G. Haasemann, J. Brummund, and V. Ulbricht. Computation of Effective Stiffness Properties for Textile-Reinforced Composites Using X-FEM. In Pedro P. Camanho, C. G. Dávila, S. T. Pinho, and J. J. C. Remmers, editors, *Mechanical Response of Composites*, volume 10 of *Computational Methods in Applied Sciences, E. Oñate, Series editor*, chapter 1. Springer, 2008.

[228] E. V. Iarve, D. Mollenhauer, and R. Kim. Theoretical and experimental investigation of stress redistribution in open hole composite laminates due to damage accumulation. *Compos Part A-Appl S*, 36:163–171, 2005.

[229] D. Mollenhauer, E. V. Iarve, R. Kim, and B. Langley. Examination of ply cracking in composite laminates with open holes: A moiré interferometric and numerical study. *Compos Part A-Appl S*, 37:282–294, 2006.

[230] D. Mollenhauer, L. Ward, E. Iarve, S. Putthanarat, K. Hoos, S. Hallet, and X. Li. Simulation of discrete damage in composite overheight compact tension specimens.

Compos Part A-Appl S, 2012. doi: `http://dx.doi.org/10.1016/j.compositesa.2011.10.020` (in press).

[231] Jeong-Hoon Song, Pedro M. A. Areias, and Ted Belytschko. A method for dynamic crack and shear band propagation with phantom nodes. *Int J Numer Meth Engng*, 67:868–893, 2006.

[232] Anita Hansbo and Peter Hansbo. A finite element method for the simulation of strong and weak discontinuities in solid mechanics. *Comput Method Appl M*, 193:3523–3540, 2004.

[233] Julia Mergheim, Ellen Kuhl, and Paul Steinmann. A finite element method for cohesive crack modelling. *Proc Appl Math Mech*, 4:350–351, 2004.

[234] J. Mergheim, E. Kuhl, and P. Steinmann. A finite element method for the computational modelling of cohesive cracks. *Int J Numer Meth Engng*, 63:276–289, 2005.

[235] J. Mergheim, E. Kuhl, and P. Steinmann. Towards the algorithm treatment of 3D strong discontinuities. *Commun Numer Meth En*, 23:97–108, 2007.

[236] Albert Turon, Pedro P. Camanho, Carlos G. Dávila, and Josep Costa. Decohesion Element for Progressive Delamination Using ABAQUS — User Manual. Technical Report SMAP 2005/01, Department of Mechanical Engineering, University of Porto, Portugal, February 2005.